



HAL
open science

The effect of minor alloying elements (Mg, Ag, Zn) on the nucleation and precipitation behaviour in AlCuLi alloys

Eva Maria Gumbmann

► **To cite this version:**

Eva Maria Gumbmann. The effect of minor alloying elements (Mg, Ag, Zn) on the nucleation and precipitation behaviour in AlCuLi alloys. Other. Université Grenoble Alpes, 2015. English. NNT : 2015GREAI092 . tel-03270748

HAL Id: tel-03270748

<https://theses.hal.science/tel-03270748v1>

Submitted on 25 Jun 2021

HAL is a multi-disciplinary open access archive for the deposit and dissemination of scientific research documents, whether they are published or not. The documents may come from teaching and research institutions in France or abroad, or from public or private research centers.

L'archive ouverte pluridisciplinaire **HAL**, est destinée au dépôt et à la diffusion de documents scientifiques de niveau recherche, publiés ou non, émanant des établissements d'enseignement et de recherche français ou étrangers, des laboratoires publics ou privés.

THÈSE

Pour obtenir le grade de

DOCTEUR DE L'UNIVERSITÉ GRENOBLE ALPES

Spécialité : **Matériaux, Mécanique, Génie civil, Electrochimie (2MGE)**

Arrêté ministériel : 7 août 2006

Présentée par

Eva Maria Gumbmann

Thèse dirigée par **Alexis Deschamps** et
codirigée par **Frédéric De Geuser**

préparée au sein du **Laboratoire des Sciences et Ingénierie des Matériaux et des Procédés**
dans l'**École Doctorale Ingénierie – Matériaux Mécanique Energétique Environnement Procédés Production (I-MEP2)**

The effect of minor alloying elements (Mg, Ag, Zn) on the nucleation and precipitation behaviour in AlCuLi alloys

Thèse soutenue publiquement le **09 novembre 2015**
devant le jury composé de :

Dr. Thierry Epicier

Directeur de recherche à l'INSA Lyon (Examineur)

Pr. Aude Simar

Professeur à l'université catholique de Louvain, Belgique (Rapporteur)

Dr. Myriam Dumont

Maître de Conférences à l'université Aix-Marseille (Rapporteur)

Dr. Anna Fraczkiewicz

Directeur de Recherche à l'École des Mines de St Etienne (Président)

Pr. Alexis Deschamps

Professeur au SIMAP (Directeur de thèse)

Dr. Frédéric De Geuser

Chargé de recherche au SIMAP (Co-encadrant)

Dr. Williams Lefebvre

Maître de Conférences à l'université de Rouen (Invité)

Dr. Christophe Sigli

Ingénieur de Recherche à Constellium (Invité)



Remerciements

Je ne suis pas de ceux qui font de grands mots, pour autant je tiens à remercier à tous ceux qui m'ont accompagnée durant ces trois dernières années, soit au travail et lors de la rédaction de ma thèse, soit pendant le temps libre. J'ai beaucoup appris pendant mes « années de doctorat » en France. J'ai amélioré mon français, j'ai goûté les meilleurs pains au chocolat, j'ai découvert le ski de rando, plein de jolis coins dans le sud et, naturellement, aussi dans le nord de la France. Je me suis faite beaucoup d'amis qui, j'espère, vont rester des amis « à vie ». En bref, la France m'est devenue une « patrie de plus » et elle va sûrement rester ma destination de vacances préférée – cela me paraît assez logique pour quelqu'un qui s'est décidée à vivre en Norvège et cherche *le* « pays complémentaire » par excellence qui est la France.

Je tiens à remercier tout particulièrement à Alexis et Fred qui m'ont accompagnée pendant ces années en France, je suis pleine de gratitude notamment pour toutes les discussions, propositions et conclusions qu'on a tirées ensemble. Je vous remercie également d'avoir eu la patience de discuter avec moi en français, même si, parfois, il fallait me répéter les choses plusieurs fois. Je suis toujours impressionnée par la rapidité avec laquelle vous répondez aux différents mails ou questions et avec quel engagement vous avez corrigé tous mes chapitres. Merci aussi pour toutes les répétitions et réunions qu'on a pu faire ensemble (même parfois à la dernière minute) – définitivement une chose qui m'a souvent permis de garder le moral. Merci !

Merci aussi au groupe Constellium pour avoir facilité ce projet et cette thèse, la mise à disposition des alliages et leur élaboration. Dans le cadre de la guidance, je veux surtout remercier Christophe Sigli qui a toujours été disponible et accessible pour discuter les résultats. Il m'a aidé à établir des contacts précieux au sein de l'entreprise pour accompagner et soutenir le mieux possible mon travail. Parmi tous ceux qui travaillent pour Constellium, je tiens surtout à dire merci à Eliane Grellier, Alain Legendre, Belen Davo et Christopher Glazerbrook.

Un grand merci aussi à Williams Lefebvre qui a passé de nombreuses heures devant le microscope avec moi à Rouen, à la recherche de précipités très petits sur des échantillons pas toujours super beaux. Cela m'a notamment permis d'apprendre à râler en français, et, par surprise, j'ai pu constater que cela marche plutôt bien. Je suis également contente d'avoir pu ajouter de nouveaux mots à ton vocabulaire!

Merci également aux rapporteurs et examinateurs d'avoir accepté de lire, d'évaluer ma thèse de doctorat et d'être venus à Grenoble pour assister à la soutenance de thèse. Merci à vous tous, pour vos commentaires, vos remarques, vos corrections qui, pour moi, représentent une source précieuse à laquelle je peux puiser aussi dans un futur.

Lors de ma thèse, on a fait des manip à l'ESRF. Dans ce contexte, je veux surtout dire merci à Nathalie Boudet et Nils Blanc et le beamline BM02 pour leur aide pendant toutes nos sessions de manipulations.

En outre je veux dire un grand merci à tous mes collègues du groupe PM qui m'ont accompagnée ces trois dernières années, parmi eux Patricia Donnadiou, Gilles Renou pour l'apprentissage du MET,

Muriel Vernon pour son aide dans la recherche des dislocations, Catherine pour notre petite collocation à Whistler, Alain pour la coupe des échantillons de toutes tailles et Marie Cheynet et Yannick Champiant avec lesquelles j'ai partagé le bureau. Merci aussi aux gestionnaires du groupe PM, surtout à Virginie Chapays, Fabienne Fonseca et Sylvie Chamapavier pour leur soutien administratif

Merci au groupe du plateforme CMTC pour leur aide et notamment merci à Florence Roubaut qui a fait des mesures innombrables à la microsonde et a toujours trouvé un créneau à la dernière minute pour faire et refaire des mesures pour moi.

Je tiens aussi à remercier à tous mes amis dont la plupart sont également mes collègues, notamment Fanny, Audrey, Maxime, Olivier, Simon, Mahmoud et Hasan. Merci Thomas et Kate pour l'organisation de nombreuses soirées chez vous et pour votre accueil incroyable en Australie. Merci Laurent pour ta grande patience, l'organisation des sorties au bar, devenues un peu moins fréquentes après ton départ, et pour ta compagnie dans notre bureau, l'endroit où tu as corrigé tant de mes emails en français. Merci Nico et Mélanie pour toutes les soirées cinéma, sushi et discours politiques. Thanks especially to Rosen, for all the discussions we were having on precipitates, aluminium, heat treatment and whatever, for your support and feedback. Thanks to Kitti, for all the sewing and knitting together and all the coffee and tea breaks we had during the past 3 years. Merci à Pauline, la meilleure stagiaire du monde, qui m'a aidé énormément pendant son stage en ayant effectué plein de manips et qui, en même temps, m'est devenue une bonne copine. Vielen Dank auch an Katharina! Es ist gut eine fränkische Verbündete im Kampf gegen den täglichen Wahnsinn zu haben. Unsere Tatortabende, Wanderungen und langen Telefonate, nachdem du mich „im Stich gelassen“ hast, werde ich nicht vergessen.

Merci aux filles de Rouen, Manon, Nooshin et Megha pour votre chaleureuse accueil. Particulièrement un grand merci à Isabelle qui m'a confortée les derniers mois à Grenoble, merci pour m'avoir remonté le morale quand c'était nécessaire, les soirées SOS pour aller boire une bière, toutes ces corrections de « mon » français et d'avoir fêté avec moi la soumission de mon manuscrit.

Ganz besonders möchte ich mich auch bei meiner Familie bedanken. Bei meinen Eltern, die ich immer anrufen konnte, wenn ich heimischen Beistand brauchte und zu denen ich jederzeit heimkommen konnte. Vielen Dank für eurer Vertrauen, eure Unterstützung und Motivation in den letzten Jahren! Auch meinen Geschwistern möchte ich danken! Es ist nicht immer leicht regelmäßig Kontakt zu halten, wenn alle in Europa verteilt sind und doch schaffen wir es ziemlich gut miteinander Verbindung zu halten –unvergesslich sind für mich das gemeinsame Wochenende in Finnland oder eure Besuche, meistens zum Ski fahren in Grenoble. Danke für eure Geschwisterliebe und dass ich bei euch jederzeit anrufen kann, egal ob etwas Dringendes ansteht, ich seelischen Beistand brauche oder einfach nur quatschen möchte.

Besonders freue ich mich über meine Großeltern, die den Weg nach Grenoble nicht gescheut haben um mich bei meiner Verteidigung zu unterstützen. Es ist wirklich fantastisch, Großeltern zu haben, die so fit sind, mit denen man diskutieren kann und die einen besuchen kommen.

Außerdem möchte ich Matthias, meinem alten Studienkollegen aus Aachen, für unermüdliche Diskussionen über Werkstofftechnik, Aachen und die Welt danken. Es freut mich sehr, dass du mich an all meinen Stationen besucht hast und sogar zur Verteidigung meiner Promotion gekommen bist.

Ich hoffe sehr, dass du natürlich auch wieder nach Norwegen kommst! Auch meinem alten Freund Tobi möchte ich danken. Nach Jahren ohne Kontakt hat uns Grenoble wieder zusammen geführt. Es ist ein unheimlich gutes Gefühl Freunde zu haben, mit denen auch über eine räumliche und zeitliche Distanz eine Verbundenheit bleibt, die jederzeit wiederbelebt werden kann! Besonders die vielen guten und auch lustigen Gespräche, die gemeinsamen Skitouren, das gemeinsame Kochen, Bügeln, Essen und natürlich das „Treiben lassen“ waren einfach super und haben ein Stück Heimat nach Grenoble gebracht!

Uten din støtte og motivasjon, hadde jeg nok ikke klart det. For alle de timene på Skype, hvor i verste fall dislokasjonsteori ble diskutert men også alt annet – fra hvor vi skal bo og hva slags kjøkkenutstyr vi trenger. Glad i deg!

Hoping that I didn't forget anyone...

Danke!

Bien à vous tous!

Eva

Résumé étendu

1. Motivation et méthodes expérimentales.....	iii
2. Cinétiques de durcissement et de précipitation	v
2.1. Caractérisation de la cinétique.....	v
2.2. La séquence de précipitation	viii
3. Analyse de la microstructure par microscopie électronique en transmission	xi
3.1. Fin de rampe.....	xi
3.2. La condition de germination	xii
3.3. La condition stabilisée	xiii
4. Couple de diffusion.....	xvii
5. Conclusion.....	xxi
6. Références	xxiii

1. Motivation et méthodes expérimentales

L'industrie aéronautique fait de nos jours face à des défis importants de réduction de poids des structures pour réduire la consommation des aéronefs. En parallèle au développement des solutions à base de composites à fibres de carbone, l'industrie de l'Aluminium a développé des alliages basés sur le système Al-Cu-Li, qui présentent une combinaison remarquable de faible densité, haute limite d'élasticité, bonne ténacité et tenue à la corrosion. Ces alliages, commercialisés sous la marque AIRWARE® par la société Constellium, doivent leurs propriétés à la présence d'une fine dispersion de précipités nanométriques, la phase principalement recherchée étant la phase $T_1 - Al_2CuLi$ qui se présente sous la forme de plaquettes d'environ 1 nm d'épaisseur pour 50 nm de diamètre, situées sur les plans {111} de la matrice. La germination efficace de cette phase durcissante entre en compétition avec d'autres précipités des sous-systèmes constituant ces alliages (comme Al-Cu et Al-Li), et nécessite des conditions particulières, en particulier la présence de dislocations (introduites par pré-déformation) et d'éléments d'alliage mineurs (Mg, Ag, Zn). Bien qu'il soit connu depuis longtemps que l'addition de ces éléments favorise la cinétique de précipitation dans ces alliages et le durcissement associé, leurs mécanismes d'action sont encore très mal compris.

L'objectif de cette thèse était donc d'étudier l'effet des éléments d'alliage mineurs (Mg,Ag,Zn) sur la germination et la précipitation dans un alliage Al-Cu-Li. Pour cela, sept alliages différents ont été investigués. La composition des alliages est donnée dans Tableau 1. L'alliage de base contient 3.5 wt% Cu et 0.9 wt% Li. Ces concentrations de Cu et Li restent identiques pour tous les alliages. Des additions de Mg, d'Ag et de Zn sont ajoutées pour clarifier leur effet sur la précipitation. L'effet combiné de (Mg et Ag) et de (Mg et Zn) et (Mg, Zn et Ag) a été également exploré.

Tableau 1: Compositions des alliages analysés dans cette étude.

	Cu	Li	Mg	Ag	Zn
AlLiCu	3.5 (3.4753)	0.9 (0.902)			
AlLiCu Mg	3.5 (3.5379)	0.9 (0.8505)	0.35 (0.3487)		
AlLiCu 0.3Ag	3.5 (3.4853)	0.9 (0.8694)		0.35 (0.3458)	
AlLiCu Mg0.3Ag	3.5 (3.4675)	0.9 (0.8849)	0.35 (0.3481)	0.35 (0.3464)	
AlLiCu Mg0.1Ag	3.5 (3.5582)	0.9 (.8778)	0.35 (0.3438)	0.11 (0.1057)	
AlLiCu MgZn	3.5 (3.5175)	0.9 (0.8838)	0.35 (0.3374)		0.6 (0.5951)
AlLiCu Mg0.1AgZn	3.5 (3.5435)	0.9 (0.8639)	0.35 (0.3358)	0.11 (0.1067)	0.6 (0.5999)

Un traitement thermomécanique est appliqué à tous les alliages pour activer la germination et précipitation et il est montré dans la Figure 1. Pour créer une solution solide sursaturée, la mise en solution est faite à température élevée, dans un four tubulaire à 505 °C pendant 30 minutes, suivie par une trempe à l'eau. Ensuite une pré-déformation de 4 % plastique est effectuée par traction, suivie de 3 jours de vieillissement naturel. Le traitement thermique de précipitation consiste ensuite en une rampe de 20 °C/h jusqu'à 155°C puis différents temps de traitement isotherme à cette température.

Pour analyser la cinétique de durcissement des alliages, la dureté Vickers a été mesurée. La diffusion des rayons X aux petits angles donne des informations sur la cinétique de précipitation. Ensuite, la microstructure pour des états du début de la précipitation (dits 'fin de rampe' et 'germination'; ce dernier correspondant à un traitement thermique de 1.5 heures à 155 °C) et pour les conditions stabilisées (de 15 à 50h à 155°C suivant les alliages) est caractérisée par microscopie électronique à transmission avec résolution atomique.

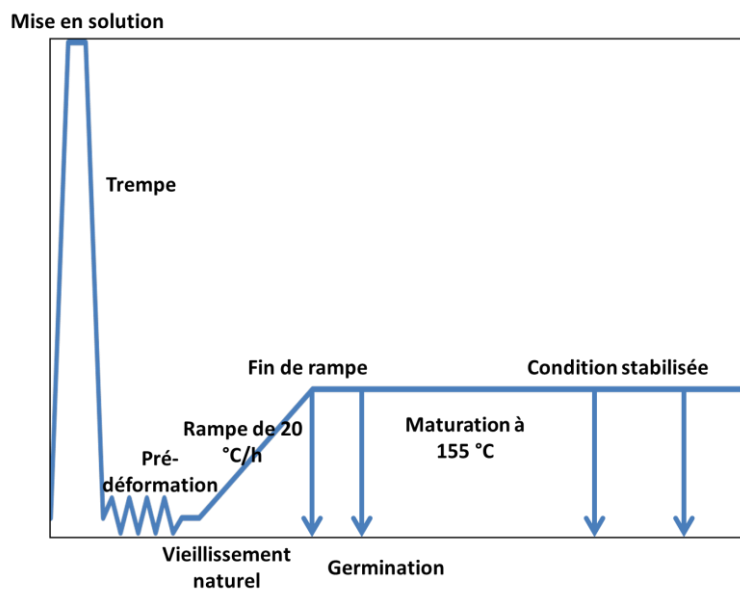


Figure 1: Schéma du traitement thermomécanique appliqué à tous les alliages.

2. Cinétiques de durcissement et de précipitation

2.1. Caractérisation de la cinétique

L'effet des éléments mineurs sur la cinétique de durcissement est présenté dans deux figures. Figure 2 présente l'effet de Mg et Ag et on voit bien que l'addition de Mg augmente la dureté directement après la pré-déformation et encore plus après 3 jours de vieillissement naturel. A ce point-là la différence en dureté est d'environ 20 HV et reste à cette valeur pendant la rampe d'échauffement jusqu'à 155°C. La continuation de la maturation à 155 °C présente une augmentation de dureté rapide pour les alliages contenant du Mg. Pour ces alliages, la valeur maximum de dureté est atteinte après environ 20 heures et l'alliage AlCuLiMg0.3Ag (173 HV) présente une dureté plus élevée, suivi par AlCuLiMg0.1Ag (170 HV) et AlCuLiMg (162 HV). Les deux alliages sans Mg augmentent presque aussi rapidement en dureté, mais leur valeur reste toujours plus basse que pour les alliages avec Mg. En plus, la valeur maximum de dureté n'est obtenue qu'après 50 heures de maturation et elle est environ 10 à 15 HV au-dessous des valeurs maximums pour les alliages avec Mg.

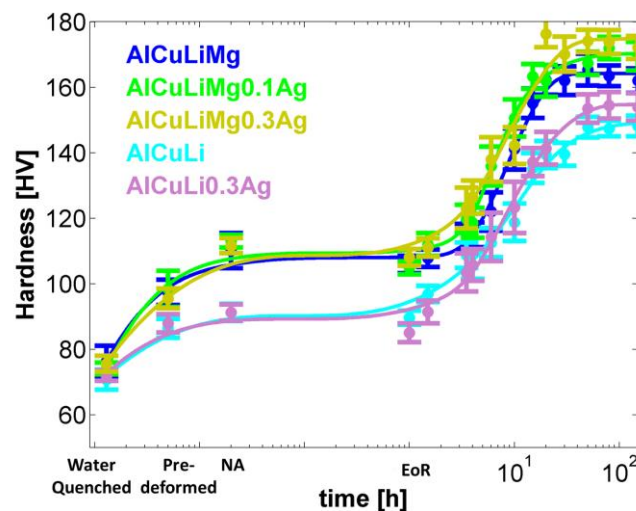


Figure 2: Comparaison de l'influence de Mg et Ag sur la cinétique de durcissement.

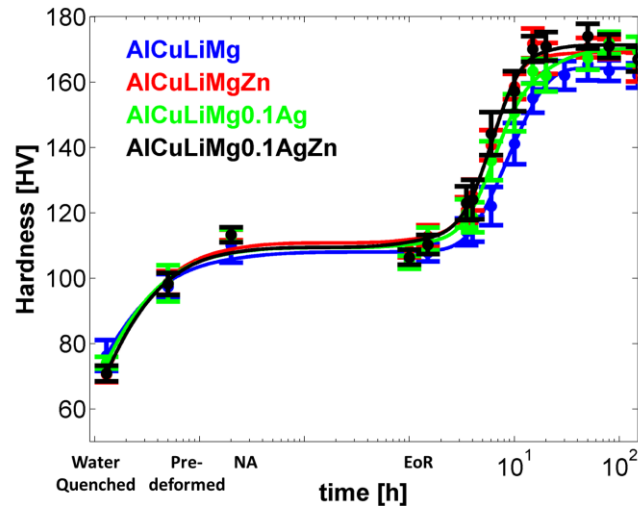
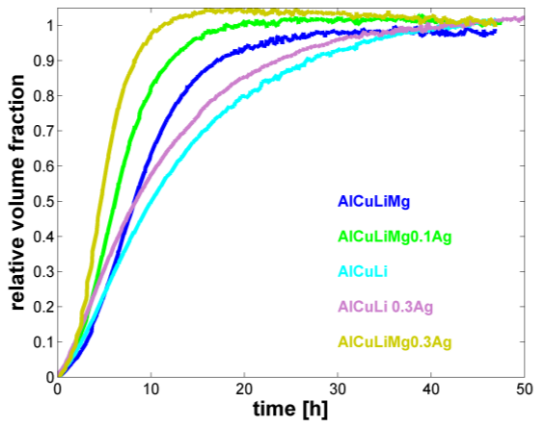


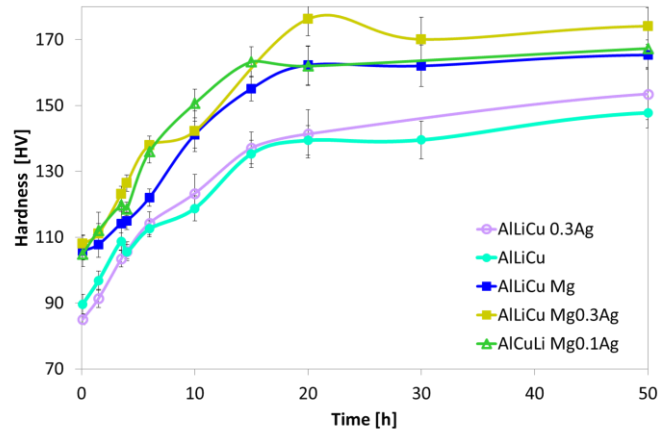
Figure 3: Comparaison de l'influence d'Ag et Zn sur la cinétique de durcissement.

La Figure 3 montre l'évolution de la dureté en comparant l'effet d'Ag et de Zn. Tous les alliages contiennent du Mg et l'augmentation de la dureté après une pré-déformation et après vieillissement naturel est similaire. On voit quand même que la présence d'Ag (courbe verte) accélère la cinétique. Cet effet est encore plus prononcé en présence de Zn (courbe rouge) ou Zn et Ag (courbe noire). La dureté maximum est obtenue pour AlCuLiMg0.1AgZn (174 HV), suivi par AlCuLiMgZn (170HV) et AlCuLiMg0.1Ag (167 HV).

Les mesures de diffusion aux petits angles permettent de déterminer l'intensité intégrée qui est proportionnelle à la fraction volumique de précipités. Pour la normalisation on suppose que la condition 'fin de rampe' ne contient aucun précipité. L'autre hypothèse est qu'après 50 heures à 155°C tous les alliages arrivent à une condition complètement précipitée et la fraction volumique est normalisée à 1. Le graphe dans la Figure 4a montre l'évolution de la fraction volumique pour les éléments mineurs Mg et Ag. Les courbes commencent à 0, ce qui correspond à la condition fin de rampe. L'augmentation de la fraction volumique est plus rapide pour les alliages avec Mg comparé aux alliages sans Mg. En plus, l'addition d'Ag accélère la précipitation en présence et en absence de Mg. A côté les courbes de dureté sont illustrées à nouveau, cette fois-ci en échelle linéaire pour mieux comparer les deux cinétiques. L'effet de Mg est frappant et le Mg influence la dureté et l'évolution de la cinétique. L'effet de l'argent est visible mais il paraît moins important que l'effet du Mg.

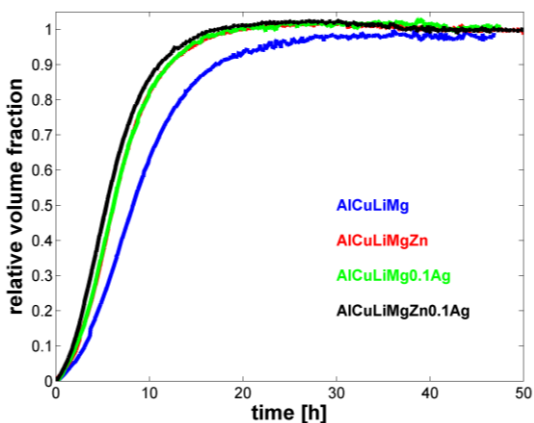


a) Evolution de la fraction volume normalisée.

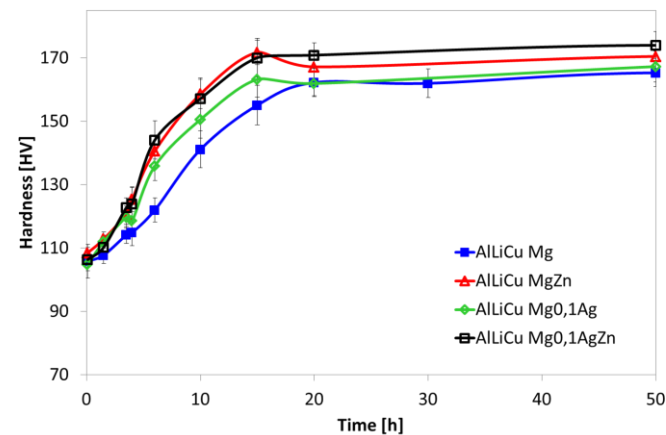


b) Mesures de dureté en échelle linéaire.

Figure 4: Comparaison de l'évolution de dureté et de la fraction volumique de précipitation pour l'influence de Mg et Ag.



a) Evolution de la fraction volume normalisée.



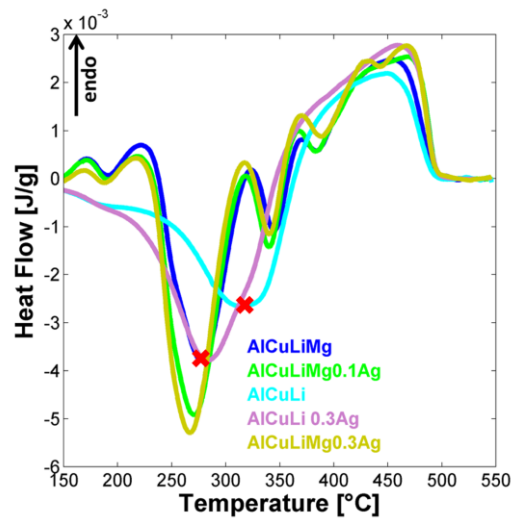
b) Mesures de dureté en échelle linéaire.

Figure 5: Comparaison de l'évolution de dureté et de la fraction volumique de précipitation pour l'influence d' Ag et Zn.

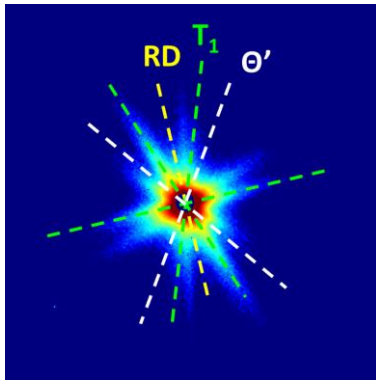
La Figure 5a montre la fraction volumique normalisée pour étudier l'effet du Zn et de l'Ag. On voit bien que l'ajout soit d'Ag, soit de Zn, soit d'Ag et de Zn accélère la cinétique comparé à AlCuLiMg. Pour ce qui est de la dureté, illustrée dans la Figure 5b en échelle linéaire, les valeurs finales sont différentes, même si la cinétique de dureté est très similaire. En normalisant la fraction volumique on perd les informations absolues des fractions volumiques. Cependant, l'intensité intégrée dépend de plusieurs facteurs comme la texture et les conditions de contraste pendant l'acquisition. La détermination de la fraction volumique en unités absolues est très difficile.

2.2. La séquence de précipitation

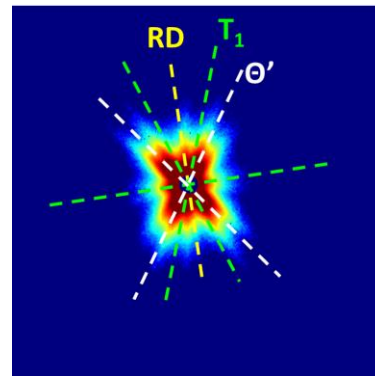
La calorimétrie différentielle à balayage effectuée à partir d'une condition de vieillissement naturel permet de caractériser la séquence complète de précipitation. Un pic exothermique correspond à un pic de précipitation et un pic endothermique respectivement à la dissolution d'une phase. La Figure 6a montre les courbes de DSC pour étudier l'influence du Mg et de l'Ag. Deux pics caractéristiques sont observés pour les alliages qui contiennent du Mg. Ces pics-là sont associés à la précipitation de la phase T_1 , comme montré par Dorin et al [1]. L'image dans la Figure 6b, prise à la température de vitesse maximale de précipitation lors du scan DSC, montre la relation d'orientation des traînées de diffusion qui sont caractéristiques de précipités en forme de plaquettes. L'orientation des traînées par rapport à la direction de laminage permet de les associer à la précipitation de la phase T_1 . Le croix rouge sur la figure 6a (courbe bleue) montre la condition dans laquelle l'image a été prise. Si on ajoute de l'Ag dans AlCuLiMg, ces pics apparaissent à une température plus faible, ce qui signifie que la précipitation est accélérée. Par contre, les pics de précipitation des alliages sans Mg se comportent très différemment. Pour comparer les deux groupes d'alliage, une image similaire à l'AlCuLiMg, c'est-à-dire à vitesse de précipitation maximale, a été prise. De la même façon, l'orientation des traînées de diffusion pour les différentes phases est indiquée et montre que non seulement T_1 précipite mais aussi θ' .



a) Calorimétrie différentielle à balayage; Influence de Mg et Ag.



b) Image SAXS du pic à 279 °C pour l'alliage AlCuLiMg



c) Image du SAXS pic à 317 °C pour l'alliage AlCuLi

Figure 6: L'influence de Mg et Ag sur la précipitation, mesurée par DSC (a). L'orientation des traînées de diffusion (streaks) des images SAXS pour AlCuLiMg(b) et AlCuLi (c) montre la différence au pic de vitesse de précipitation maximale (indiqué avec une croix rouge dans a).

Les mesures de DSC pour les additions de Zn et Ag sont présentées à la Figure 7. Tous les alliages contiennent du Mg et cependant deux pics caractéristiques pour la précipitation de T₁ sont visibles. Pour les alliages avec des additions de Zn, Ag ou (Zn et Ag) on voit que le pic apparait à une température plus basse que pour l'AlCuLiMg, indiquant que la précipitation est accélérée.

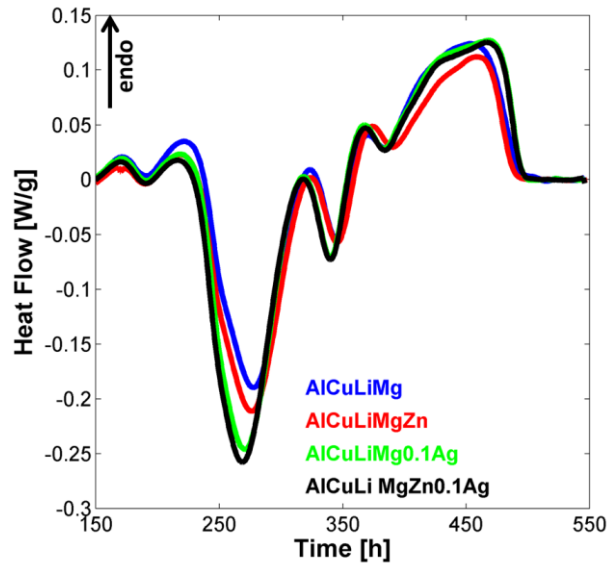


Figure 7: L'influence de Ag et Zn sur la précipitation, mesurée par DSC

3. Analyse de la microstructure par microscopie électronique en transmission

La microstructure est analysée pour trois conditions différentes, la 'fin de rampe', après germination (1.5 heures à 155 °C) et stabilisée (entre 18 – 20 heures à 155 °C pour les alliages avec du Mg et 50 heures à 155 °C pour AlCuLi).

3.1. Fin de rampe

Pour les alliages avec du Mg, les alliages AlCuLiMg0.3Ag et AlCuLiMg0.1AgZn ont été investigués. Les Figure 8 et Figure 9 montrent des images en champs sombre annulaire à grand angle (HAADF) dans les axes de zones $\langle 001 \rangle$ pour AlCuLiMg0.1AgZn et $\langle 011 \rangle$ pour AlCuLiMg0.3Ag. Le contraste vu dans la Figure 8 indique qu'il y a des ségrégations de cuivre, sans doute associées à du Mg sur les dislocations. Une examination plus attentive montre la présence d'une structure, ce qui indique que des précurseurs se forment déjà sur les dislocations malgré ces temps très court de traitement thermique. Ces phases précurseur ont été aussi observées pour AlCuLiMg0.3Ag. Dans la Figure 9 on voit la présence d'un précipité de T_1 . L'observation de cette phase dans cette condition est cependant très rare, et est toujours associée à la présence d'un défaut cristallin, comme un sous-joint de grains ou le champ de contrainte associé à une dislocation. Pour l'alliage AlCuLiMg0.3Ag, les précipités T_1 sont décorés par des atomes d'argent à l'interface du précipité avec la matrice.

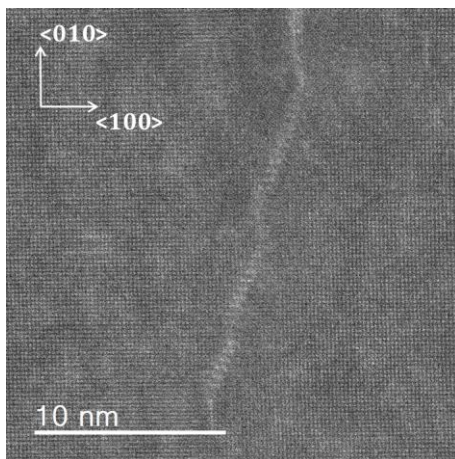


Figure 8: AlCuLiMg0.1AgZn observé en axe de zone $\langle 001 \rangle$.

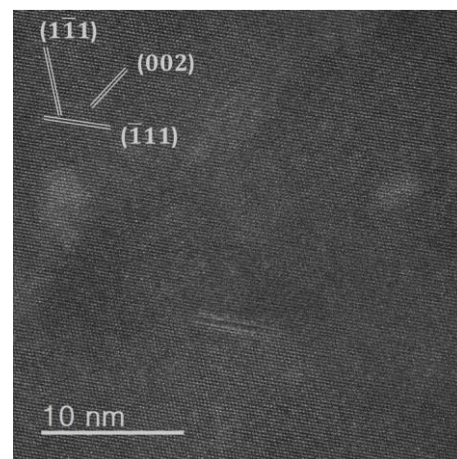


Figure 9: AlCuLiMg0.3Ag observé en axe de zone $\langle 110 \rangle$.

Les observations de l'alliage AlCuLi sont présentées dans les Figure 10 et Figure 11 pour les axes de zones $\langle 001 \rangle$ et $\langle 110 \rangle$ respectivement.

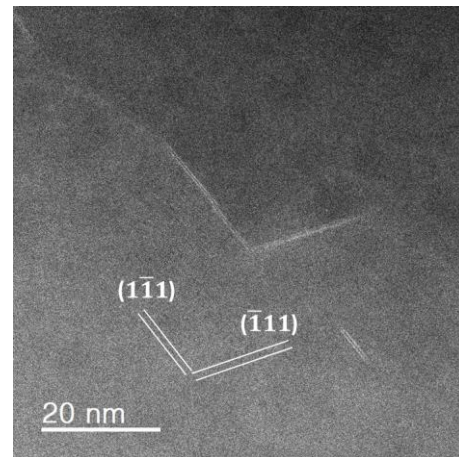
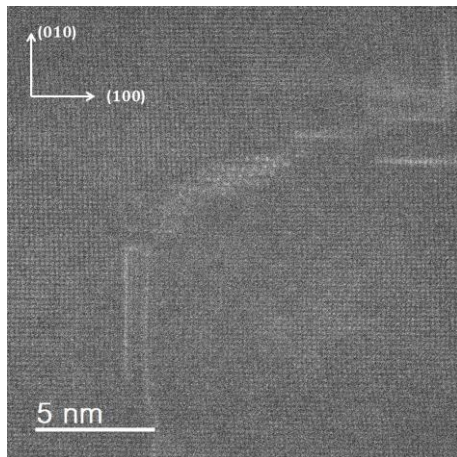


Figure 10: AlCuLi observé en axe de zone $\langle 001 \rangle$. Figure 11: AlCuLi observé en axe de zone $\langle 110 \rangle$.

Cette fois-ci, on ne voit que des zones GP qui probablement sont connectées à une dislocation. Par contre on ne voit pas des phases structurées comme observées dans la Figure 8. L'observation en axe de zone $\langle 110 \rangle$ met en évidence la présence sporadique de phases T_1 qui sont, comme dans les alliages avec Mg, associées aux défauts cristallins, ici aux dislocations.

3.2. La condition de germination

Pour la condition de germination (1,5h à 155°C), AlCuLiMg0.3Ag et AlCuLi ont été investigués. L'observation en axe de zone $\langle 011 \rangle$ indique la présence de la phase T_1 dans les deux alliages. Elle est associée aux défauts cristallins et surtout trouvée connectée aux dislocations. La densité numérique de ces précipités T_1 apparaît plus élevée que pour la condition 'fin de rampe', mais ce n'est qu'une observation qualitative qui n'a pas été vérifiée quantitativement à cause d'un nombre insuffisant de précipités observés pour obtenir des statistiques satisfaisantes. On observe pour AlCuLiMg0.3 des ségrégations d'Ag à l'interface entre la matrice et les précipités T_1 . Les images en axe de zone $\langle 011 \rangle$ sont présentées dans le document principal de la thèse. Par ailleurs, l'investigation de ces alliages en axe de zone $\langle 001 \rangle$ montre des différences importantes, illustrées en Figure 12 pour AlCuLiMg0.3Ag et Figure 13 pour AlCuLi. Pour AlCuLiMg0.3Ag, la structure des précurseurs peut être analysée et est indiquée dans la Figure 12. L'orientation des précurseurs avec la matrice est mesurée pour deux phases à la Figure 12 et correspond très bien à la phase S' du système AlCuMg [2], [3]. Cela nous permet d'affirmer que ces phases contiennent Cu et Mg et on peut supposer qu'il s'agit des précipités S' . Des phases inclinées sont aussi trouvées dans AlCuLi comme illustré à la Figure 13. L'angle d'inclinaison est assez proche avec la relation d'orientation 2 pour la phase S' . Par contre, comme il n'y a pas de Mg on suppose que ces phases sont du θ' . La déviation de l'orientation par rapport au plan d'habitat habituel de cette phase peut être expliquée par la présence des dislocations qui met en place des sites hétérogènes de germination.

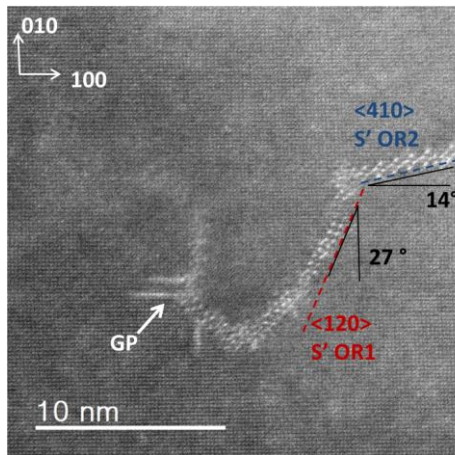


Figure 12: AlCuLiMg0.3Ag observé en axe de zone <001>.

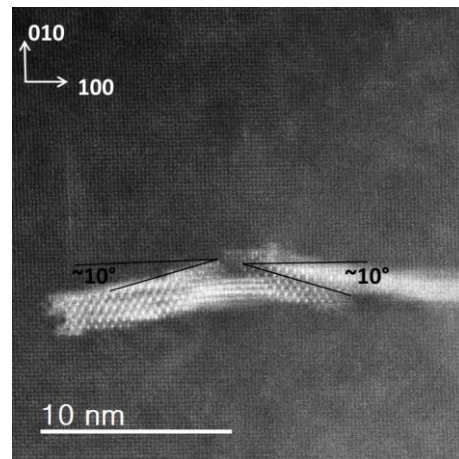


Figure 13: AlCuLi observé en axe de zone <001>.

3.3. La condition stabilisée

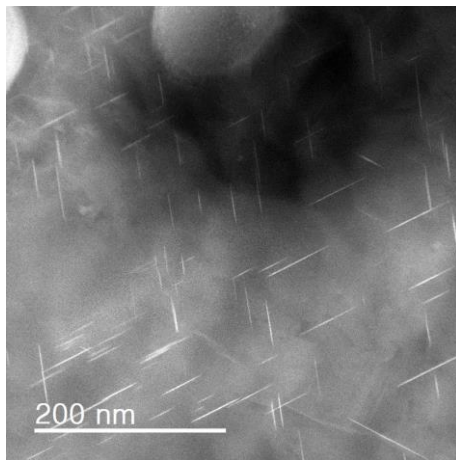


Figure 14: Distribution dense de la phase T_1 dans AlCuLiMg0.3Ag.

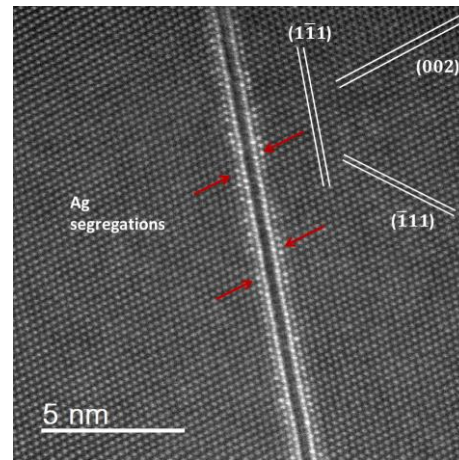


Figure 15: La phase T_1 dans AlCuLiMg0.3Ag en axe de zone <011>. Les ségrégations d'Ag sont bien visibles à l'interface de T_1 avec la matrice.

La phase T_1 dans l'alliage AlCuLiMg0.3Ag est la phase principale qui a précipité dans cette condition, comme le montre la distribution homogène illustrée à la Figure 14. L'image montre deux variants de la phase T_1 dont le plan d'habitat est $\{111\}$, comme l'axe de zone est en direction $\langle 110 \rangle$. On voit la phase T_1 à plus haute résolution à la Figure 15. Les points brillants qui décorent l'interface entre la

phase T_1 et la matrice indiquent la ségrégation d'Ag. Ces ségrégations sont présentes pour toutes les conditions analysées dans cet alliage.

La condition stabilisée dans l'alliage AlCuLiMg0.1AgZn montre la présence de précipités non-ordonnés en relation avec des précipités bien structurés, présents sur les dislocations. L'orientation de la phase structurée par rapport à la direction $\langle 001 \rangle$ indique qu'il s'agit de la phase S' . La phase non-ordonnée correspond probablement à la phase GPB, qui a été investiguée par [3]–[5]. On voit sur le côté gauche un précipité θ'' qui peut être distingué par 2 plans de cuivre séparés par 3 plans d'aluminium.

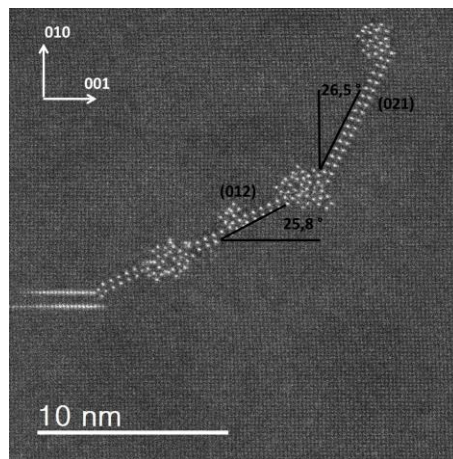


Figure 16: Présence de phases S' et GPB dans AlCuLiMg0.1AgZn observé en axe de zone $\langle 001 \rangle$.

La phase T_1 est également la phase principale qui a précipité dans l'alliage AlCuLiMg0.1AgZn (l'image n'est pas montrée ici). L'analyse EDX pour la phase T_1 aide à identifier les éléments associés à la phase T_1 . La Figure 17a montre un précipité en mode HAADF et la cartographie des éléments de Mg en b et de Zn en c respectivement. On voit bien que le Mg est présent dans la matrice, mais il est aussi ségrégué dans le précipité. De même dans la Figure 17c, on observe une forte association du Zn au précipité T_1 . Par contre, on ne peut pas identifier par manque de résolution quelle position atomique dans le précipité est adoptée préférentiellement par les éléments mineurs.

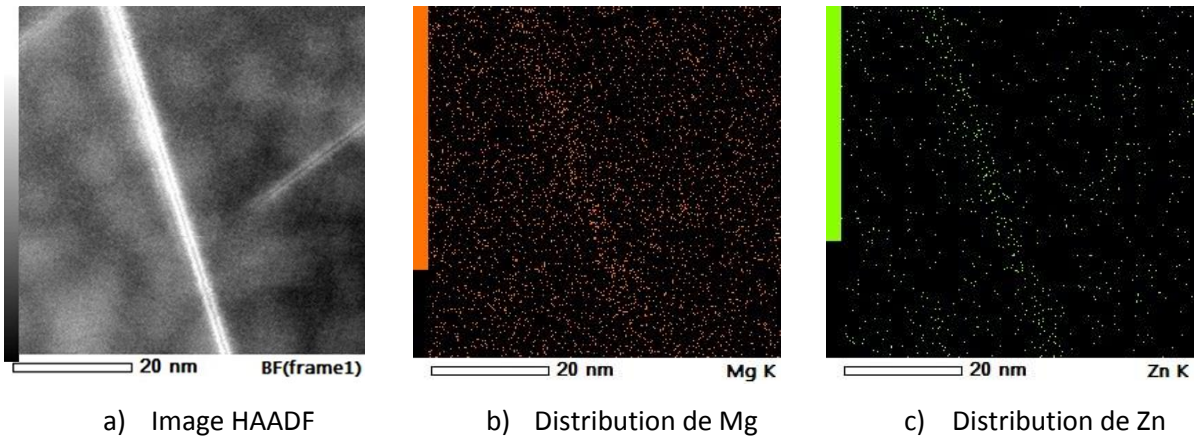
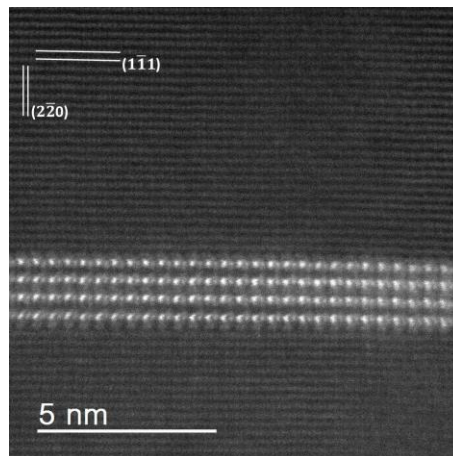


Figure 17: Image en mode HAADF d'un précipité T_1 dans l'alliage AlCuLiMg0.1Ag (a). Les images b et c montre la distribution des atomes de Mg et Zn respectivement mesurés par EDS.

L'alliage AlCuLi montre également la précipitation de la phase T_1 . De plus, on trouve facilement la phase T_1 en double épaisseur dans cette condition. La Figure 18a montre un précipité T_1 en double épaisseur observé en axe de zone $\langle 112 \rangle$.



a) T_1 épaisi en mode HAADF

Figure 18: La phase T_1 épaisie dans l'alliage AlCuLi dans l'axe de zone $\langle 112 \rangle$.

La phase θ' qu'on peut observer en direction $\langle 001 \rangle$ est présente en grande quantité dans cette condition-là (Figure 19). Même à faible grandissement, on observe que cette phase peut être inclinée par rapport aux directions $\langle 100 \rangle$. L'investigation plus détaillée est illustrée dans la Figure 20. La phase θ' est entourée par la phase δ' ce qui est bien visible quand θ' est aligné en direction $\langle 001 \rangle$.

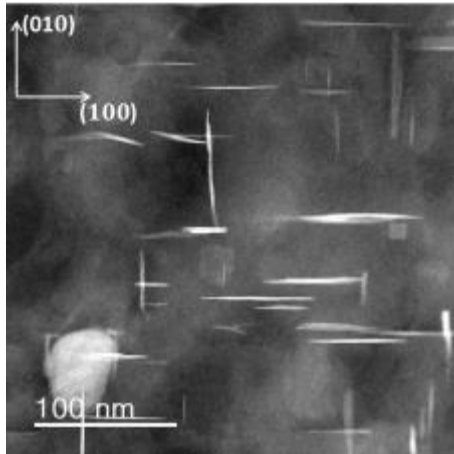


Figure 19: Quantité importante de la phase θ' , observée en axe de zone $\langle 001 \rangle$.

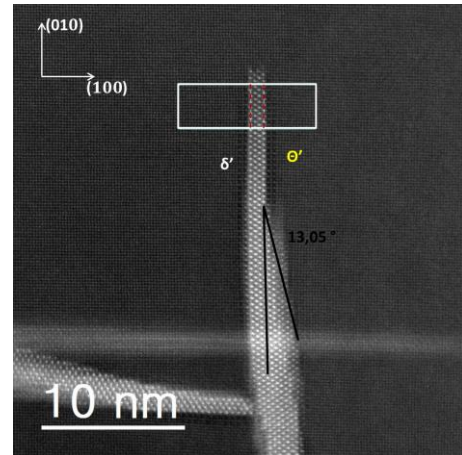


Figure 20: La phase θ' ayant bien évolué et en partie inclinée. Elle est enveloppée par la phase δ' .

4. Couple de diffusion

Pour étudier l'effet de la concentration d'un élément mineur sur la précipitation, des couples de diffusion ont été fabriqués par soudage par friction linéaire. Après le soudage, un traitement thermique à 515 °C pendant 15 jours est effectué pour créer un gradient de concentration qui est ensuite encore élargi par laminage. L'évolution du gradient est montrée dans la Figure 21 pour le couple AlCuLi / AlCuLiMg et le gradient final a une largeur de 10 mm.

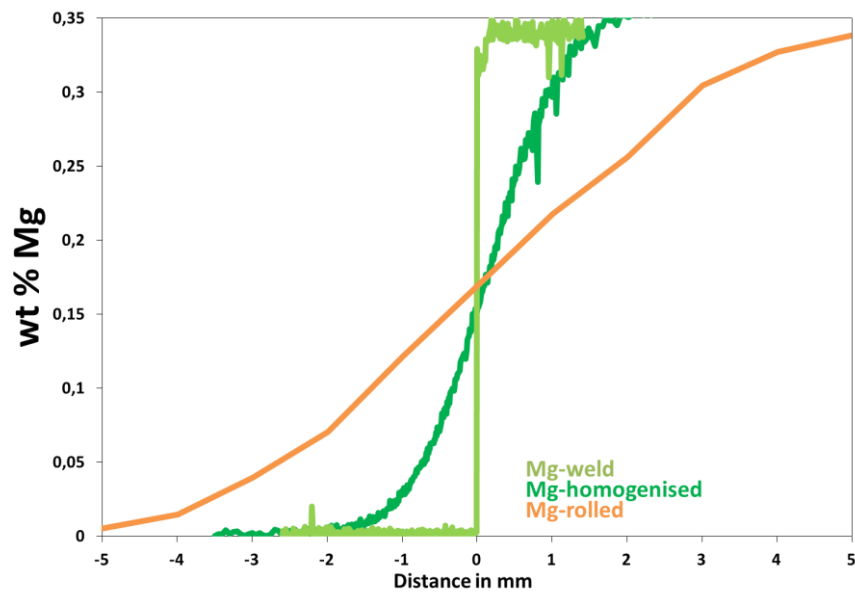


Figure 21: Evolution du gradient de concentration après le soudage (courbe verte), le traitement thermique (courbe vert foncé) et le laminage (courbe orange) pour le couple AlCuLi / AlCuLiMg.

L'effet de Mg sur la cinétique de dureté et de précipitation est caractérisé par dureté et SAXS, en suivant la même procédure de traitement thermomécanique que pour les alliages individuels présentés auparavant.

Les mesures de dureté en travers du gradient de concentration montrent que la dureté est toujours plus basse sur le côté qui ne contient pas de Mg. Des conditions différentes pendant le traitement thermique sont indiquées dans la Figure 22. La dureté augmente progressivement avec l'augmentation de la concentration en Mg.

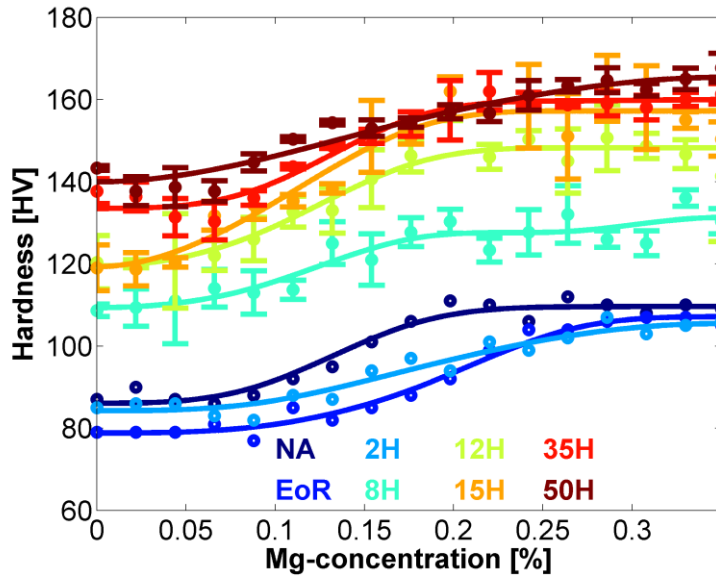


Figure 22: Dureté en travers du gradient de concentration.

Pour mieux illustrer la cinétique en fonction de la concentration dans le gradient, la dureté est tracée en fonction du temps de vieillissement pour certaines concentrations de Mg. On identifie une augmentation de cinétique de dureté assez abrupte à partir de la présence de 0.1 wt% de Mg. Les résultats de mesures de SAXS présentent la fraction volumique normalisée en fonction du temps de traitement thermique et sont présentés dans la Figure 24. La cinétique de précipitation change également brusquement lorsqu'on dépasse la concentration seuil de 0.1 wt% Mg.

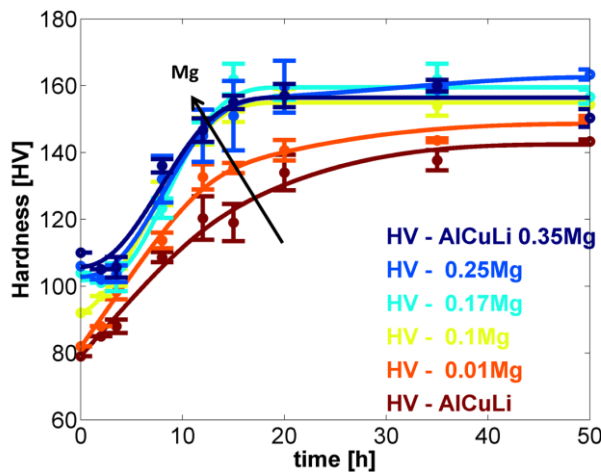


Figure 23: La cinétique de dureté pour des concentrations de Mg différentes.

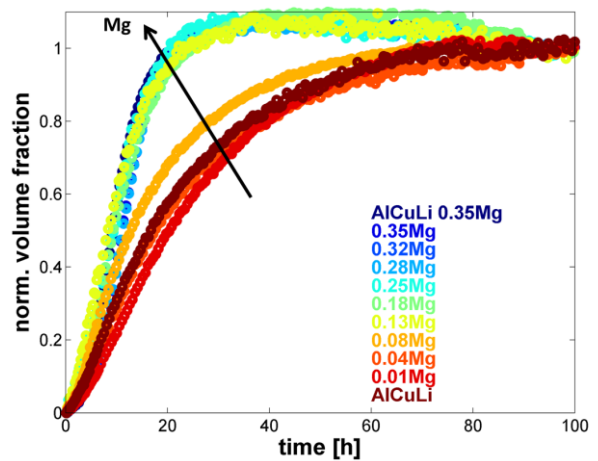


Figure 24: La cinétique de précipitation pour des concentrations de Mg différentes.

Ces résultats montrent bien qu'il existe une valeur seuil d'environ 0.1 wt %Mg. Au-dessous de cette valeur la précipitation est plus lente et de la même façon les duretés obtenues sont plus basses. Au-delà de cette valeur l'addition de plus de Mg ne change presque plus le durcissement ou la cinétique de précipitation.

Le couple de diffusion entre AlCuLi0.3Ag et AlCuLi0.3AgMg, qui contient également un gradient de concentration de Mg, présente le même comportement. A partir de 0.1 wt %Mg la cinétique est accélérée et des valeurs de dureté plus élevées sont mesurées.

Le couple de diffusion AlCuLiMg / AlCuLiMg0.3Ag contient une quantité constante de Mg et un gradient d'Ag d'une largeur d'environ 10mm. L'influence d'Ag est très faible et n'affecte ni la cinétique, ni la dureté (voir Figure 25), ni la précipitation (pas montrée ici). Par contre les duretés finales sont légèrement plus élevées comme montré à la Figure 25.

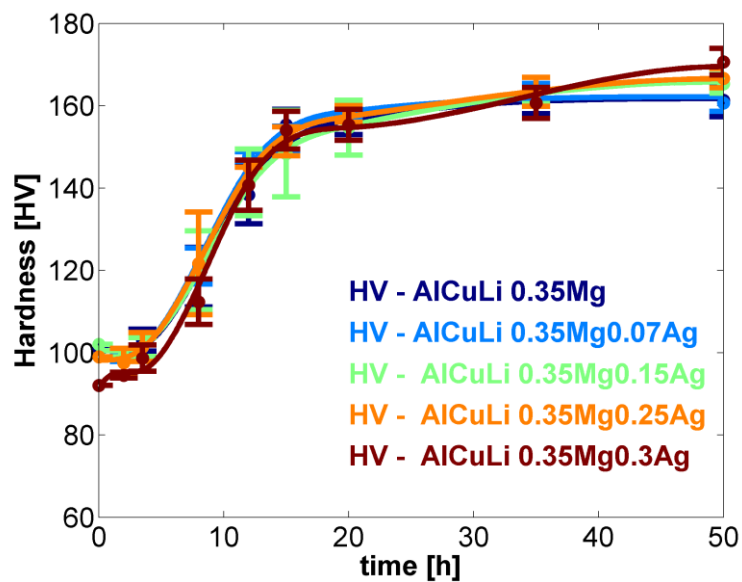


Figure 25: Evolution de la dureté pour des concentrations différentes d'Ag.

5. Conclusion

La Figure 26 présente un schéma montrant la manière dont les éléments mineurs affectent la précipitation dans les alliages AlCuLi. On suppose que la microstructure de départ est identique pour tous les alliages comme le même traitement thermomécanique a été appliqué. Au stade de germination, l'effet du Mg est prédominant sur les cinétiques de précipitation et de durcissement. Dans ces conditions de vieillissement précoce, on observe que les dislocations sont décorées par des précurseurs de type S' , et on forme donc l'hypothèse que la présence de ces précurseurs assiste la germination de la phase T_1 . En l'absence de Mg, les sites de germination sur les dislocations sont occupés très tôt par la phase θ' . Or cette phase entre en compétition avec T_1 pour le soluté limitant la cinétique qui est le Cu. Il semble que la nature de la phase précipitée sur les dislocations joue un rôle important pour la suite de la précipitation. Pour que la phase T_1 , soit la phase principale pendant la précipitation il faut ajouter du Mg, car en son absence les dislocations sont couvertes rapidement par la phase θ' . La précipitation et croissance de θ' va désormais dominer la microstructure. L'analyse des couples de diffusion suggère qu'il suffit d'ajouter environ 0.1 wt% Mg pour activer la cinétique de précipitation de la phase S' sur les dislocations, et en conséquence de T_1 . En présence de Mg, la poursuite du traitement thermomécanique montre l'effet des autres éléments c'est-à-dire l'Ag et le Zn. Les observations MET ont permis d'identifier que l'Ag s'accumule à l'interface entre la matrice du précipité et que le Zn est incorporé dans T_1 . Leur effet sur la cinétique de précipitation n'a pas pu être entièrement résolu. Il est possible qu'ils diminuent les contraintes de cohérence entre la matrice et les précipités, ou bien qu'ils jouent sur l'énergie d'interface de ceux-ci. Il est aussi connu que l'addition de Mg et Ag diminue l'énergie de faute d'empilement dans l'Al [6]. La formation de la phase T_1 est associée avec un mécanisme par faute d'empilement [7], [8] et il est donc possible que leur addition diminue la barrière de germination. Cependant, cette interprétation est sans doute trop simple en présence des précurseurs qui précède la germination de T_1 . Pour ce qui est du lien entre précipitation et durcissement, le mécanisme de renforcement se produit par le cisaillement de la phase T_1 [1]. Quand l'Ag et le Zn sont ajoutés, les valeurs de dureté sont plus élevées dans la condition stabilisée. L'énergie de cisaillement d'un précipité T_1 par une dislocation peut dépendre de l'addition d'éléments d'alliage mineurs, qui changent les paramètres énergétiques du précipité (en volume ou à l'interface). L'effet sur la dureté a été aussi observé dans le couple de diffusion avec une variation de la proportion d'Ag. La cinétique de précipitation ne dépend que très peu de la présence d'Ag par contre les duretés obtenues à la fin du traitement thermique augmentent continûment avec la concentration en Ag.

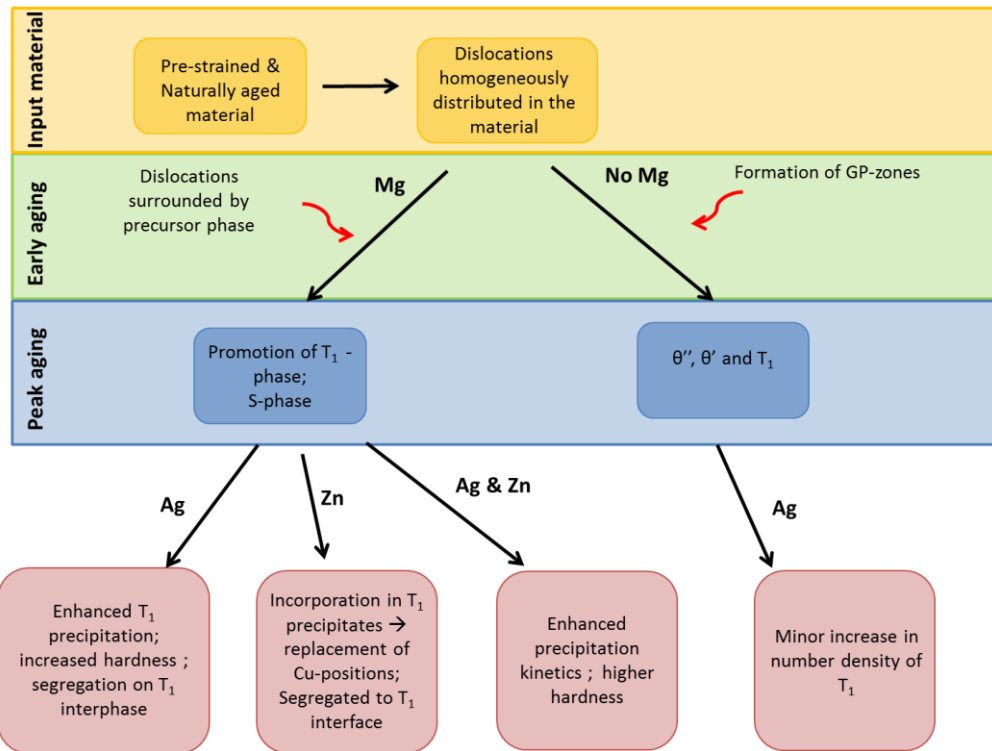


Figure 26: L'influence des éléments mineurs sur la séquence de la précipitation.

6. Références

- [1] T. Dorin, A. Deschamps, F. De Geuser, W. Lefebvre, and C. Sigli, "Quantitative description of the T1 formation kinetics in an Al–Cu–Li alloy using differential scanning calorimetry, small-angle X-ray scattering and transmission electron microscopy," *Philosophical Magazine*, vol. 0, no. 0, pp. 1–19.
- [2] G. B. Winkelman, K. Raviprasad, and B. C. Muddle, "Orientation relationships and lattice matching for the S phase in Al–Cu–Mg alloys," *Acta Materialia*, vol. 55, no. 9, pp. 3213–3228, May 2007.
- [3] Y. Bagaryatsky, "Mechanism of Artificial Aging of Al-Cu-Mg Alloy," *Doklady Akad Nauk SSSR*, pp. 397–400, 1952.
- [4] J. Silcock, "The structural ageing characteristics of Al–Cu–Mg alloys with copper: magnesium weight ratios of 7: 1 and 2.2: 1," *J. Inst. Met*, vol. 89, pp. 203–210, 1960.
- [5] L. Kovarik, S. A. Court, H. L. Fraser, and M. J. Mills, "GPB zones and composite GPB/GPBII zones in Al–Cu–Mg alloys," *Acta Materialia*, vol. 56, no. 17, pp. 4804–4815, Oktober 2008.
- [6] T. C. Schulthess, P. E. A. Turchi, A. Gonis, and T.-G. Nieh, "Systematic study of stacking fault energies of random Al-based alloys," *Acta Materialia*, vol. 46, no. 6, pp. 2215–2221, März 1998.
- [7] W. A. Cassada, G. J. Shiflet, and E. A. Starke, "Mechanism of Al₂CuLi (T 1) nucleation and growth," *Metallurgical Transactions A*, vol. 22, no. 2, pp. 287–297, Feb. 1991.
- [8] J. M. Howe, J. Lee, and A. K. Vasudévan, "Structure and deformation behavior of T 1 precipitate plates in an Al- 2Li- 1 Cu alloy," *Metallurgical Transactions A*, vol. 19, no. 12, pp. 2911–2920, Dec. 1988.

General content

Introduction.....	5
1. Literature review	11
1.1. Classification of aluminium alloys	11
1.2. Precipitation reactions	11
1.3. Influence on precipitation – heterogeneous nucleation.....	13
1.4. Overview of precipitating phases from different phase systems	14
1.4.1. The Al-Cu system	14
1.4.2. The Al-Li system.....	16
1.4.3. The Al-Cu-Mg – system.....	17
1.4.4. Al-Cu-Mg-Ag system	20
1.4.5. Al-Cu-Li system: the T_1 structure	20
1.5. The effect of minor alloying elements in heat-treatable aluminium alloys.....	23
1.6. New generation of Al-Cu-Li alloys	26
1.7. Competition between different phases in Al-Cu-Li-X alloys.....	26
1.7.1. The effect of pre-deformation	27
1.7.2. The effect of Li and Cu.....	28
1.7.3. The effect of Mg and Ag	28
1.7.4. The effect of Zn.....	30
1.8. Summary.....	31
2. Materials and experimental methods.....	33
2.1. Analysed material.....	33
2.2. Heat treatment.....	33
2.3. Hardness.....	36
2.4. Transmission electron microscopy.....	36
2.4.1. Conventional TEM	37
2.4.2. HAADF-STEM	39
2.4.3. EDS spectroscopy	41
2.4.4. Observations directions in Al-Cu-Li alloys	41
2.4.5. Equipment and sample preparation.....	43
2.5. Small Angle X-ray Scattering.....	44
2.5.1. Analysis.....	46

2.5.2.	Equipment and sample preparation.....	50
2.6.	Microprobe.....	52
2.6.1.	Set-up and basic design.....	52
2.6.2.	Equipment and sample preparation.....	53
2.7.	Differential Scanning calorimetry.....	53
3.	Influence of minor alloying elements on precipitation kinetics.....	55
3.1.	Precipitation kinetics measured by hardness	55
3.2.	Precipitation kinetics measured by Small Angle X-ray scattering	57
3.3.	Results of DSC measurements.....	63
3.3.1.	Difference between Mg and Mg-free alloys.....	63
3.3.2.	Influence of heating rate	67
3.4.	Further analysis	68
3.4.1.	Normalisation of SAXS volume fraction by DSC measurements for Mg containing alloys 68	
3.4.2.	Summary.....	72
4.	Microstructure analysis of different aging conditions.....	73
4.1.	Observation of different phases in AlCuLi alloys - orientations of the sample.....	73
4.2.	Precipitation distribution after aging –‘stabilised’ condition.....	73
4.3.	The ‘End of Ramp’ condition	80
4.3.1.	AlCuLiMg0.3Ag	80
4.3.2.	AlCuLi Mg0.1AgZn.....	86
4.3.3.	AlCuLi	89
4.4.	The ‘nucleation’ condition.....	91
4.4.1.	AlCuLiMg0.3Ag	92
4.4.2.	AlCuLi	94
4.5.	The ‘stabilised’ condition	97
4.5.1.	AlCuLiMg0.3Ag	97
4.5.2.	AlCuLi Mg0.1AgZn.....	98
4.5.3.	AlCuLi	102
4.6.	‘Thickened’ condition –AlCuLiMgZn.....	107
4.6.1.	‘Stabilised’ condition of AlCuLiMgZn.....	107
4.6.2.	‘Thickened’ condition of AlCuLiMgZn.....	110
4.7.	Summary.....	113
5.	Diffusion couples as a tool to map compositional space.....	115
5.1.	Processing and microstructural observations of the weld.....	118
5.1.1.	Processing of diffusion couples	118
5.1.2.	Microstructure of the weld	119
5.2.	Precipitation kinetics in the diffusion couples	120

5.3.	Diffusion of Mg.....	123
5.3.1.	AlCuLi vs. AlCuLi Mg.....	124
5.3.2.	AlCuLi0.3Ag vs. AlCuLi0.3Ag Mg.....	127
5.4.	Diffusion of Ag: AlCuLiMg vs. AlCuLiMg0.3Ag.....	131
5.5.	Summary.....	133
6.	Discussion	135
6.1.	The effect of the addition of Mg on precipitation and strengthening.....	135
6.2.	The effect of Ag and Zn on precipitation and strengthening	146
6.2.1.	Influence of Ag addition in the Mg-free alloy	146
6.2.2.	Influence of the addition of Zn and Ag in the presence of Mg.....	147
7.	Conclusion.....	155
	References	159
	Appendix I - Hardening kinetics at 140°C	167
	Appendix II.....	171

Introduction

In the aerospace industry the main drivers for improving the material performance are reducing fuel consumption, reducing the maintenance costs and ensuring maximum safety. In terms of structural components, there has been a continuing effort to decrease the weight of structures, which involves improving the specific properties of materials in combination to optimizing the components design. The last generation of large civil aircrafts has seen the reduction of the aluminium share of the structural components to the benefit of carbon-based composites, which were claimed at the time of their introduction to offer a much higher potential for weight saving and maintenance cost reduction. In response to this major material shift, the aluminium industry has responded by developing new solutions for aircraft structures, based on new alloy formulations together with a high level of integration to the user's needs including scrap recycling, improved design etc. This integrated alloy solution, called AIRWARE™, is now present on numerous major airplane programs.

The addition of 1 wt% Li to aluminium decreases the alloy density up to 3 % and at the same time increases the Young's modulus by 6 % [1]–[3]. This exceptional set of effects has been recognised quite early on, and has driven the interest for Al-Li alloys in the aerospace industry, whether for space crafts (rockets or shuttles), or airplanes. The interest of applying Al-Li alloys is presented in the following example. The evolution of US space shuttle tanks is described, as used in the expendable launch systems Atlas V & Delta IV NEELV. The first generation of this space shuttle tank was made of AA2219 (an Al-Cu based alloy). For the third generation of the space shuttle tank, a weight reduction of 7500 pounds which corresponds to 11 % could be achieved thanks to the application of an Al-Cu-Li alloy, AA2195. Compared to the former tank it was 30 % stronger and at the same time 5 % less dense [4].

The first two generations of Al-Li alloys contained high Li additions (> 2 wt%), their design was aiming to take advantage of the low density. In Figure 1 they are positioned in the upper left part and Figure 2 points out their material's properties. However, detrimental properties such as anisotropy of mechanical properties and poor thermal stability limited their successful commercial application. This was associated to precipitation of the δ' phase (Al_3Li) in high volume fraction, which has a detrimental effect on toughness. By reducing the Li concentration, the formation of this phase can be avoided and mechanical properties can be enhanced. The 3rd generation of Al-Cu-Li alloys is characterised by a much lower Li concentration (up to 1.3 wt%) than the first alloy series, achieving a new combination of high strength, low density and high toughness / high fatigue resistance. These alloys are mainly strengthened by the T_1 phase (Al_2CuLi), which precipitates as thin platelets on $\{111\}_{\text{Al}}$ planes [1], [5], [6]. These alloys are found in the lower right corner of the diagram in Figure 1 and their characteristic properties are sketched in Figure 2.

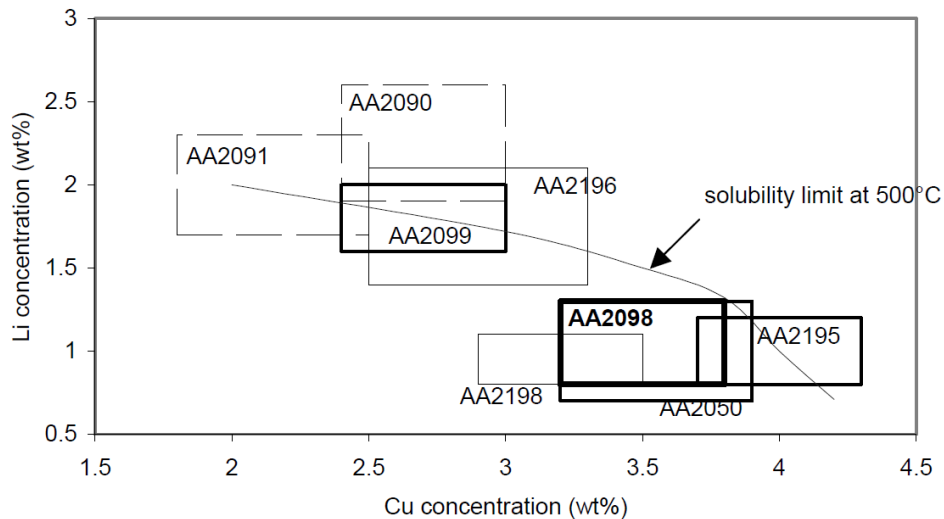


Figure 1: Illustration of several industrial Al-Cu-Li alloys with different Cu and Li contents. The new generation of Al-Cu-Li alloys lies in the bottom right corner of the diagram [6].

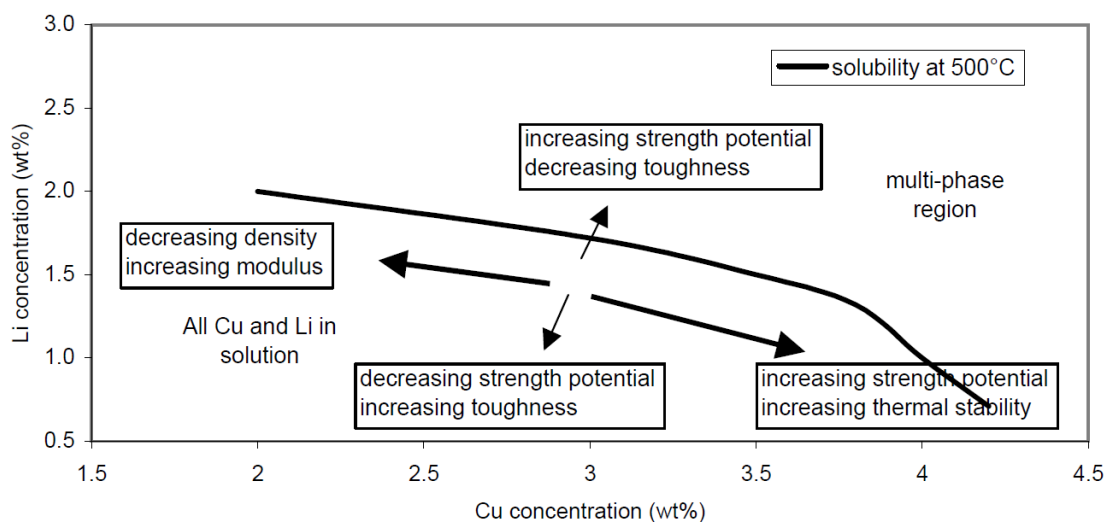


Figure 2: Properties of Al-Cu-Li alloys dependent on Cu-Li additions [6].

These 3rd generation Al-Cu-Li alloys are the basis of Constellium's AIRWARE™ solutions. Different series of the Al-Cu-Li alloys have been developed for specific applications on airplanes. Figure 3 shows the improvement of the AIRWARE™ product AA2050 compared to the alloy from the 7xxx series which is currently in use. It is striking that both corrosion and fatigue resistance have increased to a great extent. Furthermore stiffness, toughness and strength are improved and the density is reduced.

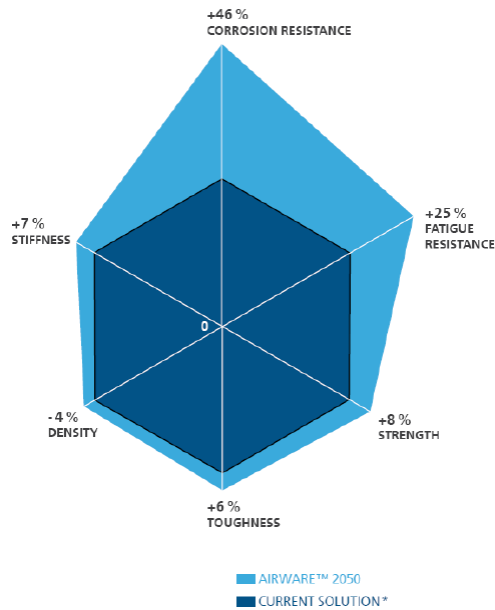


Figure 3: Comparison of performance of 7xxx alloy and the newly developed AIREWARE™ -product AA2050 (ECAA 2011 presentation Christophe Sigli).

The optimised design of Al-Cu-Li alloys is a complex task, even if we concentrate only on the last stage of their thermo-mechanical processing, namely the precipitation heat treatment that leads to strengthening and controls to a large extent the end properties. As described before, the alloy's properties are strongly dependent on the Cu and Li contents, and the effect of these alloying additions has been relatively well documented. In addition, precipitation in these alloys is very sensitive to the presence of structural defects in particular dislocations that act as nucleation sites for the precipitates. Moreover, the presence of minor solute additions such as Ag, Mg and Zn is known to also modify profoundly the kinetics of precipitate formation and the very nature of the phase formed, and these effects are coupled to that of the dislocations. Although these effects have been studied to some extent in the literature, no systematic evaluation of the influence of minor solute additions on precipitation strengthening in recently developed alloy compositions is available, and more importantly the mechanisms by which these solute additions modify the microstructure in a favourable way are not understood.

In this context, Figure 4 presents the scope of the present work. It is aimed at characterizing systematically and understanding, as much as possible, the effect of additions of Mg, Ag, Zn and combinations of these on an Al-Cu-Li alloy of fixed composition. This will first involve fabricating a series of alloys of different compositions and the systematically characterization of the precipitation kinetics and the associated strengthening. On selected microstructures advanced electron microscopy will be carried out to help understanding the mechanisms by which the minor solutes influence the microstructure. Finally, the fabrication and characterization of compositionally graded

materials will make it possible to determine the influence of the amount of minor solute addition on the alloy microstructure and properties. The foreseeable outcome of this research is that the improvement of our understanding of the effect of minor solute additions should lead to an improved design of alloys and thus to new alloy compositions with improved properties.

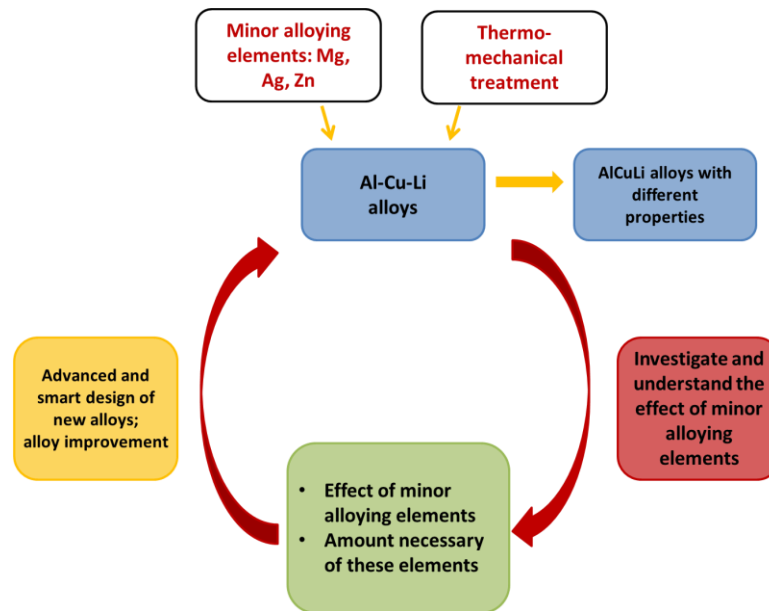


Figure 4: Graphical representation of the scope.

The thesis is thus structured in several chapters.

The first chapter gives a short introduction to aluminium alloys and reviews the different phases that can precipitate. In Al-Cu-Li alloys, T_1 (Al_2CuLi), is the main precipitating phase that is sought. However, the processing conditions and the addition of minor alloying elements can add supplemental phases in competition with T_1 , and they will be reviewed.

The second chapter introduces the seven different alloys studied in this work and the thermo-mechanical treatments applied to them, including the manufacturing of compositionally graded alloys. The second part of this chapter is dedicated to the different characterisation techniques used in this work, mainly:

- Hardness testing for mechanical characterisation of the effect of minor alloying elements on the hardening kinetics.
- Small angle X-ray scattering (SAXS), and differential scanning calorimetry (DSC) to provide information on the precipitation sequence and the precipitation kinetics.
- Conventional and atomic resolution transmission electron microscopy (TEM) to characterise in details the nature and structure of the formed phases.

Chapter 3 presents the hardening and precipitation kinetics of the seven investigated alloys and the results are divided into two main effects: the influence of Mg and Ag and the effect of Zn and Ag on the precipitation behaviour. The results obtained for precipitation kinetics provide aging conditions of high interest that were studied by more local characterization in the next chapter.

A global view on the microstructure in the fully precipitated condition of all alloys is given in the beginning of chapter 4. Then, atomic resolution TEM results supplemented by chemical mapping in the TEM, are presented for three main alloys in three different aging conditions, representative of early and stabilised precipitation conditions.

Chapter 5 is devoted to the study of compositionally graded materials. The first part describes the processing and elaboration of the diffusion couples in order to obtain good conditions for analysing the material. The effect of alloy composition in these gradients on precipitation during artificial aging treatment is then evaluated.

An overall discussion is conducted in the last chapter, where mechanisms by which the minor solutes influence the precipitation processes and strengthening are proposed in light of our experimental results.

1. Literature review

1.1. Classification of aluminium alloys

Aluminium alloys find many applications in transportation systems, heat exchangers or packaging. This variety is given by the possibility to add different elements to pure aluminium, which influences the materials properties in different ways and thereby makes it suitable for different applications [7]. Two groups of aluminium alloys are distinguished, casting alloys and wrought products. In the following, wrought products will shortly be introduced. Their classification is done by 4 digits in which the first digit is representative for the main alloying elements. Furthermore, some of these alloys can be hardened by means of a heat treatment, whereas others can only be strengthened by mechanical processing. The classification with respect to the main alloying elements is given in Table 1, separated in non- and heat-treatable alloys.

Table 1: Classification of aluminium alloys with respect to hardening mechanism and main alloying element.

Non-heat-treatable alloys		Heat-treatable alloys	
1xxx	Pure aluminium	2xxx	Al-Cu
3xxx	Al-Mn & Al-Mn-Mg	6xxx	Al-Mg-Si
4xxx	Al-Si	7xxx	Al-Mg-Zn & Al-Mg-Zn-Cu
5xxx	Al-Mg		
8xxx	Other elements		

Non-heat treatable alloys experience increased mechanical properties due to solid solution hardening and mechanical processing. Heat treatable alloys are hardened by second phases which in most cases are metastable and form during heat treatment [7].

1.2. Precipitation reactions

Solid-state phase transformations occur when a second phase becomes energetically stable due to a change in temperature. In the case of precipitation hardening in aluminium alloys, this transformation happens via nucleation and growth. The nucleation of a new phase consists of long range diffusion of the solutes necessary in the new phase and subsequently their arrangement into the crystal structure of the new phase. The transformation into the new phase releases energy, since the new phase should be thermodynamically more stable than the initial phase. However, the formation of a nucleus entails the creation of a phase boundary between nuclei and matrix as well as strain energies due to differences in crystal structure. Homogeneous nucleation occurs, when an

unstable nucleus of the newly formed phase increases to a subcritical size. The transformation of an unstable cluster into a growing precipitate happens when the nucleus reaches the critical size and receives an extra solute atom. Further growth of this nuclei leads to continuous reduction in free energy of the system [8]. The requirements for homogeneous nucleation are quite demanding, since only very coherent particles with a low interfacial energy and high driving force can actually nucleate homogeneously as it is seen for example in AlZr [9] and AlSc [10]. The mismatch between precipitate and matrix plays a very important role during nucleation. Good matching of the interface exhibit a coherent interface. This is the case if both have the same crystal structure and only slight differences in lattice parameter, which can be absorbed by elastic strain. For larger precipitates the accommodation of mismatch by elastic strain would be too costly and it is more favourable to accommodate the mismatch by interface dislocations. If the crystal structure of precipitate and matrix area is very different, matching is very poor and the interface is incoherent. Figure 5 gives an overview on the different types of precipitate coherency.

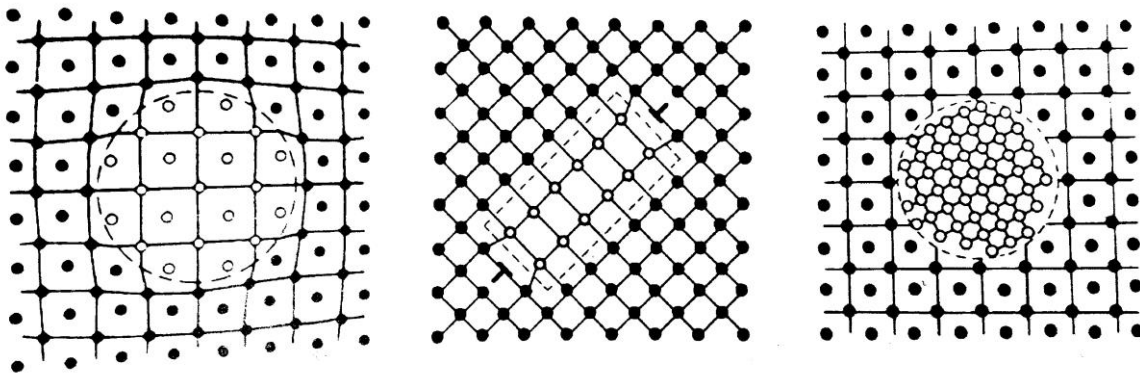


Figure 5: Coherent, semi coherent and incoherent particles sketched exemplarily [11].

When matrix and nucleus have different crystal structures, the interface energy rises. However, usually atomic matching of matrix and precipitate is found for one common plane or one direction. Along the good matching plane/direction the interface energy is low, however the other parts of the precipitates are incoherent and elevated interfacial energies are found. Nevertheless, the total interface energy is lower than in case of random orientation. In case of a common plane between matrix and precipitate, a plate-like structure is observed, whereas in the presence of a common direction a needle-like structure for precipitates is observed [8].

The theory of homogeneous nucleation assumes that each atomic site can act as a nucleation site for a precipitate to form. But, as said before, high driving forces and very coherent precipitates are required in order to observe homogeneous nucleation. In real systems, the nucleation rates appear

to be faster than predicted from homogeneous nucleation. This is made possible by means of heterogeneous nucleation sites, which play a major role in real systems. Heterogeneous nucleation sites are found on defects in the lattice such as grain boundaries, grain edges and corners, but also dislocations and interfaces of pre-existing precipitates. The formation energy of the nucleus is reduced and the pre-existing energy due to the presence of the defect is consumed during the nucleation of the precipitate. Although the nucleation rate is definitely increased due to a lower energy barrier to overcome for nucleation, the possible nucleation sites are reduced in number density. As a result, if large driving forces for precipitates with very low interfacial energies are present, homogeneous nucleation is expected. Usually, the driving forces for homogeneous nucleation are not large enough, and often the nucleation inside a grain which appears to be homogenous is associated to a heterogeneous mechanism [8], [12].

1.3. Influence on precipitation – heterogeneous nucleation

In aluminium alloys, precipitation is very complex and influenced by the presence of crystal defects as well as happens through complex kinetic paths. An overview of effects which facilitate nucleation in real systems are listed in the following [8], [12]:

- 1) The presence of different types of crystal defects in the material is very important to consider. Vacancies, voids and dislocations provide heterogeneous nucleation sites and facilitate precipitation. The nucleation on a dislocation releases energy, since a misfit with the matrix can be compensated by nucleation. Furthermore, dislocations can provide solutes to the growing nucleus by pipe diffusion. Vacancies play an important role in early clustering and nucleation processes, since they allow solutes to diffuse.
- 2) Nucleation can also happen by a sequence of different metastable precipitates. In this case, the first precipitating phase might form homogeneously because it is very coherent with the matrix and the interface energy is very low due to small differences in structure. These phases are however only metastable with respect to aging temperature and aging time. They can act as heterogeneous nucleation sites during further aging, but also a transition into another phase is possible (e.g. $\theta'' \rightarrow \theta'$ [13]). A classic example for this kind of metastable precipitates are Guinier-Preston zones that consist of only one single layer of Cu alloys in Al-Cu alloys (see section 1.4.1). These homogeneously nucleated phases act further on as heterogeneous nucleation sites during subsequent heat treatment and more stable, semi-coherent or even incoherent phases can form subsequently. This form of precipitation is observed quite frequently in aluminium alloys.
- 3) Different types of solute segregations can help to nucleate precipitates. On the one hand Solute can segregate on defects, such as dislocations, and locally change the defect

structure or energy landscape, e.g. the stacking fault energy. In aluminium alloys the stacking fault can be reduced by the addition of Mg or Ag [14]. This has been assumed to be of major importance for the nucleation of hexagonal phases lying on $\{111\}$ matrix planes, such as γ' in Al-Ag or T_1 in Al-Cu-Li – alloys.

On the other hand, segregations on the interface of nucleated phases may influence both the interface energy and the misfit strain energy. In both cases these interface segregations influence nucleation behaviour and might facilitate a new phase to form. Another aspect of segregations is of chemical nature; segregations of solutes at defects can help to reach the composition for a new phase to form and subsequently only the energetic barrier for change in crystal structure has to be overcome.

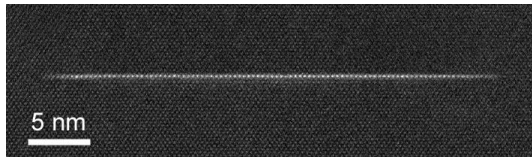
1.4. Overview of precipitating phases from different phase systems

Based on the alloy composition, both precipitation sequences of Al-Cu, Al-Li and obviously Al-Cu-Li have to be taken into account in order to identify all possible phases. Furthermore, small additions of other alloying elements in minor quantity are present, which can significantly influence the precipitation sequence and precipitation kinetics. Especially Mg is known to interact strongly with Cu and Al, so that phases based on Al-Cu-Mg will also be presented.

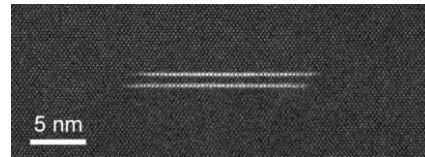
1.4.1. The Al-Cu system

GP zones were first discovered in the binary Al-Cu system. The first hardness increase in this group of alloys is associated with the presence of GP zones (Guinier-Preston zones) which were evidenced by X-ray diffraction experiments by Guinier and Preston [15], [16] from which they got their name. Hardening by these zones is attributed to chemical and coherency strain hardening. Being completely coherent with the matrix, they have a low interfacial energy which makes their initial nucleation favourable compared to intermediate, less coherent phases that precipitate later on. GP zones are defined as single-layers of Cu on $\{100\}_\alpha$ planes [15], [16]. This single-layered structure was also found by Gervold [17]. An atomic resolution image is shown in Figure 6 a. The presence of clusters prior to GP zone formation, which influences both kinetics and nature of the GP zone formation process is still in discussion [18]. During subsequent heat treatments, GP zones act as nucleation sites and are mostly replaced by more stable phases [18]. Microstructure observations exhibit both the presence of single-layer GP zones and at the same time multi-layered GP zones in early aging stages [19] [20]. Subsequent to GP zone formation there is a sequence of metastable precipitates that form in the Al-Cu system. As indicated in the phase diagram, Figure 7, θ'' or GP2 form at slightly higher aging temperature than GP zones and have lattice parameters of $a = 0.404$ nm, $c = 0.763$ nm [21], [22]. This

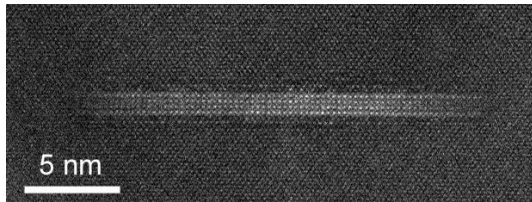
phase is identified by 2 Cu containing layers on $\{001\}_{Al}$ planes that are separated by 3 Al planes, seen in Figure 6b. Its thickness is 0.8 nm. θ' precipitates are slightly thicker (1.2 nm) and nucleate in general on θ'' precipitates [13], [23]. The θ' phase grows likewise on $\{001\}_{Al}$ planes, and the lattice parameters of this tetragonal phase are $a=0.404$ nm and $c=0.580$ nm [24] [22]. A θ' precipitate is shown in Figure 6c). The stable phase θ forms for either very long aging times or at higher temperatures (see Figure 7). Its unit cell parameters are $a=0.607$ nm, $c=0.487$ nm [21] [22].



a) GP zone



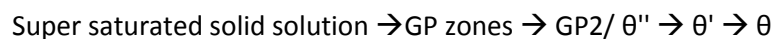
b) GP2 zone



c) θ' phase

Figure 6: GP zone, GP2 zone, θ' in an Al-Cu-Li alloy observed in $\langle 110 \rangle$ matrix zone axis [25].

The complete precipitation sequence can be written as:



The stoichiometric composition for both θ' and θ is Al_2Cu and the main differences between these two phases are found in their misfit with the matrix.

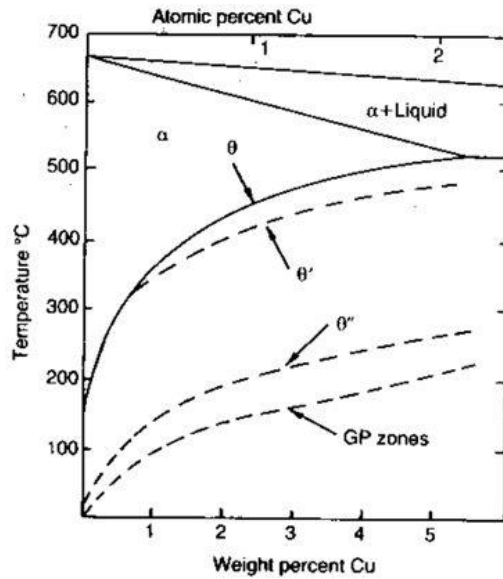


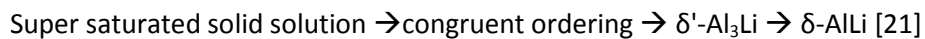
Figure 7: Temperature dependence of metastable phases [12].

The precipitation sequence in these alloys depends on quenching condition, aging temperature and time. Peak hardness is often attributed to a mixture of θ'' /GP2 and θ' [22]. Possible nucleation sites for θ' precipitates are heterogeneous nucleation sites such as dislocations or previous coherent θ'' /GP2 phases [13], [21][22].

1.4.2. The Al-Li system

The formation of the stable phase of this system, δ -AlLi, is not observed in conventional ageing conditions [26]. It is generally replaced by the L12 phase Al_3Li , a cubic phase with a crystallographic structure of $Pm\bar{3}m$ with a lattice parameter of $a=0.405$ nm. The stoichiometric composition for δ' is Al_3Li although the actual Li content is commonly lower due to some Al substitution on the Li sublattice [27]. Its stability can be explained by very high coherency of this phase with the Al matrix which is also reflected in the orientation relationship: $(100)_{\delta'} // (100)_{\text{Al}}$ and $[001]_{\delta'} // [001]_{\text{Al}}$.

The precipitation sequence can be summarized as follows:



Nucleation may occur both homogeneously in the matrix after quenching [21] and on dispersoids, such as β' (Al_3Zr) by forming a shell of δ' around these particles [26] [28]. A homogeneous distribution of δ' is illustrated in Figure 8. However, if the Li content is equal or below 1 wt% [25], [29], homogeneous nucleation of δ' is not observed, since the solubility of Li in Al is quite high. As seen in the previous Figure 6c) in Al-Cu-Li alloys, θ' is observed to be wetted by δ' . This sandwiched

structure is thermally more stable compared to single θ' precipitation, even for longer aging times. Misfit with the matrix is relieved due to high coherency of δ' [24].

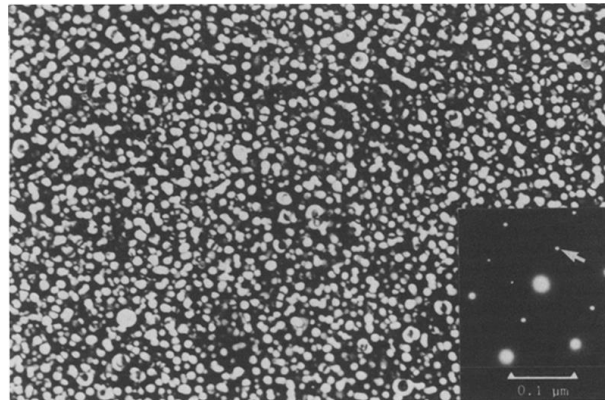


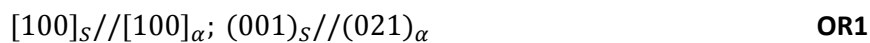
Figure 8: Homogeneous δ' precipitation in Al-Cu-Li [28].

1.4.3. The Al-Cu-Mg – system

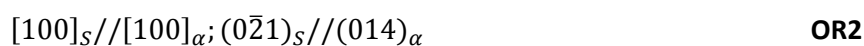
The precipitation sequence suggested by Bagaryatsky for the Al-Cu-Mg system with S as main precipitation phase [26], [30] summarizes to



and orientation relationship (OR)1 of S'/S phase with the aluminium matrix is [31] [5]



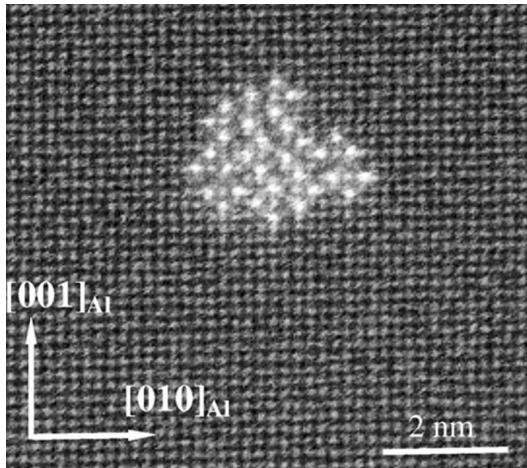
There exists a second orientation relationship which has been determined by Winkelmann et al. [31]:



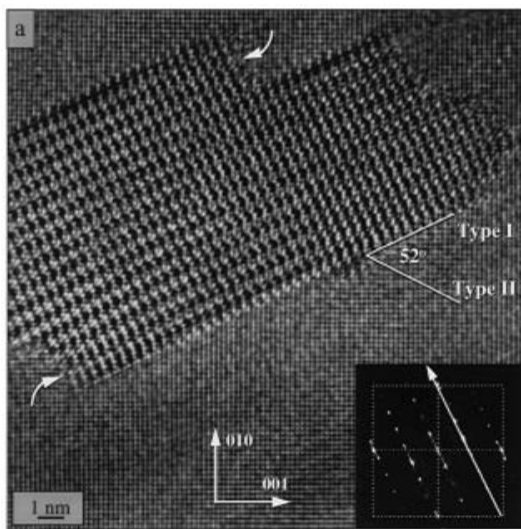
The S phase is orthorhombic with a Cmc₂m structure and following lattice parameters: a=0.400 nm, b=0.923 nm and c=0.714 nm. This structure model was confirmed by Mondolfo [32] using X-ray powder diffraction. It has been proposed that the S phase nucleates via a ledge mechanism on {102} planes [30].

Early aging conditions in Al-Cu-Mg alloys are characterised by Cu-Mg clusters and GPB zones which contribute to initial hardening in quenched Al-Cu-Mg alloys. Dependent on the Cu/Mg ratio, these clusters give rise to an initial hardening increase in early aging conditions, which has been proposed

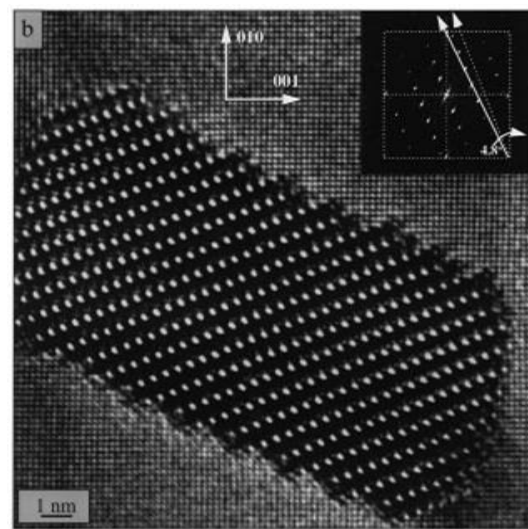
as the cause for the so-called rapid hardening phenomenon [26], [33]–[36]. GPB zones were first detected by Bagaryatsky [37]. GPB zones have been detected during aging at room temperature independently of the Cu/Mg ratio. In high Cu/Mg alloys, additional GP zones were found [5]. The GPB zones are most likely aligned in [100]-direction and different models in terms of atom position and composition are available. Nevertheless, the exact unit cell and crystal structure are not determined yet and are still in discussion [5], [38], [40]–[43]. They appear very early in the precipitation sequence and Figure 9 a shows a GPB zone which is aligned along [100]. The structure should be fairly simple and stable [5], due to early precipitation and good thermal stability. The appearance of GPB zones and their contribution to strength is in debate. On one side, their precipitation was seen to appear early in the precipitation sequence [44], on the other side other groups found that GPB zones contribute to peak strength, which is related to a second rise in hardness [35], [36]. The S phase precipitates subsequently to GPB zones and is the main precipitating phase in the Al-Cu-Mg system [26], [30]. Two different orientation relationships of the S phase have been reported [42], [43], [45] and the question if there is a continuous transition between these two orientations [31] or if two distinct structures exist [41], [42], [46] is still under discussion. The two types of S phase differ by a lattice rotation. Winkelmann et al. [31] formulated a rotation relationship along a common rotation axis $[001]_s // [100]_{\alpha}$, present in both types of S and claimed that several orientations of S'/S phase can co-exist. The range of S' phase orientation is limited by the two orientation relationships given above (OR1 and OR2). In opposite to Winkelmann [31], recent studies [41], [42], [46] have proposed that only two distinct structures are present. By using diffraction techniques a larger volume than in TEM can be analysed which allowed the conclusion of two distinct S phases due to a clear peak separation [41]. Both types are illustrated in Figure 9b and c.



a) GPB-rod aligned in [100]



b) S phase of type I



c) S phase of type II

Figure 9: Different metastable and stable phases observed in Al-Cu-Mg [38], [45].

The Cu/Mg ratio determines to which extent GPB zones and subsequently S phase form. In the presence of high Cu concentration the precipitation sequence is closely related to the Al-Cu system [5]. The amount of Mg affects the nucleation mechanism of the S' phase, i.e. a high Mg content permits homogeneous nucleation and a low or intermediate content favours heterogeneous nucleation sites, respectively [47]. These heterogeneous nucleation sites can be former GPB zones [44] or dislocations introduced by pre-stretch that enhance in addition the formation of S' and S [47]. Both types of S phases can be found on dislocations. The so called Type II, can however also precipitate by a stepwise change due to the strain field along dislocations and thereby change lattice orientation [48].

1.4.4. Al-Cu-Mg-Ag system

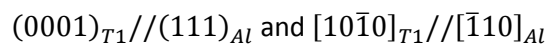
In addition to the aforementioned phases of the AlCu and Al-Cu-Mg systems, the hardening phase in Al-Cu-Mg-Ag alloys is the so called Ω phase, which precipitates on $\{111\}_{Al}$ planes and appears to be very similar to the T_1 phase in Al-Cu-Li alloys. The precipitation sequence can be summarized as



The Ω phase has a face centred orthorhombic structure with lattice parameters $a=0.496$ nm, $b=0.859$ nm and $c=0.848$ nm and a space group Fmmm. The orientation relationship with the matrix is: $\{111\}_{\alpha} // \{001\}_{\Omega}$; $[10\bar{1}]_{\alpha} // [010]_{\Omega}$; $[1\bar{2}1]_{\alpha} // [100]_{\Omega}$ [18], [49]. It has the same stoichiometric composition as θ (Al₂Cu) but is slightly distorted [50], [51]. K. Hono et al. [52] showed that Ag and Mg are homogeneously distributed in an Al-Mg-Cu-Ag alloys right after quenching. Short artificial aging times (only 5 seconds at 180 °C) result in clustering of Ag & Mg atoms. It is possible to find Mg-Ag co-clusters, but their shape is in general not well-defined. Initially Cu is not involved in the clustering process. For longer annealing times (~120 seconds at 180 °C) Cu becomes involved in Ag-Mg co-clusters and they appear to be oriented along $\{111\}$ planes. These first plate-like precipitates have no distinct structure yet and are completely coherent with the matrix. These clusters are believed to be strongly associated with the nucleation process of the Ω phase. While pre-deformation enhances T_1 precipitation (see section 0 for more details), the effect of pre-deformation in Al-Cu-Mg-Ag seems to be detrimental to Ω precipitation and assists θ' precipitation [51]. Hutchinson et al. [53] investigated the origin of the coarsening resistance of Ω precipitates. The redistribution of Mg and Ag segregated to the broad Ω interphase does apparently play a minor role during coarsening. Thickening is associated to growth ledges and is activated during high temperature exposure.

1.4.5. Al-Cu-Li system: the T_1 structure

Al-Cu-Li alloys were first studied by Hardy and Silcock [5], [54] who observed T_1 together with several other phases. The patterns of T_1 obtained by X-ray diffraction reveal a hexagonal structure with a composition close to Al₂CuLi. Its Laue group is determined as 6/mmm. The hexagonal structure is further characterised by its lattice parameters $a = 0.496$ nm and $c = 0.935$ nm. Furthermore, it has been identified that T_1 grows as thin platelets on $\{111\}_{Al}$ planes with the following orientation relationship:



Silcock showed that the structural characteristics of the T_1 phase observed in bulk/powder samples are the same as the hexagonal phase observed during artificial aging at 165 °C [5]. The structural

observations, made by Hardy and Silcock, were confirmed by Noble and Thompson [55] using transmission electron microscopy. They further suggested that structural ordering of the T_1 phase is along its c -direction, e.g. on $(111)_{Al}$ planes. The thickness of these particles was estimated from streaking in the diffraction patterns to be around 1-2 nm. The proposed mechanism of nucleation is via a stacking fault mechanism [56] in which a perfect dislocation of Burgers vector $\frac{1}{2}[\bar{1}10]$ splits into 2 Shockley partial dislocations, of respective Burgers vectors $\frac{1}{6}[\bar{2}11]$ and $\frac{1}{6}[\bar{1}2\bar{1}]$. Similar behaviour is seen in Al-Ag alloys in which the hexagonal, plate-like γ' phase nucleates on stacking faults [57], [58]. In contrary to Al-Ag, it was observed that T_1 can nucleate homogeneously, when supersaturation is large enough [55]. Based on this nucleation behaviour, several T_1 structures were proposed over the past decades. A hexagonal structure of 4 $\{111\}_{Al}$ planes was used as basic concept for modelling the structure. A first attempt to describe the T_1 structure by this concept was proposed by Huang and Ardell [59]. Closely packed structures, but with different distributions of the atoms were further proposed by Cassada et al. [60], Radmilovic et al. [61] and Howe et al. [62]. Figure 10a and b shows the structure proposed by Huang and Ardell (a) and Howe et al. (b).

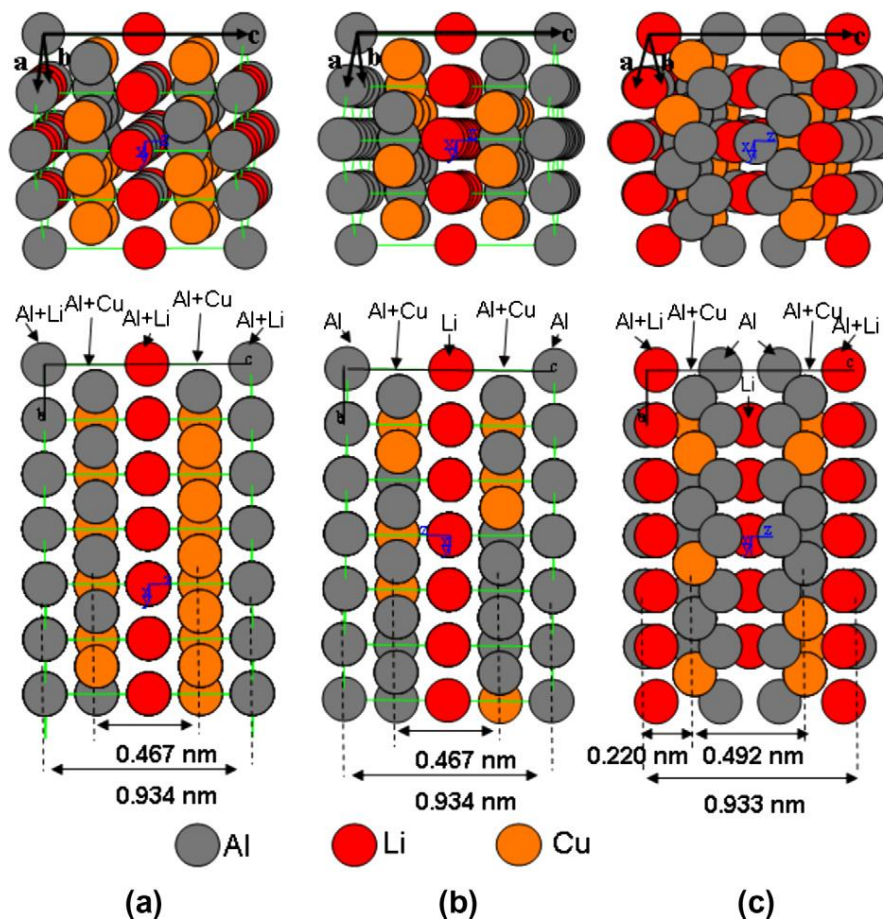


Figure 10: T_1 structure proposed by Huang and Ardell (a) Howe et al (b) and van Smaalen (c)[63].

Based on the Huang and Ardell structure, van Smaalen et al. [64] used X-ray diffraction to refine the crystal structure of Al_2CuLi on a bulk crystal. Differences to the proposed Huang and Ardell structure were found with respect to atom positions. Single atom positions for Lithium and Copper from the Huang-Ardell model were modified into two atom positions with different z-spacing, i.e. instead of one defined position the atom can chose between two. Thereby, their layers are not completely planar anymore but corrugated. By introducing these corrugated layers the characteristic distances of $\{111\}$ matrix planes are not present anymore [63], [64]. Two recent studies presented by Donnadiou [63] and Dwyer et al. [65] resolved the microstructure of T_1 . Donnadiou et al. [63] described the T_1 structure based on the previous discussed results of van Smaalen. Typical high resolution images taken from this paper show a single and a double layered T_1 precipitate investigated in $\langle 110 \rangle$ zone axis, see Figure 11a and b. By introducing coordination polyhedra, stable and unstable atom positions can be reported and by this the discussion on the precipitate/matrix interface suggests a replacement from an Al-Li to an Al-Cu-interface, since Li-position would not be stable in the polyhedral approach. These polyhedra can be an interesting approach to keep in mind when studying the effect of minor alloying elements. It is suggested [63] that Mg for instance could substitute atom positions of Li and thereby play an important role during nucleation.

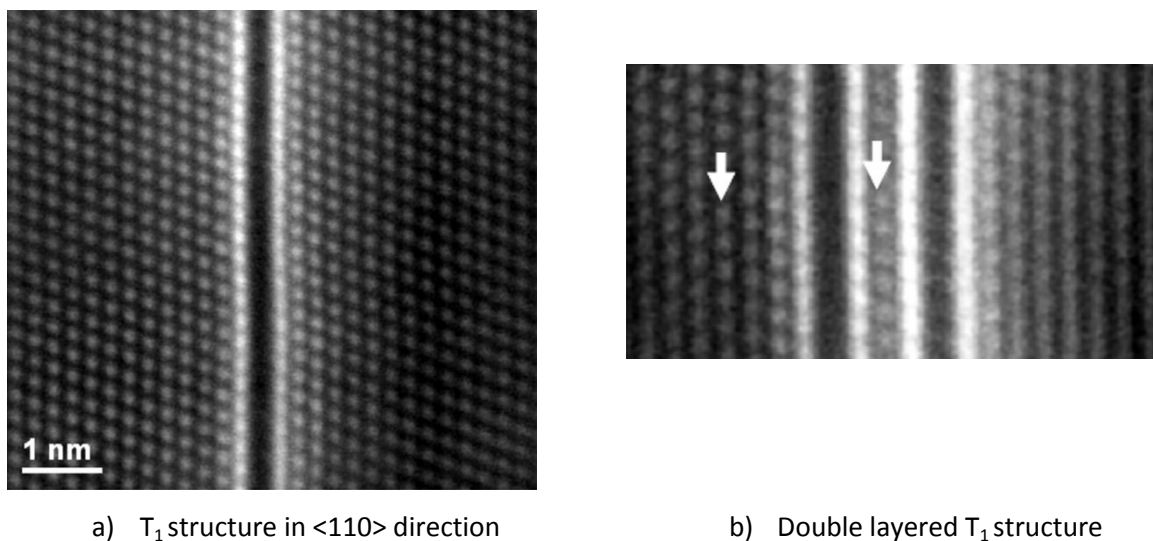


Figure 11: T_1 structure, observed in $\langle 110 \rangle$ matrix zone axis [63].

Using HAADF-STEM, HRTEM and ab initio modelling, Dwyer et al. [65] showed that the Huang and Ardell structure is not stable. They resolved the structure of T_1 by looking in $\langle 112 \rangle_{\text{Al}}$ direction, which permits identifying all atomic positions due to larger interatomic distances than in $\langle 110 \rangle_{\text{Al}}$ observation direction. A model of the T_1 structure is shown in Figure 12. It is proposed that the interface between T_1 and Al matrix contains Al, Cu and Li, in which Li positions are slightly shifted,

normal to the interphase plane. At the centre of the plane sequence, two Copper-rich Al-Cu layers surround a Li-rich layer. Energetic analysis by using DFT-calculations reveals that these positions are stable with respect to the proposed structure. The space group P6/mmm is in agreement with earlier proposed structures. The obtained thickness of one unit cell T_1 is 1.39 nm, including 5 $d_{(111)}$ layers. A T_1 precipitate observed along the $\langle 112 \rangle_{Al}$ zone axis is sketched in Figure 13. On the right side of the image the described model structure is superposed to the TEM image.

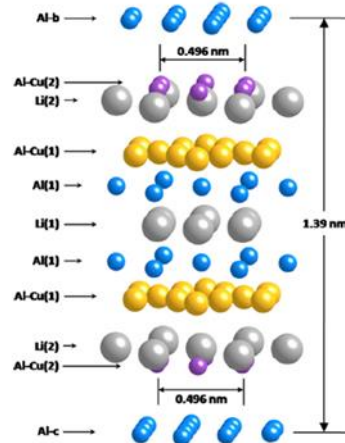


Figure 12: Structure of T_1 determined by Dwyer et al [65].

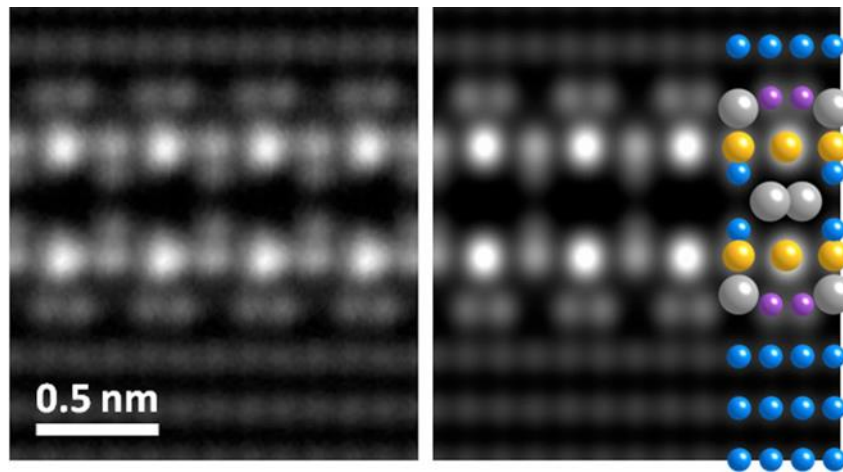


Figure 13 : T_1 structure in $\langle 112 \rangle$ zone axis. HAADF image with model structure superposed.

1.5. The effect of minor alloying elements in heat-treatable aluminium alloys

As seen in Table 1 there are different age hardening aluminium alloy systems, characterised by different main solute additions and related precipitating phases. In all of these systems, the addition of minor alloying elements (defined as being added in a much lower quantity as compared to the main solutes) might alter the precipitation sequence, change nucleation and precipitation kinetics

and affect mechanical properties. Many studies have been dedicated to understand and characterise the effect of different minor alloying elements.

The effect of adding Sn, Cd and In to the Al-Cu system was investigated by several authors [66]–[68]. If one of these minor alloying elements is present, the GP zone formation is suppressed. Instead, a fine distribution of θ' phases was observed to nucleate on dislocations loops and clusters consisting of these trace elements [67]–[69]. Sn has a high vacancy binding energy, and the pre-precipitation of Sn-rich phases was observed. Subsequently, θ' nucleates heterogeneously on these Sn-rich precipitates [66]. It was claimed that the addition of minor alloying elements was actually more effective to achieve a fine dispersion of θ' than pre-deformation due to the interference of dislocation and solutes [66]. The vacancy binding energy is likewise high for Cd and In so that vacancy-trace-element interaction should be similar as for Sn and cluster formation should occur [68], [70]. In [66] no segregation of Sn to θ' were observed by APT. However, other studies claim that Cd, In and Sn are incorporated in θ' precipitates and thereby the interfacial energy of the θ' phases might be reduced. In consequence, nucleation of θ' might be affected [67], [68].

The effect of Mg and (Mg and Ag) additions to Al-Cu alloys has been investigated by Zahra et al. [71], using calorimetric measurement in combination with microscopic studies. The formation kinetics of GP zones in early aging conditions is slightly retarded in the presence of Mg and (Mg and Ag), but a refined distribution of these phases is observed. Furthermore, the precipitation sequence is altered. The addition of Mg leads to the formation of S' phase as main precipitating phase. The combined addition of Mg and Ag supports the formation of the Ω phase. This phase forms prior to θ' precipitation and its formation is strongly stimulated by Mg and Ag. It is the main precipitating phase in this alloy [71].

The effect of minor alloying elements has been studied in Al-Cu-Mg alloys, since they find many applications in aerospace structures [72]–[74]. The precipitation sequence is influenced by the presence of Ag, Si and (Ag and Si) and the effect is strongly affected by the Cu/Mg ratio. In the presence of Si, the Mg/Si ratio also plays a role on the precipitation sequence [72]. In the as-quenched condition, Ag and Si additions affect cluster and GPB zone formation due to trapping of vacancies by Ag and Si [74]. Highest hardness was observed when both Ag and Si are present. Hardening kinetics is enhanced, but also overaging occurred faster, which might be detrimental for structural components. The microstructure consists of both X' and Ω phases [73]. The Cu/Mg ratio and the heat treatment strongly affect further precipitation and has led to some controversy. It is claimed that Si favour θ' formation and Ag so-called X' , respectively [74]. A very small Cu/Mg ratio (~ 0.4) reveals Cu-Mg clusters and subsequent S-formation on dislocations. Ag additions results in an increased formation of so-called Z phase compared to the ternary alloy [75]. As seen before [71], for very high Cu/Mg ratios, S' formation is favoured and in the presence of Ag, the precipitation

sequence is altered, Ω becoming the main precipitating phase [71]. The effect of Ag and Cd was likewise investigated, resulting in highest hardness values for Ag containing Al-Cu-Mg alloys. Microstructure observations for combined additions of Ag and Cd reveal the presence of both Ω , which is stimulated by Ag and θ' , which is influenced by Cd additions. It is claimed that Ag and Cd act independently [76].

The effect of minor alloying elements has been studied in Al-Mg-Si alloys for several years because of its industrial interest, particularly growing in the automotive industry. In these alloys, Cu and Zn are often found as remainders after recycling and therefore the effect of these elements on precipitation is of high interest [77]–[79]. Different precipitating phases are detected in these alloys, and β'' is identified as the main precipitating phase, which gives the material optimal properties. The effect of Cu to an industrial AA6060 was investigated. Increased hardness values are measured in the presence of 0.1 wt% Cu compared to AA6060. Investigations of the microstructure exhibit a finer distribution of precipitates in the presence of 0.1 wt% Cu compared to 0.01 wt% Cu additions, which is in good agreement with higher hardness values for the first named alloy. The precipitation sequence has not altered, but an increased number of disordered β'' precipitates are found in the presence of 0.1 wt% Cu compared to AA6060. Cu-rich columns were only found in the disordered β'' structure, whereas ordered β'' did not accommodate any Cu at all. The effect of 0.1 wt% Cu additions has also been investigated with 10% pre-deformation prior to artificial aging. During artificial aging the precipitation sequence has not altered compared to pre-deformed AA6060. Heterogeneous nucleation on dislocation is dominant [78]. An earlier study likewise measured an increased density of precipitates in the presence of low Cu additions and remarked additionally a positive effect on the quench sensitivity [80]. High copper additions of ~ 0.3 wt% alter the precipitation sequence and the Q' phase precipitates with high volume fraction [81]–[83]. Small additions of chromium showed a negative effect on quench sensitivity, due to the formation of dispersoids on which heterogeneous nucleation can occur [80]. Small hardness increases are observed with increasing Zn concentration in Al-Mg-Si alloys and highest hardness is obtained in the presence of 1.0 wt% Zn. The microstructure for 1.0 wt% Zn containing alloys shows a higher precipitate number density than alloys with lower or no Zn- additions. At the same time, Zn was still found in solid solution for high Zn addition (1.0 wt%). No precipitates related to the AlMgZn system are observed, but again a higher number of disordered β'' phases were present, as similarly observed for low Cu additions. Zn is found in the disordered β'' phase, but it also exists in ordered β'' substituting to certain atomic positions (so called Si_3/Al). Its occupancy is though very low [79].

The AlMgZn alloy is strengthened by the η' phase and its equilibrium phase η of composition $MgZn_2$. The addition of Cu as a minor alloying element does not alter the precipitation sequence, but is included in the precipitate structure. This is dependent on the aging temperature and aging time as

well as the Cu content [84]. Atomic resolution analysis showed that Cu substitutes the Zn positions in η [85]. The addition of Sn to these alloys shows the presence of an additional Sn containing phase. Low additions of Sn increased strength due to the formation of fine dispersed Mg_2Sn particles, however too high additions show detrimental effect due to coarsening of these Mg_2Sn phases [86]

1.6. New generation of Al-Cu-Li alloys

Al-Cu-Li alloys, belonging to the 2xxx-series of aluminium alloys, have been investigated for aerospace applications for more than 50 years. The first Al-Cu-Li alloy introduced by Alcoa has been flying for 20 years without showing any corrosion issues [2]. These alloys were very attractive, because of the low-density in combination with high stiffness brought by the addition of Li. In order to take advantage of the properties of Li, i.e. the reduction in density and the increase in elastic modulus, Li-rich alloys were the main focus of the research in Al-Cu-Li alloys with Li concentrations above 2 wt% in the 80's. Indeed, density reductions of 7 – 10 % were achieved and also the elastic modulus could be increased up to 15 % with respect to that of pure Al. However, several detrimental factors appeared, such as high anisotropy of tensile properties, low plane stress fracture toughness and long term stability at moderate temperatures [2]. By the introduction of the 3rd generation of Al-Cu-Li alloys in the late 1990s, weak points such as low toughness and anisotropic mechanical properties could be improved to a great extent. It was necessary to reduce the Li content compared to the second generation of Al-Cu-Li alloys [1], [2]. The microstructure can be controlled by optimisation of chemical composition and thermo-mechanical processing. It is important to control the precipitating phases and their nucleation sites to provide good mechanical behaviour. New research has made this family of alloys very attractive for aerospace application [2]. The main precipitating phase sought in the newly developed alloys is $T_1 - Al_2CuLi$ [21], [87], [88], however dependent on the alloy composition, other phases can precipitate [2], [26] and the competition of these different phases will be presented in the following.

1.7. Competition between different phases in Al-Cu-Li-X alloys

Minor alloying elements and mechanical processing of the material influence the presence of crystalline defects and the precipitation process. The influence of these different components will be summarized in the following.

1.7.1. The effect of pre-deformation

Pre-deformation plays an important role in Al-Cu-Li alloys and affects nucleation and precipitation kinetics. Both Cassada et al. [60], [89], Ringer [51] and Gable et al. [23] showed that precipitation of the T_1 phase is enhanced. The number density of T_1 is increased and they appear to be shorter and thinner than in undeformed Al-Cu-Li alloys [23], [89]. In the presence of an increased number of heterogeneous nucleation sites, T_1 nucleates at the expense of θ' , which is in competition for solute. Higher strength is achieved [23], [90]. Figure 14 shows the effect of different degrees of pre-deformation on the yield strength during aging at 150 °C [23]. It clearly reveals that a pronounced effect is seen between 0 % and 2%.

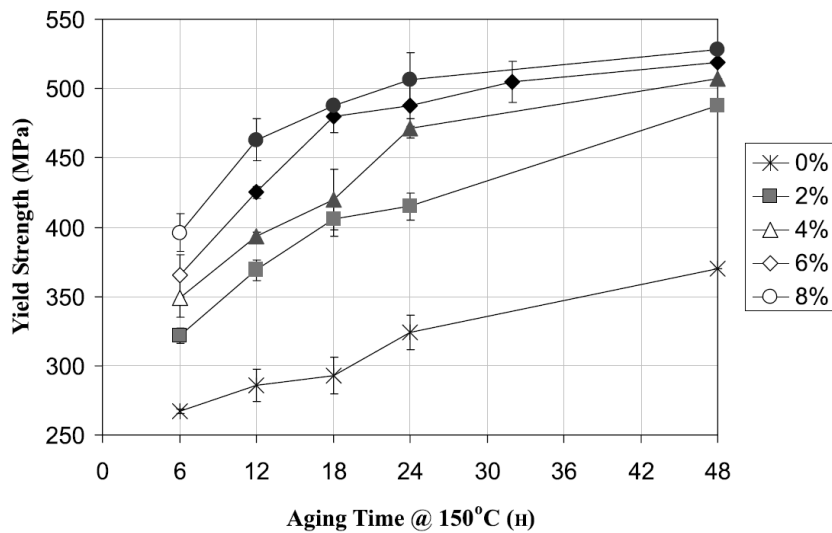


Figure 14: Effect of pre-deformation on the yield strength over aging time [23].

Decreus et al. [90] showed that the succession of natural aging (NA) and pre-deformation plays only a minor role on subsequent precipitation of the T_1 phase. Artificial aging for the same time, subsequently to either pre-deformation and NA or NA and pre-deformation, shows similar microstructures, as determined by SAXS. However, the lack of deformation prior to artificial aging reveals big differences in precipitation volume fraction. A systematic study, in order to investigate the influence of precipitation volume fraction and yield strength with respect to pre-deformation was performed by Dorin et al. [91]. His study showed that with increased pre-deformation an increased number density of T_1 precipitates is present and the precipitation kinetics was higher; however, the resulting diameter was consequently lower [91].

1.7.2. The effect of Li and Cu

In Al-Cu-Li, the presence of δ' right after quenching depends on the Li content [25], [29], [87]. In Al-Cu-Li alloys with low Li content, these quenched-in δ' phases are not observed, whereas a Li concentration above 1 wt % results in the presence of the coherent phase. For longer aging times, in both low and high Li containing alloys, a combined structure of θ' phases flanked by δ' is observed. This composite structure is thermally quite stable [29]. The δ' structure was observed to cover θ' as observed in [25]. At constant Li content, the Cu content was varied in a study performed on weldalite™ 049 alloy which was one of the first alloys with reduced Li content. The strength values were not changed with increasing Cu additions, but ductility was increased for a lower Cu content [92]. There are several contributions of different phases that contribute to strength and elongation. Increased Cu concentration can affect the number density of T_1 precipitation, and nucleation and precipitation conditions for θ' . The ratio of these two phases determines the final mechanical properties.

1.7.3. The effect of Mg and Ag

The effect of minor additions of both Mg and Ag and their combination on precipitation in Al-Cu-Li alloys has been the subject of several studies [92]–[98]. In Al-Cu-Li several phases can precipitate and the effect of Mg and Ag influences this competition [99]. So far, the exact role of these elements has not been determined yet and their effect is discussed controversially. One important aspect of discussion is the influence of Li/Cu ratio, which is much higher in early studies [29], [94], [97], [100] than in more recent ones [93], [99], [101], [102]. Figure 15, taken from Itoh et al. [93], in which a relatively low Li/Cu ratio is present, illustrates the effect of single and combined addition of Mg and Ag on hardness over aging time in non-pre deformed material aged at 180 °C. Many studies investigated material in undeformed condition and were artificially aged at temperatures between 170 to 220 °C [29], [92]–[94], [97]–[99], [101], [103]. For pre-deformed material the artificial aging temperature was slightly lower than in undeformed material and was between 150 to 160 °C [92], [102]. Early aging conditions were produced either by natural aging or by a heat treatment below 120 °C [29], [95], [100].

These studies clearly reveal that Ag additions alone do not alter hardening characteristics to a great extent. Solely Ag addition to Al-Cu-Li showed reduced GP zone formation. T_1 precipitation was stimulated and the lengthening rate of T_1 and θ' was enhanced [99]. It was furthermore observed that Ag does not play an active role during nucleation [94] and T_1 precipitation occurs on few heterogeneous nucleation sites such as dislocation loops around Zr-bearing precipitates [93]. Zheng

et al. [98] observed that the presence of pre-deformation prior to artificial cancels out the small effect on hardness that was observed for Ag additions in undeformed material.

Mg additions show a great enhancement in hardening kinetics during aging at 180 °C. The initial hardening response is altered to a great extent. Several authors showed that Mg additions enhance GP zone formation in Al-Cu-Li alloys [95], [100]. This effect was attributed to high Mg-vacancy binding energy, which in consequence contributes to the formation of Mg/Cu/vacancy complexes. This might also explain the high natural aging response observed by several groups [93], [95], [99], [100]. T_1 precipitation is promoted by the addition of Mg, and at the same time an increase in number density of θ'' and θ' was observed [95], [99]. Furthermore, the T_1 phase precipitated with finer distribution due to an increased number of heterogeneous nucleation sites [93].

The combined addition of Mg and Ag has been shown to further improve hardening kinetics and higher hardness values compared to Al-Cu-Li Mg alloys. It was proposed that precipitation is changed due to the presence of a higher number of heterogeneous nucleation sites (the material was undeformed). The precipitation of θ' which is in competition with the T_1 formation was reduced [93], [99]. The presence of Mg-clusters has been reported by [94], however Mg-Ag containing clusters, as present in Al-Cu-Mg-Ag alloys prior to Ω precipitation, were not observed in Al-Cu-Li-Mg-Ag [94], [101], [103].

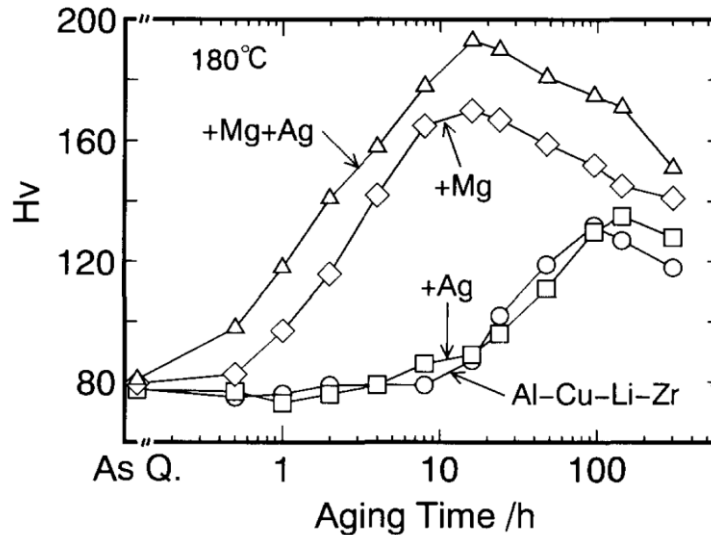


Figure 15: Influence of single and combined additions of Ag and Mg on hardness over aging time [93].

Microstructural observations by Itoh et al. [93] indicate that the nucleation of T_1 is altered by the presence of an increased number of structural defects when adding Mg and Ag. These defects, such as voids and dislocation helices serve as heterogeneous nucleation sites [93]. Many studies, however, attribute favourable precipitation kinetics to a decrease in stacking fault energy when Ag and Mg are added. A reduced stacking fault energy facilitates the dissociation of dislocations and it is proposed

that this facilitates the formation of a hexagonal phase within dissociated dislocations [94], [95]. The latter explanation is in good agreement with the described nucleation mechanism by Cassada et al. [56].

An atom probe tomography study by Gault et al. [96] on a model alloy containing Mg and Ag additions showed that Mg results in the formation of GPB zones and Mg-rich S phases. A catalytic effect on T_1 precipitation was attributed to the incorporation of Mg and Ag into T_1 precipitates in early aging conditions, which according to the authors were rejected for longer aging times [96]. This latter result could be related to the relatively high temperature used in this study (200°C) and related thickening of the T_1 precipitates. Araullo-Peters et al [102] carried out a similar APT study on the AA2198 alloy aged at a lower temperature of 155°C. They showed that the solute concentration of Mg and Ag in the matrix stabilised at a lower level when reaching a fully precipitated condition. In these ageing conditions, no thickening of the T_1 phase happened. The analysis of T_1 composition after longer aging times, showed that Mg was incorporated in the precipitate whereas Ag was only present at the precipitate's interface [102]. This was likewise seen by [94], where artificial aging was performed at 180 °C. These observations could not be made in the earlier mentioned study [96]. The detection of Mg and Ag on the T_1 interface is dependent on the sample orientation during APT experiments. When the APT experiment was performed along the (111) pole Ag and Mg segregations on the T_1 interphase were clearly seen [94], [102]. In [96] the APT experiments were not performed along a specific pole and these segregations were not visible which is attributed to a different evaporation field of matrix and precipitate which overlap when the precipitate and the matrix are evaporated at the same time. Thereby the spatial resolution is reduced [104]. In [102], early-aging conditions reveal Cu-Mg segregations on dislocations, on which T_1 could already nucleate in early aging conditions [102].

1.7.4. The effect of Zn

In Zn containing Al-Cu-Li alloys, XEDS and APT- analysis demonstrated that Zn was present in the T_1 phase. Zn is added for solid solution strengthening and improvement of corrosion properties. Its efficiency with respect to solid solution strengthening and corrosion properties is most likely reduced, when incorporated into the T_1 phase [105]. It was furthermore seen that Zn can be incorporated into δ' [105], [106]. The effect of Zn was also evidenced by [107] showing that Zn is partitioned into the T_1 phase. It may stabilise the T_1 phase and it is assumed to reduce the misfit with the matrix and thereby reducing coarsening of T_1 [107].

1.8. Summary

As seen in the previous section, the nucleation and precipitation behaviour in Al-Cu-Li alloys is very complex. It has been shown that the presence of dislocations is very important to facilitate and enhanced T_1 nucleation. In addition, the presence of different minor alloying elements clearly affects precipitation. It is seen from literature that Mg is important during T_1 nucleation; however its precise role is not defined yet. Ag affects precipitation kinetics to a lower extent than Mg, but shows likewise some effect. Both elements are incorporated into the T_1 phase. The addition of minor alloying elements might not only affect the T_1 formation itself but perhaps alter the precipitation sequence. The formation of other phases might either create a competition to T_1 precipitation or act as heterogeneous nucleation sites for these phases.

2. Materials and experimental methods

The following chapter is divided into 2 parts. The first part introduces the different alloys that were studied, the material processing and the final thermo-mechanical treatment that was performed. The second part is dedicated to the characterisation methods that were used in order to study the precipitate microstructure and its formation kinetics.

2.1. Analysed material

The study aims at understanding the precipitation mechanisms of the T_1 phase in Al-Cu-Li alloys and particularly the effect of minor alloying elements during nucleation and further growth. In order to achieve this goal, seven different alloys were cast (dimensions after machining the surface: 235x175x27mm) and provided by Constellium C-TEC. The target values and the measured compositions are given in **Table 2**.

Table 2: Alloys' composition in wt % provided by Constellium C-TEC. Target value and measured composition (in the liquid before solidification) in parentheses.

	Cu	Li	Mg	Ag	Zn
AlCuLi	3.5 (3.4753)	0.9 (0.902)			
AlCuLi Mg	3.5 (3.5379)	0.9 (0.8505)	0.35 (0.3487)		
AlCuLi 0.3Ag	3.5 (3.4853)	0.9 (0.8694)		0.35 (0.3458)	
AlCuLi Mg0.3Ag	3.5 (3.4675)	0.9 (0.8849)	0.35 (0.3481)	0.35 (0.3464)	
AlCuLi Mg0.1Ag	3.5 (3.5582)	0.9 (.8778)	0.35 (0.3438)	0.11 (0.1057)	
AlCuLi MgZn	3.5 (3.5175)	0.9 (0.8838)	0.35 (0.3374)		0.6 (0.5951)
AlCuLi Mg0.1AgZn	3.5 (3.5435)	0.9 (0.8639)	0.35 (0.3358)	0.11 (0.1067)	0.6 (0.5999)

2.2. Heat treatment

A homogenisation treatment was performed after casting, including a 10 hours ramp heating up to 500 °C and holding at 500 °C for 20 hours. The homogenised blocks were then hot rolled at C-Tec Constellium. Prior to rolling, the blocks were pre-heated to 505 °C for several minutes. Subsequently, several rolling steps were performed, keeping the materials temperature above 350 °C during rolling

in order to avoid recrystallization during the next pre-heating step. By this, the initial thickness of 27 mm was reduced to approximately 4 mm. The samples were then machined down to the dimensions given in Figure 16. A thin layer was removed on both sides, resulting in plane-parallel samples 3 mm in thickness. Width and length are 15 and 100 mm, respectively.

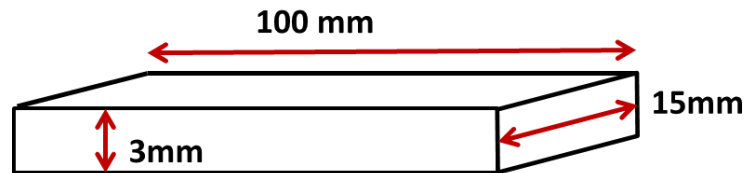


Figure 16: Dimensions of samples after machining.

The thermo-mechanical heat treatment (sketched in Figure 17) started with a solution heat treatment at 505 °C in an air circulating tube furnace. Subsequently, the samples were directly water quenched and stored in a freezer at -52 °C in order to limit the amount of natural aging. Pre-deformation was introduced after water quench. If the sample was stored in the freezer it was brought to ambient temperature by rinsing in cold water prior to installation in the tensile test machine. The amount of natural ageing before pre-deformation is estimated to 5 min. 4 % plastic pre-deformation (after removing the elastic strain of approximately 0.3 %) was performed on a ZWICK ROELL 1455 tensile test machine using an extensometer. After pre-deformation, all samples were kept at room temperature for 72 hours natural ageing. This condition will be designated as 'Naturally Aged' (NA) in the following. Artificial aging started with ramp heating of 20 °C/h up to 155 °C. Water quenching right after reaching 155°C produces the so-called 'End of ramp' ('EoR') condition. Different aging conditions were produced, by quenching the samples after various aging times at 155 °C. Ex-situ heat treatments were performed in an oil bath 'Lauda P18'. In-situ heat treatment performed during Small Angle X-ray experiments (see Section 2.5) were conducted in a custom-made furnace. By this, the heat treatment and continuous data acquisition were realised at the same time.

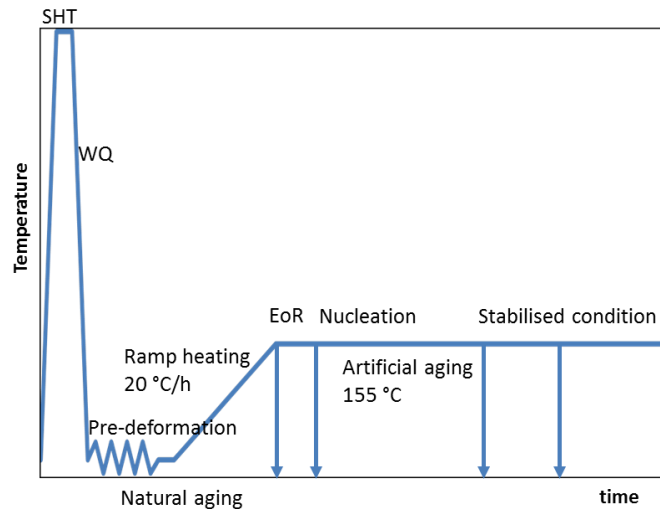


Figure 17: Heat-treatment in order to achieve different aging conditions in Al-Cu-Li alloys.

In parallel with the study on the individual alloys, some of them were combined as diffusion couples. The aim was to measure precipitation kinetics depending on the concentration of one diffusing element. Dissimilar alloys were joined by linear friction welding. Prior to the joining process, the input materials (cast ingots with compositions as indicated in **Table 2**) were submitted to a homogenisation treatment, combining a ramp heating for 10 hours up to 500 °C and subsequently isothermal homogenisation for 20 hours at this temperature. To obtain a symmetrical deformation during welding, a similar hardness on both alloys is preferable. Thus a solution treatment at 505 °C for 30 minutes was performed, followed by water quench to room temperature. A 10 to 15 % pre-deformation was achieved by cold rolling. Two different artificial aging temperatures were chosen. Mg containing alloys were artificially aged at 190 °C, for 50 hours or 100 hours respectively. Mg-free alloys were heat treated at 155 °C for either 30 hours or 50 hours. The resulting hardness values for all alloys were measured to be in the range 150 -160 HV, which corresponds to a peak aged condition for Mg-free alloys and an over-aged condition for Mg containing alloys, respectively. Heat-treated samples were then machined to suitable dimensions for linear friction welding, which were 50 mm*50 mm*25 mm. Linear frictions welding was performed by Thompson Friction Welding (UK). The alloys' combinations are listed in Table 3, including the diffusing element.

Table 3: Alloy combinations prepared by Linear friction welding.

Alloy 1	Alloy 2	Diffusing element
AlCuLi	AlCuLi Mg	Mg
AlCuLi 0.3Ag	AlCuLi Mg0.3Ag	Mg
AlCuLi Mg	AlCuLi Mg0.3Ag	Ag

Subsequently to the friction process, a concentration gradient was created by submitting the welded joints to a diffusion heat treatment at 515 °C for 14 days. Approximately 6.5 mm thick slices parallel to the diffusion gradient were then cut from the weld. Hot rolling to a sample thickness of approximately 1.8 mm was performed in order to further enlarge the diffusion gradient. The pre-heating temperature was 500 °C and the rolling process was performed by one single processing step. The rolled sheets were cut into similar sample dimensions as seen in Figure 16. The final sample dimensions are 15 mm*100 mm*1.8 mm. Thereafter, the same artificial aging treatment, as illustrated in Figure 17, was performed on the diffusion couples.

2.3. Hardness

Measuring hardness is a very simple method to characterise mechanical properties, which is also particularly suitable to characterise compositionally gradient materials. Vickers hardness is conducted by pressing a diamond pyramid with a predefined load P for a specific time into the material. The length of the diagonal d_1 , which is subsequently measured, can be converted to an hardness value.

$$HV = \frac{1.854 * P}{d_1^2} \quad \text{Equation 1}$$

In general, the obtained values cannot be directly related to yield strength or tensile strength; however conversion tables exist in order e.g. to transform obtained data into tensile strength. The following approximation holds for cold worked materials [108].

$$TS (MPa) \sim 3 * HV \quad \text{Equation 2}$$

Comparing hardness measurement from different experimental series to each other, it is important to know the applied load as well as the indentation time for each of the different series, since both influence the hardness value [109].

In the present work, Vickers hardness measurements were performed using a fully automatic Buehler Tukon™1102 instrument. The sample was ground and mirror polished prior to hardness measurements. The applied load was 500 gr with an indentation time of 10 sec.

2.4. Transmission electron microscopy

Transmission electron microscopy (TEM) was used in the present study to obtain local information on the precipitate microstructure, from the atomic resolution up to a wider view. In order to achieve these goals, several instruments and observation modes were used. The following section will shortly

introduce a generic instrument with its different elements and overview the different operating modes that were used.

Two different types of electron sources are distinguished, thermionic sources and field emission guns (FEG). In general, the current density and brightness is higher for FEG and the cross over size and energy spread of the beam is smaller. These features are important for stable imaging condition with good temporal and spatial coherency. In order to achieve a magnified image, several magnetic lenses are used. A lens system is illustrated in Figure 18. Condenser lenses control different illumination conditions such as parallel or convergent beam and are positioned above the specimen. Below the sample, the objective lens system controls the focus of the object and the resolution of the image. It creates a first magnified image. The objective aperture, situated in the focal plane of the objective lens, is an important feature used to create contrast conditions. The projector system magnifies further the image of the objective lens. The current in the intermediate lenses determine if the focal plane or the image plane is imaged on the phosphorus screen. This allows imaging the diffraction patterns on one side and the image of the sample in real space on the other side. Magnetic lenses allow magnifying the images to a great extent; however they are associated to aberrations which restrict resolution, magnification and image quality [110].

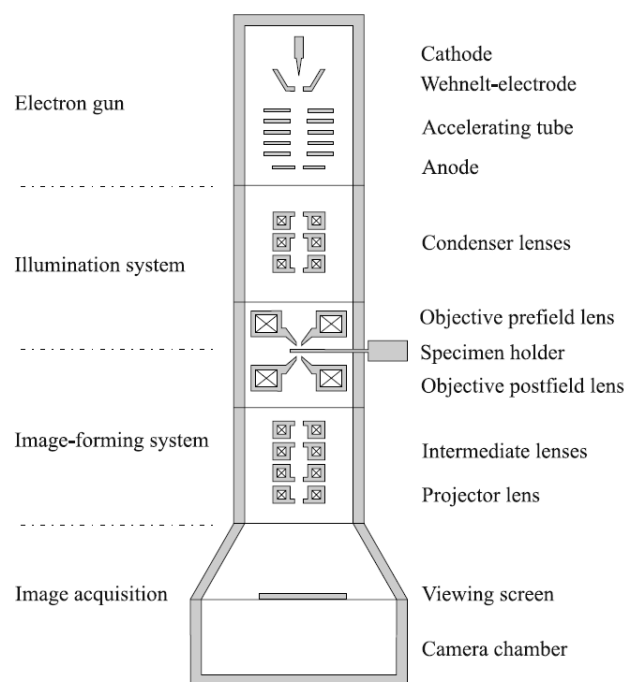


Figure 18: Scheme of a TEM with its different lens systems (Figure taken from [111]).

2.4.1. Conventional TEM

In the present work, conventional TEM was operated in 2 different modes, the image mode and the diffraction mode. Ray diagrams for both modes are illustrated in Figure 19a and b, respectively. The

diffraction mode gives information in reciprocal space and provides characteristics of the crystal structure, specimen shape and lattice distances. The image mode shows the real image.

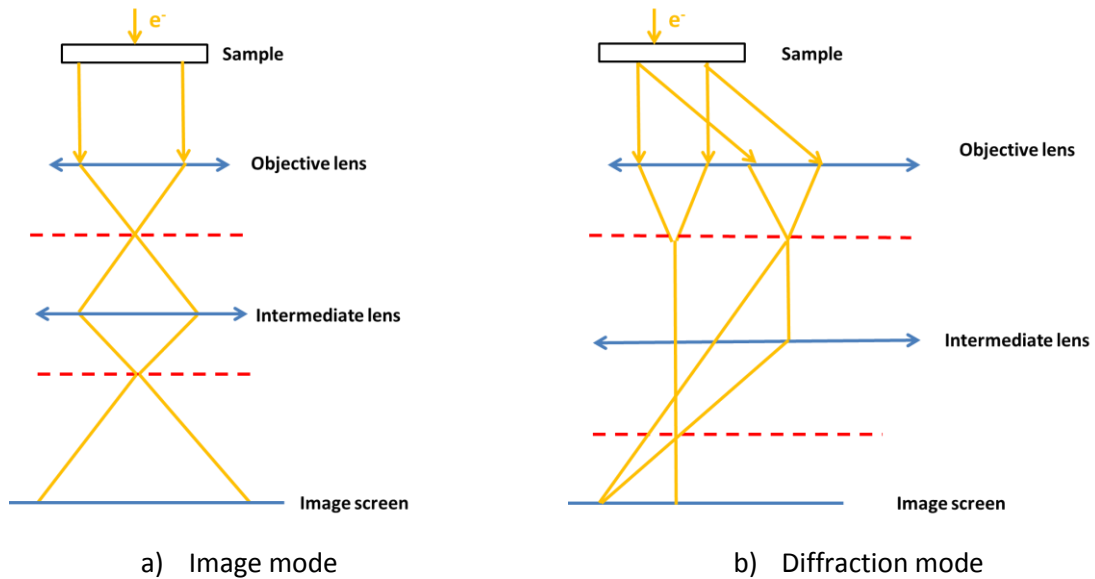
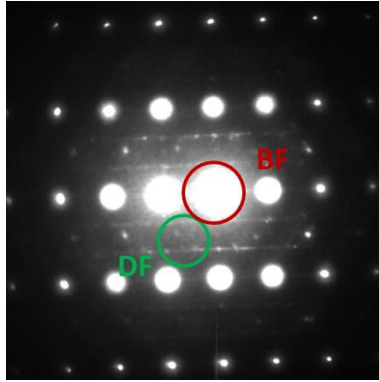
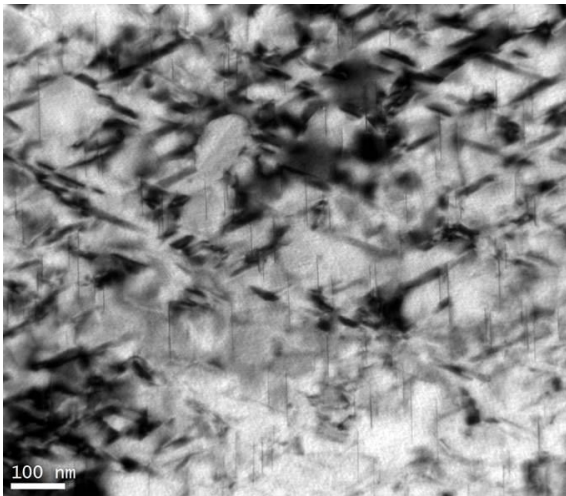


Figure 19: Simplified ray diagram for the image mode a) and diffraction mode b). Different imaging conditions are possible due to changes in the intermediate lens system.

By means of diffraction patterns, conventional TEM can be operated in both bright and dark field mode, which determines contrast conditions of the final image. From a selected area, the diffraction patterns are imaged. Diffraction pattern oriented along the $\langle 112 \rangle$ matrix zone axis are given as an example in Figure 20. Selecting the central spot with the objective aperture, as indicated by the red circle in Figure 20a, a bright field image is produced as seen in Figure 20b. A dark field image is obtained when selecting a distinct (hkl) spot or streaks along a certain orientation of the diffraction pattern, as pointed out by the green circle in Figure 20a. A dark field image of the same position as Figure 20b is illustrated in Figure 20c). It clearly shows that different microstructural features are imaged by selecting either a BF or a DF mode, respectively. In the present example, the dark field image reveals precipitates along one direction, which are much harder to identify in Figure 20b due to different contrast conditions.



a) Diffraction patterns



b) Bright field image



c) Dark field image

Figure 20: a) Diffraction patterns of $\langle 112 \rangle$ matrix zone axis; the red circle around the central spot indicates the position of the aperture to obtain a BF images as seen in (b) and the aperture position marked in green results in a DF image as illustrated in c).

2.4.2. HAADF-STEM

Scanning transmission electron microscopes require a convergent beam that scans across the sample. The image is created over several seconds or minutes, depending on the scan rate. Magnification is achieved not by increasing the current of the lenses, but by adjusting the probe dimension and scanning area.

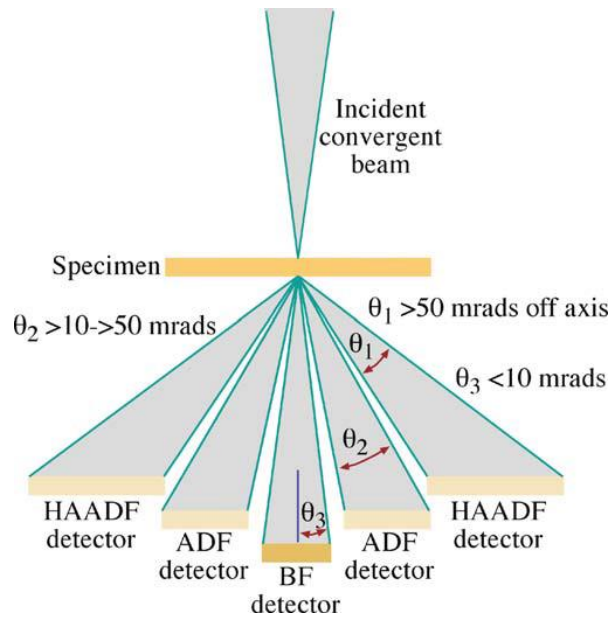


Figure 21 : Different detectors in STEM [110].

In addition to the diffraction contrast as used in conventional TEM, STEM can also produce contrast with respect to the atomic number, due to inelastically scattered electrons. The different types of detectors used in STEM are shown in Figure 21.

As seen before for conventional TEM diffraction, contrast occurs due to elastic scattering of electrons on crystal planes. In STEM, this contrast conditions apply when using the bright field (BF) detector and the annular dark field (ADF) detector. A bright field (BF) detector collects electrons, unscattered from the central beam and the corresponding dark field image taken by and an ADF detector collects diffracted electrons. The contrast of BF and ADF images is complementary.

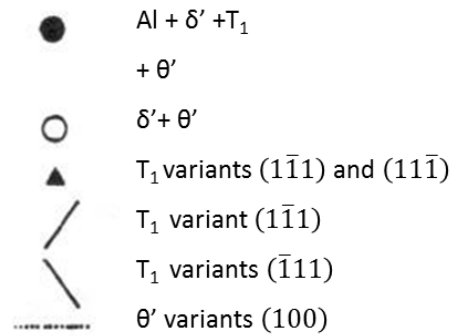
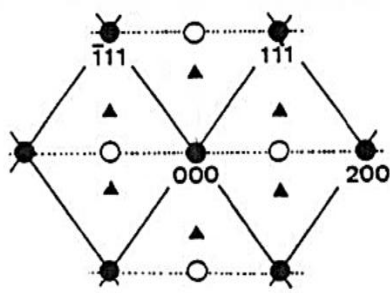
The HAADF detector, which has a larger radius than the ADF detector collects only inelastically scattered electron. Based on inelastic scattering a so-called mass-thickness contrast arises. Dependent on the thickness of the sample and the atomic number of the chemical species in the sample, scattering is affected. Assuming constant thickness, the contrast depends only on the atomic number ($\sim Z^2$). A zone with a high atomic number scatters strongly and appears brighter in the image than a zone with lower average atomic number. The HAADF detector however does not allow determining the exact chemical species or their concentrations. The contrast is only relative to the other chemical species, but usually when the present elements are known the contrast can be attributed to the chemical elements. This is a very useful tool in materials with different elements in which the atomic number differences are quite elevated [110], [112].

2.4.3. EDS spectroscopy

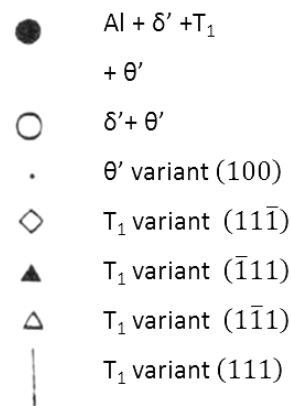
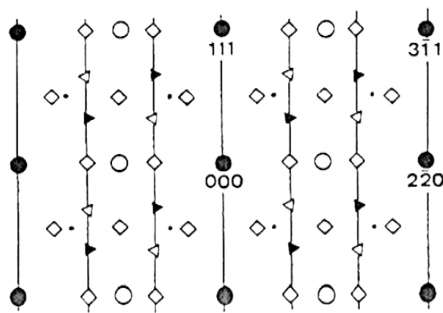
EDS spectroscopy collects characteristic X-rays that are emitted by the interaction of the electron beam with the sample. It permits distinguishing elements with similar atomic numbers that are impossible to separate by HADDF-STEM, such as Mg ($Z = 12$) and Al ($Z = 13$) or Cu ($Z = 29$) and Zn ($Z = 30$). It is a useful tool to complete the analysis of chemical elements in precipitates. In general, an area of the sample is selected and scanned for several minutes, in order to acquire a reliable chemical spectrum. The position of the different elements can be made visible [110].

2.4.4. Observations directions in Al-Cu-Li alloys

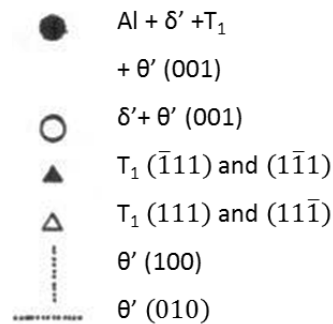
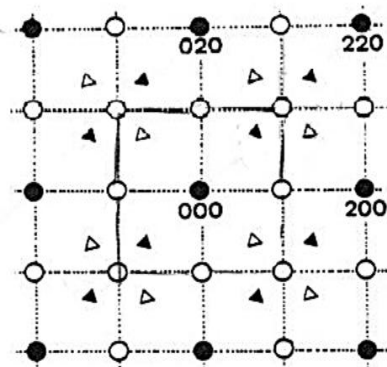
In Al-Cu-Li-X alloys, different phases may precipitate during artificial aging. As described in Chapter 1.4, all these phases have different orientation relationships with the matrix. For anisotropic precipitates, such as platelets or needles, best observations can be performed when precipitates are visualized edge-on, i.e. when they lie parallel to the electron beam. It is therefore necessary to perform microscopic observations along different zone axes, to ensure that all possible precipitates are visualized. Figure 22 illustrates three different diffractions patterns, which provide different information on precipitates in Al-Cu-Li alloys. T_1 precipitates that lie on $\{111\}_{Al}$ planes are best visualized in $\langle 0\bar{1}1 \rangle$ and $\langle 11\bar{2} \rangle$ zone axis, in which two or respectively one family of T_1 are seen edge-on. Figure 22a shows schematically the diffraction pattern of the $\langle 0\bar{1}1 \rangle$ zone axis and the corresponding explanation of the diffraction features. Two families of T_1 are observed in form of continuous streaks passing through the central spot and through the (111) and $(\bar{1}11)$ matrix spots, respectively. These streaks appear due to the very high form factor of these precipitates. Furthermore, one family of precipitates along (200) are seen, indicated by a broken line, and is characteristic for the orientation of θ' . The filled triangles are representative for T_1 precipitates and open circles are attributed to super-lattice spots, which correspond to δ' precipitation, when present in the microstructure. Figure 22b shows the diffraction pattern of the $\langle 11\bar{2} \rangle$ orientation. One family of T_1 is visualized edge-on, indicated by a continuous line in direction of the (111) matrix spots. Along this direction filled and open triangles are seen as well as open diamonds, which are attributed to the three other variants of T_1 , which are not seen edge-on. Reflections on the position of open circles appear in the presence of δ' . Last, the $\langle 001 \rangle$ zone axis is illustrated in Figure 22c. In this zone axis no T_1 precipitates appear edge-on. Their corresponding diffraction spots are indicated by filled and open triangles. In $\langle 001 \rangle$ matrix zone axis, two families of precipitates along $[100]$ or $[010]$ direction are seen, which in Cu containing aluminium alloys are attributed to precipitation of Cu containing phases such as GP zones and θ' . Open circles illustrate again super-lattice spots of the aluminium matrix which are appear in the presence of δ' .



a) Scheme of $\langle 0\bar{1}1 \rangle$ zone axis



b) $\langle 11\bar{2} \rangle$ zone axis



c) $\langle 001 \rangle$ zone axis

Figure 22 : Diffraction patterns for different zone axes. Different characteristic features can be pointed out by investigating Al-Cu-Li alloys in these different orientations [113].

The diffraction patterns in Figure 22 show the orientation of the most common phases in Al-Cu-Li alloys. In the presence of Mg, it is possible that additional S'/S phase precipitates. It can take different orientation relationships with the aluminium matrix. The precipitates form along the [001] direction and are therefore visible in the $\langle 001 \rangle$ matrix zone axis. Orientation relationship 1 of the S'

phase, $[100]_{S'}/[100]_{\alpha}$ and $(001)_{S'}/(021)_{\alpha}$, has been simulated by Wang and Starink [26], [42]. The results of simulated diffraction pattern for one out of 12 variants is shown in Figure 23 for a $\langle 001 \rangle$ matrix zone axis. The aluminium matrix is indicated by big grey circles and the S phase by small black points. Open circles indicate double reflection of the S phase [26].

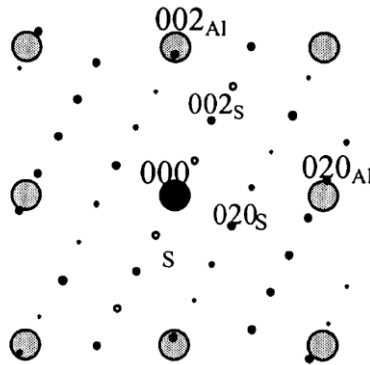


Figure 23: $\langle 001 \rangle$ zone axis including simulated spots expected for one out of 12 variants of the S' phase by Wang and Starink [26].

2.4.5. Equipment and sample preparation

Conventional TEM was performed at the SIMaP laboratory on a JEOL 3010 instrument, operated at 300 kV. These experiments were performed to measure the diameter of T_1 precipitates and their surface fraction (see Figure 20c). Given the aperture diameter available on this instrument, the $\langle 112 \rangle$ orientation was favourable to form good dark field images given the larger distance between matrix diffraction spots as compared to the $\langle 110 \rangle$ zone axis.

HAADF-STEM images were acquired both at SIMaP laboratory on a JEOL 2100F instrument and in atomic resolution mode on a JEOL ARM 200F instrument at the University of Rouen.

The JEOL 2100F at SIMaP laboratory, equipped with a thermally activated field emission gun, is operated at 200 kV and a resolution with Z-contrast of 0.23 nm is possible. It is equipped with a wide collection angle (1 strd) EDS detector for chemical analysis.

The JEOL ARM 200F has a thermally activated field emission gun and an accelerating voltage of 200 kV. It is equipped with an extra spherical aberration correction lens. Thereby a STEM resolution of 0.08 nm is possible, i.e. atomic resolution. The objective aperture semi-angle is 22.5 mrad and the detector half-collection angle is between 40 and 150 mrad. During our experiments the probe size was 0.1 nm and for HAADF images the collection angle of the detector laid between 50 – 180 mrad and for ADF images between 20 – 80 mrad. Both ADF and HAADF-STEM images were taken. In addition, EDS spectra were acquired by an Oxford instruments SSD detector X-Max^N 100 TLE.

Samples for TEM analysis need to be very thin so that the electron beam passes through. Specimens were mechanically ground below 100 μm . Disks with 3 mm in diameter were punched out and jet-polishing was performed with a Tenupol. The electrolyte consisted of 70 % CH_4O and 30 % HNO_3 and was cooled down to below $-20\text{ }^\circ\text{C}$. The sample was subsequently rinsed in methanol. Jet-polishing creates a hole in the sample which preferentially should be situated in the centre of the specimen. Close to the hole the specimen is thin enough (between 30 to 70 nm) to perform good TEM characterisation.

2.5. Small Angle X-ray Scattering

Small Angle X-ray Scattering (SAXS) is a technique that measures the scattering of X-ray light by a sample possessing inhomogeneities of electron density. The scattering process is the same as with X-ray diffraction, but the smaller collection angles mean (in reciprocal space) that the probed electron density fluctuations are larger than the inter-atomic distances, typically in the range 0.5-100 nm. Such fluctuations of electron density are caused by composition changes within precipitates, whose characteristics can therefore be obtained using SAXS.

When illuminating a sample with a monochromatic, parallel X-ray beam, information on the size of precipitates and their volume fraction can be obtained. The scattering vector is defined as $q = \frac{4\pi}{\lambda} \sin\theta$. It describes the difference of the incident and the scattered beam (2θ is the scattering angle and λ the wave length of the photons). The resulting wave for a given scattering angle 2θ is given by the sum of the contributions of all interfering waves $\varphi = \exp(-i\vec{q}\vec{r})$. The amplitude is defined as $A(\vec{q}) = \iiint \rho(\vec{r}) \exp(-i\vec{q}\vec{r}) dV$ and the intensity is in consequence $I(\vec{q}) = |A(\vec{q})|^2$. $\rho(\vec{r})$ is the electron density which depends on the local concentration. Figure 24 illustrates schematically the setting of a SAXS-experiment. An X-ray beam penetrates a sample. The sample thickness depends on the analysed material and the energy of the X-ray beam and lies between 30 to 500 μm . The beam is scattered and depending on the distance between sample and detector and on the beam energy, the acquisition covers a given range of scattering vectors (q-range). The transmitted beam is stopped by a beam-stop since its very high intensity would damage the detector, and would anyhow mask the much weaker scattered intensity.

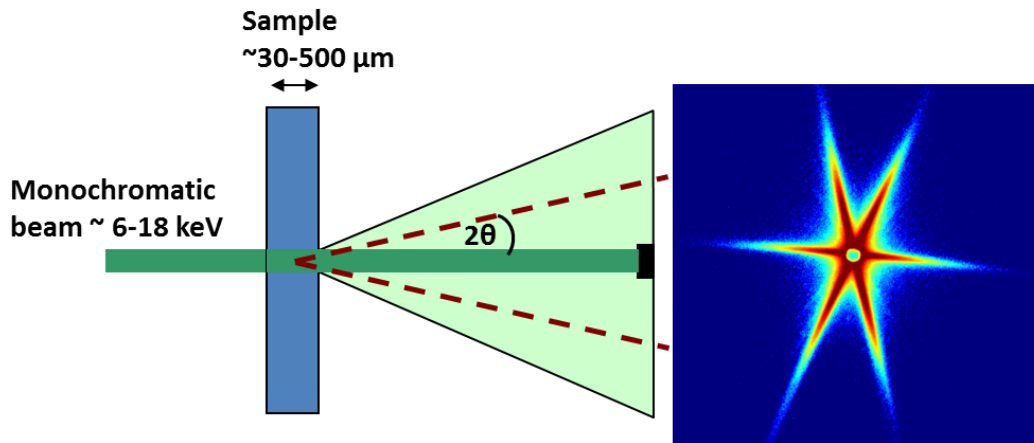


Figure 24: Scheme of SAXS-setting.

Due to reciprocity in diffraction, flat plate-like particles, observed edge-on, are seen as streaks in SAXS measurements. This is schematically shown in Figure 25a and b. Consequently, the thickness and the diameter of the precipitates are inversely proportional to the length and the thickness of the streaks, respectively. Knowing the thickness and the diameter of the precipitates, the volume fraction can be estimated in certain conditions [114], [115].

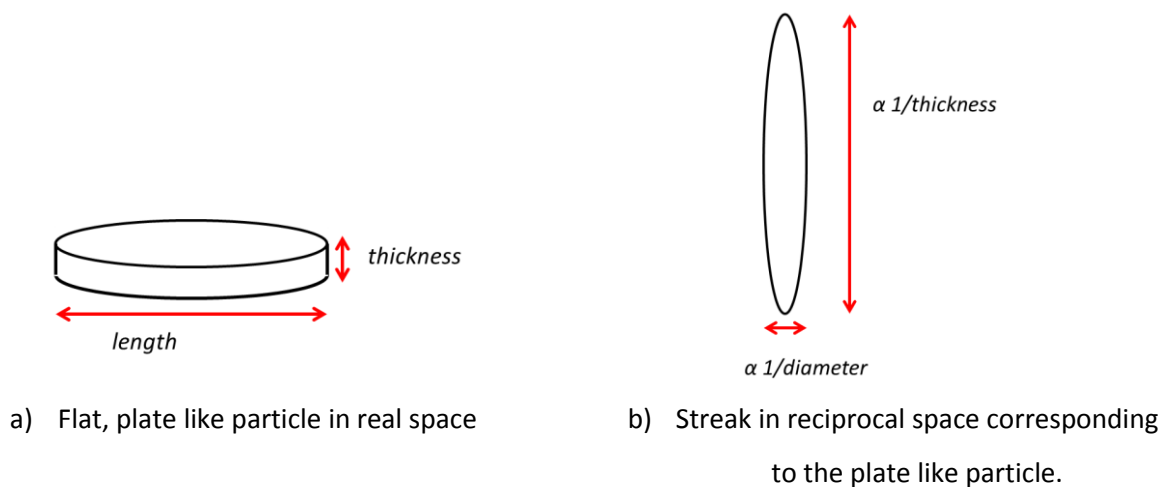
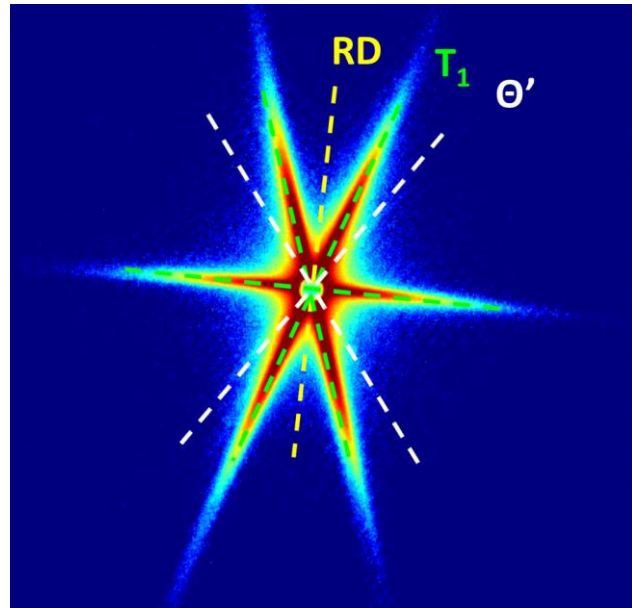
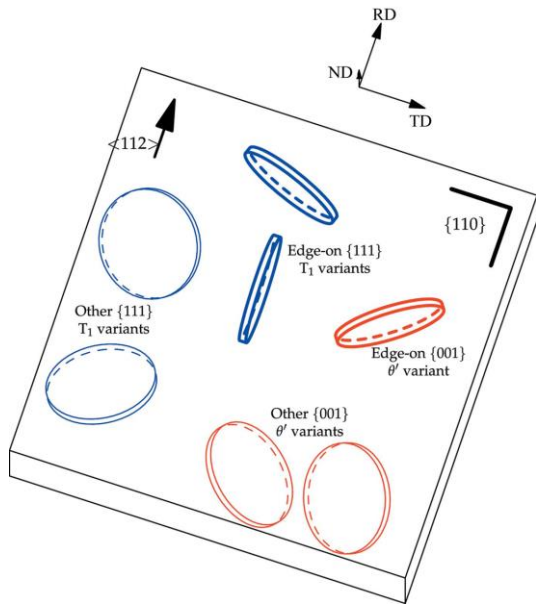


Figure 25: Illustration of the relationship between particle in real space and corresponding streak in reciprocal space.

Sample orientation

The main precipitating phase in Al-Cu-Li alloys, lies on $\{111\}_{Al}$ planes. The existence of a moderate rolling texture (Brass-texture component $\{110\} \langle 112 \rangle$) provides favourable acquisition conditions. Figure 26a shows a sketch of different phases precipitating in Al-Cu-Li and their orientation in a moderate textured sheet.



a) Sketch showing how precipitates lie in the $\{110\}$ matrix plane

b) SAXS image in a moderately textured material including the orientation relationship of T_1 and θ' [116].

Figure 26: Orientation relationship of precipitates in Al-Cu-Li with respect to the rolling texture. It indicates that in $\langle 110 \rangle$ direction two T_1 orientations are edge-on and on θ' (Figure taken from [117]).

The rolling direction is along $\langle 112 \rangle$ and the normal direction is perpendicular to $\{110\}$ planes. 2 families of T_1 precipitates lying on $\{111\}_{Al}$ planes are seen edge-on in ND. In addition, one family of θ' , precipitating on $\{001\}_{Al}$ is visualized edge-on. In the presence of a rolling texture, the scattering of precipitates lying edge-on appears as streaks (see Figure 25a and b). The orientation relationship with respect to the rolling direction permits identifying the different phases. A SAXS image is illustrated schematically in Figure 26b in which the orientation of both T_1 and θ' is indicated with respect to the rolling direction. As seen in the present example, the streaks corresponding to T_1 precipitates are clearly seen, whereas the absence of streaks in θ' direction indicates the absence of this phase in significant amount.

2.5.1. Analysis

Al-Cu-Li alloys, in which T_1 is the main precipitating phase, show in case of a moderate rolling texture, defined streaking in SAXS images. An example is taken from Dorin et al. [116] and is shown in Figure 26b.

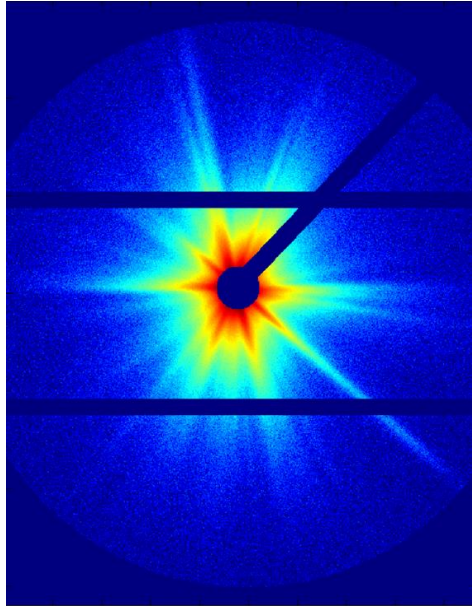


Figure 27: SAXS images in AlCuLiMg0.1AgZn of the present work with less pronounced texture components. Image taken by DECTRIS Pilatus 300K X-ray Detector.

The investigation of these anisotropic precipitates can be performed by analysing each streak individually and thereby obtaining information on the precipitate thickness, diameter and volume fraction [116], [117]. Although, in the present study very similar alloys in composition as in [116], [117] are investigated, there are big differences in their processing route. In the present study, laboratory cast alloys have leaner impurity contents and are elaborated on laboratory scale, leading to a less pronounced rolling texture than in industrial rolled alloys such as AA2198 [116]. The final microstructure is determined by the thermo-mechanical treatment, which is influenced by the degree of rolling, pre-stretch and applied temperature during processing. The SAXS images, one is illustrated in Figure 27, show less pronounced streaking as observed in the industrial processed alloy AA2198. On such images it is impossible to analyse separately each streak to determine the thickness and diameter of platelet precipitates. As a consequence, the signal was treated as if it was isotropic, which means that the average intensity for each q was calculated. We then worked on the averaged signal. A practical consequence is that the average diameter of the precipitates could not be determined, because the high value encountered in these alloys (typically 50 nm) gives a measurable signal at angles that are too small for the setup. However information on the precipitate thickness (typically 1-2 nm) and volume fraction could still be retrieved.

The radially average intensity of plate-like precipitates can be approximated to [114], [118]:

$$I = A \frac{2\pi}{q^2} (\Delta\rho)^2 t^2 \frac{\sin\left(\frac{qt}{2}\right)^2}{\left(\frac{qt}{2}\right)^2} \quad \text{Equation 3}$$

A is the surface area and t the thickness of precipitates. When a number of precipitates n_V with same volume is introduced the volume fraction can be written as $f_V = n_V A t$. Re-organising Equation 3 results in Equation 4, which is further developed for data fitting.

$$I = f_V \frac{2\pi(\Delta\rho)^2}{q^4 t} \sin\left(\frac{qt}{2}\right)^2 \quad \text{Equation 4}$$

In order to extract characteristic data such as thickness and volume fraction, the measured data need to be fitted with a model function, taking into account the distribution of precipitate sizes, and particularly the thickness distribution. The thickness of T_1 precipitates, which is expected to be the main precipitating phase, can only take discrete values [56], [62]. The stepwise increase in thickness is characterised by an integer n , which is the number of additional layers of T_1 . The thickness of one layer T_1 is $t_1 = 9.5 \text{ \AA}$ and each increase in thickness is $dt = 9.2 \text{ \AA}$ (because one plane is common with the already existing T_1 precipitate). To model the distribution of T_1 thicknesses present in a given sample, a Poisson-based distribution was chosen, which is a discrete probability function and therefore appropriate in the present case. The definition of the Poisson distribution is as following:

$$f(k; \lambda) = P_\lambda(X = k) = \frac{\lambda^k}{k!} e^{-\lambda} \quad \text{Equation 5}$$

The variables, k stands for the number of intervals, $k!$ is the factorial of k , e is Eulers number. We define λ as an additional average thickness compared to a single-layered T_1 . $\lambda = \frac{t-t_1}{dt}$ and t is the actual average thickness over the whole distribution. dt is, as mentioned before, the thickness of an additional unit cell. Furthermore, the thickness t_n corresponding to each additional unit cell n , is defined as $t_n = t_1 + n * dt$. The average thickness is then: $\langle t \rangle = \sum_n t_n$.

Figure 28a shows the distribution of layers of T_1 for an average thickness of 11 \AA and Figure 28b for an average thickness of 20 \AA , respectively. It clearly reveals that in the first case the number of double layered T_1 is very low and triple layered T_1 or more are negligible in number density. In the second case, in which the average thickness is set to 20 \AA the probability to find double or even triple layered T_1 is much higher. The model describes well the thickening behaviour of T_1 precipitates. In some of the microstructures other phases are also present, in particular θ' precipitates. The

contribution of these phases cannot be separated and an average value of the thickness is obtained. θ' precipitates plate-like shaped, so that the description of the intensity should still be valuable. However, θ' precipitates are not restricted to a minimum size as it is the case for T_1 and also their thickening behaviour is rather continuously than discrete. This should be kept in mind when interpreting thickness evolutions.

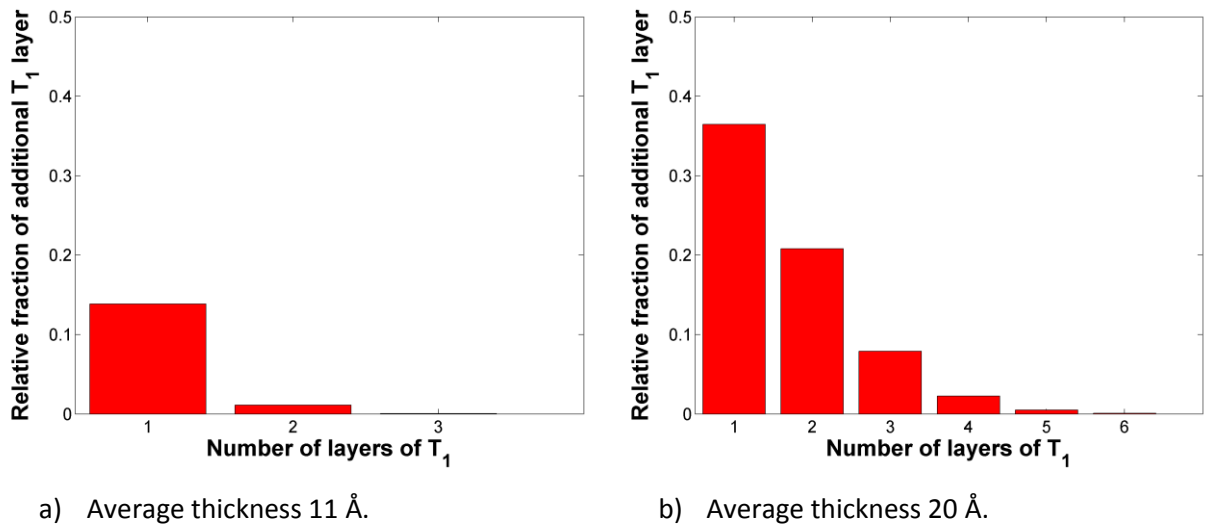


Figure 28: Poisson distributions of additional T_1 layers for average T_1 thickness of 11 Å (a) and 20 Å (b).

The SAXS intensity is fitted by the sum of several intensities contributions. There is the contribution calculated by the distribution for T_1 precipitates and an additional constant intensity contribution, originating from the solid solution scattering (Laue scattering) or other incoherent scattering such as fluorescence [115]. Another contribution is added that takes into account the scattering from large particles such as dispersoids. It is dominant at the beginning of the experiment and is proportional to $1/q^4$. The complete fitting function summarizes to:

$$I = \sum_n f_V \frac{2\pi(\Delta\rho)^2}{q^4 t_n} f(k; \lambda) \sin\left(\frac{qt_n}{2}\right)^2 + Laue + \frac{BP}{q^4} \quad \text{Equation 6}$$

A log-log plot of intensity vs. scattering vector q is helpful to validate the fit. The measured data in blue with its corresponding error bars are sketched in Figure 29. In green the actual range of q -values (0.05 – 0.5 Å⁻¹) for the data analysis is indicated and in red the fitted curve is superimposed on the measured data. It is seen that a good agreement is achieved, enabling the determination of the thickness and volume fraction of precipitates. Only a relative volume fraction, however, can be

determined. This is due to the fact that the exact concentration of the phase (and thus its electronic contrast with the matrix) is unknown and to the lack of randomness of the sample texture, which does not guarantee a homogeneous distribution of intensity along all directions.

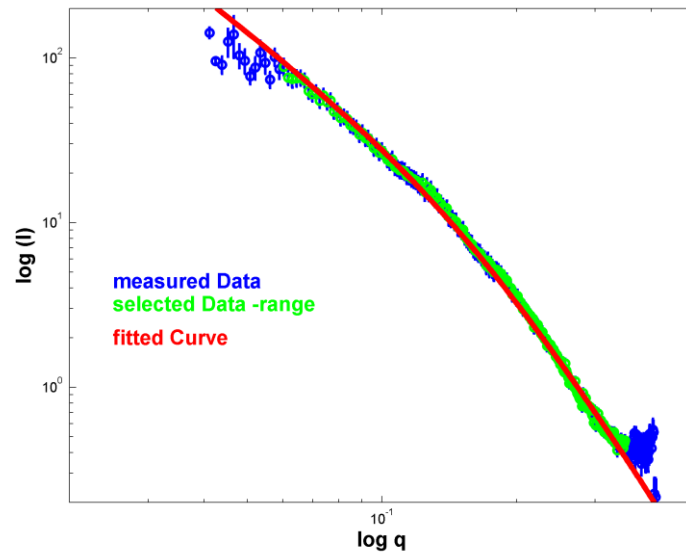


Figure 29: $\log(I)$ - $\log(q)$ plot : original data and fitted curve; q -range $0.05 - 0.5 \text{ \AA}^{-1}$.

2.5.2. Equipment and sample preparation

Small angle X-ray Scattering measurements were performed both on a laboratory rotating anode (Rigaku MicroMax-007 HF, Cu K_{α} source) and on the BM02-D2AM beamline at the European Synchrotron Radiation Facility (ESRF).

Samples thickness depends on the energy of the incident photon beam. For Cu K_{α} the energy is 8.048 keV. The optimal sample thickness depends on the absorption coefficient. For aluminium alloys the optimal sample thickness it is around 75 μm at this energy.

The data were acquired by a DECTRIS Pilatus 300K X-ray Detector, which performs single-photon counting on each pixel. Noise and dark current is reduced in a great way and becomes negligible.

Precipitation evolution of diffusion couples, that were produced as explained in Section 2.1, was likewise determined by using SAXS measurements. Thereby a space and time resolved approach was chosen. By displacing the sample in horizontal direction, the different measuring points correspond to different compositions in the homogenised weld. At the same time heating was performed so that precipitation kinetics could be measured dependent on the composition. This is sketched in Figure 30. An acquisition time of 100 seconds allowed the acquisition of the kinetics every 30 minutes for each point.

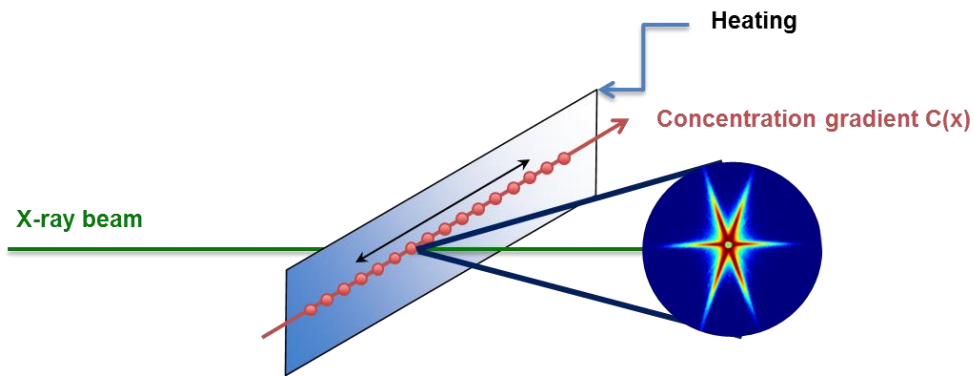


Figure 30: Scheme of combinatorial approach; the sample is scanned along x-direction. Due to a concentration gradient, each change in x corresponds to a different alloy composition.

In order to realise time and space resolved measurements along a distance of around 20 mm, a furnace was designed and manufactured in the laboratory for this study. Figure 31 shows the furnace. A sample of length up to 20 mm is mounted in the furnace. A resistance heating wire is coiled and heats up the furnace. In order to provide stable temperatures and avoid overheating, water cooling is added. The copper block, seen in the background is cooled and directly connected to the furnace. Furthermore, a 1 mm type K thermocouple is closely fitted in a furnace hole as close as possible to the sample to measure its temperature.

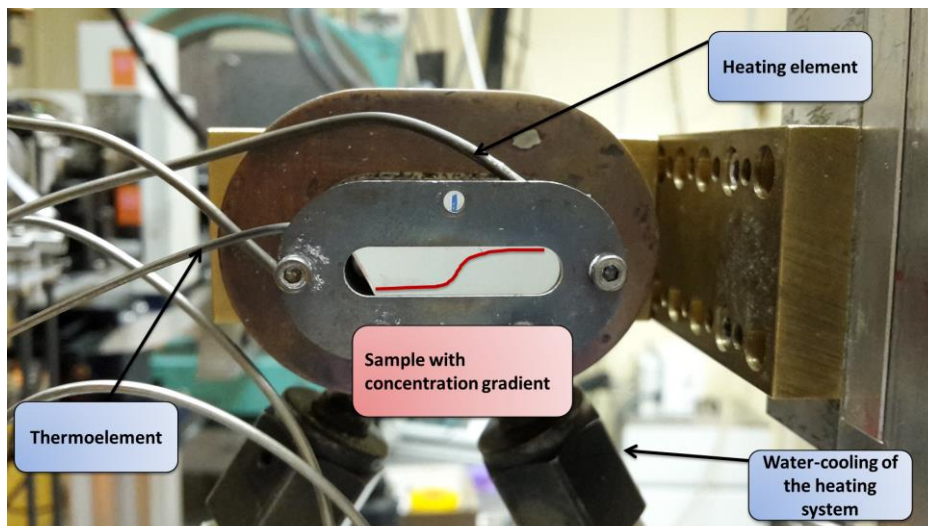


Figure 31: Laboratory elaborated SAXS-furnace in order to perform space and time resolved experiments.

2.6. Microprobe

2.6.1. Set-up and basic design

Electron Probe Micro Analysis (EPMA) is used for chemical analysis. An electron beam generates an X-ray signal, which can be analysed and quantified to obtain composition measurements. Monochromatic crystals select distinct wavelengths and focus them on detectors (gas flow proportional counter). Bragg's law of diffraction determines interference conditions and is illustrated schematically in Figure 32. The incident beam is scattered by an angle θ . If the path difference between atomic planes is an integral number of the wavelength constructive interference occurs. In Bragg's formula this is summarized as $n\lambda = 2d \sin \theta$, in which $n\lambda$ is the wavelength, d the interplanar distance of atom planes and θ the scattering angle.

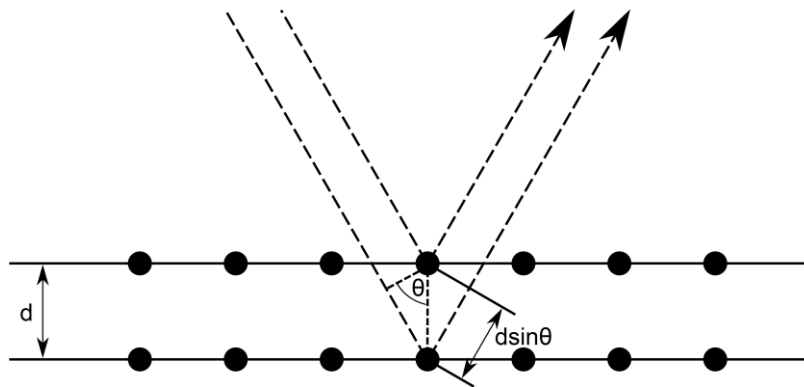


Figure 32: Sketch of Bragg's law (image adapted from Wikipedia).

In the microprobe set-up, however, the incident beam on the crystal is not parallel due to a point – source on the sample (the beam is strongly convergent in order to illuminate only a small surface of the sample). Therefore, the analysing crystals are curved in order to maximise the detector signal. Optimal conditions are obtained when sample, analysing crystal and proportional counter lie on a so-called focusing circle. Different crystals are available, which all cover a certain range of wavelengths. In general, EPMA are limited to short wavelengths, but newer synthetic crystals and multi-layered analysers extend the detection limit to longer wavelengths (i.e. lighter elements). On a micro probe instrument usually several different crystals are mounted in order to ensure optimal conditions for different wavelength ranges. Different possibilities to mount these detectors are either vertical, horizontally or inclined. For qualitative analysis or concentration mapping horizontal or inclined detectors are very efficient. Vertical detectors are highly sensitive to defocusing, but in turn are better for quantitative analysis of plane polished surfaces. For mapping the compositions of a sample

at different points, it is however best to move the sample instead of displacing the beam, since usually a pre-alignment is present which relates the optical focus with the X-ray focus [119], [120].

2.6.2. Equipment and sample preparation

The microprobe CAMECA SX 50 was operated at 20 keV and 300 nA. Different crystals mounted vertically are present and are calibrated for the element, Mg, Ag, Cu and Zn. Li was set to constant, since it is very difficult to detect. Likewise minor alloying elements such as Zr and Mn were set constant in order to calculate a correct mass balance for Al.

Samples were mechanically ground and mirror polished to 1 μm . After polishing they were cleaned for several minutes in an ultrasound bath using ethanol. In order to perform reasonable quantitative concentration measurements, it is absolutely necessary that the sample is perpendicular to the incoming beam and in correct z-focus.

2.7. Differential Scanning calorimetry

Differential Scanning calorimetry (DSC) is an indirect experimental technique that gives information on phase transformations. Both quantitative and qualitative information can be obtained. In a power compensated DSC a sample and a reference are measured in two separated furnaces and either a ramp heating or isothermal heating is performed. The set-up used in the present work is seen in Figure 33. The difference in supplied power necessary to keep the sample and the reference at the same temperature during the whole process, is a direct measure of the heat flow and permits drawing conclusions on the type of phase transformations. In solid-state phase transformations, such as ageing, exothermic signals are attributed to precipitation, whereas endothermic signals refer to dissolution of different phases [121].

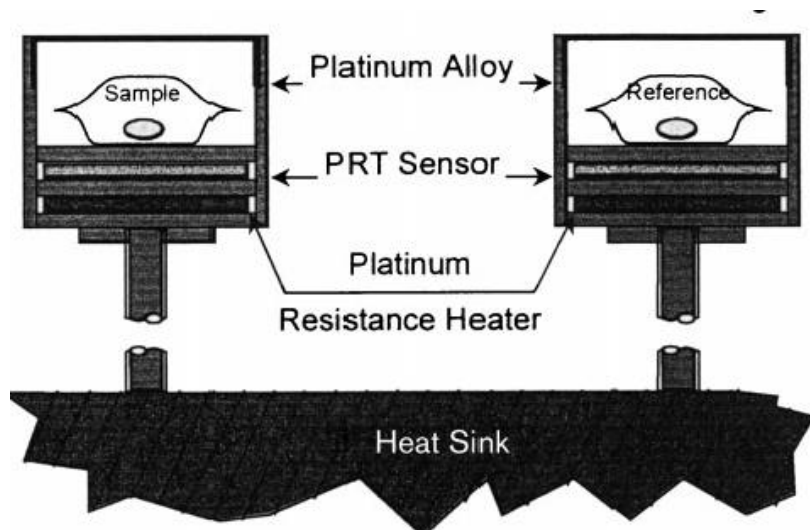


Figure 33: Sketch of power compensated DSC [121].

Samples and data treatment

DSC samples need to have a flat surface in order to provide good contact between the sample, the pan in which the sample is placed and the measurement unit. In general, samples have a diameter of 4-5 mm and a thickness of 0.5 – 1 mm. Their weight lies around 30-50 mg. An empty aluminium pan was used as reference. The DSC is calibrated for temperature by pure In and Zn melting. The scanned temperature interval goes from 25 to 550 °C. Baseline corrections are done, by adjusting temperature intervals between 50 to 100 °C and above 500 °C to zero heat flow by using a polynomial function of 3rd order. These temperature intervals are chosen, because precipitation is expected to occur above this lower temperature boundary and all present phases should have been dissolved above 500 °C [116]. In naturally aged samples, it is seen that the integral of the exothermic and endothermic sections level out to 0, which is in good agreement for a sample in which no precipitation process has occurred.

3. Influence of minor alloying elements on precipitation kinetics

The following chapter is dedicated to describe the effect of minor alloying elements on precipitation and hardening kinetics in Al-Cu-Li alloys. The hardening kinetics is measured by hardness, while small angle X-ray scattering (SAXS) and differential scanning calorimetry (DSC) are used to evaluate the kinetics of precipitation and the precipitation sequence in respectively isothermal and non-isothermal conditions.

3.1. Precipitation kinetics measured by hardness

Figure 34 and Figure 35 present the evolution of hardness over aging time at 155°C for the different alloys, separated in two groups. The time scale is plotted in logarithmic scale with respect to the time of the 'End of Ramp' ('EoR'). The conditions prior to 'EoR' are placed arbitrarily on the time scale. In Figure 34, the influence of Mg and Ag on the hardening kinetics is illustrated. After water quench, the hardness of all alloys is very similar and lies around 70 – 75 HV. Pre-deformation after quench separates the alloys in two groups. The first group contains Mg and hardness increases up to 95 HV. The second group, with no Mg additions, shows an hardness around 10 HV below Mg containing alloys after pre-deformation. However, no additional effect of Ag is observed. Three days of natural aging ('NA') amplify the differences between Mg containing and Mg-free alloys. In the absence of Mg the hardness increases only up to around 90 HV, whereas in the presence of Mg hardness increases up to 110 HV after 3 days of natural aging. Subsequently, a ramp heating up to 155 °C is performed. The hardness slightly decreases at the so called 'EoR' condition compared to the hardness values at 'NA'. The difference between Mg containing and Mg-free alloys is still 20 HV. When subjected to artificial aging heat treatment at 155 °C the hardness increases within 1 hour of artificial aging. After 4 hours artificial aging, the effect of Ag in Mg containing alloys becomes visible. Both alloys containing some Ag additions increase faster in hardness and highest hardness is measured for AlCuLiMg0.3Ag (173 HV), followed by AlCuLiMg0.1Ag (170 HV) and AlCuLiMg (162 HV). For Mg-free alloys, the hardness increase follows a similar shape as for Mg containing alloys, however the average hardness is around 10 HV lower compared to AlCuLiMg and 20 HV lower compared to Mg and Ag containing alloys, respectively. Slightly higher hardness is obtained for AlCuLi0.3Ag (154 HV) than in AlCuLi (148 HV). It is important to mention that maximum hardness in Mg-free alloys is reached after at least 50 hours of artificial aging at 155 °C, whereas in the presence of Mg, the plateau of maximum hardness is reached for earlier aging times (after around 20 hours).

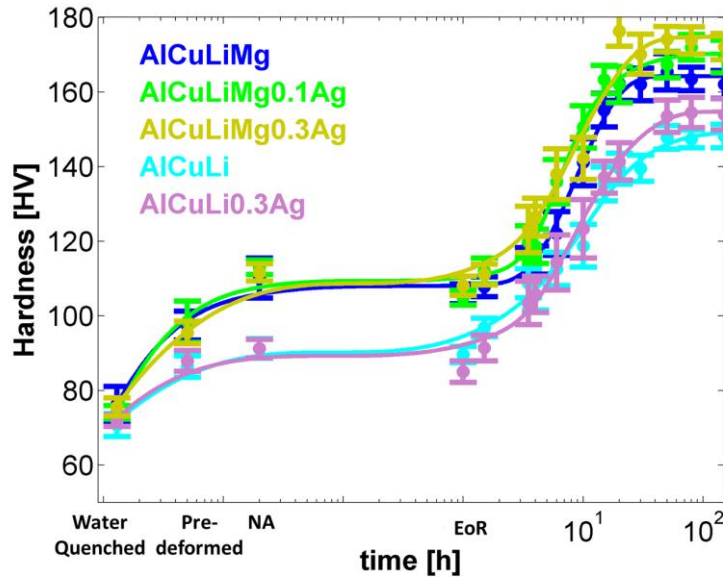


Figure 34: Hardness measurements; presenting the effect of Mg and Ag.

In Figure 35, all measured alloys contain Mg and the influence of Zn and Ag is emphasized. The hardness curves start likewise with as-quenched condition. For AlCuLiMgZn and AlCuLiMg0.1AgZn the measurements for as-quenched and pre-deformed conditions were conducted one year later (yet with the same heat treatment procedure) than the other measurements. A deviation in hardness of around 5 % was observed for the latter measured conditions. Repeating these measurements on a common alloys similar deviations in hardness were observed. These might be due to changes in the hardness measurement image analysis procedure. Hence we used a correction factor in order to approximate the data with respect to the former performed hardness measurements. In the 'NA' condition, all alloys possess approximately the same hardness of around 110 HV, which is likewise observed in Figure 34 for Mg containing alloys at 'NA'. The ramp heating shows again a slight decrease in hardness, followed by a rapid increase after 1.5 hours of artificial aging at 155 °C. The addition of Ag, Zn or their combination enhances precipitation kinetics compared to AlCuLiMg. After around 25 hours of artificial aging, a hardness plateau is reached for all alloys. At this point, both Zn containing alloys have reached slightly higher hardness than AlCuLiMg and AlCuLiMg0.1Ag. Further aging increases hardness only to a small extent. After 50 hours at 155 °C the hardness for AlCuLiMg0.1AgZn is highest (174 HV) followed by AlCuLiMgZn (170HV), AlCuLiMg0.1Ag (167 HV) and AlCuLiMg (166 HV). Compared to Figure 34, it is seen that the combined effect of (0.6Zn + 0.1 Ag), i.e. AlCuLiMg0.1AgZn, reaches as high hardness values as AlCuLiMg0.3Ag.

In summary, hardness observations show a large influence of the presence of Mg on the hardening kinetics, but also the effect of Ag and Zn cannot be neglected. In order to better understand the precipitation evolution during artificial aging, in-situ SAXS measurements are conducted for all alloys.

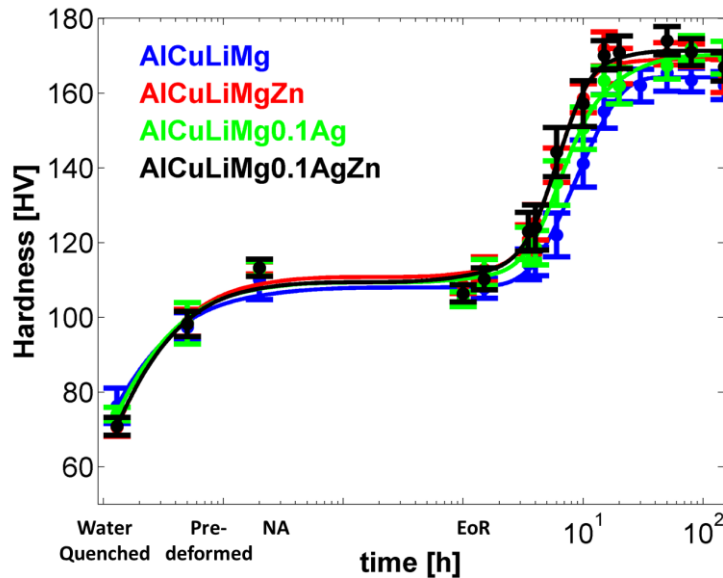


Figure 35: Hardness measurements; Influence Ag and Zn.

3.2. Precipitation kinetics measured by Small Angle X-ray scattering

The images acquired obtained during SAXS experiments illustrate the scattering signal of small objects. During artificial aging in aluminium alloys, the precipitating phases nucleate and grow and their volume fractions increase, resulting in an increase of the scattering signal. The integrated intensity measured by SAXS is proportional to the volume fraction of precipitates.

Two series of SAXS pictures acquired during the experiments are illustrated for AlCuLiMg0.3Ag and AlCuLi in Figure 36 and Figure 37, respectively. Both series illustrate images for different aging times and show the evolution of precipitation during artificial aging. In the 'EoR' condition nearly no intensity is observed and very weak streaking is observed in both figures after 1.5 hours artificial aging. The appearance of these streaks is defined as the onset of nucleation. After 4 hours of artificial aging (compare Figure 36c and Figure 37c), the signal has increased in both alloys, however to higher extend in AlCuLiMg0.3Ag than in AlCuLi. In AlCuLiMg0.3Ag, further heat treatment up to 8 hours shows an increase in intensity, as observed in Figure 36d and only very small differences in intensity are observed up to 15 hours artificial aging, Figure 36e). This condition is identified as the stabilised condition at which full precipitation has occurred. In AlCuLi, the intensity signal due to precipitation increases still after 8 and 15 hours and even up to 50 hours, as illustrated in Figure 37d, Figure 37e and Figure 37f respectively. The fully precipitated condition is achieved only after 50 hours of artificial aging.

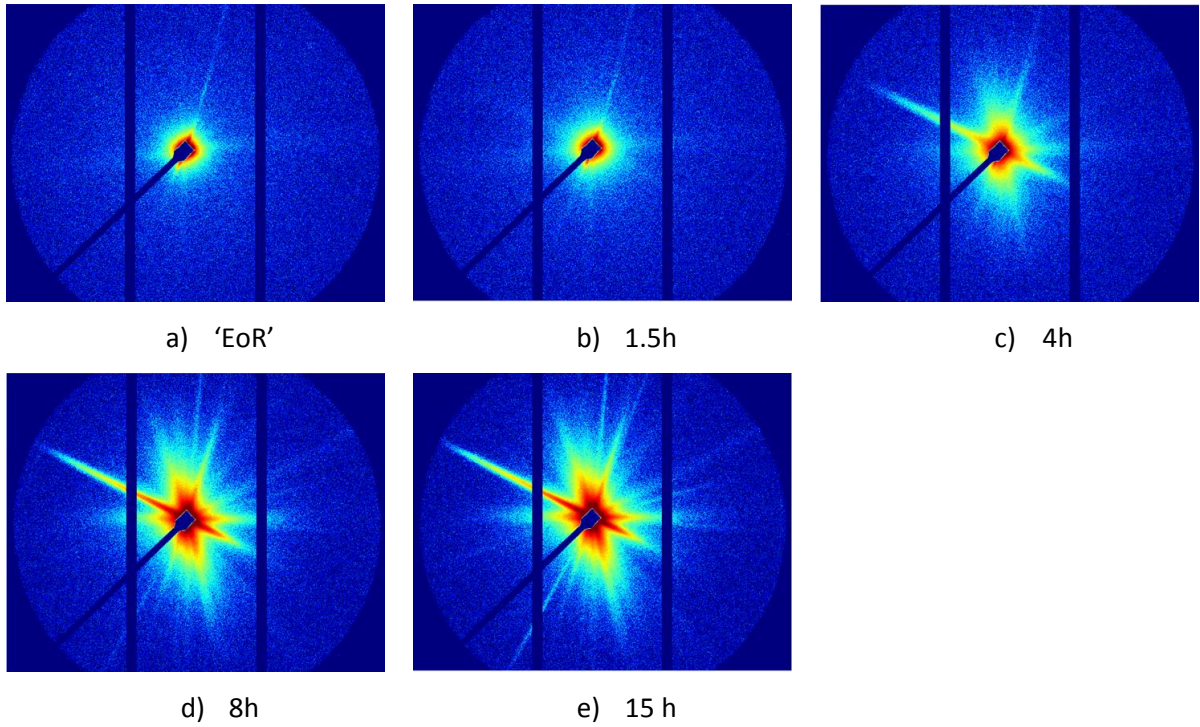


Figure 36: Evolution of precipitation measured by SAXS in the AlCuLiMg0.3Ag alloy.

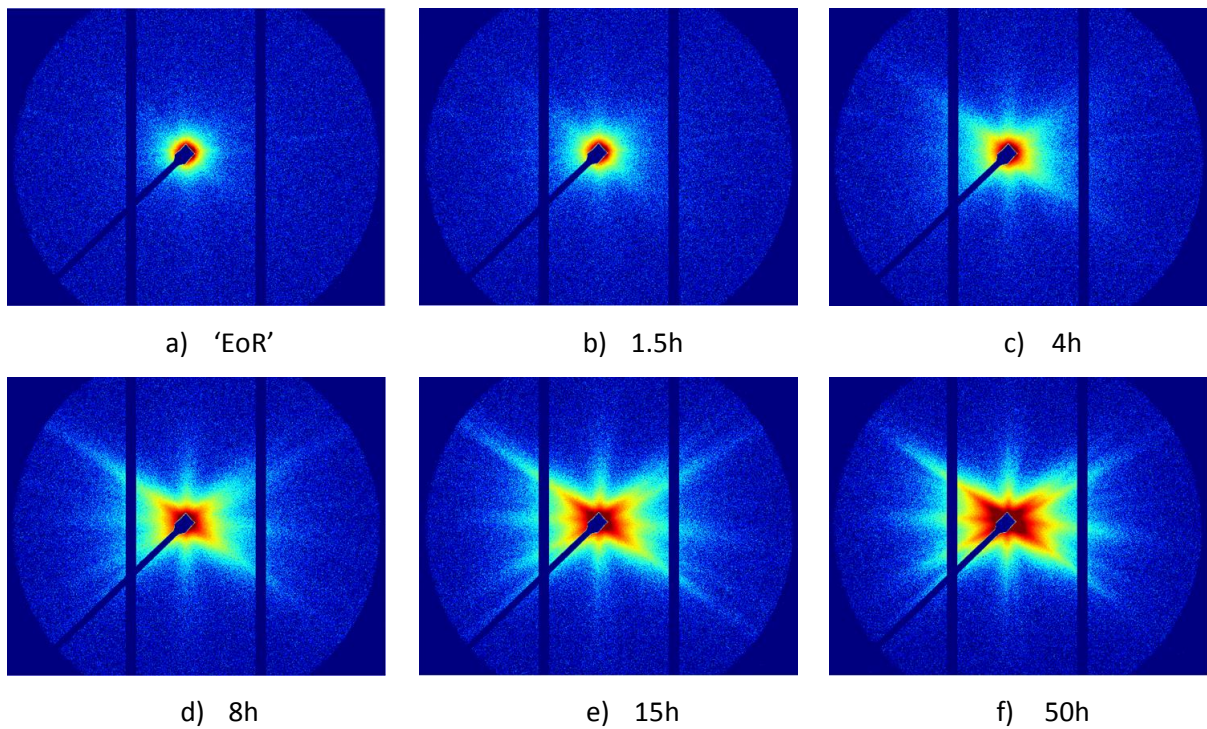


Figure 37: Evolution of precipitation imaged by SAXS for the AlCuLi alloy.

The volume fraction is extracted from the fit of the intensity as described in Chapter 2.5. This allows further analysis and comparison of the different alloys with each other.

Figure 38 and Figure 39 show the results from in-situ SAXS measurements. The volume fraction presented in these figures is normalised based on two assumptions. First, the 'EoR' condition is considered not to contain any precipitates. The value of the volume fraction at this point is therefore set to 0. As will be observed in subsequent chapters, this assumption is certainly not true for the local microstructure at the dislocations, however averaged on the material's volume the volume fraction of precipitates in this condition is considered to be negligible. Secondly, after aging for 50 hours it is assumed that a constant volume fraction is reached in all alloys, which is defined as maximum precipitation and is set to 1. These assumptions allow comparing kinetics. It is not possible to obtain absolute values for the precipitation density by solely measuring the SAXS integrated intensity, since contrast conditions of the precipitating phases are not exactly known and the effect of texture on the intensity is not negligible. The graphs, sketched in Figure 38 and Figure 39, start both with the 'EoR' condition. In Figure 38, the influence of Mg and Ag on precipitation kinetics is illustrated. The volume fraction rises quite rapidly during artificial aging at 155 °C. Similarly to hardness measurements, Mg containing and Mg-free alloys can be clearly distinguished. A large difference is seen in the initial slope of the volume fraction evolution, which is much steeper for Mg containing alloys. A plateau of precipitate volume fraction for Mg containing alloys is reached after 15 hours for AlCuLiMg0.3Ag, 18 hours for AlCuLiMg0.1Ag and 22 hours for AlCuLiMg, respectively. Mg containing alloys show intensities above 1 for aging times of around 20 hrs. This is due to the normalisation after 50 hours, which does not correspond to maximum intensity. A decrease in intensity can be explained by a change in contrast conditions. Small changes of the chemical composition of the T_1 -phase can result in big changes of the contrast conditions and thereby change the global intensity. In the absence of Mg the precipitation process takes much longer time and maximum precipitation is not achieved until 50 hours at 155 °C. The addition of Ag in the ternary AlCuLi alloy shows slightly enhanced precipitation kinetics.

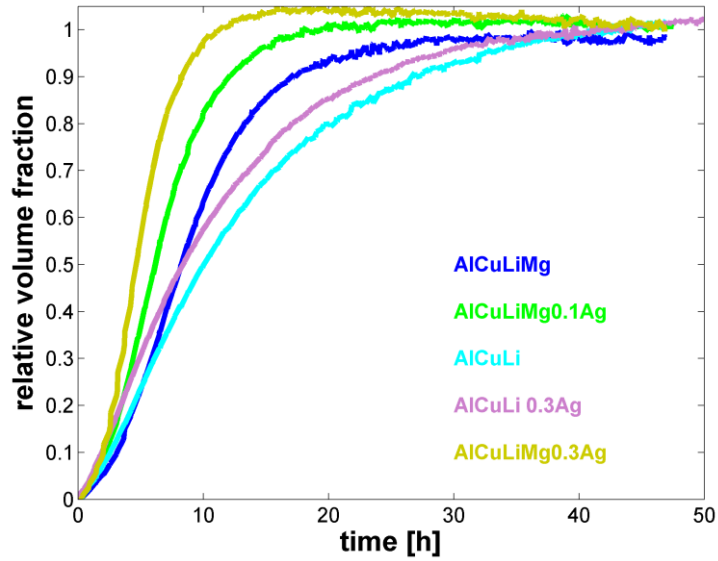


Figure 38: Relative volume fraction of precipitates measured by SAXS – influence of Mg and Ag.

The relative volume fraction of precipitates in the presence of Zn and Ag is illustrated in Figure 39. The addition of Zn, Ag or (Zn & Ag) affects the precipitation volume fraction in a very similar way. All of these three alloys reach the plateau of maximum precipitation after around 18 hours. Only AlCuLiMg, which does not contain any additional alloying elements, shows slightly slower kinetics.

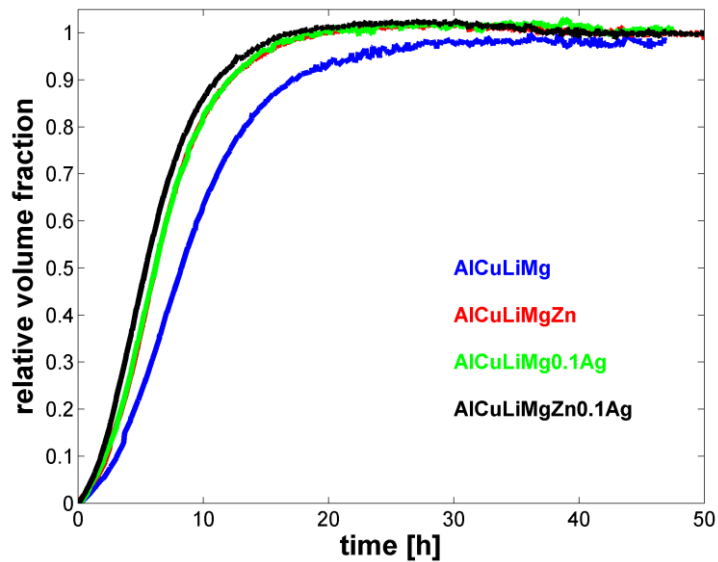


Figure 39: Relative volume fraction of precipitates - influence of Ag and Zn.

Additionally, the evolution of the average thickness of the precipitates can be extracted from the obtained SAXS data and results are illustrated in Figure 40. The thickness represents the average thickness of all scattered objects and variations are very small.

The obtained thicknesses for all alloys lie between 11 and 13 Å for the investigated time range at 155°C. Figure 40a shows the influence of Mg and Ag. It appears that the addition of both Mg and Ag is most effective to avoid thickening. At this point, it is important to recall that the results present the average thickness of all scattered objects. The fit is based on a discrete size distribution, which describes quite well the thickening behaviour of the T_1 phase. The measurements tempt to attribute the thickness increase only to T_1 thickening. However, this should be regarded carefully since other phases might be present in these alloys, in particular θ' in Mg-free alloys, as it will be seen later. The attempt to fit the thickening behaviour discreetly might be suitable for T_1 precipitates, since the thickness of T_1 changes discreetly [56], [62]; however thickening of the θ' phase is rather continuously. In addition, the fit includes a minimum plate thickness of T_1 . This lower boundary is probably not suitable for other phases that are not restricted to a minimum plate thickness. In Figure 40b the additions of only Zn or Zn and Ag shows constant thickness, which does not evolve over time but which is slightly higher than for AlCuLiMg0.1Ag. Slight differences in the average thickness are observed to be in the order of 2 Å and are negligible. Again, the average thickness might not only be attributed to T_1 precipitates but also to other scattering phases.

The thickness of T_1 is closely connected to heat treatment temperature. Aging at 155 °C results mainly in precipitation of single layered T_1 [102], [116] and Dorin et al. observed only thickening when changing the heat treatment temperature to 190 °C [116]. In conclusion, it can thus be said that for the present results precipitated T_1 phases are mostly single-layered. Thickening might be attributed to the presence of other phases. This is also in good agreement with the observed constant hardness plateau in section 3.1. Thickening of T_1 precipitates is attributed to a sharp loss in hardening. In the present case the microstructure should therefore contain mostly single layered T_1 [116].

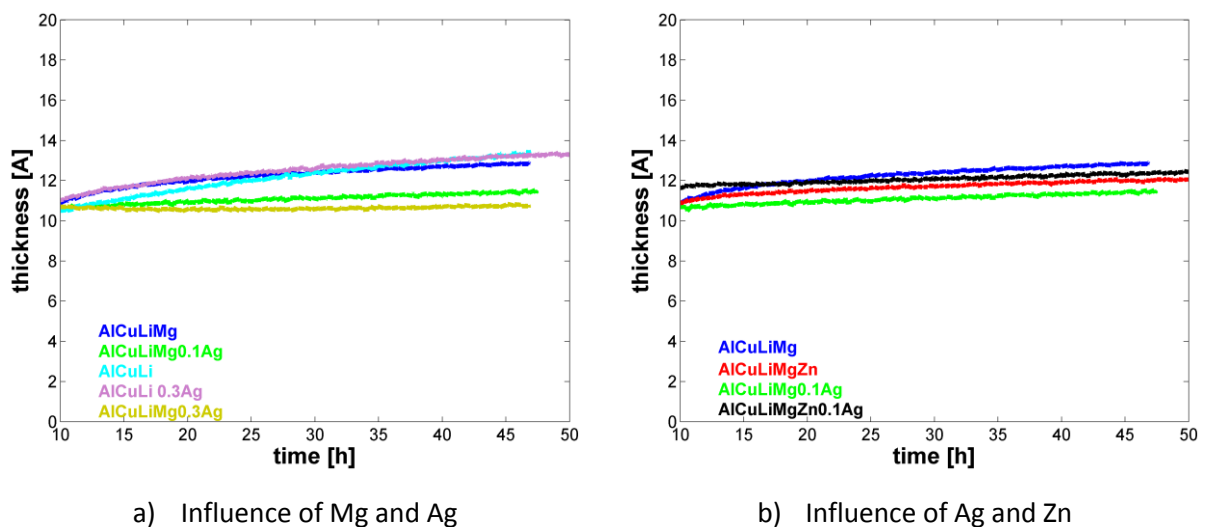
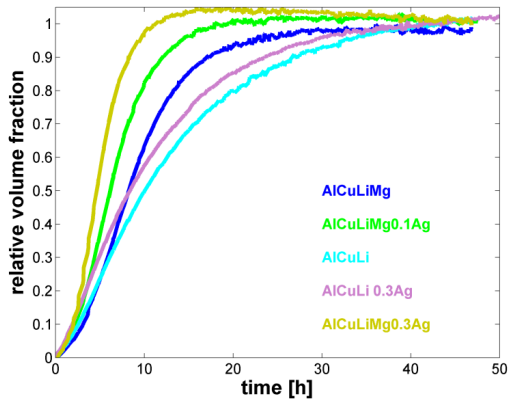
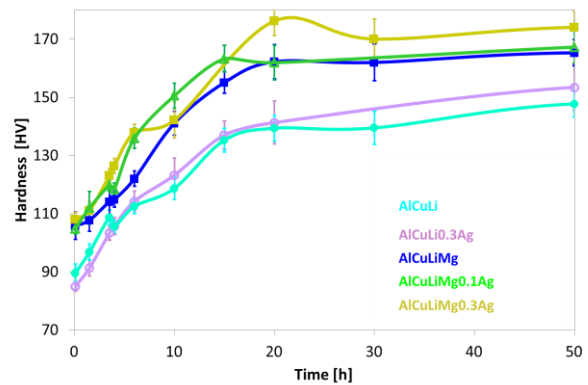


Figure 40: Average thickness of T_1 precipitates measured by SAXS.

Figure 41 and Figure 42 compare the results from hardness and SAXS measurements. The hardness measurements are presented on a linear scale and it is seen that the hardness increase falls together with the increase in precipitate volume fraction. The time for reaching the plateau in precipitate volume fraction is in good agreement with that for maximum hardness. Likewise the differences between Mg containing and Mg-free alloys are visible.

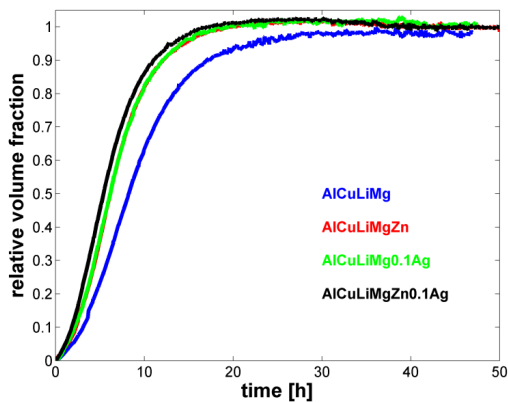


a) Evolution of the rel. normalised volume fraction

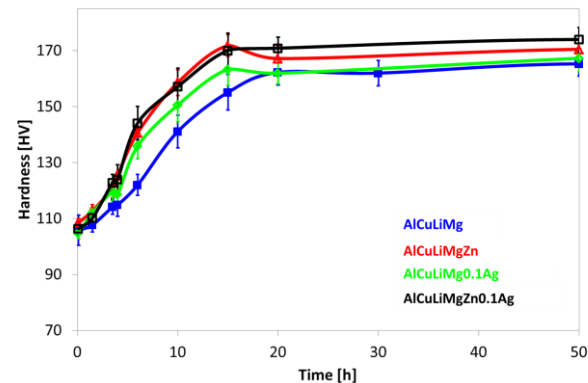


b) Hardness measurements, presented on linear scale.

Figure 41: Comparison of hardness evolution and precipitation volume fraction for the AlLiCu (Mg, Ag) alloys.



a) Evolution of the rel. normalised volume fraction



b) Hardness measurements, presented on linear scale.

Figure 42: Comparison of hardness evolution and precipitation volume fraction for the AlCuLiMg (Ag, Zn) alloys.

Similarly, the hardness measurements and volume fraction evolutions are observed to agree when considering the addition of Zn and Ag. In general, the precipitation evolution does not show large differences between different alloys. However, differences are observed in maximum hardness, which are all reached after approximately the same artificial aging period. The understanding of these differences requires absolute and not only relative volume fraction measurements.

3.3. Results of DSC measurements

Good agreement of hardness measurements and SAXS data highlight the effect of minor alloying elements on precipitation kinetics. However, more experiments are necessary to understand differences between these different alloys. DSC measurements in combination with in-situ SAXS-experiments realised with the same heating rate help to determine the precipitation sequence. Furthermore, varying the heating rate for DSC measurements provides insight on precipitation kinetics.

3.3.1. Difference between Mg and Mg-free alloys

DSC in combination with SAXS measurements of the naturally aged materials, were performed in order to characterise the precipitation sequence in the different alloys in non-isothermal conditions. For commercial AlCuLi alloys, usually containing Mg, Ag and other minor alloying elements, these different peaks were identified by Dorin et al. [116]. Figure 43 illustrates the heat flow normalized by the samples' mass for the AlCuLiMg alloy heated at 50 °C/min. Characteristic points similar as in [116] are indicated in the DSC graph and the corresponding snapshots from SAXS experiments are displayed in Figure 44.

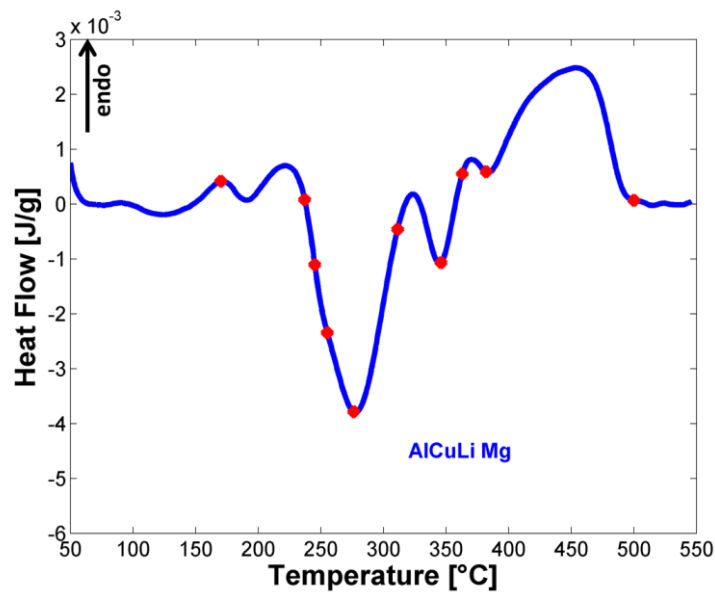


Figure 43: AlCuLiMg alloy; DSC curve measured with 50 °C/min of a naturally aged condition.

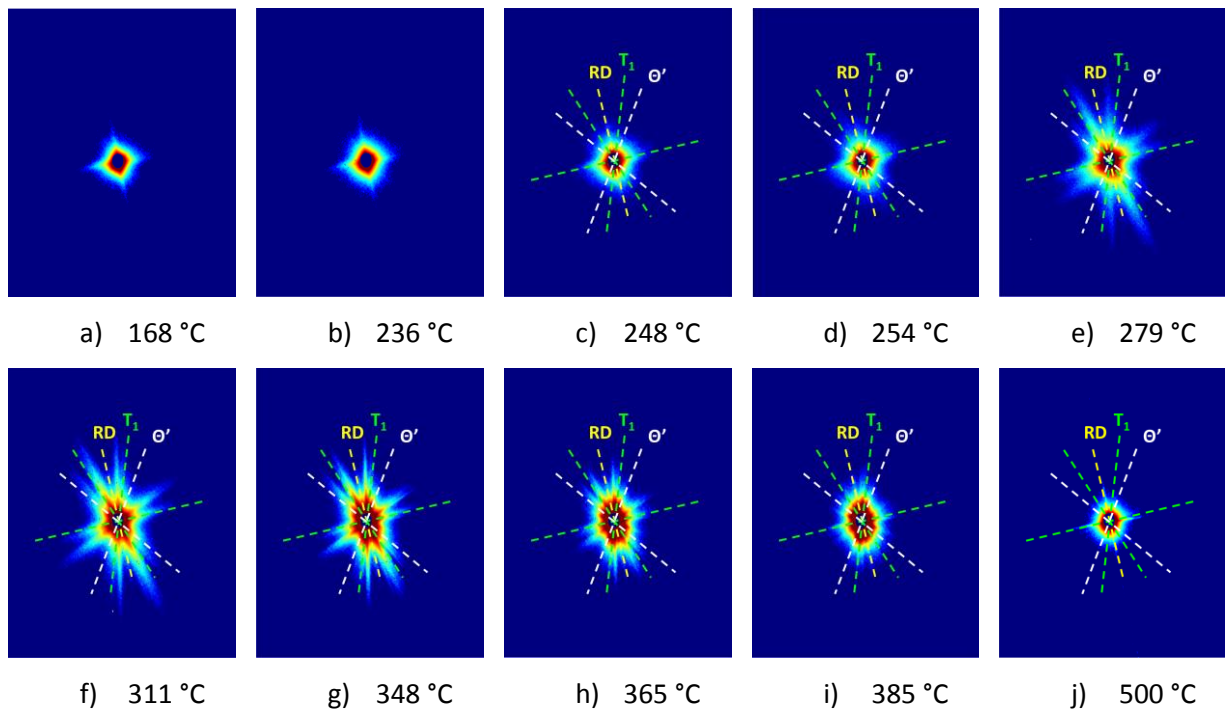


Figure 44: SAXS images at different temperatures during ramp heating at 50 °C/min corresponding to the points indicated in Figure 43.

Small endothermic peaks in the temperature range below 230°C are attributed to dissolution of clusters formed during natural aging (Figure 44 a). Thereafter, the SAXS intensity in the pictures increases slightly (Figure 44 b – d), but characteristic T_1 streaks are not seen before reaching the maximum exothermic peak at 280 °C (Figure 44 e). In the following, the intensity of the streaks further increases (Figure 44 f) and above 350 °C thickening occurs, which is characterised by shorter

streaks (Figure 44 g and h). Above 370 °C, as seen in [116] the signal is endothermic, however a small peak is identified which is attributed to precipitation on $\{001\}_{Al}$ planes, such as θ' . This could not be observed in the present case, and it appears in image i) that mainly thickening has occurred. Further on, complete dissolution of all precipitates is observed in image (j). Small differences in temperature and peak identification compared to the graph shown in [116] can mainly be attributed to the different character of alloys. In this study, laboratory alloys were used, in which the thermo-mechanical treatment results in less pronounced rolling texture components. Further on, the AlCuLiMg alloy shown here has a leaner composition and does not contain any Ag contrarily to the industrial AA2198. Nevertheless, similar characteristic behaviour is seen for all Mg containing alloys presented in Figure 45a and b. All graphs are normalised by the samples weight. The effect of alloying elements affects the height of the main exothermic peak, which is qualitatively representative for the volume fraction of precipitates, since the peak boundaries are approximately at the same temperatures. The temperature at which the peak reaches its maximum can be qualitatively related to precipitation kinetics. It shows that in Figure 45a, the addition of 0.1 wt % and 0.3 wt % Ag results in a stronger peak, i.e., an increased volume fraction for T_1 . The kinetics is slightly enhanced as well by the addition of Ag, since the main precipitation peak reaches its maximum at lower temperature as compared to the AlCuLiMg alloy. In Figure 45b the effect of Zn and Ag additions, likewise show that the fastest precipitation kinetics and maximum volume fraction is obtained in AlCuLiMg0.1AgZn, followed by AlCuLiMg0.1Ag and subsequently AlCuLiMgZn. Again, AlCuLiMg possesses the slowest precipitation kinetics and lowest volume fraction of T_1 .

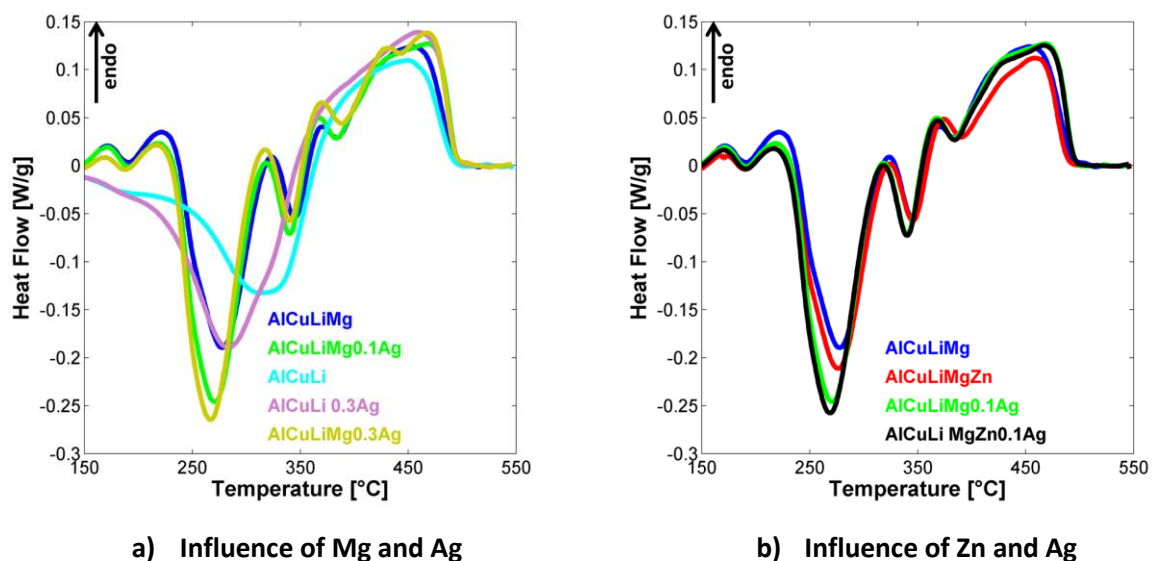


Figure 45: DSC measurements at 50 °C/min from NA conditions; a) influence Mg and Ag b) influence of Ag and Zn.

Large differences are observed for Mg-free alloys, namely AlCuLi and AlCuLi0.3Ag, illustrated in Figure 45a. No endothermic peaks indicating cluster dissolution are observed in the temperature range up to 250 °C. Only one broad exothermic peak is observed at 280 °C for AlCuLi0.3Ag and at 320 °C for AlCuLi, respectively. This indicates that precipitation kinetics is faster in the presence of Ag. To obtain a better understanding of the precipitation behaviour in these Mg-free alloys, a heating ramp has been performed with in-situ SAXS measurements and can directly be correlated to the DSC curve. The results for AlCuLi are illustrated in Figure 46 and Figure 47.

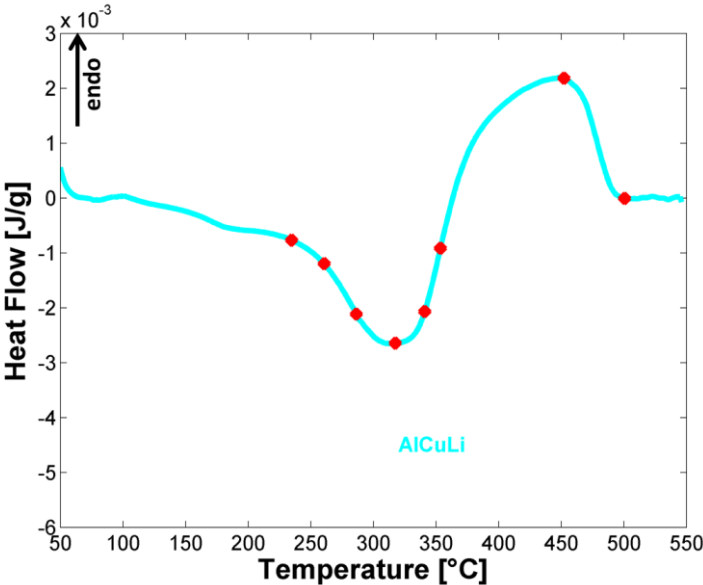


Figure 46: AlCuLi alloy; DSC curve measured with 50 °C/min of naturally aged condition.

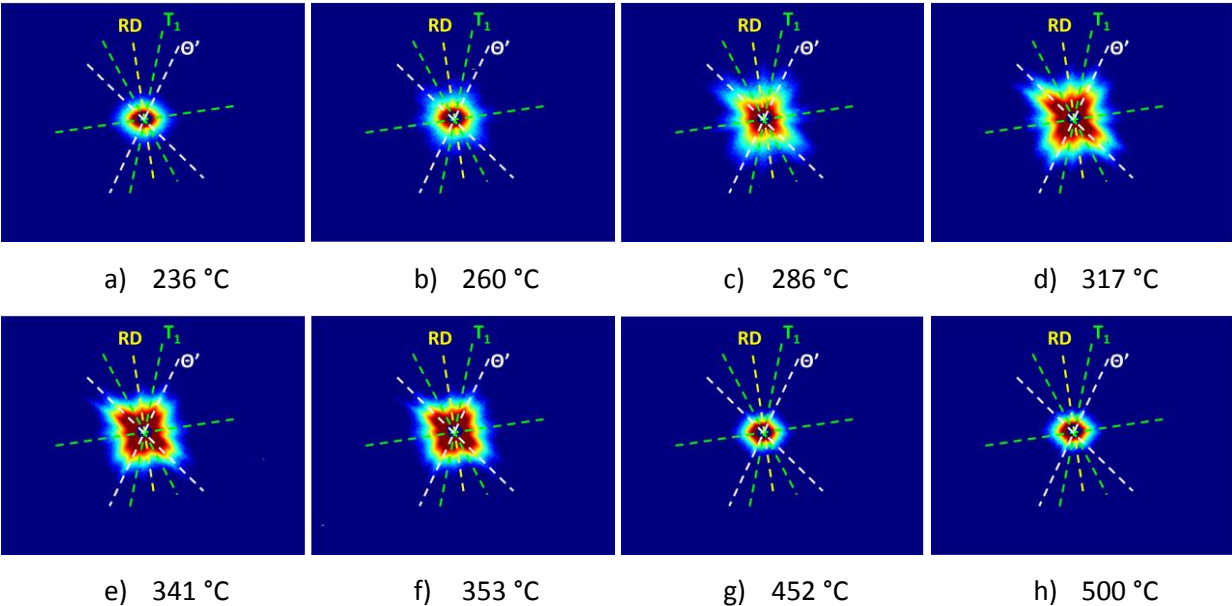


Figure 47: SAXS images at different temperatures during ramp heating 50 °C/min corresponding to the points indicated in Figure 46.

In Figure 46 the heat flux of AlCuLi normalized by the samples weight is sketched. The heating rate was 50 °C/min. Some temperatures are marked, for which the corresponding SAXS images are illustrated in Figure 47. In Figure 47a no precipitates or clusters are present. The signal slowly rises in Figure 47 b) at around 260 °C and becomes more important in position c. The indicated orientation relationship, with respect to rolling direction shows that both T_1 and θ' are present. There is no specific dominance of one of these phases as it was clearly the case in [116] and in Figure 44, in which T_1 is the main precipitating phase. The signal increases for temperatures up to 317 °C (Figure 47 d – e) which is the position of maximum precipitation. Further heating shows the shortening of the scattering streaks, which are related to thickening of the existing phases (Figure 47 f and g). At 452 °C, which lies clearly on the endothermic side of the DSC graph, complete dissolution has occurred. The broad DSC peak can therefore be attributed to combined precipitation of T_1 and θ' .

3.3.2. Influence of heating rate

The influence of the heating rate is given exemplarily for both AlCuLiMg in Figure 48 and AlCuLi in Figure 49. The measurements were performed at 20 °C/min (green curve), 50 °C/min (blue curve) and 100 °C/min (red curve), respectively. All DSC data are normalised by their respective heating rate, β , in order to show them in the same graph. The units are transformed from W/g/ β to J/g/K.

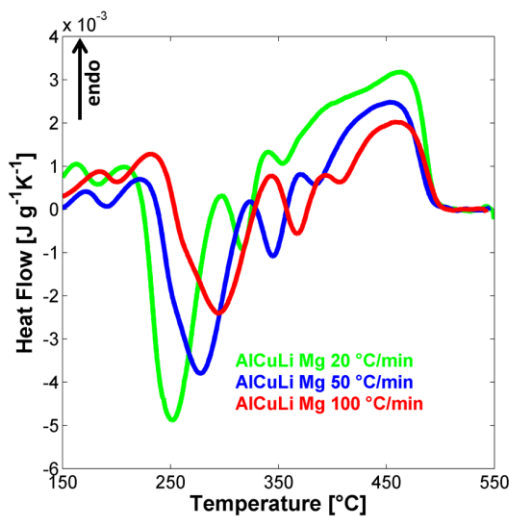


Figure 48: Influence of heating rate on DSC thermograms in AlCuLiMg.

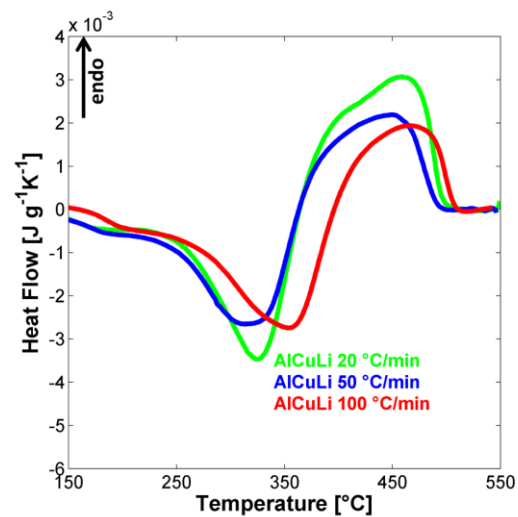


Figure 49: Influence of heating rate on DSC thermograms in AlCuLi.

As expected, increasing the heating rate shifts the precipitation sequence to higher temperature. However, as seen both in Figure 48 and Figure 49 the two different characteristic shapes of the DSC curves for Mg containing alloys or Mg-free alloys, respectively, are unchanged for different heating rates. Figure 48 reveals clearly that with higher heating rate the peaks are shifted towards higher

temperature. This shift in peak temperature is less pronounced in AlCuLi. It can be interpreted as an indication that the activation energy for precipitation differs between Mg containing and Mg-free alloys. For Mg containing alloys, mainly T_1 precipitation is expected, whereas in AlCuLi not only T_1 , but also precipitation of θ' plays a major role. It suggests that θ' nucleation has lower activation energy.

3.4. Further analysis

3.4.1. Normalisation of SAXS volume fraction by DSC measurements for Mg containing alloys

In order to better understand the effect of minor alloying elements on the precipitation kinetics, it is of interest to determine in absolute units the precipitation volume fraction. For T_1 precipitates, Dorin et al. [116] established a relationship between the normalised enthalpy measured by DSC and the precipitate volume fraction measured by TEM for the AA2198 alloy by a systematic study of different aging conditions. We applied this relationship to DSC experiments carried out on the stabilised condition of the different alloys. As assumed by Dorin et al [116], T_1 is the main precipitating phase in the AA2198 alloy, which contains Mg and Ag. The integral of the DSC curve which describes the thermal events $Q_i(T)$ varies for different aging conditions and is proportional to the volume fraction of precipitates f_V present in the sample at the beginning of the DSC scan. The normalised enthalpy is defined as:

$$\Delta H = \frac{1}{\beta} \int_{100^{\circ}\text{C}}^{520^{\circ}\text{C}} Q_i(T) dT \propto f_V \quad \text{Equation 7}$$

β is the heating ramp of the experiment. The indicated integration boundaries are the same as in [116], assuming that below 100 °C no thermal events are happening and above 520 °C all former precipitated phases have dissolved. The T8 condition of AA2198 contains a precipitation volume fraction of 2.6 % and measures a normalized enthalpy of 13.9 J/g in DSC analysis, respectively [116]. In the present study, the alloys differed by minor alloying elements. As a result, a fully precipitated condition (also called 'stabilised') is reached after different aging times and is defined as the plateau reached during kinetic measurements performed by SAXS. The aging times to reach the stabilised condition are presented in Table 4 for the different alloys. Only Mg containing alloys were taken into account, since an important assumption of the procedure is that the microstructure contains only T_1 precipitates.

Table 4: Artificial aging times to obtain a stabilised condition in Mg containing AlCuLi alloys.

Alloys	Artificial aging time for stabilised condition
AlCuLiMg	20 hours
AlCuLiMgZn	18 hours
AlCuLiMg0.1Ag	18 hours
AlCuLiMg0.1AgZn	18 hours
AlCuLiMg0.3Ag	15 hours

DSC measurements of the stabilised conditions were performed and the integral, which stands for the normalised enthalpy was calculated. In Figure 50 a and b DSC curves for fully precipitated conditions measured with a heating rate of 200 °C/min are illustrated. Most of the thermal events are endothermic and related to dissolution. Figure 50a shows the dissolution of a fully precipitation condition for different concentrations of Ag and Figure 50b the dissolution peaks dependent on Zn and Ag additions, respectively. All alloys are characterised by several peaks that are all endothermic.

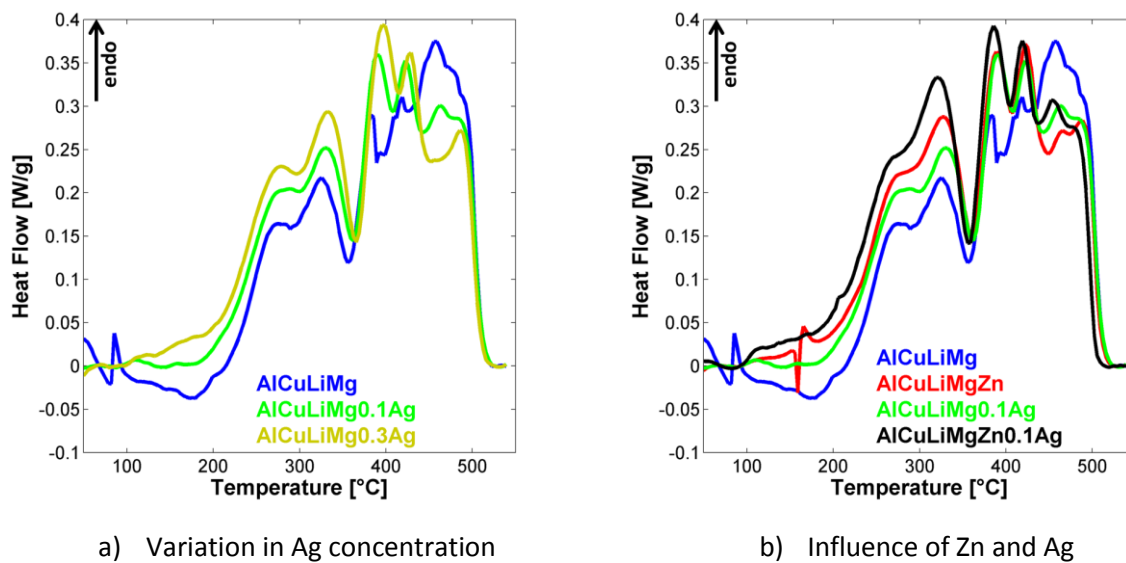


Figure 50: DSC curves of the stabilised condition for Mg containing alloys a) variations in Ag concentration, b) additions of Zn and Ag.

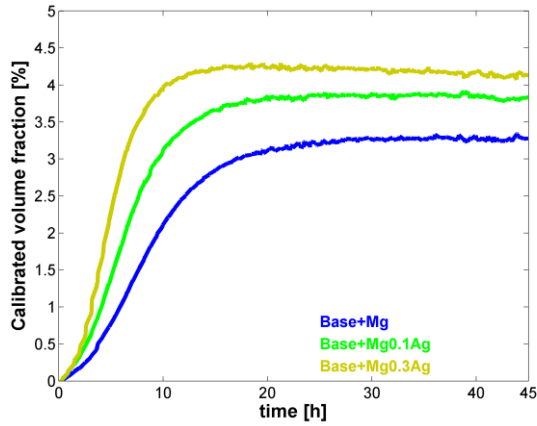
Table 5 gives the area, calculated by integration of the heat flow with time and the corresponding volume fraction calculated from the relationship given by Dorin et al. [116] It shows that highest volume fraction is obtained for AlCuLiMg0.1AgZn and AlCuLiMg0.3Ag. The obtained data are self-consistent, however Dorin et al. [116] determined a lower volume fraction for the T8 condition in AA2198 which corresponds to the fully precipitated condition in the present case. Uncertainties arise due to different base line corrections performed in the different studies. The systematic study of

different aging conditions by Dorin et al. [116] could extend the temperature range for base line correction to 400 °C for the dissolution peak. Furthermore the higher heating ramp in the present study (200°C/min) increase uncertainties due to instabilities up to around 100 °C, the temperature range in which baseline corrections are performed. Earlier studies show that the degree of pre-deformation alter strength and mechanical properties in AlCuLi and also with increasing pre-deformation a higher number density of T_1 precipitates was observed [23], [122]. The degree of pre-deformation should not affect the volume fraction in such a great way. In [91], it was seen that different deformation, (0.5 %, 2.5 % and 12 %) result in very similar volume fractions.

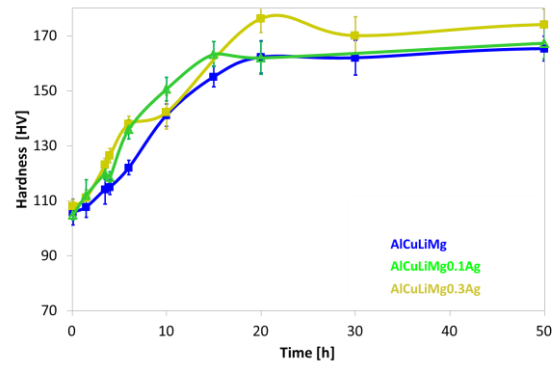
Table 5: Calculated area below the DSC curve in (J/g) and volume fraction, by using the relationship from [116].

Alloys	Calculated area from DSC [J/g]	Volume fraction [%]
AlCuLiMg	17.73	3.31
AlCuLiMg Zn	21.73	4.00
AlCuLiMg0.1Ag	20.45	3.77
AlCuLiMg0.1AgZn	23.62	4.35
AlCuLiMg0.3Ag	21.94	4.04

Figure 51 and Figure 52 show in a) the precipitation kinetics curve, normalised by the volume fraction and in b) the corresponding hardness profiles, respectively. Figure 51 illustrates the influence of different Ag contents. All curves in Figure 51a show similar precipitation behaviour, however differences in volume fraction are obtained. AlCuLiMg, i.e. the blue curve does not contain any Ag and reaches a plateau at a volume fraction of 3.3 %. The addition of 0.1 wt% Ag, see the green curve, has throughout a higher volume fraction than AlCuLiMg and reaches a maximum volume fraction of 3.8 %. Highest T_1 volume fraction is obtained for AlCuLiMg0.3Ag, the yellow curve, which reaches a value of up to 4%. In combination with the hardness measurements of Figure 51b, it clearly reveals that additions of Ag alter the obtained hardness values and highest hardness values are obtained for AlCuLiMg0.3Ag, followed by AlCuLiMg0.1Ag. These observations suggest that the reached hardness depends on the precipitation volume fraction. The differences in hardness between AlCuLiMg0.1Ag and AlCuLiMg0.3Ag are quite small. Significant differences both in hardness and volume fraction are found for AlCuLiMg, which has much lower hardness and volume fractions compared to Ag containing alloys.

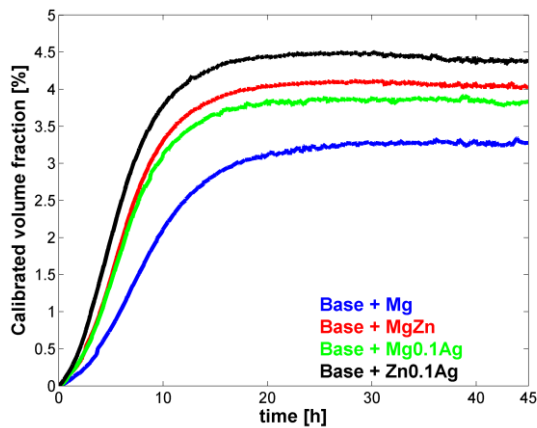


a) Calibrated precipitation curve

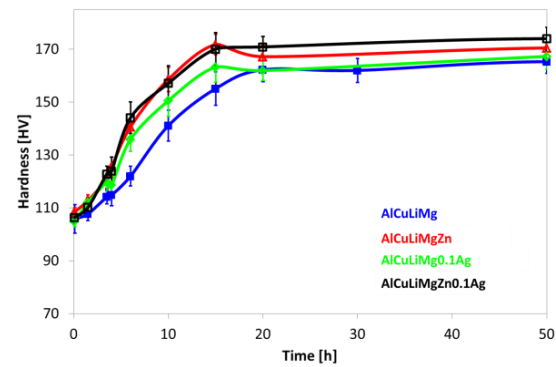


b) Hardness profile

Figure 51: SAXS curves normalized by the precipitation volume fraction obtained by DSC measurements, showing the influence of different Ag additions; b) corresponding hardness profile.



a) Calibrated precipitation curve



b) Hardness profile

Figure 52: SAXS curves normalized by the precipitation volume fraction obtained by DSC measurements, showing the influence Ag and Zn; b) corresponding hardness profile.

Figure 52 shows the influence of Ag and Zn on precipitation behaviour and hardness measurements. In Figure 52a the precipitation kinetics measured by SAXS and normalized with respect to the volume fraction obtained from DSC measurements, shows that AlCuLiMg reaches the lowest volume fraction. The addition of 0.1Ag increases, as seen before the volume fraction of T_1 . Similar precipitation behaviour is observed in the presence of Zn, see the red curve, which reaches a maximum volume fraction of 4 %. The addition of both Zn and Ag, illustrated by the black curve, shows even higher volume fraction of 4.35 %. Relating these observations to hardness measurements, it is seen that indeed the Zn and Ag containing alloy reaches highest hardness. The differences in hardness between the alloys are not that remarkable as in the volume fraction. It is however clearly seen that AlCuLiMg exhibits the lowest hardness and 0.1Ag or Zn additions both increase the final hardness.

In summary, the normalisation with respect to volume fraction in the presence of only one main precipitation phase, as it is the case for Mg containing alloys, shows consistent results. Furthermore, the results reveal good agreement with hardness measurements. With increasing precipitation volume fraction, higher hardness was obtained.

3.4.2. Summary

Different experimental methods were applied to characterise hardening and precipitation kinetics. It clearly reveals that minor alloying elements play an important role during nucleation and precipitation in AlCuLi alloys. Most pronounced effects are clearly obtained for the addition of Mg to AlCuLi. Its presence enhances both precipitation kinetics, but also hardness values in a great way. Combined DSC and SAXS measurements show that the differences in precipitation and hardening kinetics can be attributed to a different main precipitating phase. By means of the orientation relationship of streaking in SAXS images, Mg containing alloys are mainly characterised by T_1 precipitation. Ag or Zn additions to Mg containing AlCuLi alloys slightly alter hardness and precipitation kinetics. In Mg-free alloys two sets of streaks with different orientation relationships are identified. They are related to combined T_1 and θ' precipitation. The latter phase seems to play a major role in Mg-free alloys. These findings with respect to main precipitating phase and nucleation conditions need to be justified by electron microscopy observations.

The effect of temperature on hardening kinetics has been characterised for all alloys. The artificial aging temperatures was reduced to 140 °C and the results are presented in Appendix I - Hardening kinetics at 140°C

4. Microstructure analysis of different aging conditions

As seen in chapter 3, the effect of minor alloying elements strongly influences precipitation kinetics. It clearly reveals that the influence of Mg is crucial; minor alloying elements such as Ag and Zn also affect precipitation kinetics but to a lower extent. To better understand the effect of these different elements, microscopic studies have been conducted. In a first step, conventional TEM images are analysed to evaluate the precipitation density in a fully precipitated condition (also called 'stabilised' condition). Then, atomic resolution TEM performed with HAADF imaging methods illustrates the evolution of precipitation for different aging conditions, including very early aging times. The investigated aging conditions are the so called 'End of Ramp' ('EoR') condition, the 'nucleation' condition and the 'stabilised' condition.

4.1. Observation of different phases in AlCuLi alloys - orientations of the sample

In order to obtain a complete image of the microstructure, it is necessary to investigate AlCuLi alloys in different zone axes. Along $\langle 0\bar{1}1 \rangle$ zone axis, two out of four variants of T_1 precipitates are parallel to the beam and are observed edge-on. In addition, one variant out of three θ' precipitates (or its more metastable precursors, GPI zones and θ'') which lie on $\{002\}$ planes can be observed. The $\langle 11\bar{2} \rangle$ zone axis permits the investigation of only one variant out of four of T_1 precipitates. θ' cannot be observed edge-on along this axis. As shown by Dwyer [65] the latter zone axis is suited to describe the structure at the atomic scale due to larger interatomic distances along $[110]$ direction. The T_1 structure can thus be better resolved. In addition, the spacing between matrix diffraction spots is sufficient in this zone axis to perform conventional dark field TEM imaging on the T_1 precipitates, which is not possible without interference from the matrix in the $\langle 110 \rangle$ zone axis on the Jeol 3010 equipment at SIMaP. The $\langle 001 \rangle$ zone axis illustrates particles that are parallel to $[001]$ and two variants of θ' are visualized edge-on. S' , S and δ' phases if present can also be observed in this orientation. It is therefore necessary to investigate 2 different zone axes in order to obtain a full insight of the microstructure, of which one should be $[001]$.

4.2. Precipitation distribution after aging – 'stabilised' condition

Conventional dark field TEM imaging was first performed in order to measure the average diameter of T_1 precipitates in a 'stabilised' condition for the different alloys. These observations were performed along the $\langle 112 \rangle$ matrix zone axis. The shape of T_1 precipitates was assumed to be disc-like, and the measured projected length on TEM was assimilated to the precipitate's diameter (thus not taking into account the effect of a finite TEM foil thickness on the observed distribution). The artificial aging time in order to reach the 'stabilised' condition was chosen as the time period

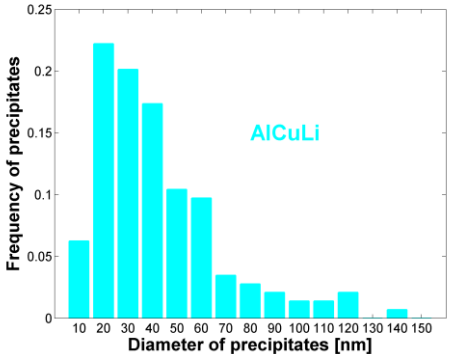
necessary to reach the plateau of maximum precipitation volume fraction determined by SAXS measurements and the artificial aging times for the different alloys are given in Table 6.

Table 6: Investigated alloys and their artificial aging time to reach ‘stabilised’ condition.

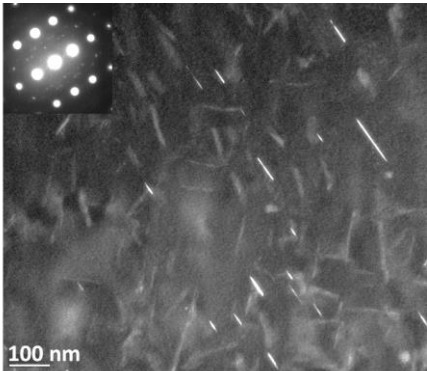
Alloys	Artificial aging time for ‘stabilised’ condition
AlCuLi	50 hours
AlCuLi0.3Ag	50 hours
AlCuLiMg	20 hours
AlCuLiMgZn	18 hours
AlCuLiMg0.1Ag	18 hours
AlCuLiMg0.1AgZn	18 hours
AlCuLiMg0.3Ag	15 hours

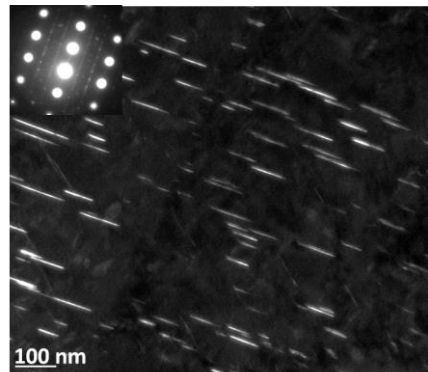
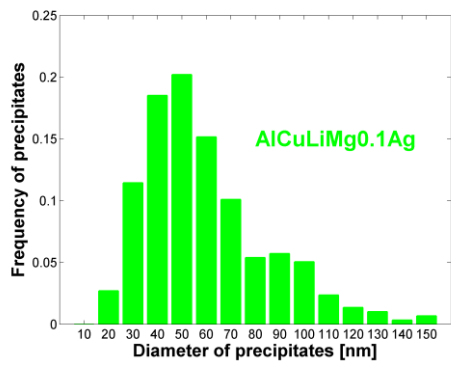
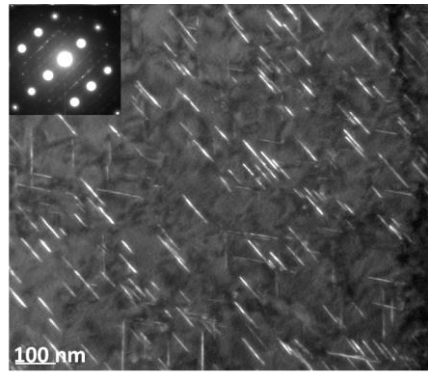
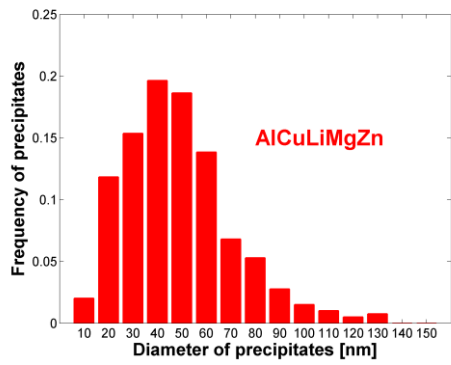
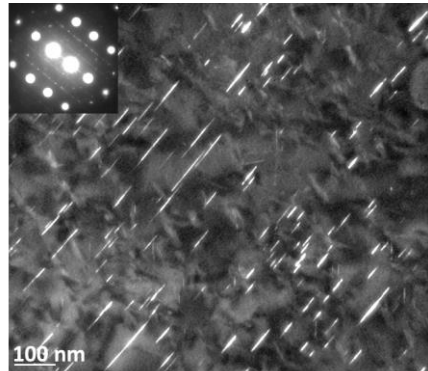
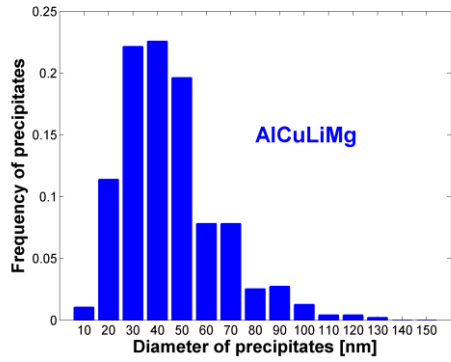
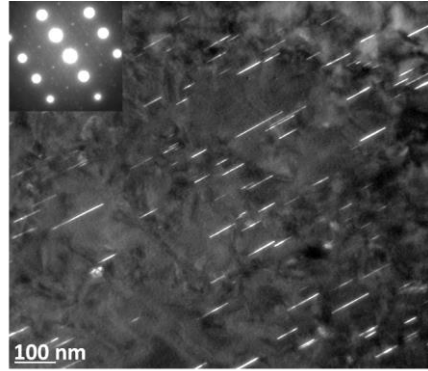
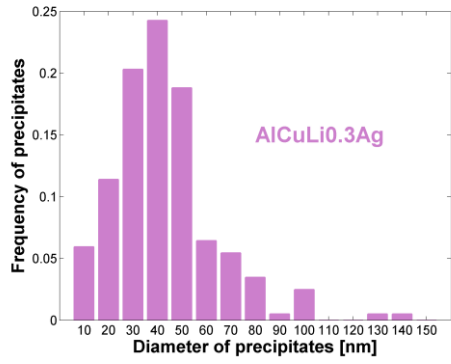
For the chosen imaging condition (along <112> zone axis) only one variant of T_1 precipitates (out of four) is imaged. In average, the diameter of 100 – 200 precipitates was measured. Before discussing the difference between the different alloys, two points must be made. First, the T_1 precipitates measured on these images do not necessarily represent the major phase in all alloys (namely not in the Mg-free alloys). Second, the conventional imaging shown here enables only the measurement of the T_1 diameter (which is measured by the length of the projection of the edge-on precipitates) and not their thickness. SAXS measurements, which will be confirmed by atomic resolution TEM images later in this chapter, show that in the ‘stabilised’ condition and in all alloys most of the T_1 precipitates have a thickness of one unit cell (approximately 1 nm).

Distribution of T_1 precipitates diameter estimated by TEM



TEM dark field image





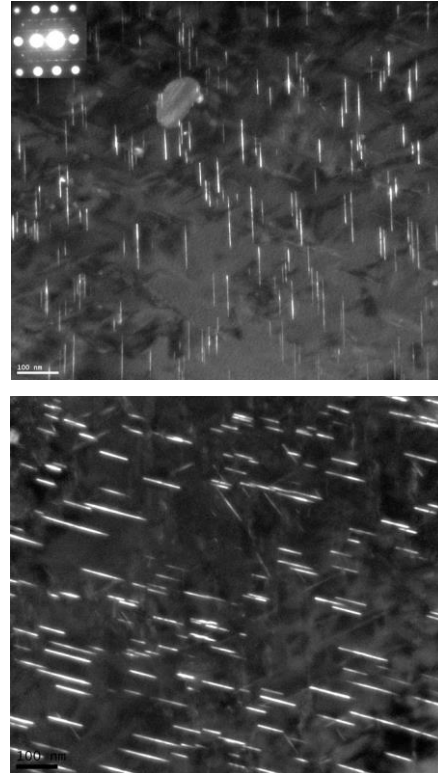
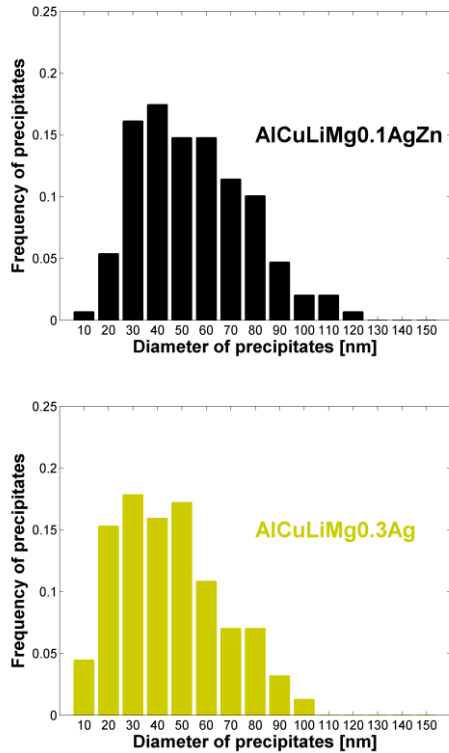


Figure 53 : Size distribution of T_1 precipitates and dark field images of the investigated alloys. Dark field images were taken along $\langle 112 \rangle$ zone axis as indicated in the diffraction patterns inserted in the upper corner of the images (if available).

The shapes of the diameter distribution of T_1 precipitates, shown on the left hand side of Figure 53, are quite similar for the two Mg-free alloys. For most images the diffraction pattern is available and inserted in the upper left corner of the dark field image. Streaking along $\langle 110 \rangle$ direction is observed in the Mg containing alloys. This feature is less pronounced in the Mg-free alloys. However, with increasing minor alloying content, it appears that the size distribution expands towards higher diameter values. For example, in AlCuLiMg most of the diameters measure between 30 to 50 nm. In AlCuLiMgZn0.1Ag and AlCuLiMg0.3Ag the range of diameters is much wider and measures between 30 to 80 nm. The average diameter for each alloy was calculated and the results are summarized in Table 7, together with their standard deviations. The average diameter for all different alloys is also illustrated in Figure 54. The diagram shows that only minor differences in average diameter are observed. The shortest diameters are found for AlCuLi (42 nm) and AlCuLi0.3Ag (43 nm). The diameter increase, when Mg is added, is very small (45 nm). Further additions of alloying elements, such as Ag and Zn, lead to slightly larger diameters. However, no clear trend with respect to the minor additions could be found. AlCuLiMgZn (48 nm) and AlCuLiMg0.3Ag (45 nm) reach similar diameters, which are very close to the diameter of AlCuLiMg. The highest values are obtained for

AlCuLiMg0.1AgZn (55 nm) and AlCuLiMg0.1Ag (60 nm). The standard deviation for all alloys is comprised between 19 to 25 nm.

Table 7: The average diameter and its standard deviation.

	Average diameter [nm]	standard deviation [nm]
AlCuLi	42	26
AlCuLi0.3Ag	43	21
AlCuLiMg	45	20
AlCuLiMg0.1Ag	60	25
AlCuLiMgZn	48	22
AlCuLiMgZn0.1Ag	55	23
AlCuLiMg0.3Ag	45	21

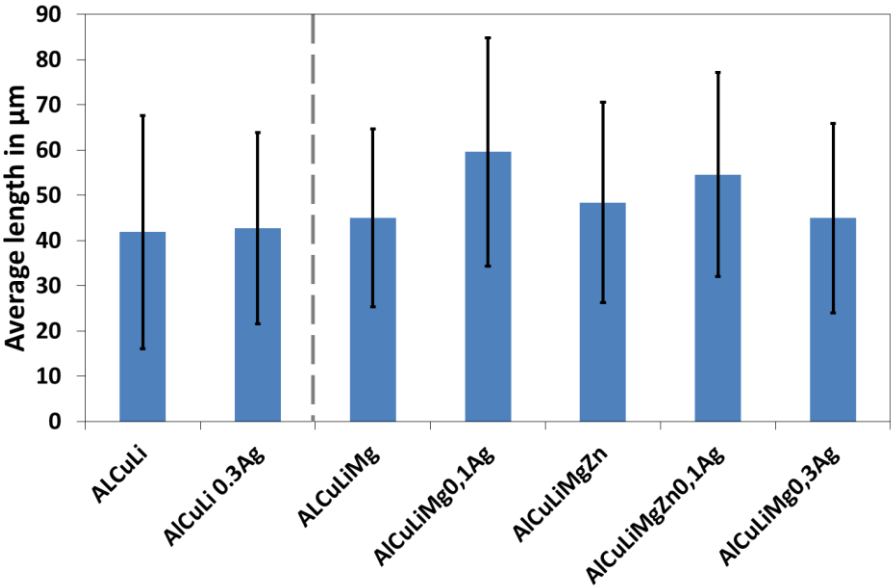


Figure 54: The average diameter for all investigated alloys.

Dark field images, shown on the right hand side of Figure 53 are taken at the same magnification for each alloy. It reveals clearly that the T_1 number density in Mg-free alloys is much lower than in Mg containing alloys. An attempt to quantify the number density of T_1 particles was made by counting the total number of precipitates per unit area. The results are summarized in Table 8.

Table 8: Number of precipitates per unit area, obtained from dark field TEM images.

Alloys	Measured #precipitates /area (μm^2)
AlCuLi	23
AlCuLi0.3Ag	92
AlCuLiMg	146
AlCuLiMgZn	147
AlCuLiMg0.1Ag	115
AlCuLiMg0.1AgZn	186
AlCuLiM 0.3Ag	187

Obviously, some differences are seen between the different alloys and it appears that with higher content of minor alloying elements the number of precipitates per unit area increases. However, it should be kept in mind that the TEM images are 2D projections of a three-dimensional sample. Due to lack of information about the thickness of the TEM foil, it was preferred to illustrate surface fractions. Nevertheless, for a given specimen, the apparent surface fraction might also vary if the specimen thickness changes strongly. To avoid this, TEM dark field images were recorded using the same conditions (i.e. similar specimen preparation, avoiding too thin or too small areas by checking the contrast of both images and diffraction patterns, recording several pictures to average the values). Of course, the estimation of surface fraction is qualitative but the values reveal a trend of the T_1 distribution. The effect of the TEM foil is not trivial and essential in order to obtain valuable results.

Figure 55 presents the results of the surface fraction of T_1 per μm^2 . Mg-free alloys show a lower surface fraction of T_1 precipitates than Mg containing alloys. The presence of Mg increases the T_1 precipitate surface fraction to a great extent. Comparing only Mg containing alloys with each other, it reveals that the addition of 0.1AgZn or 0.3Ag further increases the surface fraction. Highest surface fraction is obtained for AlCuLiMg0.1AgZn and AlCuLiMg0.3Ag. The effect of solely Zn and Ag additions is less clear. It is possible to conclude that the combined effect of MgZn0.1Ag and Mg0.3Ag lead to an increased surface fraction of T_1 . In comparison to this, the effect of lower additions (Mg0.1Ag or MgZn) is less clear.

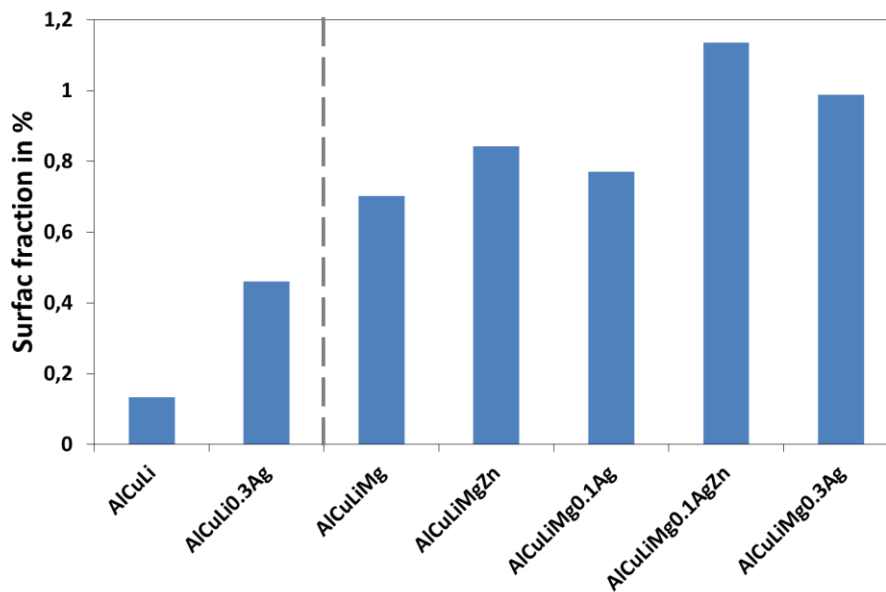


Figure 55: Estimation of the surface fraction for different sample thicknesses, for all analysed alloys.

As discussed in chapter 3, DSC and SAXS measurements suggest that in Mg-free alloys, precipitation of θ' plays an important role. The 'stabilised' condition of AlCuLi along $\langle 001 \rangle$ zone axis is imaged in Figure 56. Two variants of θ' out of three are illustrated. Qualitatively, the density of θ' appears to be quite high. In comparison, AlCuLiMg0.1Ag, representative for Mg containing alloys is illustrated in 'stabilised' condition along the $\langle 001 \rangle$ zone axis in Figure 57. The corresponding diffraction pattern is included in the upper right corner of the image. The image shows θ' precipitates edge-on and the diffraction patterns show streaking characteristic of plate-like precipitates. The amount of θ' is very small compared to its amount in AlCuLi illustrated in Figure 56. In addition, the contrast exhibit a plate-like phase which is not edge-on to the $\langle 001 \rangle$ zone axis. They are most likely T_1 phases which are inclined to the zone axis. This confirms the assumption that in AlCuLi, precipitation of θ' plays an important role, whereas it is of smaller importance in the presence of Mg.

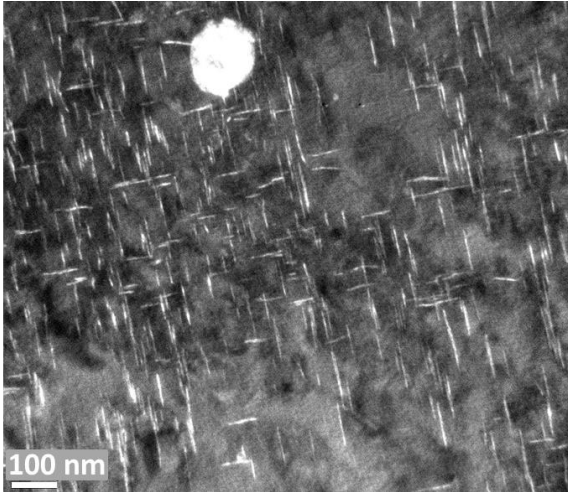


Figure 56: AlCuLi in 'stabilised' condition observed along <001> zone axis.

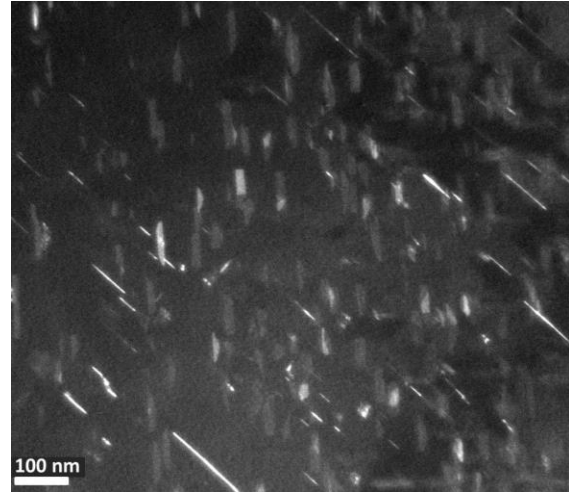


Figure 57: AlCuLiMg0.1Ag in 'stabilised' condition along <001> zone axis.

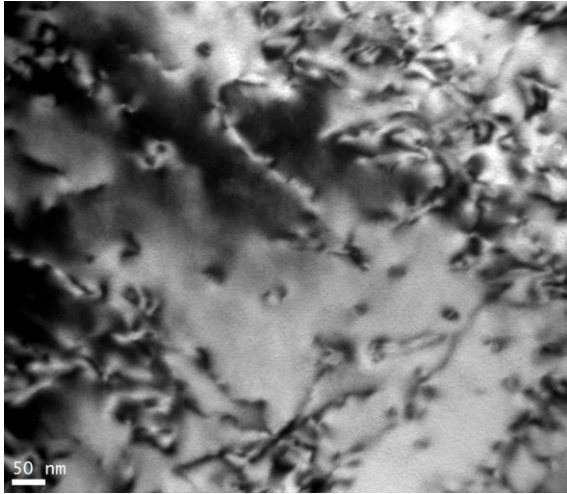
The analysis of the T_1 precipitate density in the 'stabilised' condition reveals differences of precipitate distribution between the investigated alloys. To understand the mechanisms that lead to these differences, we chose to study in more details earlier ageing times. The first studied condition is the so called 'EoR' which corresponds to the moment when the samples just reach the ageing temperature (155°C). The second condition, 'nucleation', corresponds to the estimated time of precipitation start (i.e. when it becomes experimentally observable during the in-situ SAXS measurements). In order to obtain a full image of the nucleation and precipitation state, whenever possible both <110> and <001> zone axes were investigated.

4.3. The 'End of Ramp' condition

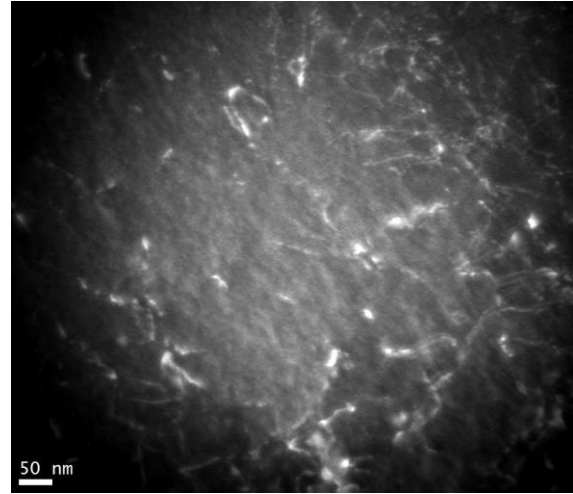
The 'EoR' condition is obtained when artificial aging is ended by a water quench just after reaching 155 °C, i.e. at the end of the heating ramp. In this condition no or very little precipitation is expected.

4.3.1. AlCuLiMg0.3Ag

The dislocation structure was qualitatively investigated by conventional TEM for AlCuLiMg0.3Ag in the 'EoR' condition. Two-wave imaging condition ($g = [100]$) was applied and it was possible to image dislocations in <001> zone axis. The purpose of these observations was not to describe precisely the dislocations but to reveal (or not) their interaction with the precipitates. In Figure 58, a bright field (BF) image in a) and a dark field (DF) image in b) of the same area are imaged. Figure 58a reveals the presence of small circular dislocation loops. Figure 58b shows some dislocations and bright spots, connected to them. As it will be seen later in atomic resolution images, these contrast features can be explained by segregations on dislocations.



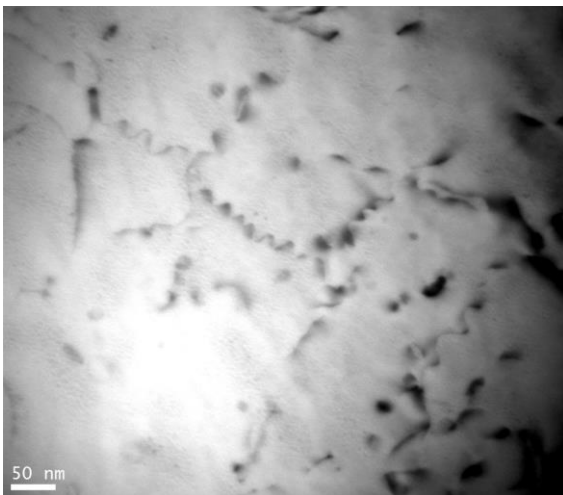
a) BF image



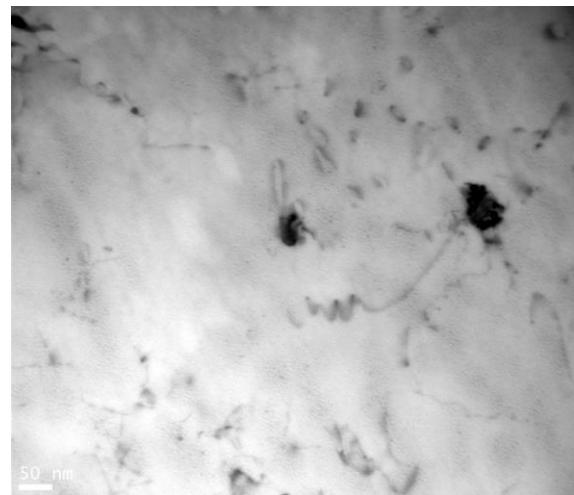
b) DF image

Figure 58: Bright field image and corresponding dark field image of dislocations in $\langle 001 \rangle$ direction (2-wave condition, $g = [100]$) for AlCuLiMg0.3Ag in 'EoR' condition.

Figure 59 shows two BF images of dislocations along $\langle 001 \rangle$ zone axis. The distribution of dislocations is not very homogeneous and it appears that dislocations are jog-like shaped. This shape can be attributed to the presence of early formed clusters that are pinning these dislocations so that they have to move around them. Some of these dislocations appear to be helices. Helix dislocations can evolve from screw dislocations, when a large enough chemical stress exists, such as caused by quench-induced supersaturation of vacancies [123].



a) BF image of dislocations



b) BF image of dislocations

Figure 59: Bright field images of dislocations reveal the presence of helices and jogged dislocations for the AlCuLiMg0.3Ag alloy in 'EoR' condition. Images were taken along $\langle 001 \rangle$ zones axes (2-wave condition, $g = [100]$).

Atomic resolution images of AlCuLiMg0.3Ag, observed along $\langle 001 \rangle$ zone axis are presented in Figure 60. An increase in contrast with respect to atomic number is observed in the HAADF image in Figure 60a. The contrast with respect to strain is shown in Figure 60b and suggests the presence of dislocations. In combination with a) it can be suggested that segregation occurs on a dislocation. The intensity differences in Figure 60a are very small. The differences in lattice spacing do not change. It appears to be more difficult to distinguish between different lattice planes in the brighter part of the image, which would be associated to the segregation. The image seems to be blurry around the segregation, which is consistent with the presence of a dislocation. Its strain field leads to deviations of the precise orientation relationship of the zone axis. The distortion of the lattice in the dislocation region is certainly a prominent parameter that facilitates segregation. It should be kept in mind that due to the collection angles of the HAADF and ADF detectors, diffraction contrast might be visible in HAADF pictures and Z contrast in ADF pictures, respectively.

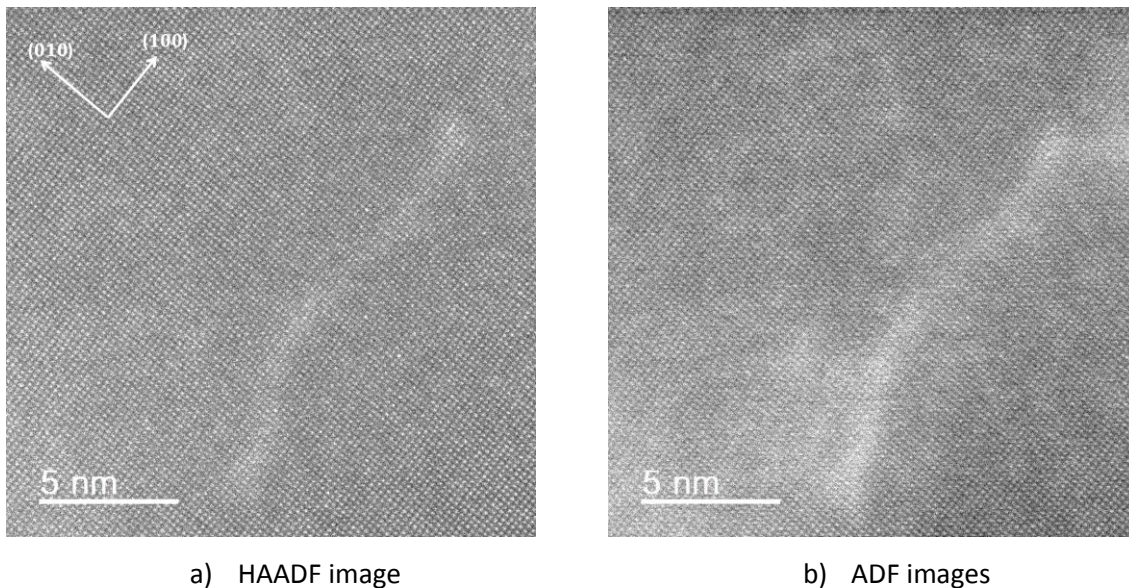


Figure 60: $\langle 001 \rangle$ matrix zone axis of the 'EoR' condition in AlCuLiMg0.3Ag - variations in intensity are observed.

Differences in intensity and contrast is also seen in Figure 61a and b. The contrast with respect to atomic number is very low, as seen in Figure 61a. In the marked area, it is additionally seen that the resolution has decreased. In Figure 61b contrast arises due to internal strain, i.e. the presence of a dislocation. Its presence can explain the observed decrease in resolution in Figure 61a. Furthermore, some GP zones are visible and are indicated by arrows in Figure 61a.

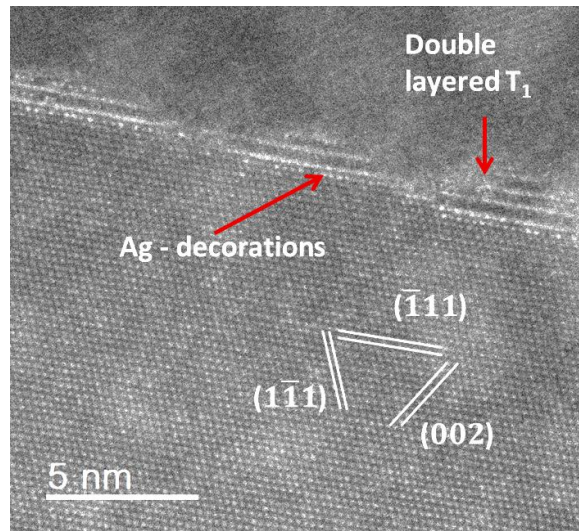
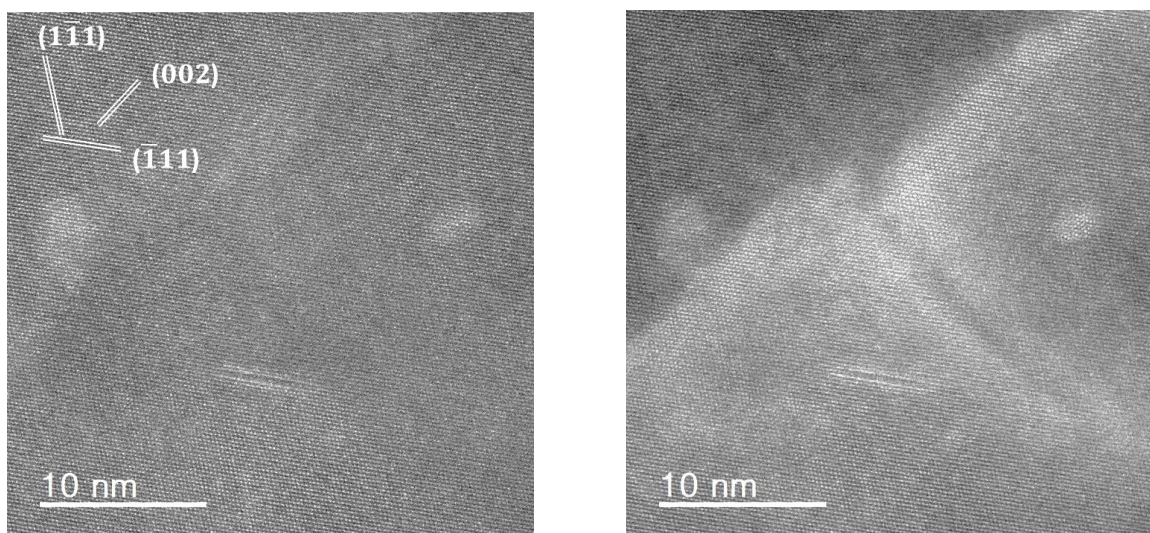


Figure 62: T_1 precipitation on a grain or sub-grain boundary in AlCuLiMg0.3Ag in the 'EoR' condition, taken along $\langle 011 \rangle$ matrix zone axis.

However, T_1 is not only observed on grain or sub-grain boundaries, but also in the matrix, as illustrated in Figure 63a. The size of this early T_1 (diameter of about 5 nm) is similar to that observed by atom probe tomography (APT) by Araullo-Peters et al. [102] in the same aging condition but for a slightly different alloy composition. By means of the annular dark field image in b), which shows contrast due to diffraction, distortions due to dislocation in the matrix can be identified. In the vicinity of these strains, T_1 has nucleated. However, these observations were extremely scarce in the samples.



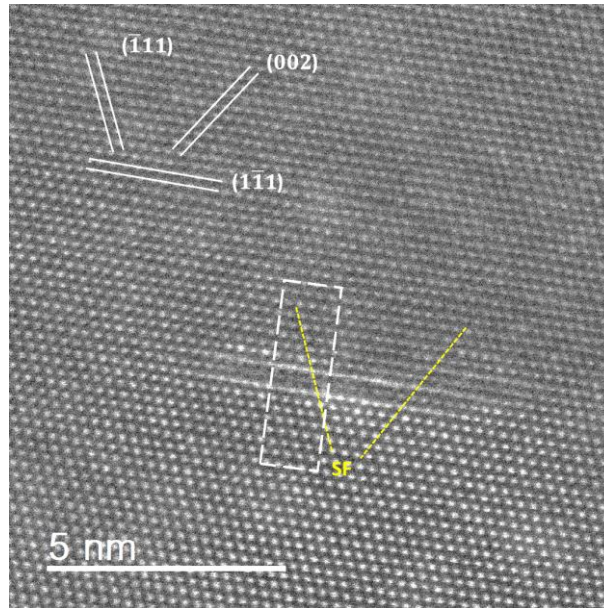
a) HAADF image

b) ADF image

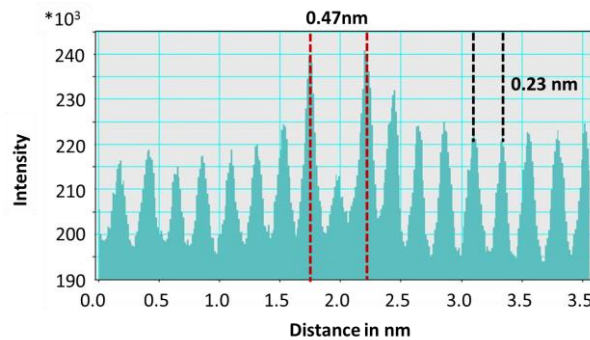
Figure 63: $\langle 110 \rangle$ matrix zone axis of AlCuLi Mg0.3Ag in 'EoR' condition.

It is furthermore of interest to investigate the structure of such early nucleated T_1 precipitates. Figure 64a images the T_1 precipitate of Figure 63 with increased magnification. In addition, a box indicates the corresponding intensity profile (illustrated in b) taken across the precipitate. The precipitate is imaged close to edge-on condition. The interplanar distance between Al planes is 0.23 nm and was measured as an average over several aluminium planes. It is in very good agreement for Al planes observed along $\langle 110 \rangle$ direction. The intensity profile shows two peaks with much higher intensity, which are characteristic for T_1 precipitates and refer to Cu-rich columns. The van Smaalen model predicts a distance of 0.49 nm [63], [64] between these two columns, however the measured distance lies slightly below and measures 0.47 nm. The intensity profile shows furthermore a small peak between the two Cu containing columns. The centre layer of T_1 consists mainly of Li [63], [65], which should only give rise to very low intensity. However, given the small diameter of this precipitate it is inevitable that the aluminium matrix is superposed with the precipitate, so that the measured intensity arises due to the aluminium matrix. The nucleation of T_1 has been discussed several times before as requiring the formation of a stacking fault [56], [62] which creates a hexagonal stacking in the FCC matrix. The translation of the matrix planes equivalent to that of a stacking fault can be identified when following the atomic arrangements across the precipitates, as indicated by yellow lines in Figure 64a. On the upper part of the precipitate the line correspond very well with the atomic planes. After passing the precipitate, the line continues between the atomic planes in the lower part of the image. This is observed for two different directions.

In addition, the intensity next to the two Cu columns is slightly elevated for a few atomic columns compared to the intensity of the matrix. This can be attributed to Ag segregations on the T_1/α interphase [94], [102].



a) High resolution image of a T_1 precipitate observed along $\langle 110 \rangle$ matrix zone axis.



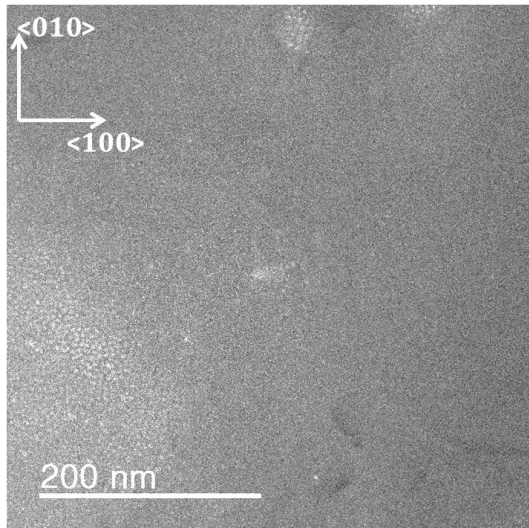
b) Intensity profile of the box sketched in a).

Figure 64: Observations of T_1 at higher magnification a) and intensity profile across the precipitate b).

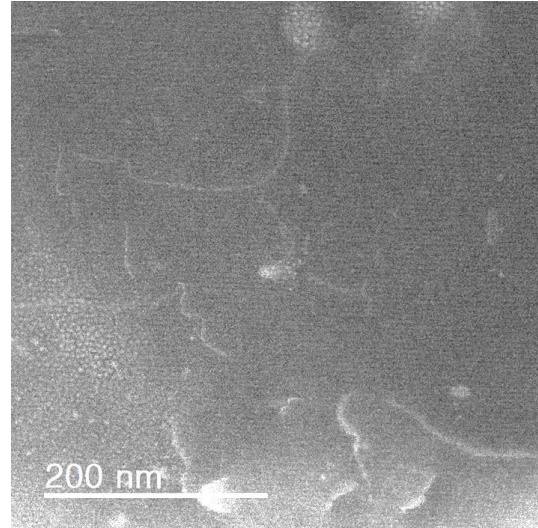
T_1 phases were observed on dislocations or other crystallographic defects, such as sub-grain boundaries. They are characterized by two Cu-rich columns with high intensity and a stacking fault across the precipitates can be identified. An intensity increase is observed for the Li-rich centre layer of the T_1 precipitates when the aluminium matrix is superimposed, which is visible for small T_1 precipitates.

4.3.2. AlCuLi Mg0.1AgZn

Figure 65a shows an HAADF image and exhibits no significant contrast at this scale. However, Figure 65b reveals the presence of dislocations in the same area due to diffraction contrast imaging conditions.



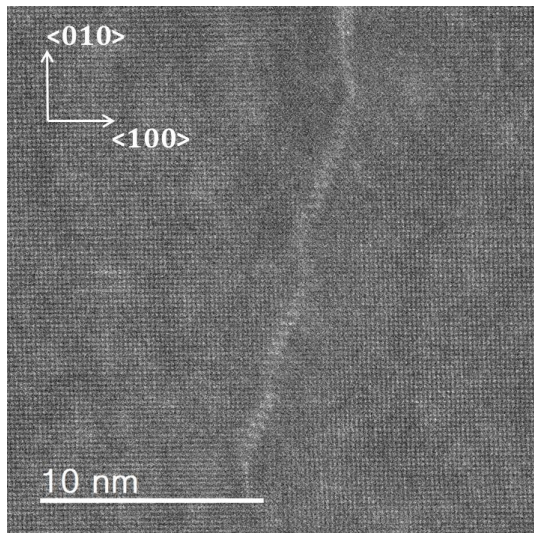
a) HAADF image



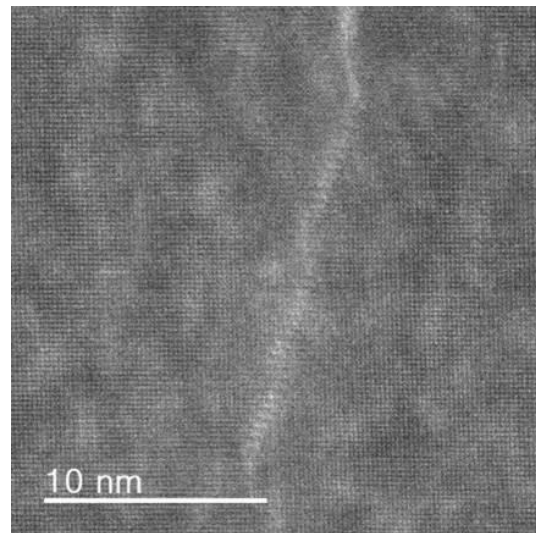
b) ADF image

Figure 65: Overview of the 'EoR' condition in AlCuLiMg0.1AgZn along $\langle 001 \rangle$ matrix zone axis; Z-contrast a) and diffraction contrast b).

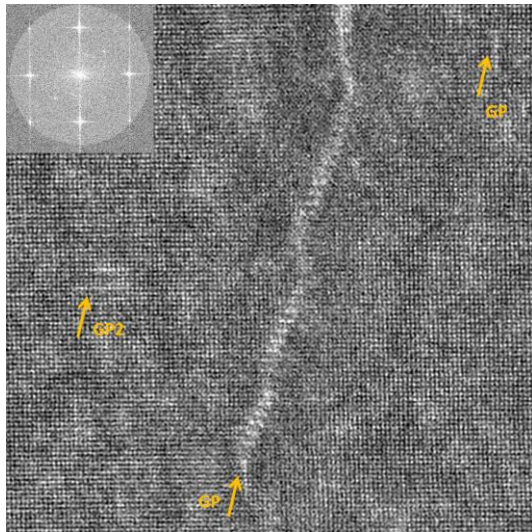
Zooming closer into detail reveals that at very small scale contrast with respect to atomic number is present (see Figure 66a). The weakness of this contrast might explain why these segregations are not visible at lower magnifications in Figure 65a.



a) HAADF image



b) ADF image



c) FTT of a and IFFT of chosen area

Figure 66: Segregations along a dislocation in $\langle 001 \rangle$ zone axis in the AlCuLiMg0.1AgZn alloy.

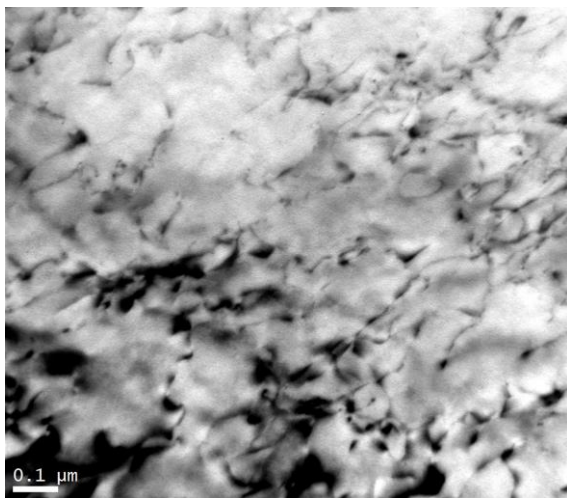
Figure 66a and b show the HAADF and ADF image, respectively. It is clearly seen that atoms with higher atomic number than Al have segregated, probably along a dislocation. These segregations consist most likely of Cu and Mg, since similar features were observed in atom probe tomography, where the solute species can be identified [102]. The contrast in the ADF image is a combination of contrast due to different atomic number and diffraction and only little differences are seen between Figure 66a (pure Z-contrast) and Figure 66b, suggesting that the contrast with respect to atomic number is more significant than the diffraction contrast. To perform further analysis on this segregation, Fourier filtering was performed with a cut-off radius of 0.14 nm^{-1} . The result is imaged in Figure 66c. It reveals that the segregations already possess a well-defined structure, so that they can

now be called precipitates. In addition, the filtered image suggests the presence of GP and GP2 zones marked by arrows.

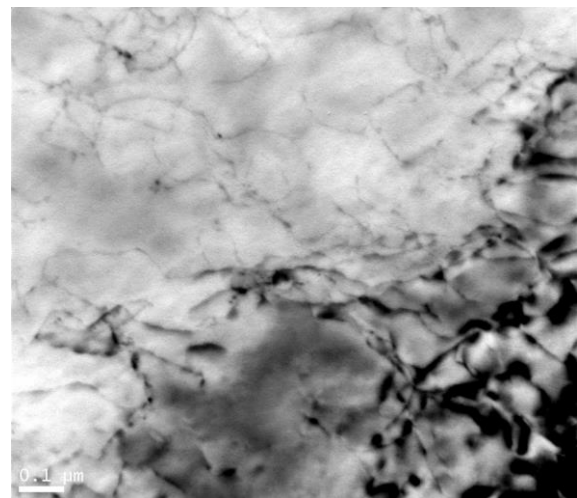
No T_1 precipitates were found, in the $\langle 110 \rangle$ direction. However, this does not mean that T_1 is not present. Indeed, in AlCuLiMg0.3Ag T_1 precipitates were observed very scarcely, probably nucleated on widely spaced heterogeneous nucleation sites. As mentioned before, only a very small area of the sample is imaged and the presence of precipitates which nucleate mostly heterogeneously is dependent on grain orientation and defect structure.

4.3.3. AlCuLi

Dislocations in $\langle 001 \rangle$ direction were imaged in the 'EoR' condition for the AlCuLi alloy. The distribution of dislocations seems to be more homogeneous than in AlCuLiMg0.3Ag (see section 4.3.1) and in addition no small dislocation loops were observed. Dislocations are bowed, but do not show jog-like shapes and no helices are observed as seen in AlCuLiMg0.3Ag. Yet, it seems that small phases have precipitated sporadically on dislocations. More detailed investigations were achieved by atomic resolution images, combined with HAADF imaging conditions.



a) BF image

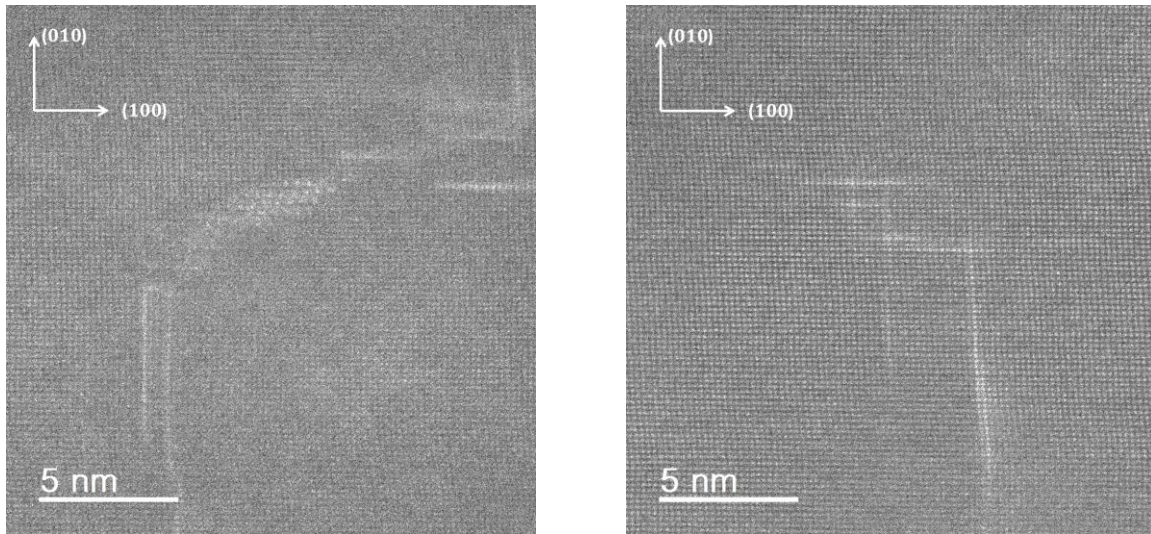


b) BF image

Figure 67: Bright field images of dislocations, observed along $\langle 001 \rangle$ zone axis in AlCuLi (2-wave condition, $g = [100]$).

Most of the investigated area along $\langle 001 \rangle$ in AlCuLi does not show any segregation on dislocations as could be confirmed by comparing diffraction and Z-contrast images with ABF images. In addition, GP and GP2 zones were sporadically observed and are illustrated in Figure 68. In the centre of image a) in Figure 68, it is seen that the resolution decreases. This is most likely due to strain in the matrix originating from a dislocation and distorting the matrix from the exact orientation relationship.

Several layers thick GP or GP2 zones nucleate on the dislocation, and an ordered precipitate of ill-defined shape is observed. In b) single-layer GP zones, rich in Cu are visible.

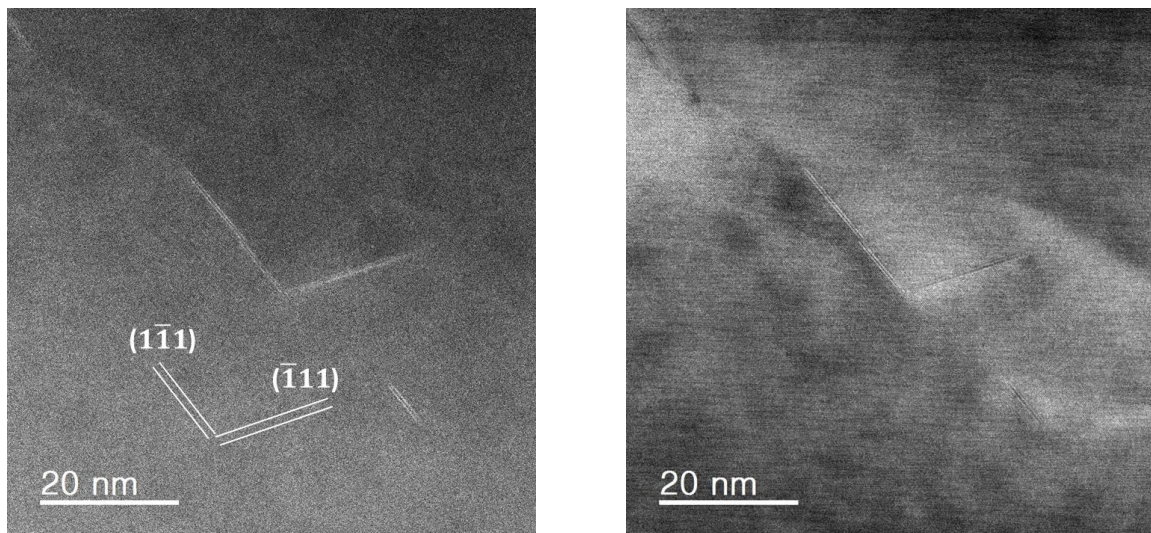


a) GP2 zones

b) GP zones

Figure 68: $\langle 001 \rangle$ zone axis in AlCuLi

Figure 69a shows the presence of T_1 precipitates which was rather unexpected. Two variants of T_1 are observed.



a) HAADF image

b) ADF image

Figure 69: 'EoR' condition for AlCuLi in $\langle 110 \rangle$; Z-contrast and diffraction contrast.

Diffraction contrast in Figure 69b shows the presence of internal stress in the matrix which can be associated to the presence of dislocations. Pre-deformation prior to artificial aging treatment provide

a high number density of dislocations and consequently heterogeneous nucleation sites. The T_1 precipitates can be associated to this dislocation line.

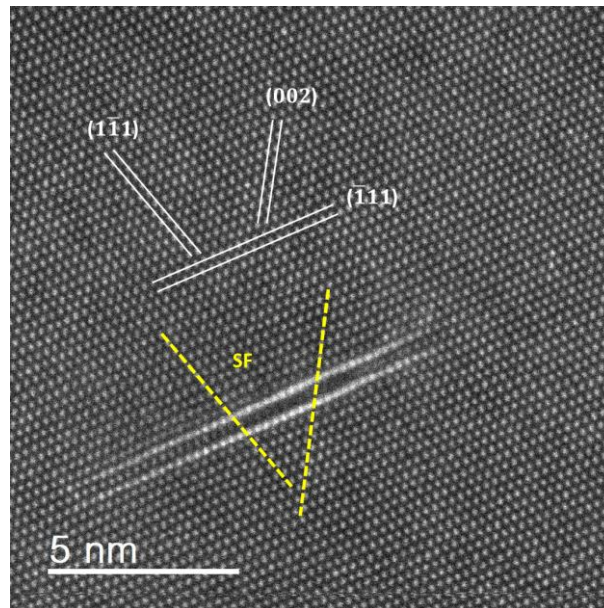


Figure 70: Closer examination of a T_1 nucleated in AlCuLi along $\langle 011 \rangle$ zone axis (HAADF image). The presence of a stacking fault is illustrated.

An example of higher magnification of the T_1 phase is illustrated in Figure 70. The shift in aluminium planes with respect to each other is illustrated by yellow lines in Figure 70a, indicating the presence of a stacking fault. As seen in the previous section 4.3.1 in Figure 64a contrast arises in the Li-rich centre layer on the edges of the T_1 precipitate. This effect is attributed to the overlap of the T_1 precipitate with the aluminium matrix, which becomes visible for thin precipitates with respect to the sample thickness. This overlap of the aluminium matrix with the T_1 precipitate is only seen on the outermost edges of the T_1 precipitate where the T_1 precipitate is assumed to be thinner due to its disc-like shape. Besides, no atomic columns with locally increased intensity can be observed at the T_1/α interphase. This is consistent with the absence of Ag as a minor alloying element in this alloy, and indirectly confirms our interpretation of the bright spots observed in the Ag containing alloys.

4.4. The 'nucleation' condition

The 'nucleation' condition is defined after an aging time of 1.5 hours at 155 °C. It corresponds to the artificial aging time when streaks appear in the SAXS image and intensity starts to increase.

4.4.1. AlCuLiMg0.3Ag

Figure 71 shows the presence of segregations or more likely of first precipitated phases along dislocations. GP zones are connected to these precipitates.

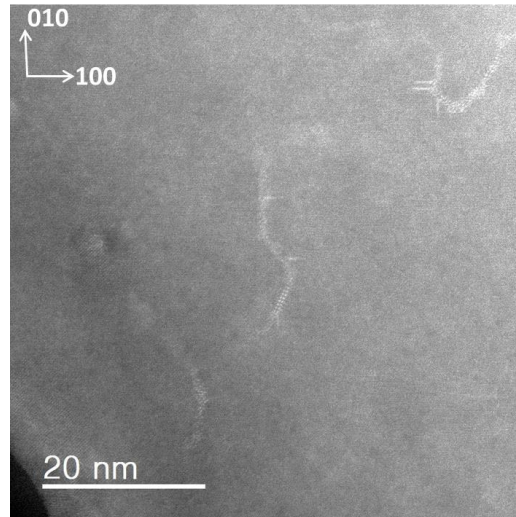


Figure 71: HAADF image of AlCuLiMg0.3Ag, in <001> direction.

A higher magnification image is shown in Figure 72.

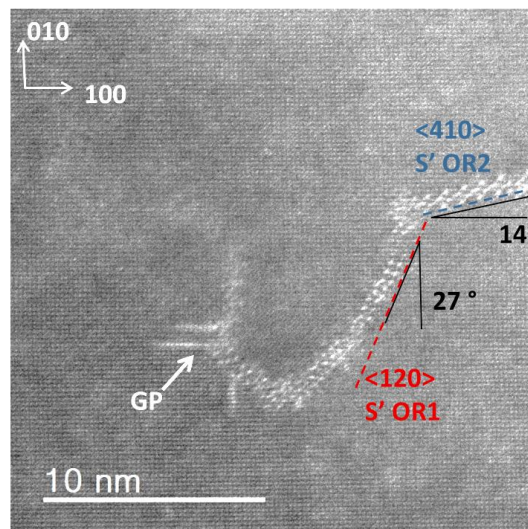
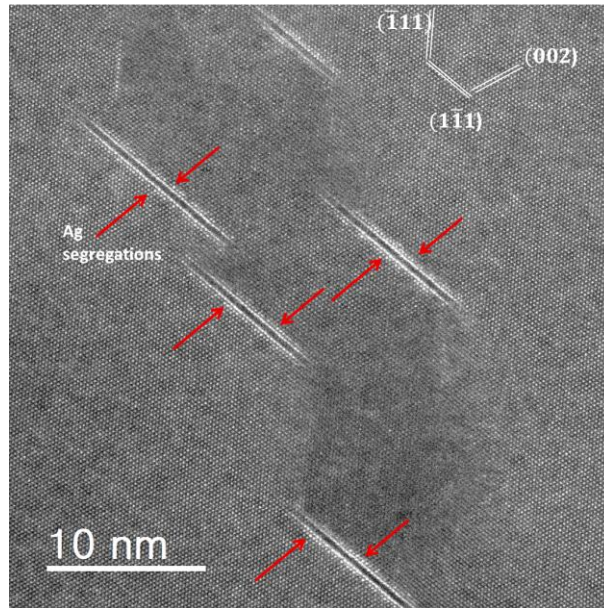


Figure 72 : Precipitation along a dislocation in AlCuLiMg0.3Ag after 1.5 hour at 155 °C along <001> zone axis.

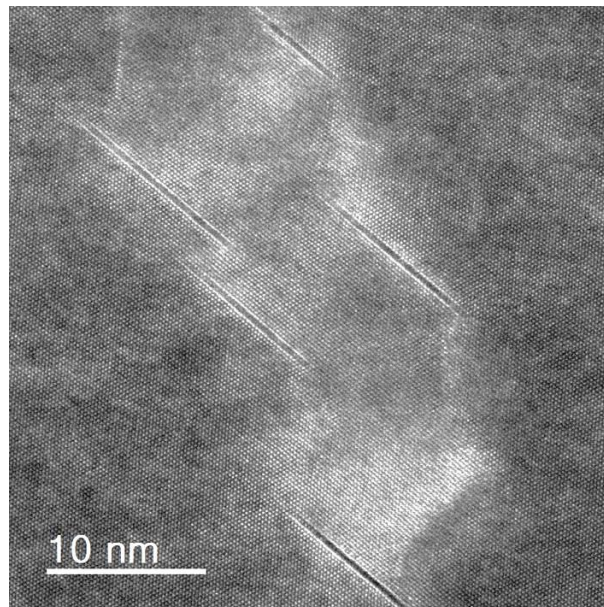
The curved shape which is seen in Figure 72 indicates a dislocation line. A similar shape of dislocations surrounded by precursors was observed in APT experiments and the chemical species were analysed to be Cu and Mg [102]. The increased contrast along this dislocation line can be

attributed to nucleation of precipitates on this dislocation, since clearly a structure is visible. The orientation with the matrix has been determined for two parts of the precipitate that shows relatively planar interfaces. The upper part is inclined 14° with respect to $[100]$ matrix direction. The lower part of the indexed structure is oriented 27° with respect to $[010]$. These orientation relationships between precipitate and matrix reveal, that the lower part fits perfectly with OR 1 for S' precipitates $[31]$, $[41]$, $[42]$ and is oriented along $\langle 120 \rangle$, whereas the upper part is oriented along $\langle 410 \rangle$ which corresponds to the OR 2 for S' precipitates $[31]$, $[41]$. The angle between these two phases measures approximately 127° (or 53°) which was observed in $[31]$. In addition, it is clearly seen that the atomic structure is ordered along these directions, which relates these precursors to be of the type of S' phase in this early aging condition.

Five T_1 precipitates of similar diameters are illustrated in Figure 73a. The average diameter for T_1 precipitates was 9.4 nm in this condition (obtained from 11 precipitates). Bright spots on the interface of the T_1 precipitates indicate the presence of Ag, which was observed on all precipitates in Figure 73a. In Figure 73b, strain contrast is imaged and suggests that all precipitates are connected to the same dislocation line. Inside this dislocation loop, it is further seen in Figure 73a, that the HAADF contrast is darker than outside the loop. This change in contrast is mostly linked to the slight changes in the orientation of Al columns, since the sharply peak contrast of Al columns is rapidly lost as soon as the perfect zone axis condition are lost in HAADH STEM, i.e. a contribution from diffraction contrast is observed in the HAADF image.



a) HAADF image



b) ADF image

Figure 73: Nucleation condition of AlCuLiMg0.3Ag along $\langle 011 \rangle$ zone axis, showing five T_1 precipitates. Diffraction contrast reveals the presence of a dislocation, to which precipitates are connected.

4.4.2. AlCuLi

Several GP zones and θ' are observed in Figure 74. Two variant of θ' are observed and it appears that θ' is not perfectly aligned with $[100]$ and $[010]$ direction and seems much distorted.

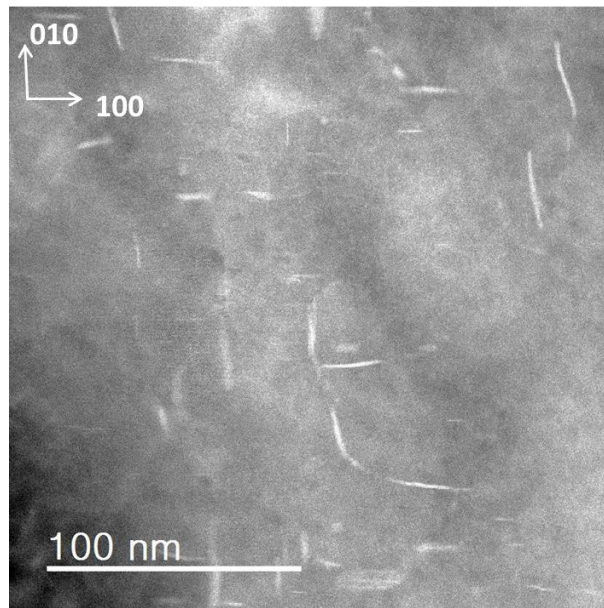
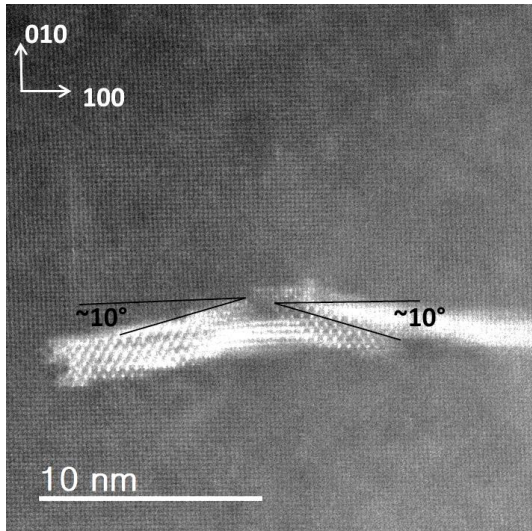
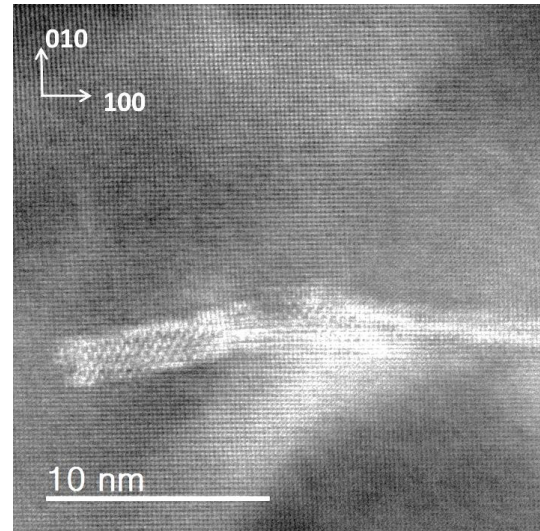


Figure 74: Distorted θ' precipitates in the 'nucleation' condition in AlCuLi, observed in $\langle 001 \rangle$ matrix zone axis.

Two deviated θ' precipitates are illustrated with higher magnification in Figure 75. These two θ' are deviated around 10° from the $[100]$ direction, as it is indicated in Figure 75a. Figure 75b (in ADF) shows additional contrast that can be attributed to the presence of strain in the matrix, likely originating from a dislocation. Yoshimura et al. [24] detected θ' phases deviated from the original orientation relationship in high Li containing alloys. The change in lattice parameter and its deviation was attributed to the high Li concentration. In the present study, alloys with much lower Li content are investigated. Deviations of θ' from the perfect orientation relationship are attributed to the interaction of θ' with dislocations present due to pre-deformation. Furthermore, the degree of deviation, i.e. the measured angles between $\langle 001 \rangle$ and θ' , are much smaller in the present study than in [24]. The angle with respect to $\langle 100 \rangle$ is very close to the angle found for S' phases, precipitated on dislocations. Combining these observations, the change in habit plane is attributed to the interaction of θ' with a curved dislocation.



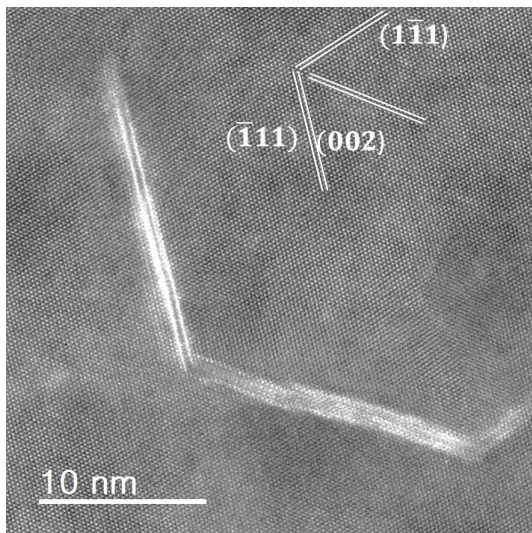
a) HAADF image



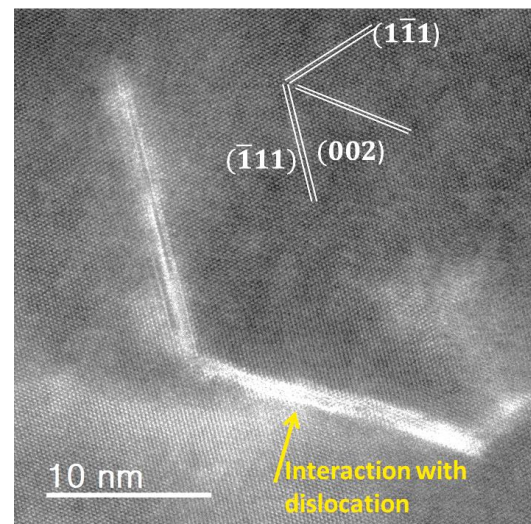
b) ADF image

Figure 75: High magnification images along $\langle 001 \rangle$ zone axis of two θ' precipitates that are inclined with respect to $[100]$ and $[010]$ matrix direction.

T_1 precipitates and a well-developed θ' precipitation are illustrated in Figure 76a. The diameter of the observed T_1 reaches approximately 15 nm. In Figure 76b diffraction contrast reveals that the interaction between dislocation and θ' phase has occurred. At the point, where interaction of θ' and dislocation occurs, the right part of θ' is deviated from the perfect lattice orientation as indicated by an arrow in the ABF image in Figure 76b. It is however difficult to determine if the T_1 precipitate is also linked to a dislocation.



a) HAADF image



b) ABF image

Figure 76: T_1 and θ' observed in $\langle 110 \rangle$ zone axis.

4.5. The 'stabilised' condition

The 'stabilised' condition was obtained for different aging times due to different precipitation kinetics. AlCuLiMg0.3Ag was thus aged for 15 hours, AlCuLiMg0.1AgZn for 18 hours and AlCuLi for 50 hours, respectively.

4.5.1. AlCuLiMg0.3Ag

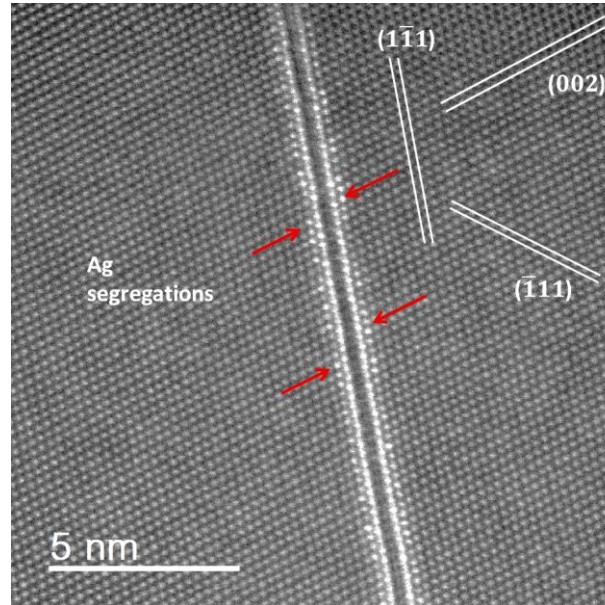


Figure 77: T_1 precipitate in AlCuLiMg0.3Ag observed along $\langle 110 \rangle$ zone axis by HAADF imaging. Bright spots on the matrix/precipitate interface indicate the presence of Ag segregations.

Figure 77 illustrates a T_1 precipitate edge-on. Bright spots, located at the interface between T_1 and the matrix, are related to the presence of Ag segregation, as discussed before. They are indicated by arrows. The Li-rich centre layer does not reveal any overlap with the Al matrix due to a larger diameter of the T_1 precipitate compared to earlier aging conditions.

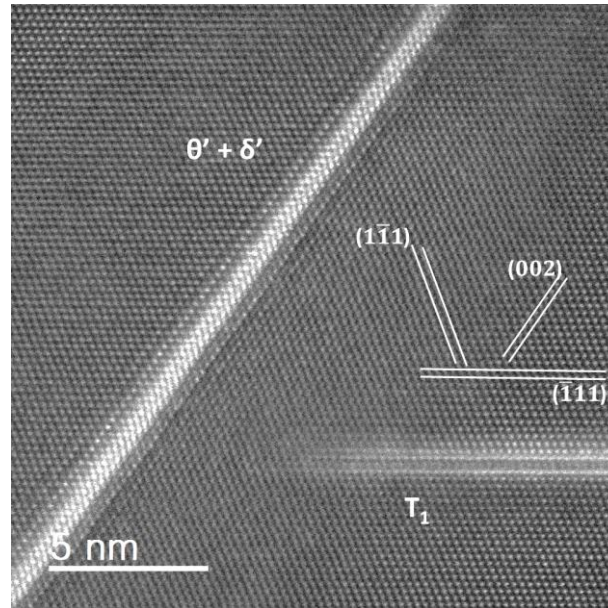


Figure 78: T_1 and θ' particles observed by HAADF imaging along $\langle 110 \rangle$ zone axis. θ' is covered with δ' .

Another T_1 precipitate next to a θ' precipitate is illustrated in Figure 78. The θ' precipitate is clearly surrounded by a layer of δ' phase. As it was observed before [25], this θ' is particularly thin, with a structure distinct from that of the bulk phase of θ' . A detailed study on θ' precipitates in Al-Cu alloys, revealed that during early aging the interface layer of θ' is enriched in Cu [13]. It appears here, that the θ' precipitate in Figure 78 consists of only two Cu-rich layers, which look very similar to the interface layers observed by Bourgeois et al. [13].

4.5.2. AlCuLi Mg0.1AgZn

Two variant of T_1 precipitates and one variant of θ' precipitate are observed in Figure 79. The number density of T_1 in this condition is high and the average diameter is around 50 nm. The brighter areas covering the whole sample surface are residues of electropolishing. Since the atomic number of Zn is very similar to the atomic number of Cu, EDS elemental mapping was performed on one T_1 precipitate with the JEOL 2100F instrument. This permits clarifying the possible presence of Zn in T_1 precipitates.

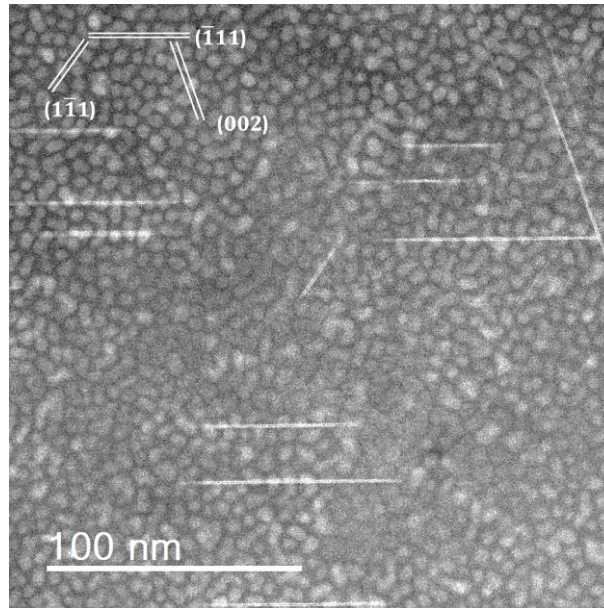


Figure 79: T_1 precipitates along $\langle 110 \rangle$ direction in AlCuLiMg0.1AgZn.

The HAADF image of the analysed T_1 precipitate is shown in Figure 80a and the corresponding elemental maps are shown in Figure 80 b-f). Qualitatively, it can be seen that the aluminium concentration in the precipitate is reduced compared to the matrix (Figure 80b). It clearly reveals that Cu is, as expected, included in the precipitate (Figure 80c). Furthermore, presence of both Mg (Figure 80d) and Zn (Figure 80e) are visible within the precipitate, although the resolution is not sufficient here to determine precisely on which positions. Segregations of Ag are not evidenced, but this lack of information can also be attributed to the very low atomic concentration of Ag in AlCuLiMg0.1AgZn (Figure 80f). The intensity profile across the precipitate confirms the presence of Cu in the precipitate (Figure 81). A slight increase is also observed for Mg and Zn, but due to smaller concentrations compared to Cu, the increase in intensity is lower. Zn incorporation in the T_1 phase has also been observed by Guinel et al. [105] using a SEM in STEM mode.

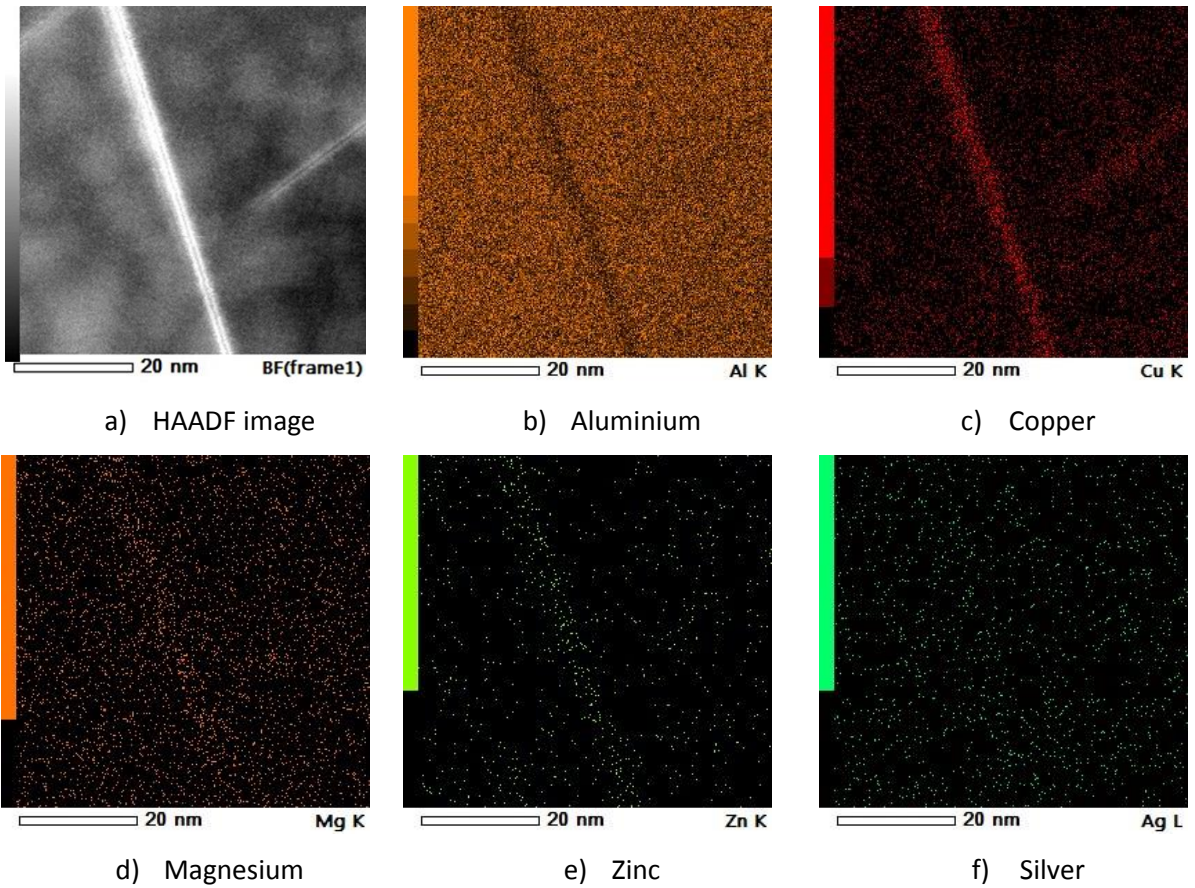


Figure 80: T_1 precipitate and the EDS images for the different chemical species.

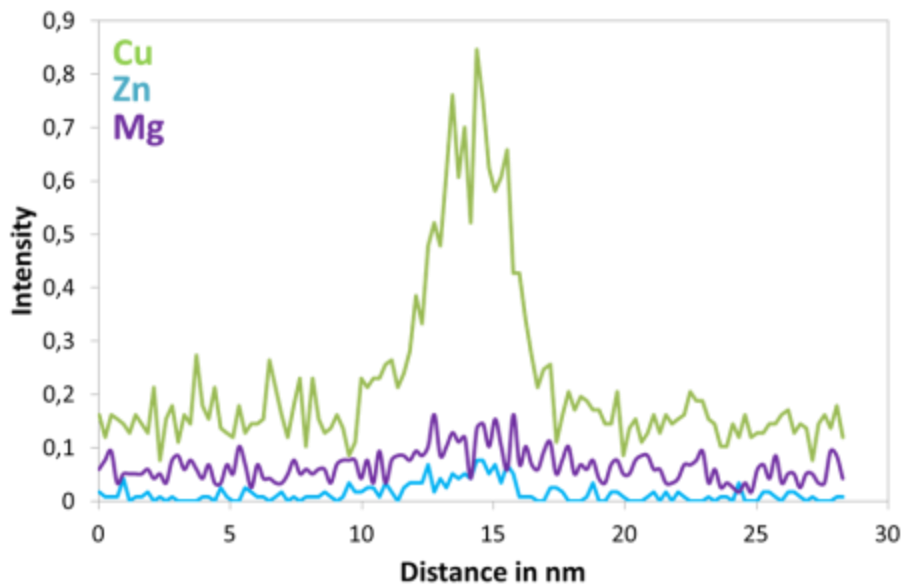


Figure 81: EDS profile across the T_1 precipitate shown in Figure 80.

Structured phases were observed in the AlCuLiMg0.1AgZn alloy and are illustrated in Figure 82. The inclination encloses an angle of approximately 25° with respect to $[100]$ and this orientation

relationship suggests that they are S' phases that lie on (021) planes. Furthermore, disordered needle-like structures are also observed, which can be identified as GPB zones [38]. On the left side, a GP2 zone is seen, recognised by 2 Cu planes that are separated by 3 aluminium planes. The picture does not reveal if the S' -like structure has nucleated homogeneously in the matrix or heterogeneously on a dislocation. The length of the precursors varies between 2 nm up to 7 nm and its width is 1 nm. The diameter of GPB needles measures between 1.2 nm up to 2.5 nm.

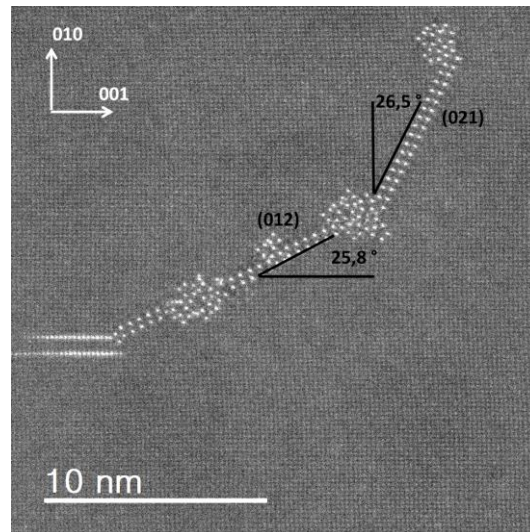
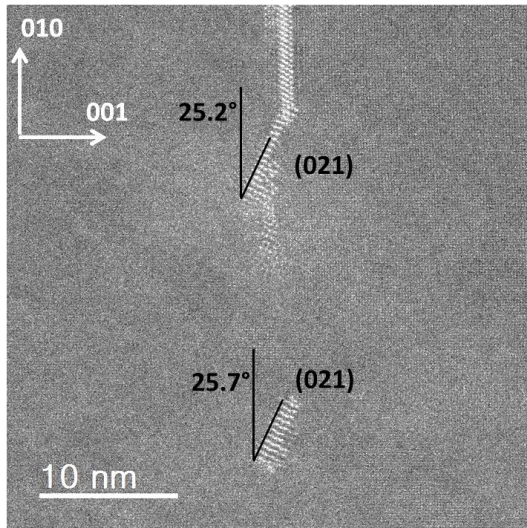
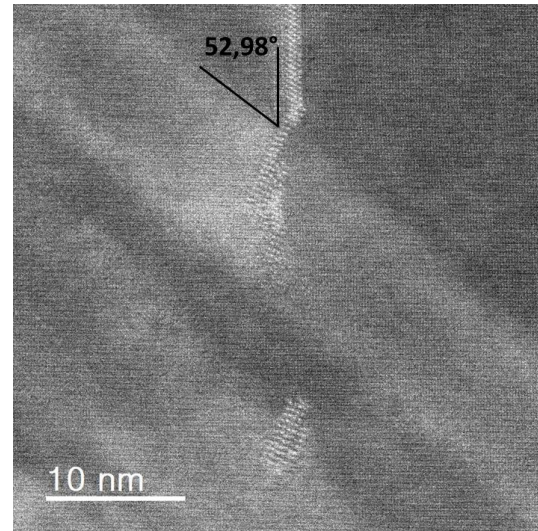


Figure 82: AlCuLiMg0.1AgZn investigated in $\langle 001 \rangle$ matrix zone axis by HAADF imaging showing S-type precipitates, GPB zones and a GP2 zone.

Inclined precipitates connected to θ' are also observed in Figure 83a (upper part of the image). The θ' structure is not fully imaged. Another inclined precipitate is seen in the lower part of the image. The angles for these two inclined precipitates measure 25.2° and 25.7°, respectively. This orientation relationship attributes these inclined phases to S' . The length of the S' structures measures between 4.5 – 5 nm and its diameter is found between 1 nm for the upper structure and 2 nm for the structure in the lower part. The latter named S' structure appears to have nucleated homogeneously. Figure 82 and Figure 83 indicated the S' phases are stable in this condition and are oriented along $\langle 021 \rangle$ direction as observed by [31], [41].



a) HAADF image



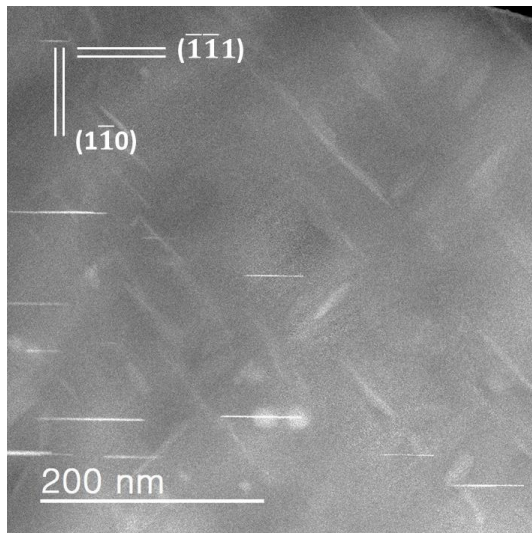
b) ADF images

Figure 83 : S-type precipitates and θ' observed along $\langle 001 \rangle$ zones axis. The ADF image shows diffraction contrast possibly originating from an inclined T_1 phase from a different variant.

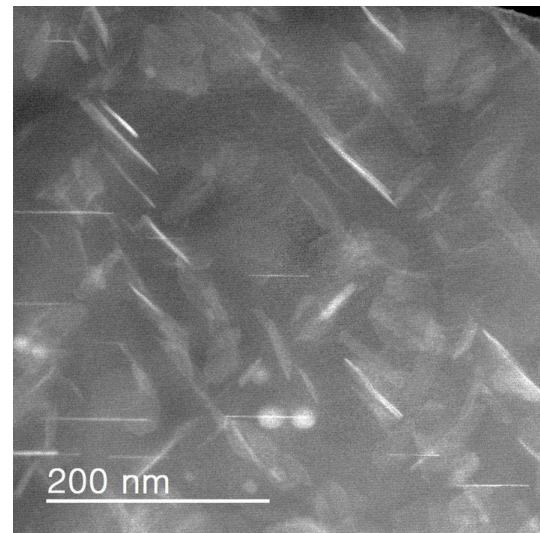
Diffraction contrast in Figure 83b reveals the presence of a plate like structure, which lies inclined to the electron beam. No corresponding Z-contrast is observed in the HAADF image in Figure 83a. This diffraction contrast most likely corresponds to a T_1 precipitate from an inclined variant. Its contrast is not seen in HAADF-mode, because the composition Al_2CuLi on an inclined precipitation of 1 nm thickness, in combination with the superposed aluminium matrix averages to an atomic number very close to that of the aluminium matrix.

4.5.3. $AlCuLi$

A significant number density of T_1 precipitates is seen in Figure 84a. One variant of T_1 is observed edge-on. The diameter of the observed T_1 phase in this image varies between 40 to 80 nm. Diffraction contrast illustrated in Figure 84b indicate the presence of plate-like phases oriented 90° to each other and which might be associated to inclined variants of θ' precipitates. These phases are inclined to the electron beam and are not seen edge on. Due to high Cu concentration in θ' , some Z-contrast of these phases is also observed in Figure 84a. However, they are best visible in diffraction contrast, observed in Figure 84b.



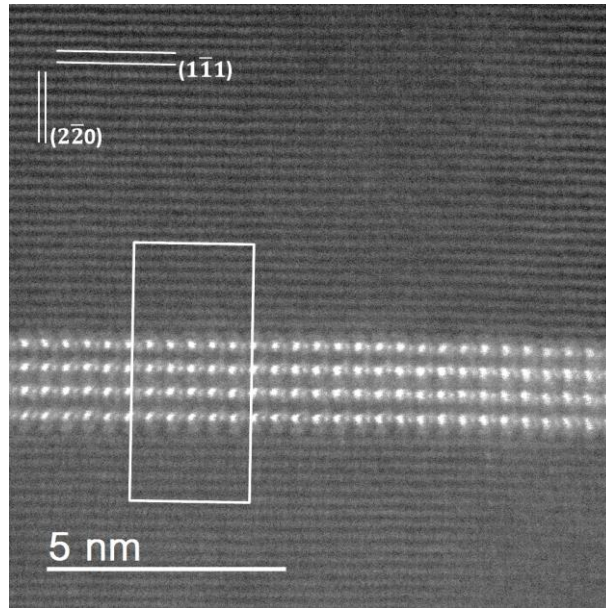
a) HAADF image



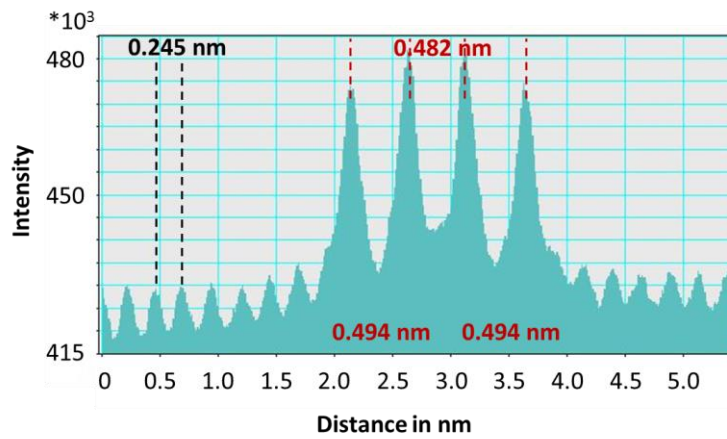
b) ADF image

Figure 84: One variant of T_1 precipitates observed in 'stabilised' condition for AlCuLi, observed along $\langle 112 \rangle$ direction.

In the 'stabilised' condition of AlCuLi, both single and multi-layered T_1 precipitates are found. Figure 85a shows a double-layered T_1 , including the intensity profile across the precipitate. The intensity profile of the double layered T_1 shows clearly four Cu-rich rows with increased intensity. The structure is in good agreement with the structure defined by van Smaalen [64] [63].



a) HAADF image of double-layer T_1 precipitate.



a) Intensity profile across T_1 precipitate.

Figure 85: Double layered T_1 precipitate observed in $\langle 112 \rangle$ matrix zone axis. a) HAADF image b) intensity profile across the precipitate.

A high number density of θ' phases aligned in $[100]$ and $[010]$ direction are observed in Figure 86a. Yet, deviations of the orientation relationship are seen. The average diameter of the precipitates illustrated in Figure 86 was around 40 nm. The contrast with respect to diffraction is illustrated in Figure 86b. Since a fully precipitated condition is present, this contrast can be attributed to both dislocations and precipitates that are inclined with respect to $\langle 001 \rangle$ direction.

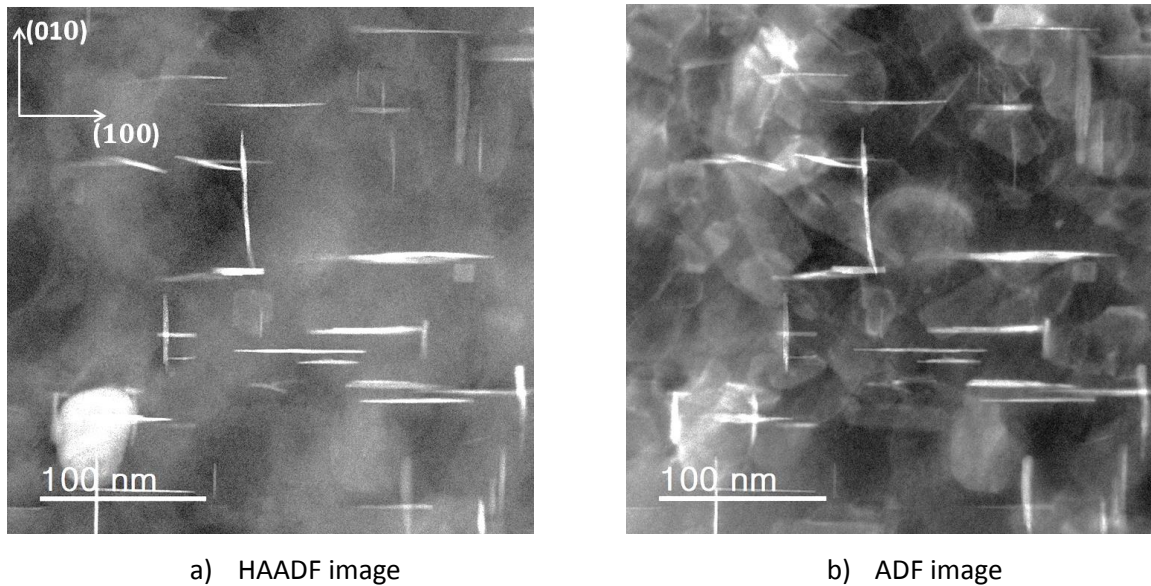
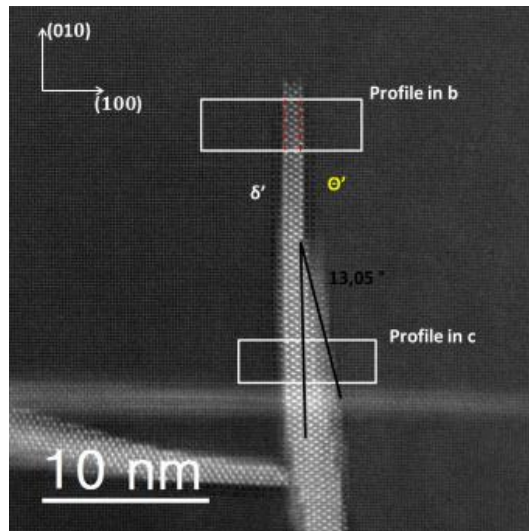
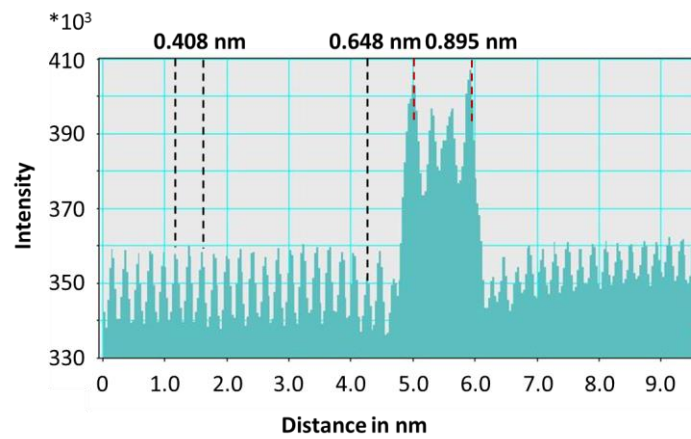


Figure 86: AlCuLi in 'stabilised' condition along $\langle 001 \rangle$ matrix zone axis.

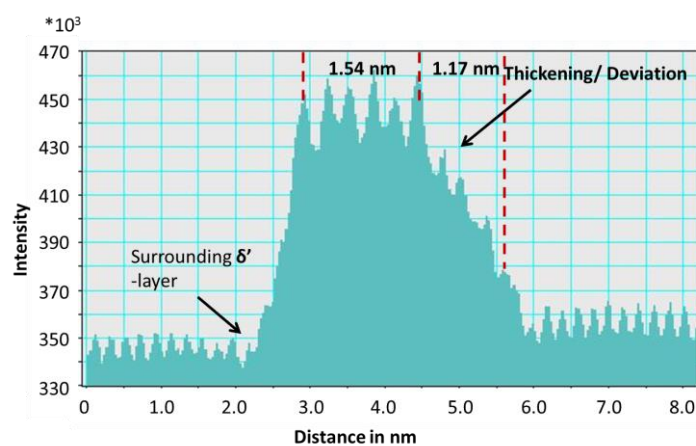
A magnified θ' precipitate which is oriented edge-on along $[010]_{\text{Al}}$ direction is shown in the upper part of Figure 87. In the lower part of the image θ' appears to be inclined and have thickened. A step-like deviation is observed, which is assumed to be caused by the interaction of θ' with a dislocation. Intensity profiles across the aligned and inclined θ' structures are illustrated in Figure 87b and c, respectively. The interplanar distances along $[001]$ direction for θ' both and the inclined part are constant. δ' is clearly seen in the intensity profile illustrated in Figure 87b. The intensity is lower than the aluminium matrix, which is consistent with presence of Li. Furthermore, δ' is observed on both sides of the θ' precipitate and corresponds well to the sandwiched structure of θ' and δ' , which has been observed before [24], [25], [29]. In Figure 87c, a decrease in intensity indicating the presence of δ' is only observed on the left hand side of the intensity profile. However, it is assumed that the δ' layer should be continuous and cover all precipitated θ' . It is not visible if the precipitates are out of edge-on condition.



a) HAADF image showing a θ' precipitate surrounded by δ' ; in the lower part the precipitate deviates from the orientation relationship.



b) Intensity profile across θ'



c) Intensity profile of the deviated θ' particle

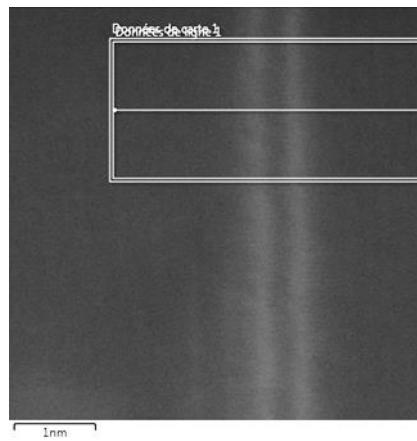
Figure 87: High magnification image of θ' precipitate in the AlCuLi alloy deviating from $\langle 100 \rangle$ -direction and intensity profiles of θ' .

4.6. 'Thickened' condition -AlCuLiMgZn

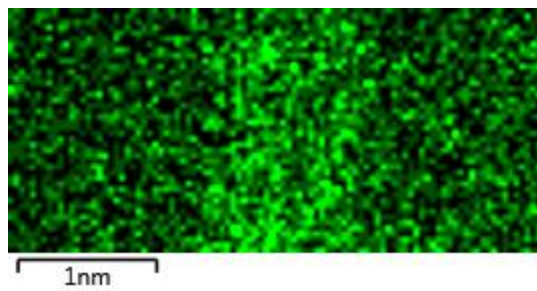
In order to better understand and identify the role of Zn during nucleation and precipitate growth, AlCuLiMgZn was studied in the 'stabilised' condition and in the 'thickened' condition. Thickening was achieved by submitting the alloy first to an artificial aging at 155°C for 15 hours followed by 70 hours at 190 °C. EDS elemental mapping was performed in the JEOL ARM instrument in order to distinguish Cu from Zn atoms, since they cannot be distinguished by Z contrast.

4.6.1. 'Stabilised' condition of AlCuLiMgZn

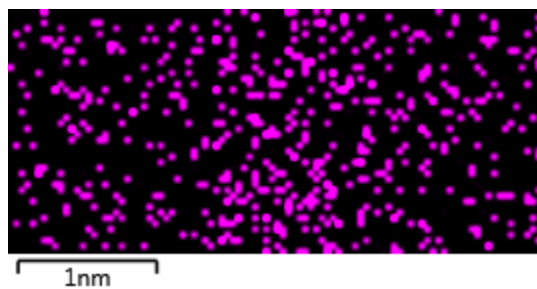
The T_1 precipitate and its element mapping is seen along a $\langle 112 \rangle$ zone axis in Figure 88 a to d). The HAADF image in Figure 88a illustrates two bright lines, which are related to Cu-rich columns typical for T_1 precipitates. The EDS mapping for Cu, illustrated in Figure 88b, evidences Cu enrichment associated to the precipitate, but the precise positioning is difficult to resolve. The element mapping of Mg and Zn, in Figure 88c and d respectively, reveal that both are present in the precipitate, but precise positioning is impossible.



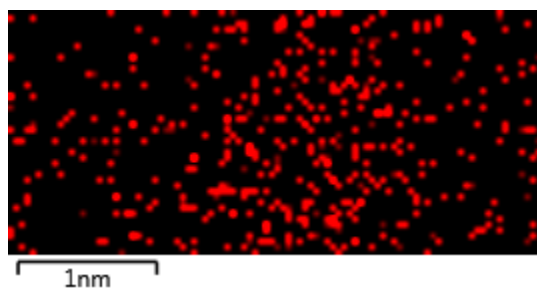
a) HAADF image



b) Copper



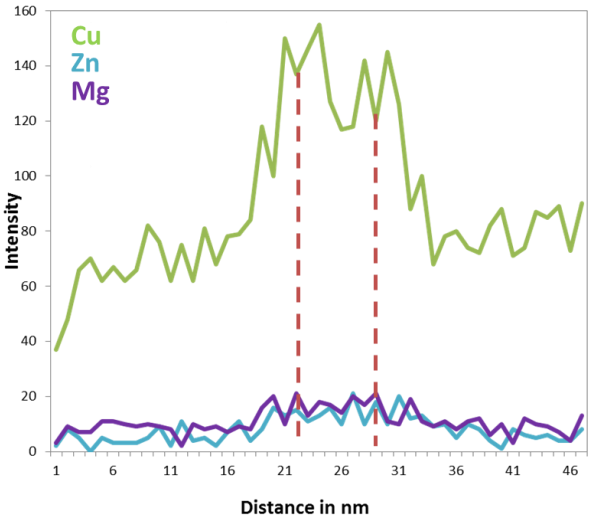
c) Magnesium



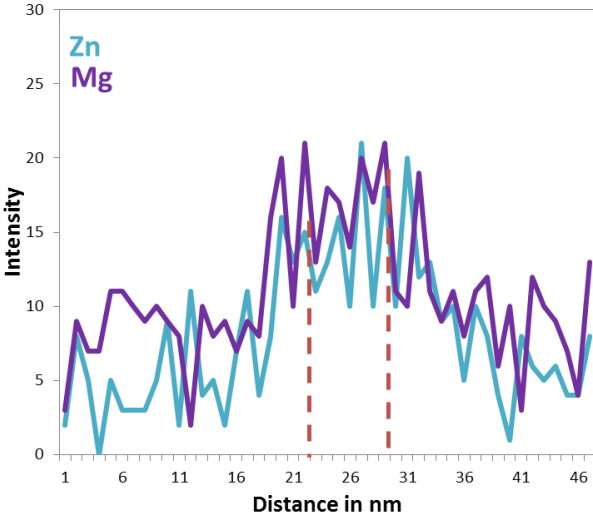
d) Zinc

Figure 88: Single layer T_1 with corresponding EDS profiles for b) Cu, c) Mg and d) Zn along $\langle 112 \rangle$ zone axis.

Figure 89 illustrates the concentration profiles across the precipitate. Figure 89a represents the profile for Cu, Mg and Zn and two peaks for Cu are identified, characteristic for T_1 precipitates. A magnified profile is sketched in Figure 89b, in which only Mg and Zn are illustrated. The positions of the Cu peaks are marked. The intensity profiles for Mg and Zn do not show as pronounced peaks as seen for Cu in Figure 89a and in the present case, the observations suggest that Mg and Zn are present across the whole T_1 precipitate.



a) Intensity profile for Cu, Mg and Zn across the T_1 precipitate.



b) Magnified intensity profile for Zn and Mg across the T_1 precipitate.

Figure 89: Intensity profiles for Cu, Mg and Zn (a) and in more detail for Mg and Zn (b).

4.6.2. 'Thickened' condition of AlCuLiMgZn

T_1 thickens discretely by the addition of one unit cell at a time [56], [63]. Figure 90 images a double layered T_1 precipitate, observed in $\langle 110 \rangle$ matrix zone axis. It clearly exhibits four bright columns which are associated to the Cu-rich layers of the T_1 structure.

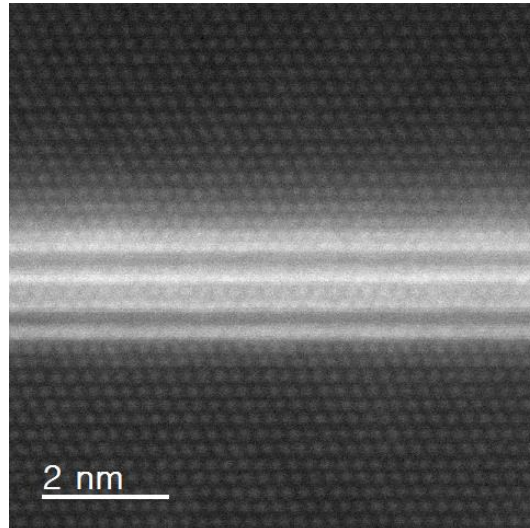
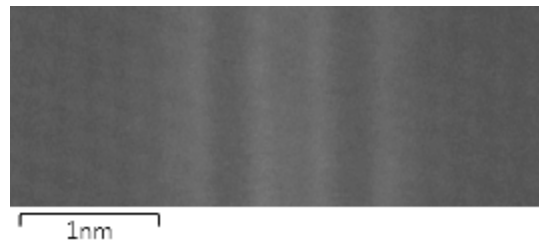
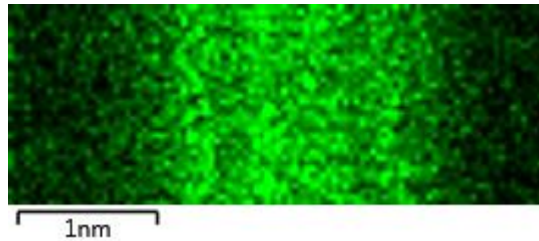


Figure 90: HAADF image of a double layered T_1 , observed along a $\langle 110 \rangle$ zone axis.

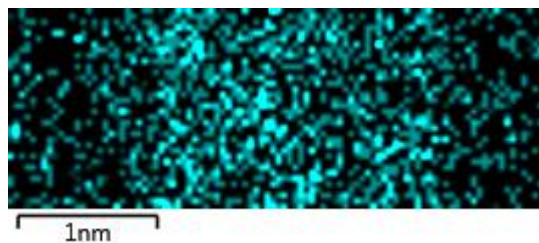
The middle centre layer, which is common for both T_1 precipitates, contains some aluminium as it was observed earlier by Donnadiou et al. [63]. EDS mapping of Cu, Mg and Zn across the T_1 precipitate is imaged in Figure 92 a - d.



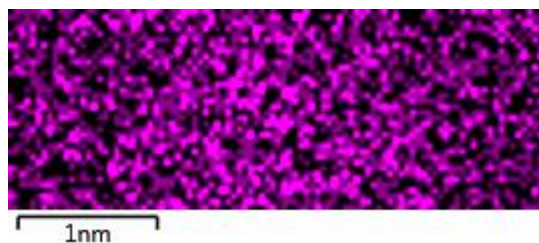
a) HAADF image



b) Copper



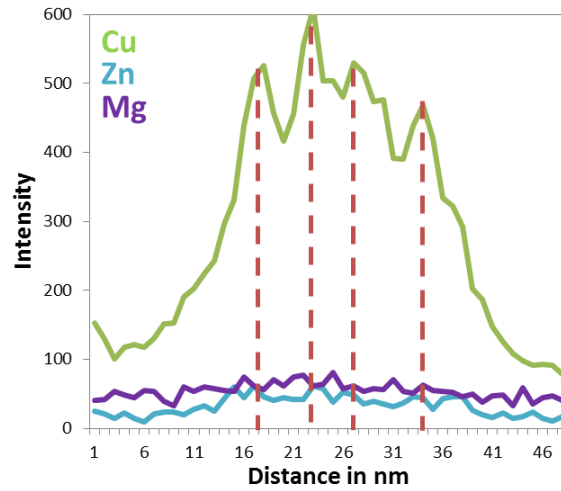
c) Zinc



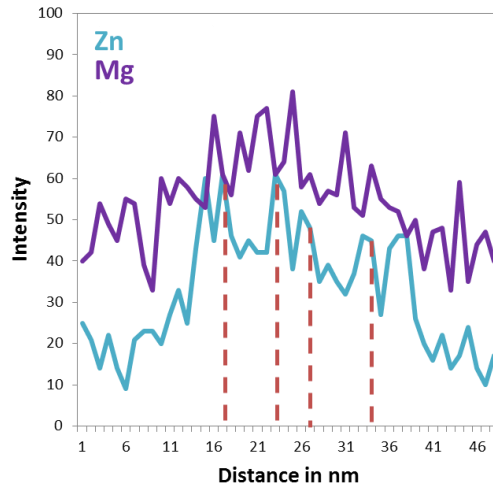
d) Magnesium

Figure 91: HAADF image of thickened T_1 and corresponding element mapping of b) Cu, c) Zn and d) Mg for the 'thickened' condition of the AlCuLiMgZn alloy.

The HAADF image is illustrated in Figure 95a and indicates the atomic position of the Cu-rich and Li-rich columns. Four Cu-rich columns can be clearly identified in the EDS mapping of Figure 92b. They are in good agreement with the bright contrast in Figure 91a. The EDS mapping of Zn (Figure 92c), supported by the intensity profiles shown in Figure 92a and b, shows a similar trend as copper indicating that Zn partitions mainly to distinct columns. The comparison of Cu and Zn EDS maps suggests that Zn substitutes Cu positions. Mg mapping (see Figure 92d) shows that Mg is included in the T_1 precipitate; however no preferential sites could be identified.



a) Intensity profile for Cu, Mg and Zn across the T_1 precipitate.



b) Magnified intensity profile for Mg and Zn across the T_1 precipitate.

Figure 92: Intensity profiles for Cu, Mg and Zn (a) and in more detail for Mg and Zn (b).

To better resolve intensity variations of Mg and Zn, Figure 92b only shows the profile of Zn and Mg. The position of Cu peaks is marked. In effect, Zn peaks are likely to be associated with the Cu-positions. Additional Zn peaks were found at the right and left hand side of the Cu/Zn peaks, which may be attributed to Zn segregations on the T_1 interface. However, the close positions of the peaks make it difficult to relate this peak clearly to the interface. The intensity profile of Mg shows likewise several peaks, however it is more difficult to associate these peaks to specific atom positions, and it is most likely that Mg is present within the whole T_1 precipitate, as it was seen by APT [102]. Similarities between the η phase ($MgZn_2$) in AlMgZnCu and the T_1 phase have been discussed by Marioara et al. [85]. They claimed that Mg positions in η are similar to the Li position of T_1 and Zn is

found at the same position as Al. In the presence of Cu, it is incorporated into the η' structure by substituting Zn-rich positions. Furthermore, Zn was found at the η' /matrix interphase. Analog observations were made in the present sample. It seems reasonable to suggest that Zn is not only present on Cu positions, but also at the T_1 /matrix interphase as indicated in Figure 92.

4.7. Summary

This chapter describes the microstructural differences in AlCuLi alloys with respect to different minor alloying elements. Both Mg containing and Mg-free alloys show the presence of T_1 in early aging conditions. They are seen very seldom and most of the matrix seems to be a solid solution. However, in the presence of Mg, dislocations were decorated very early on with Cu and Mg. These structured precursors were further on observed after 1.5 hours of artificial aging at 155 °C and show an orientation relationship similar to S' phases. In the absence of Mg, these precursors on dislocations could not be observed. In AlCuLi, the microstructure consisted of GP zones connected to dislocations and after 1.5 hours, first θ' has been detected. These phases appear to interact with dislocations and deviate from the original orientation relationship for θ' precipitates.

In the 'stabilised' condition, both Mg containing and Mg-free alloys contain T_1 precipitates with increased diameters and higher number density than in early aging conditions. However, the number density for Mg containing alloys is higher than for Mg-free alloys, which shows that T_1 precipitation is favoured in the presence of Mg. Additional to T_1 precipitates, S' and GPB zones are seen in Mg containing alloys both on dislocations and homogeneously nucleated in the matrix. There exists an important quantity of θ' precipitates in the Mg-free alloy, which are surrounded by a layer of δ' . θ' precipitates often show deviations from their original orientation relationship with the matrix. These deviations are attributed to interactions with dislocations. The differences in microstructure are summarized in Table 9.

Table 9 : Differences in microstructure in Mg containing and Mg-free alloys for different aging conditions.

	'EoR'	'nucleation'	'stabilised'
Mg containing alloys (AlCuLiMg0.3Ag, AlCuMg0.1AgZn)	Sporadic T_1 ; GP zones Precursors on dislocation	Elevated number of T_1 in connection with dislocations ; GP zones; Pre-S' precipitation on dislocations	High density of T_1 precipitation, some θ' precipitates; S'
Mg-free alloys (AlCuLi)	GP zones ; GP2 ;	Aligned θ' and inclined θ' due to interactions with dislocations; Sporadic T_1	Both θ' and T_1 are present; however dominant θ' precipitation surrounded by δ' ; θ' is inclined due to interaction with dislocations.

Ag segregations on the T_1 interphase

Ag segregations on the T_1 /matrix interphase were observed in Mg and Ag containing alloys, namely in AlCuLiMg0.3Ag. These segregations were found in all observed conditions, 'EoR', 'nucleation' and 'stabilised'. TEM micrographs present a 2D image of a 3D sample and it is difficult to obtain reliable information on concentrations for Ag segregations of the T_1 interphase. However, in Mg-free containing alloys no bright spots were observed on the T_1 interphase, so that we associate bright atom columns to Ag segregations. As observed by atom probe tomography experiments, Ag segregations were present on the broad surface of the T_1 phase [102].

Zn substitution in the T_1 phase

T_1 incorporates Zn in its structure. EDS analysis across T_1 precipitates reveal that Cu and Zn occupy similar atomic columns in the precipitate structure, which was best seen for thickened T_1 . In Al-Mg-Zn, alloys Zn is a major component of the main precipitating phase η' . The addition of Cu to these alloy system showed that Cu substitutes Zn positions [85].

5. Diffusion couples as a tool to map compositional space

The two former chapters showed that the influence of minor alloying elements on precipitation in the studied AlCuLi alloy is striking. Their presence influences precipitation kinetics and affects the precipitation sequence. The former analysis was performed on alloys with distinct compositions in order to compare them among each other. The use of diffusion couples is an exciting approach for analysing the variation in concentration for one element, while all other components stay constant. In the present case, couple combinations were produced from alloys of which hardening and precipitation kinetics was determined in the former chapters. The formerly identified characteristics act as boundary conditions. The aim of this approach is to identify the minimum concentration of different minor alloying elements necessary to see an effect on kinetics, and also to investigate potential non-monotonous effects of minor solute concentration. The approach of diffusion couples is very promising and a wide range of compositions can be characterised with respect to materials' properties and behaviour [124], [125].

In order to obtain a diffusion gradient it is necessary to join two dissimilar materials (however with close composition and properties). For materials that tolerate high temperatures, hot isostatic pressing [125], [126] and the use of a Gleeble machine [127] showed good results for joining. Another rather simple approach is to press the two pieces together and apply a heat treatment at the same time [34], [124], [128]. However, this method was less favourable for aluminium alloys as seen in [34]. A subsequent performed rolling procedure was not possible, since the weld broke at the interface, due to the existing oxide layer. Therefore, it is important to choose a proper joining method, which allows further thermo-mechanical processing if necessary.

For aluminium alloys, but also many other materials, friction stir welding (FSW) is a very good joining method. A rotating tool passes along the joining axes. Friction creates heat and deformation and thereby joins the material in solid state condition, without passing into the liquid phase. A great advantage of this method is that no special sample preparation prior to welding is necessary and it is possible to join a wide range of different geometries [129], [130]. The weld does not show any defects from melting and solidification, and in case of optimised parameters, defect free joints can be produced. Three different zones are present after the friction stir welding process, which are affected by heat and deformation to different degrees. The welds created by this method allow further mechanical processing. However, a disadvantage of this joining method for the present study is the mixing of the material during the welding process [131], and the complex shape of the boundary between the two joined materials. Studying diffusion couples often requires controlled diffusion, which is obtained during the diffusion heat treatment. In consequence, a sharp interface after welding is favourable. Linear friction welding (LFW) is based on a friction process, similar to

friction stir welding. However, after joining a step-like interface is present. Two pieces are joined by keeping one of them fixed while the other piece is oscillating and moving towards the fixed one, combined with a large normal force. The surfaces heat up when both blocks are in contact. Eventually they deform plastically, which expels material from the interface, i.e. the oxide layer is removed. A flash forms [132], [133]. Figure 93 sketches schematically the process of linear friction welding [134].

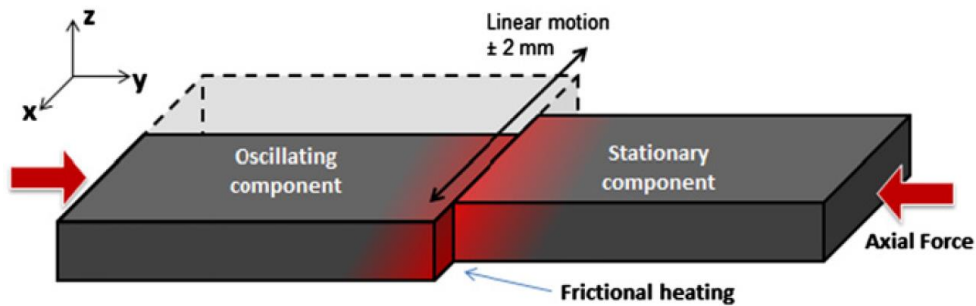


Figure 93: Schematic illustration of linear friction welding. Figure taken from Rotundo et al. [134].

First studies of LFW were mainly performed on titanium alloys [132], [133], but this method was expanded to aluminium alloys [134] and it was seen that a good joint could be obtained. There are several advantages of using linear friction welding in the present study. First, by repelling the oxide layer of the two initial aluminium blocks, the weld allows further mechanical processing without risking breaking the weld. Second, a planar step like interface is present after welding so that diffusion can be controlled during a subsequent diffusion heat treatment.

The approach of diffusion couples has been used for several decades, mostly in order to calculate phase diagrams and validate data bases. These studies were based on local equilibrium at the phase interfaces [135]. Furthermore, bulk diffusion experiments allowed determining diffusion characteristics, such as diffusion coefficients. These binary or even ternary diffusion couples were however not used to determine any other materials' properties dependent on composition. The possibility of measuring properties on a micro-scale rose the interest and use of diffusion couples in order to determine properties with respect to composition [135].

Amongst others (examples for thermal conductivity, electric conductivity and many more can be found in the review by Zhao [135]) studies have used diffusion couples in order to determine diffusion characteristics [125], [126], thermoelectric properties [136], or phase transformations [34], [124], [127], [128], [137]–[139].

There are several studies, which by means of diffusion couples gave insight in metallurgical problems. The following section shortly reviews some of these studies to show the effectiveness of this

approach. The $\gamma \rightarrow \gamma + \alpha$ phase transformation was studied dependent on the Ni concentration in a Fe-1Ni and Fe-5 Ni diffusion couple during decarburisation. Increased nickel concentration influences the transformation kinetics. A smooth transition for the α volume fraction has been observed with increasing Ni content, measured by optical microscopy [124], [137]. In another study, a diffusion couple of pure Fe and Fe-Ni-Al was used to determine the influence of variations in Fe concentrations on the precipitation behaviour in Fe-Ni-Al alloys. A lower Ni and Al concentration decreased the β' precipitation, and fewer coarsened precipitates and increased coarsening resistance were observed [128]. In order to determine diffusion coefficients for multi-component system, different Ni-based super alloys were joined and heat treated [125], [126]. In order to evaluate the influence of Nb concentration on recrystallization of Fe, a symmetric diffusion gradient was created by encapsulating a Nb containing iron piece between two ultra-high purity Fe blocks. This ensemble was joined in a Gleeble applying pressure at elevated temperature. Further heat treatment was then performed in a Gleeble machine. An advantage of using a Gleeble machine is that the temperature is measured at several positions along the diffusion gradient during the heat treatment. The result showed the influence Nb concentration on recrystallization in combination with its temperature dependence [127]. Rapid hardening response in aluminium alloys depending on Cu-Mg concentration was evaluated by Marceau et al. [34]. After the diffusion heat treatment hardness measurements were performed in order to identify rapid hardening kinetics as a function of solute content [34].

In the present study, we thus chose a combinatorial approach to investigate the influence of a wide range of compositions for minor alloying elements. As seen in the former chapter the effect of Mg was striking on precipitation and hardening kinetics. To a lower extent, a small contribution to hardening and precipitation was found for Ag additions. In order to study a continuous range of concentration variations of Mg and Ag, the approach of diffusion couples has been chosen. Hardness and in-situ SAXS measurements were then conducted. Due to spatial resolution limits for these experimental techniques it is necessary that the diffusion gradient is sufficiently large, giving constraints on the thermo-mechanical processing of the gradients that have been accounted for. These diffusion couples with a sufficient large width of the gradient were then subjected to artificial aging treatment. Hardness measurements were performed across the gradient for different ageing times. In Chapter 3, it was seen that differences in precipitation kinetics existed, dependent on minor alloying elements. A time and space resolved approach was applied to characterize it, in which in-situ SAXS measurements were performed for different positions in the gradients, i.e. for different compositions.

5.1. Processing and microstructural observations of the weld

5.1.1. Processing of diffusion couples

Figure 94 shows diffusion couples after linear friction welding. Figure 94a shows a series of different welds. It is clear that for all different combinations, joining was achieved effectively. Figure 94b magnifies the flash that forms during linear friction welding. The deformation is homogeneous thanks to tailoring a similar hardness in all materials by appropriate heat treatments before welding (see chapter 2.2), since the flash size is similar on both sides of the weld. For further processing, the flash was removed.

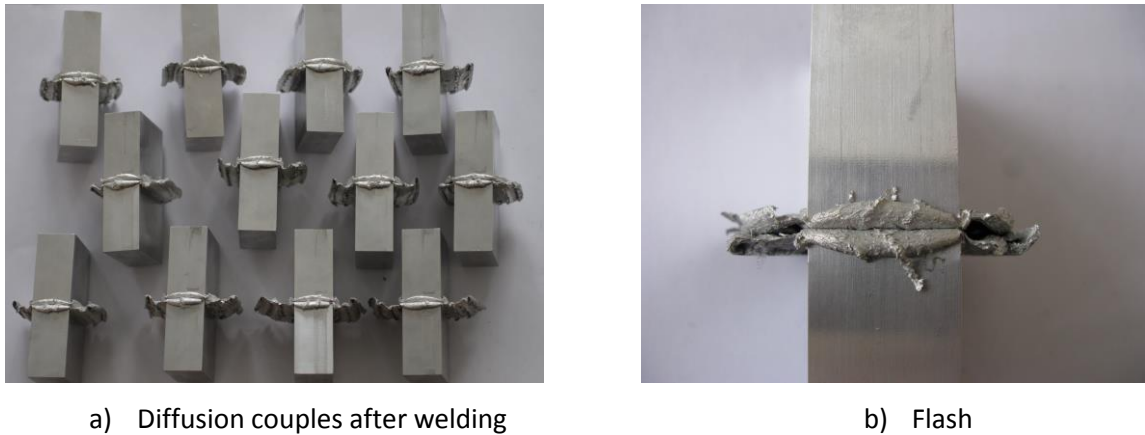
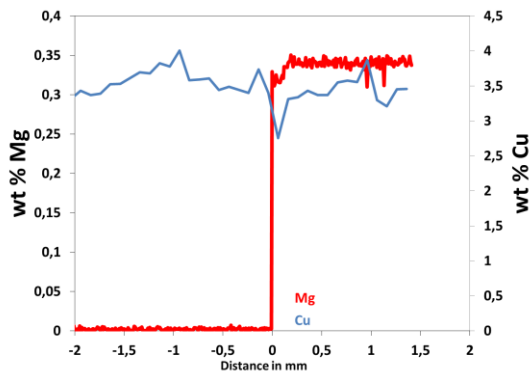
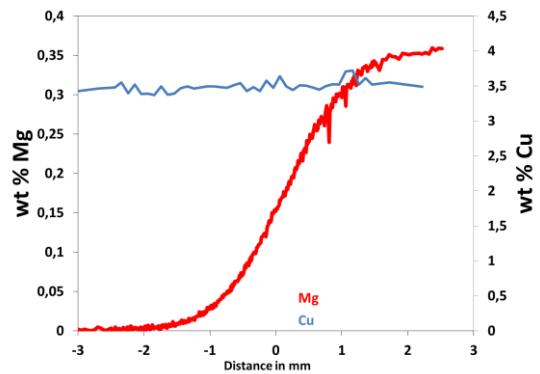


Figure 94: Diffusion couples after welding; a) overview; b) enlarged view of the flash. The dimensions of each block prior to welding were 25mmx50mmx50mm.

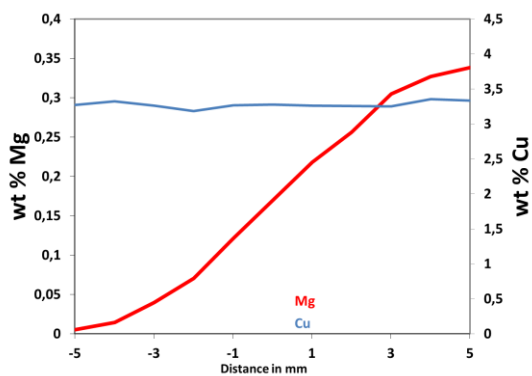
The evolution of the concentration gradient during the different thermo-mechanical processing steps (as described in section 2.2) is presented exemplarily for one couple. Figure 95a - c presents the Mg concentration after welding, homogenisation treatment and rolling, respectively. All concentrations were measured by EPMA. After welding, a step like interface is present, as seen in Figure 95a. The homogenisation heat treatment at 515 °C for 14 days activates diffusion and creates a gradient of width 3 mm, as seen in Figure 95b. Hot rolling further enlarges the concentration gradient to 10 mm, seen in Figure 95c. The extension of the diffusion gradient is then sufficiently large with respect to the spatial resolution of SAXS measurements (beam size 1 mm) and of hardness measurements (diagonal for soft material around 90 μm). One difficulty in our case is that the Li concentration in the diffusion couple could not be monitored. We assume that it remains constant (its concentration being identical in the two end materials) similarly to Cu. In fact, there might be some interaction of the diffusion of some minor solutes (especially Mg) and Li; however the atomic concentration of Mg is at maximum 0.35 at% as compared to 3.5 at% for Li, so that it can be safely assumed that any gradient of Li content in the diffusion couples remains negligible.



a) After welding



b) After homogenisation; 515 °C for 14 days



c) Diffusion gradient after rolling

Figure 95: The diffusion weld measured by EPMA after linear friction welding.

5.1.2. Microstructure of the weld

The microstructures for the different thermo-mechanical steps were imaged along the normal direction using optical microscopy. The normal direction is the surface, which is in contact with the rolling mill during the rolling process. The grains are seen from ‘above’.

The microstructure of the weld is seen in Figure 96a after the welding process. The deformation is symmetric which indicates successful joining and removal of the oxide layer. After the homogenisation heat treatment, the weld is fully recrystallized as seen in Figure 96b. No defects are visible. The grains enlarge during rolling as seen in Figure 96c and have larger diameters as compared to the recrystallized structure Figure 96b, after homogenisation. The rolled grain structure is illustrated in Figure 96c and shows that indeed the grain diameter has increased .



a) As-weld



b) homogenised



c) after rolling

Figure 96: Microstructure after welding (a), homogenisation heat treatment (b) and rolling (c). All pictures are taken along the normal direction.

5.2. Precipitation kinetics in the diffusion couples

The homogenised and hot rolled diffusion couples were subjected to a slow ramp heating in order to avoid recrystallization during solution heat treatment. Deformation, such as rolling increases the number density of dislocations. By heating the material above the recrystallization temperature ($T_R \geq 0.5 T_m$), nuclei of newly formed grains can form which are free in dislocations and hence lower the total energy of the system. The newly nucleated grains are randomly oriented. Due to the orientation of T_1 precipitates, it is however more favourable to produce material with a moderate rolling texture, which allow seeing T_1 precipitates edge-on. During a heat treatment at lower temperature or a slow ramp heating dislocation movement is activated and thus dislocations arrange in sub-grain boundaries. This process is called recovery and does not affect the texture components. The presence of a recovered grain structure is favoured due to their rolling texture component and was confirmed by optical microscopy. The ramp heating was performed up to 505 °C. The samples were then solutionized at 505 °C for at least 30 minutes and were water quenched subsequently. 4 % plastic deformation was introduced by stretch and 3 days of natural aging at room temperature was maintained, similarly to the single alloys.

Since stretching was applied parallel to the solute gradient (i.e. normal to the welding interface), a different strain level may be reached in the different areas with varying solute content due to

variations of flow stress. Actually, we have seen in chapter 3.1 that the individual alloys showed somewhat different hardness increases, particularly as a function of Mg content, the effect being less pronounced after deformation and more pronounced after natural aging. This is associated to strain hardening and the interaction of dislocations with solutes, namely Mg. In order to analyse the strain distribution in diffusion couples with a Mg gradient, digital image correlation (DIC) was performed. A random pattern of paint dots was sputtered on the tensile sample corresponding to a diffusion couple stretching experiment, and images were taken during the deformation. A good contrast is achieved by applying an opaque paint (in white) on the sample. Thereafter black paint is sputtered on top of it, in order to obtain a randomly distributed point pattern. The application of the paint needs to be done after solution heat treatment and takes around 30 minutes (in order to make sure that the paint has dried). Displacements and strain were then be obtained by correlating the deformed dot pattern with respect to the original pattern [140]. Figure 97a shows the sample in the grip in the un-deformed condition and Figure 97b in the deformed condition.

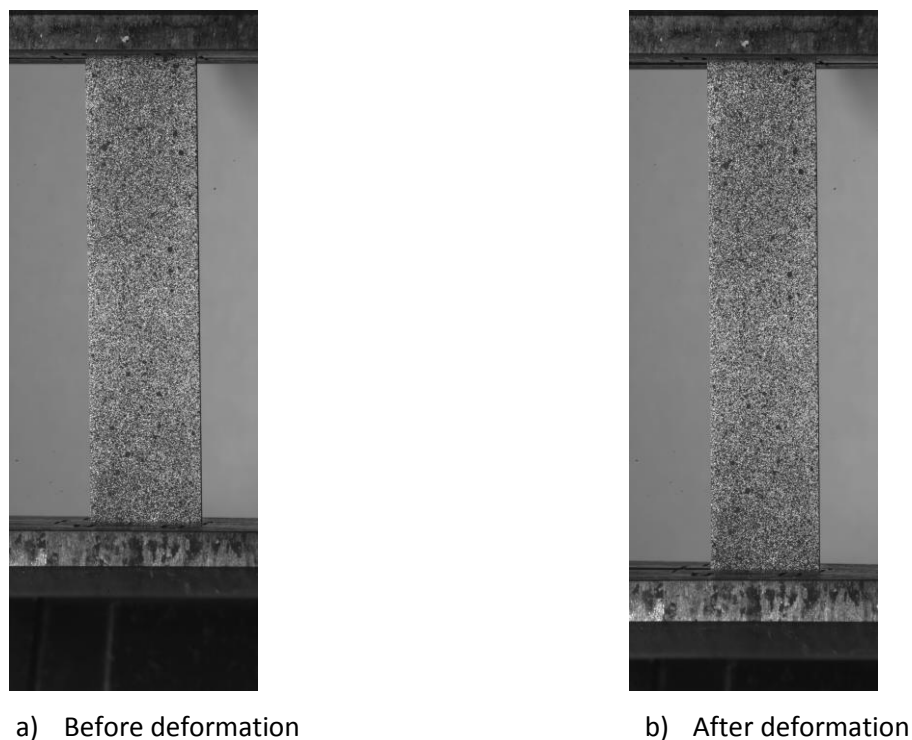
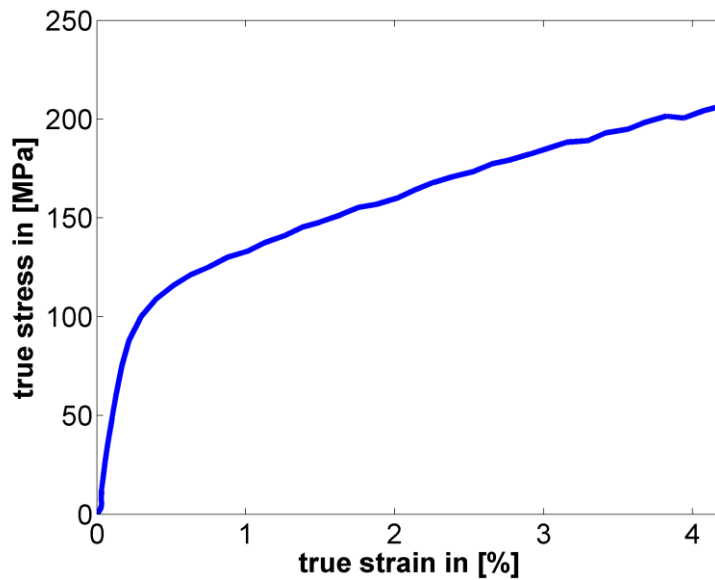


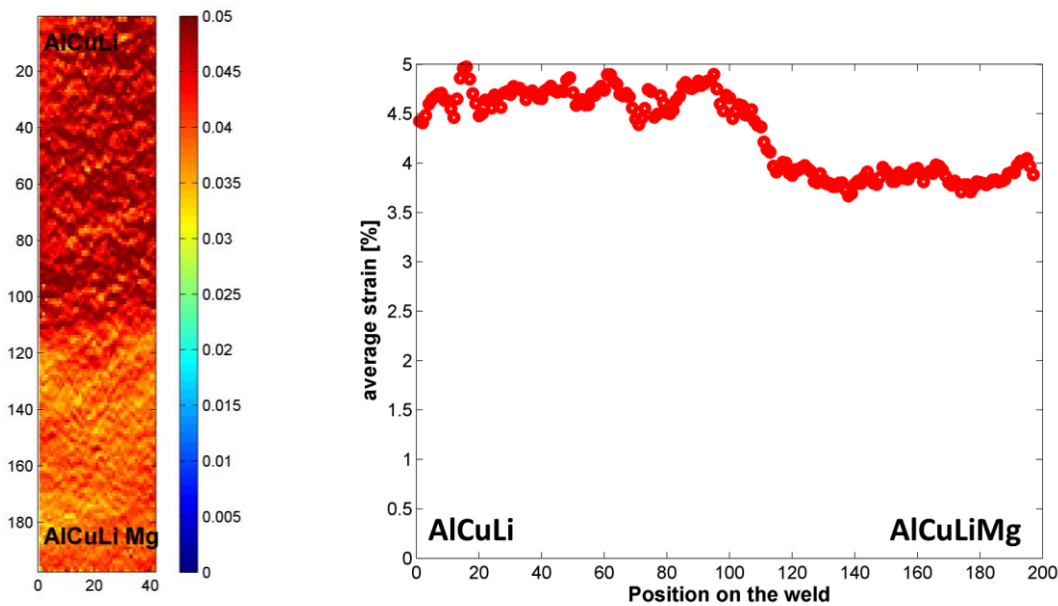
Figure 97: Diffusion couple with paint sputtering before and after pre-deformation.

In Figure 98a shows the overall true-stress – true-strain curve of the diffusion couple AlCuLi and AlCuLiMg which was obtained from DIC. The increase is quite homogeneous. The strain distribution across the diffusion couple illustrated in Figure 98b shows the strain distribution at the end of the true-stress-strain curve, i.e. at 4,3 % global deformation. The Mg-lean side is deformed to a higher extent and in average 5 % strain is obtained. The Mg containing side, in which after 30 minutes

natural aging most likely Cu-Mg clusters have formed and restrict dislocation movement, reaches a strain of 4 % in average. This is also sketched in the graph next to the picture. It shows lower strain for the Mg-rich side and a nearly step-like increase of strain in the Mg-lean side.



a) True stress- true strain curve up to 4.3 % strain.



b) Strain distribution across the diffusion couple; maximum strain of around 5 % is reached in the Mg lean part and 4% strain is obtain in the Mg containing part.

Figure 98: (a) True-stress-strain curve and (b) strain distribution for a diffusion couple with different Mg concentration.

The effect of pre-deformation was studied by Dorin et al. [91]. A higher degree of pre-deformation accelerates precipitation kinetics and result in higher dislocation density. Consequently, shorter T_1 diameters are observed for a higher degree of pre-deformation. The strengthening contributions are dependent both on number density, but also on the precipitate diameter. Figure 1c in [91] shows hardness measurements for different degrees of pre-deformation after an artificial aging treatment. The difference in hardness values for pre-strain of 4 and 5 % is very little. It seems reasonable to assume that the deformed microstructure should be quite similar, and especially if natural aging times of only 5 minutes are present as it is the case for the samples analysed in the following by hardness and in-situ SAXS. Thus in the following, we will neglect the effect of minor solute content on the level of stretch experienced prior to artificial ageing.

The artificial aging procedure following the stretching operation was consistent with that of the individual alloys, namely it consisted of 3 days of natural ageing followed by a ramp heating 20 °C/h up to 155 °C and isothermal heat treatment at 155 °C for several days. Both in-situ SAXS and hardness measurement were performed to characterise precipitation and hardening kinetics. The following diffusion couples summarized in Table 10 were measured.

Table 10: Different diffusion couples investigated in the present work with their diffusing element.

Alloy 1	Alloy 2	Diffusion element
AlCuLi	AlCuLi Mg	Mg
AlCuLi 0.3Ag	AlCuLi 0.3AgMg	Mg
AlCuLi Mg	AlCuLi Mg0.3Ag	Ag

5.3. Diffusion of Mg

Differences in precipitation kinetics and hardness in Mg-free and Mg containing alloys were quite pronounced and consequently it is of interest to determine how much Mg is actually necessary to see the aforementioned effects in precipitation and hardening kinetics.

Figure 99 illustrates different SAXS images that were obtained during an in-situ heat treatment of a diffusion couple of quaternary AlCuLi0.3Ag in which Mg was the diffusing element. After 1.5 and 4 hours little differences in intensity are observed for the different alloy compositions. After 8 hours artificial aging the intensity has increased in all alloys. For the alloys containing 0.17 wt% Mg and 0.3 wt% Mg streaking is visible, whereas at 0wt% Mg only a slight isotropic intensity increase is observed. After 15 hours artificial aging all alloys have fully precipitated which is clearly seen by a much higher intensity contribution and pronounced streaking.

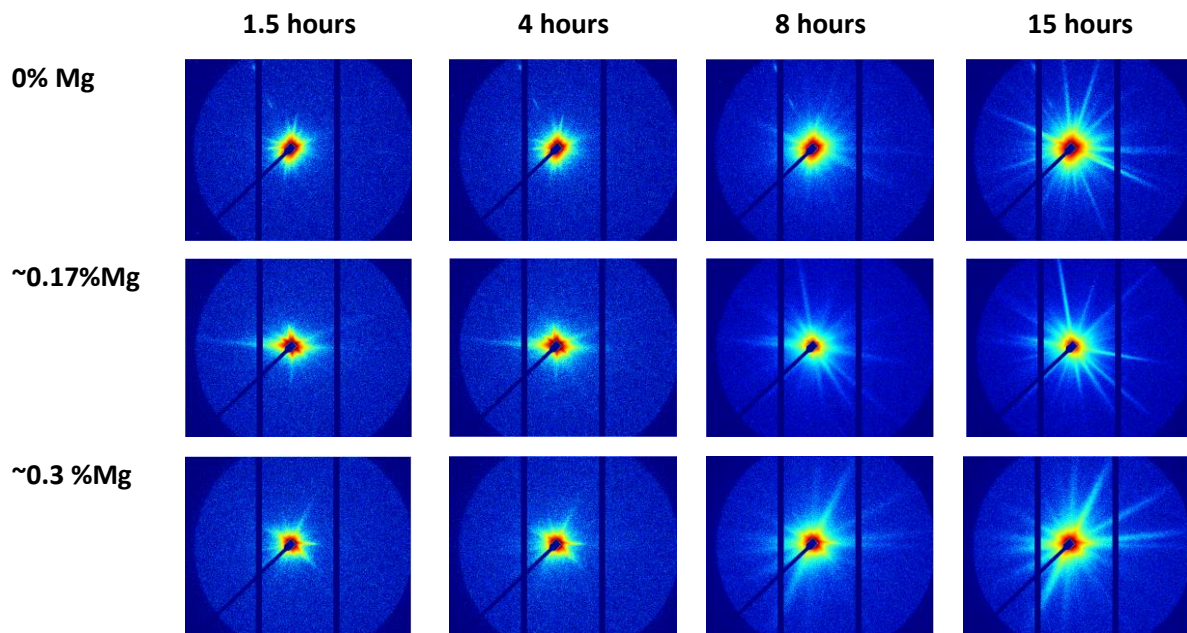


Figure 99: Overview of different SAXS images for different aging times and different Mg concentrations, obtained by performing artificial aging treatments for a diffusion couple.

In the diffusion couples, it was not possible to attribute unambiguously the observed streaks to specific precipitating phases such as was done on the individual alloys (see chapter 3.2). This was due to a less favourable crystallographic texture and grain distribution, caused by the specific thermo-mechanical processing conditions used to enlarge the diffusion couples. As a result, the SAXS data in the case of diffusion couple was systematically treated as isotropic data and no further discussion will be made on the images.

5.3.1. AlCuLi vs. AlCuLi Mg

In this section we present the results corresponding to the diffusion of Mg in AlCuLi, where Cu and Li concentrations are constant across the weld. Figure 100 shows the evolution of the Mg concentration after the different processing steps. These measurements reveal that after friction welding a step-like concentration gradient is present (light green). The heat treatment, performed at 515 °C for 14 days activates diffusion and the Mg gradient covers a width of 3 mm (dark green curve). Subsequently, hot rolling enlarges the concentration gradient to a width of 10 mm (orange curve). These results correspond to the diffusion couples presented in section 5.1.1 in Figure 95. Replotting these 3 curves in one graph shows quite clearly the evolution of the concentration gradient for the different processing steps.

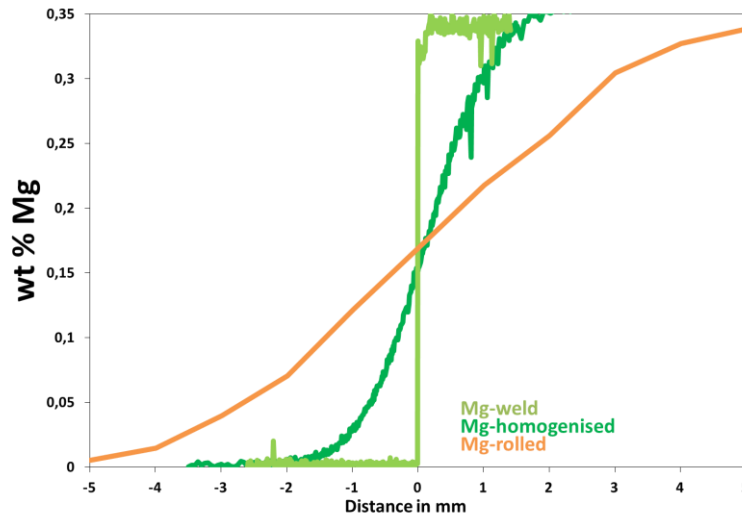


Figure 100: Evolution of the concentration gradient during the different processing steps for the joint between AlCuLi and AlCuLiMg.

Figure 101 illustrates hardness measurements as a function of Mg concentration for different aging times at 155°C. In the 'NA' condition which is illustrated in dark blue, a continuous hardness increase across the gradient is visible. The Mg-free side has an initial hardness of 80 HV and a continuous increase in hardness across the weld is observed until reaching an hardness of 100 HV in the natural aged condition for Mg containing alloys. This continuous increase in hardness is observed for all aging conditions. This presentation of the hardness measurements clearly reveal differences between Mg containing and Mg-free alloys, however it is difficult to interpret them with respect to hardening kinetics. Therefore, the hardness evolution for different Mg concentrations is plotted over aging times and illustrated in Figure 102a.

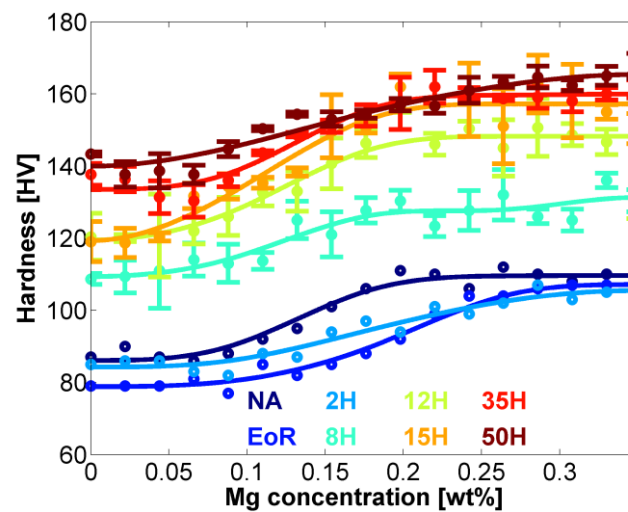


Figure 101: Hardness across the weld as a function of Mg concentration for different ageing times at 155°C for AlCuLi.

Figure 102a shows that little additions of Mg do not affect hardening kinetics to a great extent. Enhancement of hardening kinetics is observed, when at least 0.1 wt% Mg is added. Above this concentration, increased Mg concentrations do not seem to influence further hardening kinetics to a large extent, however slightly higher end hardness values are obtained for higher Mg concentrations.

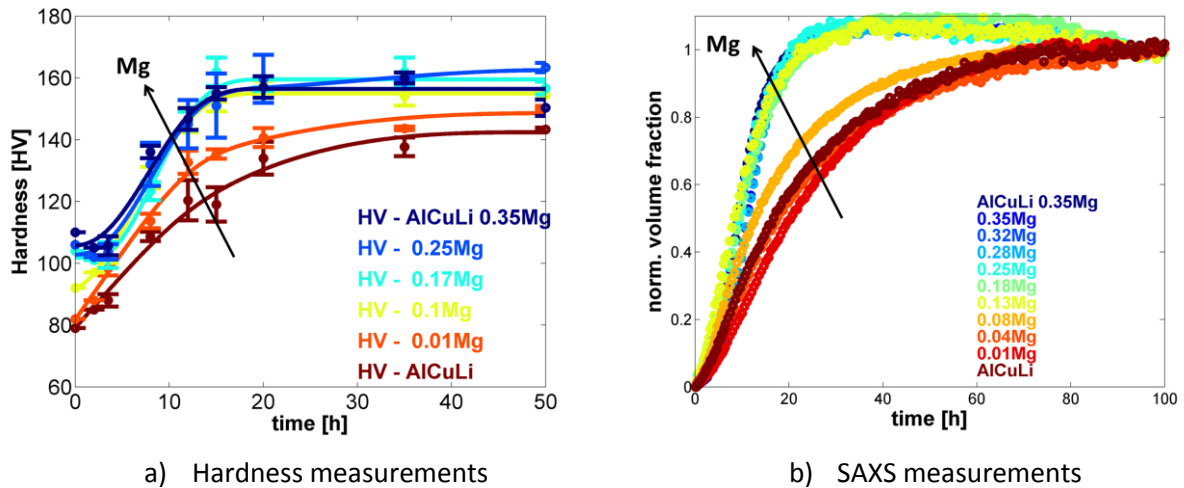


Figure 102: Hardening (a) and precipitation kinetics (b) measured for different Mg concentrations (in wt%).

In situ SAXS measurements were performed by combining space and time-resolved experiments on the diffusion gradients, in order to characterise precipitation kinetics dependent on the Mg concentration. Figure 102b shows the normalised precipitate volume fraction over the whole range of Mg concentrations. The data shows that precipitation kinetics is enhanced when at least 0.1 wt% Mg is added. Furthermore, the plateau in volume fraction, which indicates maximum precipitation, is reached for earlier aging times when the Mg concentration is above approximately 0.1 wt%. Above this threshold, similarly to the hardness evolution, little further modifications on the precipitation kinetics is observed.

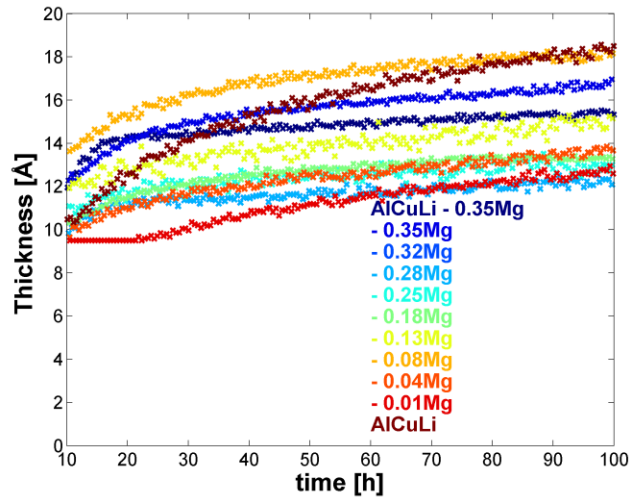


Figure 103: Evolution of T_1 thickness for different Mg concentrations

Figure 103 summarizes the evolution of precipitates thickness during aging time for different Mg concentrations. The thickness of some positions increases to quite an important extent. No explicit trend is observed distinguishing Mg-rich from Mg-lean alloys. As mentioned before, the average thickness comprises not only the contribution of T_1 precipitates, but also the thickness of other phases such as θ' precipitates. The SAXS signal is the sum of all contributions of all phases that scatter. In Mg containing alloys we assume that T_1 is the main precipitating phase, but for Mg-free alloys this is certainly not the case. A large quantity of θ' was observed in these alloys. This phase grows continuously and not discretely. Since the underlying model of data fitting assumes a discrete growth of precipitates, one should be careful with interpreting the data. In addition, the scattered intensity is quite sensitive to the local microstructure and texture components. Due to the aforementioned reasons, the thickness evolution for all diffusion couples will be presented for the sake of completeness, but will not be further discussed.

Hardness and SAXS measurements suggest a threshold value of Mg additions which lies around 0.1 wt% Mg, above which hardening and precipitation kinetics are enhanced. Consistently with this threshold value, only a small effect of Mg concentration is observed among values below, or above, this critical concentration, suggesting that the effect of Mg is related to a change of mechanism, which requires a certain Mg concentration, to be activated or the crossing of a solvus line.

5.3.2. AlCuLi0.3Ag vs. AlCuLi0.3Ag Mg

In industrial alloys a certain amount of Ag is usually present and therefore a diffusion couple of AlCuLi0.3Ag and AlCuLi0.3AgMg was produced. As in sec. 5.3.1 the effect of Mg is investigated. The evolution of the Mg gradient is illustrated in Figure 104. Similarly to Figure 100, a distinct Mg

interface was obtained after welding with a step-like concentration gradient, which extends to 3 mm after the diffusion heat treatment. Subsequent rolling enlarges the gradient to 10 mm.

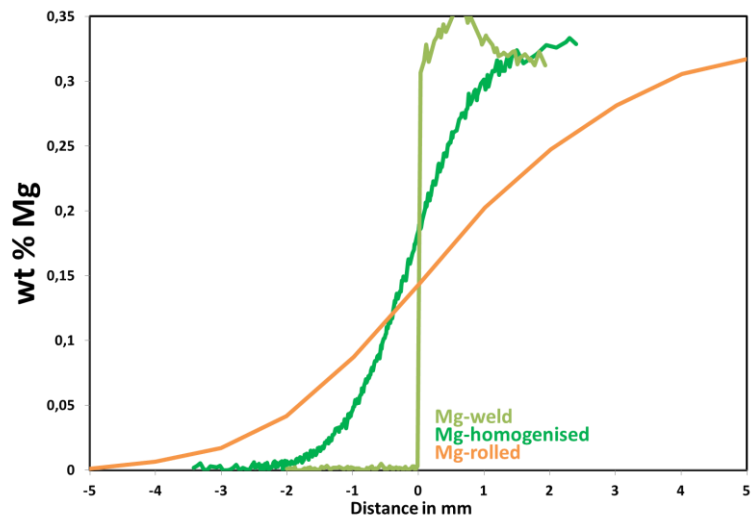


Figure 104: Evolution of the concentration gradient during for AlCuLi_{0.3}Ag and AlCuLi_{0.3}AgMg.

Hardness measurements versus Mg concentration are illustrated in Figure 105. Hardness increases with increasing Mg concentration. In the naturally aged condition, (blue curve) the initial hardness for no Mg addition is around 90 HV and increases to around 110 HV for the Mg containing side. The difference in hardness after natural aging lies around the same value of 20 HV as in section 5.3.1. The observed hardness differences stay around 20 HV during further aging. A maximum of this value is observed after 12 hours of artificial aging, when the Mg containing side approaches peak hardness, whereas the Mg-free part is still in an intermediate precipitation state. The hardness differences in this condition lie at around 40 HV. It is worth to note that compared to Figure 101 the hardness increases for lower Mg concentrations. This effect can most likely be traced back to the presence of Ag, which affects hardening kinetics in AlCuLi alloys as seen in chapter 3.1.

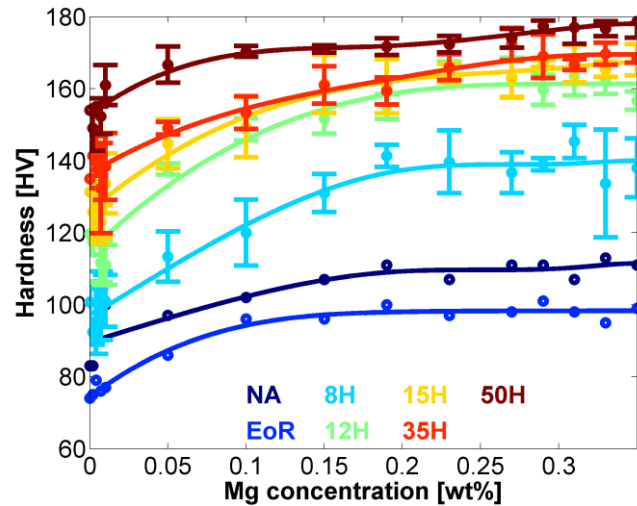


Figure 105: Hardness across the weld as a function of Mg concentration for different ageing times at 155°C with AlCuLi0.3Ag as base alloy.

In order to facilitate the determination of hardening kinetics, the hardness for different Mg concentrations are plotted versus artificial aging time and results are illustrated in Figure 106a. Hardening kinetics seems to alter with an increasing Mg concentration. It appears that there exists a threshold value for a certain Mg concentration at which precipitation kinetics are altered, similarly as observed in Figure 102a. However, this behaviour is less pronounced in the present couple. Even above 0.1 wt% Mg, the hardening kinetics continues to alter slightly with increasing Mg concentration. This effect can be associated to the presence of Ag atoms in the present couple. It needs to be pointed out, that different Mg additions influence the end hardness values to a significant extent and higher hardness values are obtained in the presence of 0.35 wt% Mg than for 0.1 wt% Mg. Precipitation kinetics obtained by simultaneous time and space-resolved SAXS measurements are illustrated in Figure 106b and exhibit a similar behaviour as precipitation kinetics observed in Figure 106a. It appears though that between 0 – 0.1 wt% Mg a continuous enhancement might be present. Again this could be attributed to the presence of Ag on precipitation in an Mg-lean alloy (see Chapter 3). However, above a threshold value of 0.1 wt% Mg, no additional increase in precipitation kinetics is observed, similarly to what was observed in section 5.3.1 .

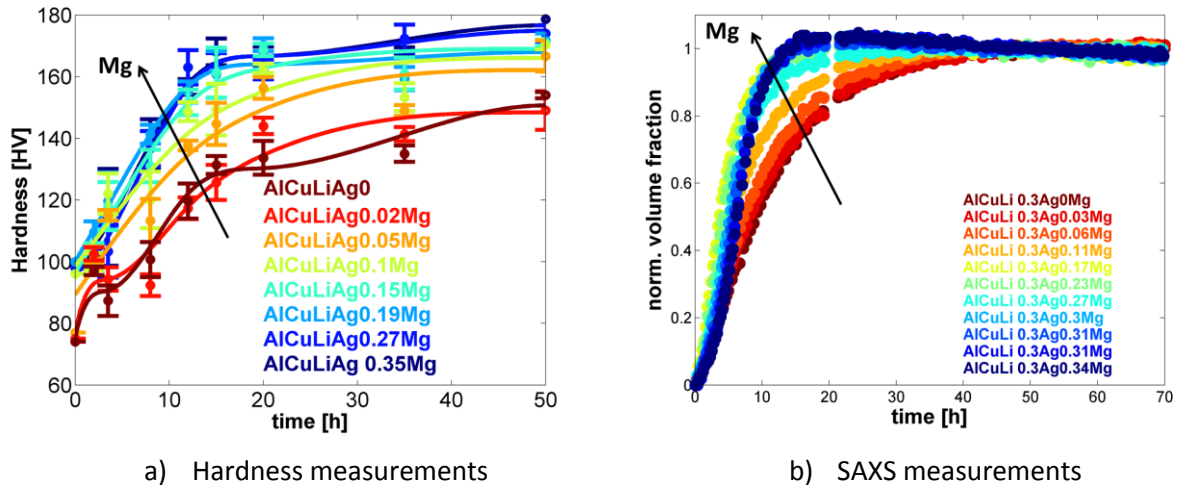


Figure 106: Hardening (a) and precipitation kinetics (b) measured for different Mg concentrations.

Figure 107 illustrates the thickness evolution over artificial aging. The data were obtained from the fit performed on SAXS measurements, but no significant effect could be observed.

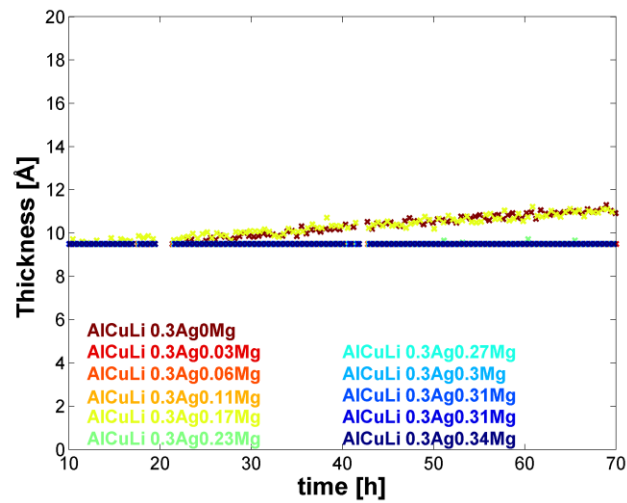


Figure 107: The effect of Mg on thickness evolution over aging time.

Both examples presented in the two sections above illustrate that Mg additions enhance both hardening and precipitation kinetics. These continuous measurements clearly reveal that a minimum concentration of Mg is necessary to observe these effects. This threshold values lies at around 0.1 wt% Mg and is slightly affected by other minor alloying elements such as Ag. Excess Mg concentrations above this threshold value do not alter precipitation or hardening kinetics. However, an effect on the end hardness is observed for increasing Mg concentrations.

5.4. Diffusion of Ag: AlCuLiMg vs. AlCuLiMg0.3Ag

From an industrial point of view, the effect of Ag is very important, since this element is quite costly and a lower addition would allow reducing material costs to a great extent. A diffusion couple of AlCuLiMg and AlCuLiMg0.3Ag was therefore produced to study the effect of Ag on T_1 precipitation.

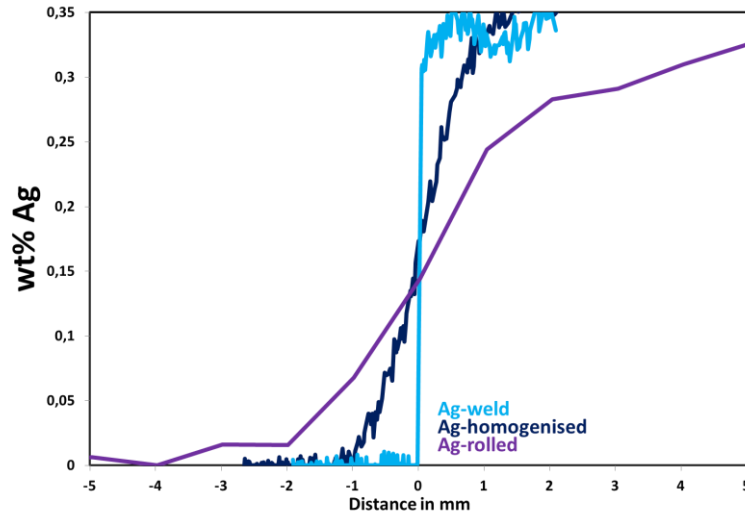


Figure 108: Evolution of the Ag concentration gradient during the processing steps for AlCuLiMg and AlCuLiMg0.3Ag.

Figure 108 illustrates the evolution of the concentration during the three processing steps. Similarly to the Mg gradient, a step-like concentration gradient is observed after welding which is enlarged to 3 mm after the diffusion heat treatment. Again rolling was applied in order to enlarge the gradient to a width of approximately 10 mm.

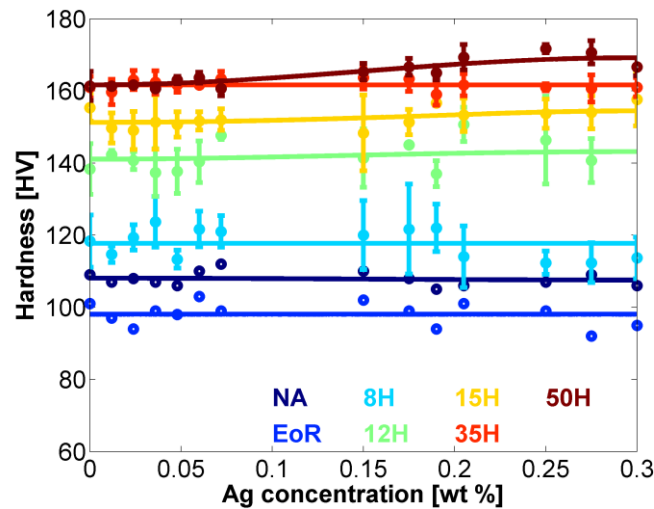


Figure 109: Hardness across the weld as a function of Ag concentration for different ageing times at 155°C with the AlCuLiMg as base alloys.

Figure 109 illustrates the hardness as a function of Ag concentration for different ageing times. It appears that for most ageing times hardness is constant and independent on Ag concentration. A significant increase in hardness is only observed after artificial aging for 50 hours for higher Ag concentrations. In order to study the effect on hardening kinetics five different Ag concentrations were picked and sketched over artificial aging time. The result is illustrated in Figure 110. It reveals that the kinetics is very similar, but end hardness has increased for the higher Ag concentrations.

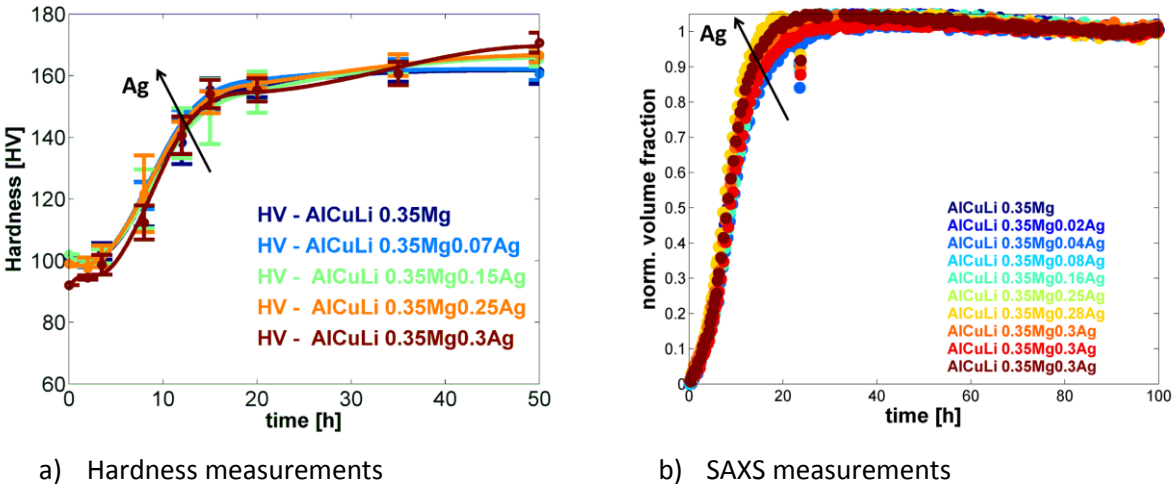


Figure 110: Hardening (a) and precipitation kinetics (b) measured for different Ag concentrations in the quaternary AlCuLiMg alloy.

Figure 110b, shows the result from simultaneous space and time-resolved SAXS measurements for different Ag concentrations present in the gradient. A slight increase in precipitation kinetics might be identified for increasing Ag additions. However, the overall results do not exhibit an as pronounced change in precipitation kinetics as observed for Mg.

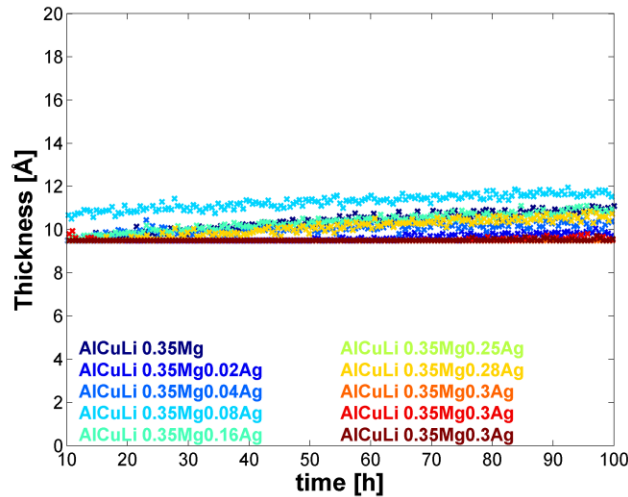


Figure 111: Influence on the thickness evolution for different Ag concentration in AlCuLiMg.

The evolution of the thickness is also sketched over aging time for different Ag concentrations in Figure 111. No clear effect on thickness could be observed.

Thus, in the presence of Mg, Ag is observed to play only a minor role during T_1 precipitation and no specific features could be identified with particular compositions in the composition range investigated.

5.5. Summary

The approach of diffusion couples allows characterising a continuous range of different Mg and Ag concentrations in AlCuLi alloys.

The effect of Mg concentration reveals threshold behaviour on precipitation and hardening kinetics, which would have been difficult to identify by a discontinuous approach using a discrete set of alloy compositions. The threshold value lies at around 0.1 wt% Mg and shows a significant enhancement of precipitation kinetics. Additional Mg affects end hardness, but does not alter precipitation or hardening kinetics.

The variations of Ag concentration exhibit only a weak effect on precipitation and hardening kinetics. A slight increase in end-hardness is observed for increased Ag additions.

Some of these results have been written as a journal paper, which can be found in Appendix II.

6. Discussion

In this section the former described results are put in relation with each other to elucidate, when possible, the effects of the addition of minor solute elements on the precipitation sequence, on the precipitation kinetics, and on the related strengthening of the Al-Cu-Li alloys under study. First, the effect of Mg will be discussed. Second, we will discuss the effect of adding Ag in the absence of Mg. Last, we will discuss the influence of the addition of Zn and/or Ag in the presence of Mg.

6.1. The effect of the addition of Mg on precipitation and strengthening

In the former chapters, we have evaluated the effect of the presence of Mg on the microstructure, precipitation kinetics and related hardening. Small angle X-ray scattering revealed that the precipitate volume fraction for Mg containing alloys increases faster during artificial ageing as compared to Mg-free alloys. Similar behaviour was observed for hardness measurements, where Mg containing alloys exhibit faster hardening kinetics and higher end hardness values. DSC measurements of naturally aged alloys showed that Mg-free alloys present a different precipitation sequence compared to Mg containing alloys. These observations were confirmed by TEM investigations. Differences in the microstructure were already observed for the 'EoR' and 'nucleation' condition. Mg containing alloys are characterised by the precipitation of Cu-Mg precursors on dislocations, whereas Mg-free alloys are characterised by the presence of GP zones progressively replaced by θ' , also at the dislocations. In the fully precipitated condition of Mg-free alloys a high number density of θ' and a low number density of T_1 precipitates is present, whereas the Mg containing alloys showed a high number density of T_1 and a low number density of θ' .

Parameters to be considered when comparing our results with existing literature

In Al-Cu-Li alloys several nucleation sites for precipitates are available. As observed by Itoh et al. [93] they are affected by the presence of minor alloying elements. Their study investigated undeformed material. The T_1 density was increased in the presence of Mg and (Mg and Ag). This was attributed to the existence of different types of nucleation sites depending on the presence of the solute additions, such as dislocations loops around Zr containing dispersoids, octahedral voids and GP zones, which act as heterogeneous nucleation sites. In the absence of Mg, only dislocation loops around Zr-bearing dispersoids were observed which greatly decreased the number density of T_1 [93]. Further nucleation sites were reviewed by Tsivoulas et al. [141]. Low-angle grain boundaries always serve as heterogeneous nucleation sites but should not be the main nucleation sites when other sites within the sub-grains can be activated. Precipitation on high angle grain boundaries of T_1 or other Cu and Li containing phases can also happen. However, it is still unclear if precipitation of T_1 on high-

angle boundaries occur or not [141]. When relating to the existing literature about the effect of Mg and Ag additions (the effect of Zn has not been investigated per se), it is important to keep in mind that in our case the alloys have been pre-stretched, providing a relatively high density of nucleation sites both for T_1 and phases from the Al-Cu precipitation sequence (particularly θ' within this sequence). As a consequence, our results are not directly comparable to those of studies of unstretched materials, and the conclusions drawn from these studies are not necessarily applicable to our situation. The other parameters that should be kept in mind when comparing results with the literature are the ageing temperature and the alloy composition. The ageing temperature has a prominent effect on nucleation. T_1 nucleation seems to occur readily when the material is aged at 200°C, even in the absence of dislocations. In our situation, the ageing temperature is relatively low to avoid the embrittlement of grain boundaries, and consequently the efficient nucleation of strengthening precipitates depends more critically on the presence of dislocations and minor solutes. The alloy composition may of course play a role in changing the precipitation sequence, phase nucleation and respective role of solutes. The Cu/Li ratio, the absolute content of these species, the amount of Mg and Ag, can all result in different phase transformation paths during ageing.

Effect of Mg on the early stages of precipitation

If we consider first Mg-free alloys, mostly GP zones were observed in the 'EoR' condition, which evolve to θ' precipitates in the 'nucleation' condition. They are still present in the 'stabilised' condition and are associated to dislocations. In addition, a few T_1 precipitates are present in the 'nucleation' condition, as well as in later precipitation stages, although they remain the minority phase in subsequent ageing conditions.

In the presence of Mg, we have shown that (Mg+Cu) containing phases form very early during artificial aging. In the so-called 'EoR' condition as well as in the 'nucleation' condition, precursors along dislocations are observed. A similar type of segregations was evidenced by means of atom probe tomography studies of an industrial AA2198 Al-Cu-Li alloy. The chemical species in these precursors could be identified and consist of Cu and Mg atoms. However, no structure could be resolved by this technique [102]. Our results confirm that these 'segregations' show from the 'EoR' condition on a defined structure, and that they are therefore precursors formed at dislocations.

Interestingly, although they evolve to what appears to be a mixture of S'/S and GPB zones (similar to the observations of [38]), they do not become much larger during artificial aging, suggesting that their growth may be impeded by a shortage of Mg atoms. In a Mg containing Al-Cu-Li alloy, Shih et al [142] observed similar lath-like precipitates on dislocations in a 'stabilised' condition at 150°C.

Although we have observed sporadically a few T_1 precipitates very early on in both Mg containing and Mg-free alloys, we do not believe that these T_1 precipitates have been nucleated in a similar way

as the majority of phases observed at later stages. Probably these precipitates are formed on very specific, low-density nucleation sites such as quench-induced octahedral voids. Therefore, in the following we will assume that in Mg containing alloys, the precursors present on the dislocations appear first in the precipitation sequence during artificial ageing.

This formation of precursors on dislocations can be attributed to the strong interaction between Mg and Cu on dislocations. Our results are consistent with the formation of phases belonging to the sequence leading to the S phase in the Al-Cu-Mg system, in which S' and S formation along dislocations is actually observed. In Al-2.5Cu-1.2Mg alloy the formation of S' phase was observed on dislocations during artificial aging, however no precursors similar to those observed here was identified prior to S phase precipitation [143]. Of course, at that time the precursors, given their small dimension, may have been overlooked. Feng et al. [144] observed S' formation on dislocation in Al-Cu-Mg alloys, which with continuing aging time evolve into S phases with different orientation relationships [144]. The formation of vacancy-Mg-Cu complexes which form on vacancy sinks, such as dislocations, were detected by Nagai et al. [145]. This was concluded by means of position annihilation spectroscopy (PAS) in combination with coincidence Doppler broadening (CDB). However, these experimental techniques give only information on vacancy interactions with the chemical species included in the clusters, and consequently no structural information is obtained. During further artificial aging, the presence of S phases on dislocations was observed [145].

Such a quick formation of precursors containing Mg and Cu during artificial ageing is actually consistent with the abundant literature on the so-called "rapid hardening" phenomenon in Al-Cu-Mg alloys. The rapid increase in hardness (of the order of minutes at 155°C) was first associated to GPB zone formation, however Ringer et al. [36] attributed this effect to Cu-Mg clustering interacting with dislocations. Reich et al. [35] could not resolve clustering in the matrix after very short aging times and their study also related the rapid hardening increase to Cu-Mg segregations on dislocations. Nagai et al [145] likewise attributed the rapid increase in hardness to the formation of Cu-Mg cluster which should preferentially precipitate on dislocations by using PAS and CDB-techniques. The rapid increase in hardness is dependent on the Cu/Mg ratio, as well as Cu and Mg concentrations. High Cu additions show only one hardening stage, whereas Cu/Mg ratios of around ~1 are characterised by two hardening stages [18]. The study of diffusion couples on the effect of rapid hardening by Marceau et al. [34] show that for a Cu content of 2 wt% (lower than that of our alloys), a hardening of 20 HV is obtained by the addition of approximately 0.3 wt% Mg, similarly to what we observe at the 'EoR' condition when we compare Mg containing and Mg-free alloys. Although there are significant differences between the two studies (different Cu amount, absence of Li and absence of pre-deformation in the study by Marceau et al.), this comparison confirms that the formation of Mg-

Cu precursors is the major microstructural modification happening in the early ageing stage in Mg containing alloys.

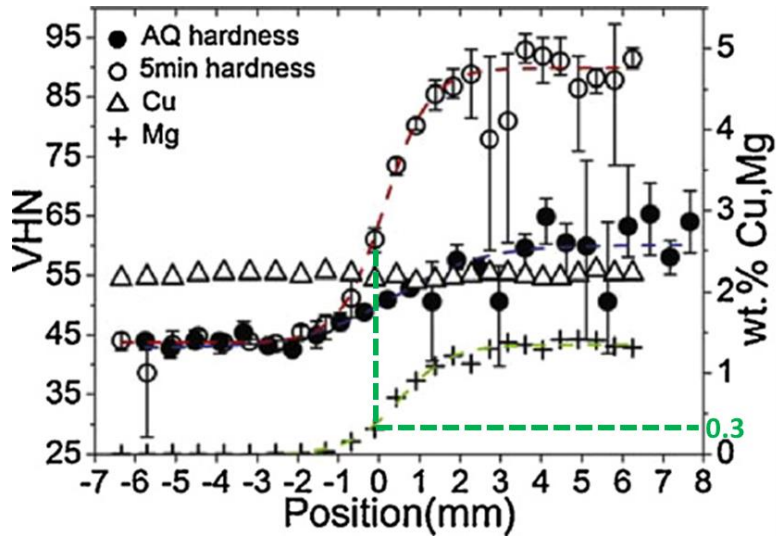


Figure 112: The effect of Mg concentration on rapid hardening in an AlCuMg alloy [34].

Now that we have established that the formation of the precursors on dislocations can be very fast and dominate the early stage microstructure, the question arises whether all dislocations can be covered with these precursor structures, and about the effect of Mg concentration on the presence of these phases, with respect to the addition of 0.3 wt% Mg. To answer this question, we performed some simplified calculations presented below.

In a first step, we need to estimate the dislocation density, which we obtain from the observed increase of tensile stress during stretching by reorganising Taylor's equation of dislocation strengthening. For the dislocation density ρ it follows:

$$\rho = \left(\frac{\Delta\sigma}{\bar{M} * \alpha * G * b} \right)^2 \quad \text{Equation 8}$$

where $\Delta\sigma$ is the increase in tensile stress during pre-deformation, approximately 100 MPa. \bar{M} is the Taylor factor equal to 3.1 for a random texture, α is approximated to 0.3, G is the shear modulus (27 GPa in aluminium) and b is the Burgers vector (2.86 Å in aluminium). The dislocation density ρ is then calculated to $2 \cdot 10^{14} \text{ m}^{-2}$, which is a reasonable value for dislocation densities in a moderately deformed material. We assume that the chemical composition of the precursors is similar to that of the S' phase (Al₂CuMg), namely the atomic concentration of Mg $X(Mg)$ is 0.25. For the total concentration of Mg associated to the dislocation X_{total}^{Mg} we calculate then:

$$X_{total}^{Mg} = \rho * \frac{\pi D^2}{4} * X(Mg) \quad \text{Equation 9}$$

where D is the diameter of segregation that covers the dislocation, which is estimated to be around 1 nm from TEM images. The resulting concentration of Mg necessary to account for the presence of the precursors on all dislocations is 0.004 at%. This value is much smaller than the addition of 0.3 wt% Mg (approximately 0.3 at%) of the studied alloys, and therefore their Mg content is sufficient to cover all dislocations by precursors with a composition similar to S' .

These calculations suggest that even a lower Mg concentration should be sufficient in order to form precursors on dislocations, and presumably have the same effect on subsequent precipitation kinetics and strengthening. The experiments conducted on the diffusion couples with a variation in Mg concentration (as presented in Chapter 5) revealed that a threshold value of 0.1 wt% Mg (which corresponds to 0.1 at% Mg) exists at which precipitation is enhanced, and below which the presence of Mg does not influence precipitation kinetics in the AlCuLi alloy. Besides, this threshold value still exists in the presence of other minor alloying elements such as silver. However, it is less pronounced most likely due to the effect of Ag on vacancy binding energy. Ag stimulates the formation of GP zones and reduced their number density [51]. The effect of Ag is mostly visible at Mg concentrations below 0.1 wt %. A reasonable hypothesis that can be formulated is that this threshold concentration is the critical Mg concentration necessary to form the precursors on all dislocations.

However, the total atomic concentration of Mg associated to precursors at dislocations calculated above (0.004 at%) is very low, compared to the threshold value obtained from the study of the diffusion couples. This discrepancy can have two origins. Either the formation of precursors in early ageing conditions is kinetically limited by volume diffusion of Mg and the observed threshold corresponds to the concentration necessary for gathering a sufficient amount of solute in a short diffusion time, either it corresponds to the solubility of Mg in the matrix, with respect to the precursors lying on the dislocation.

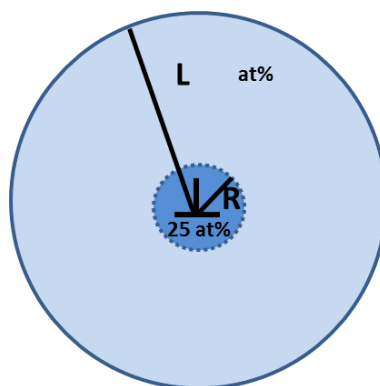


Figure 113: Sketch in order to identify the diffusion length necessary to cover all dislocations with precursors.

For testing the first hypothesis, we can calculate the average diffusion length of a Mg atom during the time leading to the 'End of ramp' condition. We assume again that the Mg concentration around the dislocation is 25 at%. Figure 113 sketches a dislocation, surrounded by a Mg concentration of 25 at% with a diameter of 1nm. L is the diffusion length of Mg that we want to determine. The diffusion coefficient between 100 and 155°C has been determined in temperature intervals of 5 °C and the corresponding diffusion distance has been calculated as follows:

$$L = 2 \sqrt{(D_{376 K} * \Delta t + D_{381 K} * \Delta t + D_{386 K} * \Delta t \dots D_{426 K} * \Delta t)} \quad \text{Equation 10}$$

Δt is equal to 900 seconds since the Diffusion coefficient was calculated in 5 °C step (heating ramp is 20°C/h). For calculation of the diffusion coefficient for different temperatures the Arrhenius equation $D = D_0 e^{-\Delta Q/RT}$ is used, in which D_0 is a pre-exponential factor and equal to $1 \cdot 10^6 \text{m}^2 \text{s}^{-1}$ and the activation energy ΔQ is equal to $110.9 \text{kJ mole}^{-1}$ [146]. The total diffusion length for this temperature and time interval results in $L = 23 \text{nm}$. It means that within a distance of the order of 23 nm, Mg atoms are able to diffuse to the dislocation during the ramp heating. The newly calculated minimum Mg concentration to cover all dislocations by precursors is then 0.012 at %. This value is lower by a factor of 10 than the observed threshold value in the diffusion couples and the diffusion length might therefore not be the limiting factor during the formation of precursors.

The second consideration for the observed 0.1 at% Mg threshold is attributed to an effect of Mg solubility with respect to the precursors. Namely, the formation of the precursors is possible only if the (metastable) solvus boundary at the ageing temperature of 155°C is reached. Thus, for the Cu content of 3.5 wt%, as it is the case in the studied alloys, the Mg solubility would be close to 0.1% (some supersaturation would be still necessary to nucleate the precursors, even if this nucleation is easy on dislocations). Once this solvus boundary is crossed, the additional amount of Mg necessary to cover all dislocations is very small as shown by the above calculations. Thus, a threshold behaviour for the addition of Mg is expected as observed experimentally. If 0.3 wt % Mg is present in the alloy, there is still a supersaturation present in the matrix after covering all dislocations. They might support T_1 precipitation, since T_1 shows Mg incorporation or S' phase might form homogeneously. The work of Marceau et al. shown above does not show a threshold behaviour as a function of Mg content, but a progressive hardening effect as a function of Mg concentration. However this work was performed on an undeformed material, where nucleation of the Mg-Cu clusters happens in the matrix.

At this point, we have evidenced that the early precipitate structure at the dislocations is fundamentally different in the alloys depending on the presence of Mg. Now we need to understand how these two early microstructures evolve to the subsequent ageing conditions.

The effect of Mg on precipitation path and kinetics

The observed influence of Mg on precipitation during the main precipitation stage is two-fold:

- Depending on the presence of Mg the proportion of the main precipitating phases is completely different, namely mainly T_1 in the presence of Mg, and mainly θ' in the absence of Mg.
- In the presence of Mg, the overall precipitation kinetics is observed to be much faster.

These two observations can have a common origin, or could result from different effects. We will now discuss the different phenomena that could explain them.

The first observations can be discussed in the light of the early stage microstructure described in the former section. In the absence of Mg, Cu containing GP zones are observed very early on the dislocations ('EoR' condition). In the 'nucleation' condition, corresponding to the time when the first precipitates are detected by macroscopic methods (SAXS), these GP zones have already evolved to θ' , which are inclined to follow the shape of the curved dislocations. Later on in the 'stabilised' condition the microstructure is dominated by these precipitates. T_1 precipitates are also observed, however in low quantities, and seem to be also related to the dislocations, since we observed one of these precipitates seemingly in contact with a dislocation in the 'nucleation' condition of the ternary AlCuLi alloy. The low density of T_1 precipitates in the Mg-free alloy with respect to the θ' phase seems therefore related to a kinetic competition between the formations of these two phases on the dislocations. The formation of T_1 on a dislocation exempt from precursors requires the dissociation of this dislocation, which in aluminium is difficult because of the low stacking fault energy. Consequently, it is kinetically unfavourable compared to θ' phase formation, which evolves from the pre-existing GP zones.

When Mg is present, we have made the hypothesis that the dislocations are completely covered with Mg-Cu precursors. It is not expected that θ' precipitates can form readily on Mg-Cu precipitates. In the ternary system Al-Cu-Mg the two phases may be kinetically competing in different locations, but should not appear in contact with each other. The rapid hardening phenomenon is closely associated to the presence of Mg and therefore it is expected that the first phase to form on the dislocation will be that containing Mg, which then prevents the formation of θ' . If the formation of θ' is suppressed, and the further growth of Mg containing phases is made difficult by the shortage of Mg, it follows that the nucleation of T_1 should be favoured. Since it is observed to happen quickly and with a high

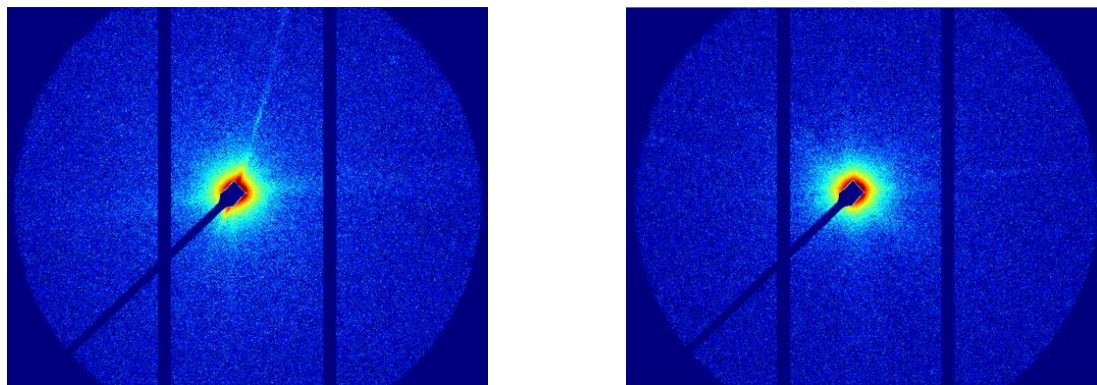
number density, one can conclude that the S' -type precursors on a dislocation have a structure which directly helps the formation of T_1 nuclei. At this stage it is not possible to explain the mechanism of this assisted nucleation, this scenario does not require the effect of Mg (and Ag) on the stacking fault energy of dislocations that has been invoked in the literature [99], [147], [148]. The remaining θ' precipitates observed in the final microstructure of the Mg containing alloys could originate from the few GPII zones observed at the dislocations, or from a homogeneous nucleation of this phase.

Now we can discuss the difference in overall precipitation kinetics observed depending on the presence of Mg. In the presence of Mg, T_1 (together with the limited number of θ') precipitates faster than the combined structure of T_1 and θ' in the absence of Mg, as observed by comparing the DSC peaks for Mg containing and Mg-free alloys (see chapter 3 (Precipitation kinetics)). The precipitation peaks associated with T_1 formation in Mg containing alloys appear at lower temperature than the broad precipitation peak related to combined θ' and T_1 precipitation in AlCuLi. Both phases, precipitating at the same time compete for the same limiting solute (Cu).

This difference in precipitation kinetics is at first sight counter-intuitive, since in both microstructures one finds the same precipitates (although in different proportions), namely θ' and T_1 , and their observed sizes are comparable.

A possible explanation may be the difference in number density of precipitates. A system with a higher density of nuclei will precipitate faster because the diffusion distance to be covered by solutes during the growth process is smaller. We performed measurements of the surface fraction of T_1 precipitates by TEM. Without knowing the thickness of the TEM foil, the calculation of the number density could not be conducted. The influence of the foil thickness is not trivial; however, we assume that the surface fraction gives a sufficiently good indication of the materials microstructure. The surface fraction for T_1 precipitates in Mg containing alloys is approximately twice that of Mg-free alloys. However the latter also contain a high density of θ' and the final size of T_1 precipitates is similar in both alloy families, which indicates that the overall density of particles is of the same order. Thus there is no indication that the two alloy families present a very large difference in total precipitate number density, which would explain the accelerated precipitation kinetics in the presence of Mg.

A second possible explanation is that the kinetics is faster in Mg containing alloys because the phase nucleates earlier. The condition 'nucleation' was defined as the condition at which first streaks appear in SAXS measurements. Interestingly, for both Mg containing and Mg-free alloys the 'nucleation' condition was found after 1.5 hours at 155°C, as illustrated in Figure 114a and b respectively.



a) AlCuLiMg0.3Ag

b) AlCuLi

Figure 114: 'nucleation' condition of Mg containing (a) and Mg-free (b) alloys.

This confirms the microscopic observations, that in the 'nucleation' condition a high number density of precipitates are present both in Mg containing and Mg-free alloys, even though they are not of the same type in majority. This rules out an effect of the nucleation time.

Another explanation of the difference in kinetics could be that the growth rate of T_1 and θ' precipitates are different. Then, when the microstructure is dominated by T_1 the overall kinetics would be faster, and when it is dominated by θ' it would be slower. One could argue that the interface structure of the T_1 phase with the matrix on the habit plane has almost no misfit strain, so that the growth of this phase can be rapid as compared to the θ' phase, which in addition requires the formation of an ordered Al_3Li phase at its interface with the matrix together with its growth. However this interpretation also leads to some inconsistencies. Namely, the T_1 precipitates observed in the Mg-free alloy should then be much larger than in the Mg containing alloy, because of their lower number density and their longer ageing time as compared to the Mg containing alloys. The only explanation that could reconcile our observations with this interpretation is that most of the T_1 observed in the Mg-free alloy appear subsequently to the θ' precipitates, because they nucleate at higher activation energy sites, so that their growth is impeded by the existing θ' , both in terms of available solute (soft impingement) and by hard geometrical impingement. This is compatible with the facts that in the 'nucleation' condition a well-developed θ' microstructure can be observed in the Mg-free alloy. Then, if this interpretation is correct, the overall observed kinetics (by non-isothermal DSC or by SAXS) would be controlled by the majority phase, whereas the minority phase grows at its pace and takes the remaining volume available in the microstructure, which is plenty in the case of platelet precipitates.

A last mechanism that we can consider is related to the influence of minor additions on the lengthening rate of precipitating phases. As observed before, the T_1 precipitate is only one unit cell

thick when aging at 155 °C. The T_1 thickness is very stable at this aging temperature, even for very long aging times [116]. Since T_1 precipitation is possible in both Mg containing and Mg-free alloys, an effect on the kinetics could be the difference in growth rate of the T_1 diameter. The presence of Mg on the T_1 interfaces and its incorporation inside the precipitates may affect the interfacial energy and hence influence the lengthening rate.

To summarise, we have evidences that the presence or absence of the Mg containing precursors is the major factor that explains the difference in precipitation path, namely the competition between T_1 and θ' , in between the Mg containing and Mg-free alloys. The situation is less clear for the difference in overall kinetics. We have reviewed several possible effects, however we cannot affirm that one effect is responsible alone for the observed difference in kinetics. Most likely a combination of effects must be taken into account: the presence of Mg promotes a moderately higher number density of precipitates earlier in the ageing process, T_1 grows somewhat faster than θ' but nucleates after this phase in Mg-free alloys, and possibly the presence of Mg accelerates the growth rate of T_1 .

Effect on hardness

The hardness increase correlated well with the increase in precipitate volume fraction as it has been determined by SAXS measurements. In the as-quenched condition the hardness for all alloys is very similar, but after pre-deformation and even more visibly after 3 days of natural aging, the hardness of Mg containing alloys increases to higher values. The difference in hardness can be attributed to the formation of precursors on dislocations in Mg containing alloys. As discussed above, Cu-Mg-vacancy co-clustering has been observed in Al-Cu-Mg alloys and is associated to the rapid hardening phenomenon [35], [36]. The hardness difference between Mg containing and Mg-free alloys remain constant even during the ramp heating, after which hardness values have slightly decreased compared to the naturally aged condition. The nearly constant hardness differences of Mg containing and Mg-free alloys can be attributed to the Cu-Mg containing precursors, which are present in the microstructure throughout the precipitation sequence.

During further aging, the hardness starts to increase at similar aging times, which is attributed to precipitation of T_1 and T_1 and θ' in Mg containing and Mg-free alloys, respectively. The increase in hardening kinetics is in very good agreement with precipitation kinetics obtained by SAXS measurements. Hardness increases from the onset of nucleation and longer artificial aging times are necessary for Mg-free alloys in order to achieve maximum hardness, corresponding to the observed slower precipitation kinetics.

The hardness contributions for θ' , T_1 and precursors are certainly different. T_1 strengthens due to a shearing mechanism [91], [149], and it has been shown that in order to achieve a high strength with T_1 precipitates it was desirable to achieve a large T_1 diameter while retaining the 1 unit cell thickness

[91]. θ' on the other hand, is much more difficult to shear, due to its incoherent interphase and is mostly bypassed. Consequently, better hardening contributions are obtained for finely dispersed θ' . The comparison between the strengthening potential from a microstructure dominated by T_1 precipitates (in the Mg containing alloy) and from a microstructure dominated by θ' (in the Mg-free alloys) is however no easy task, because it involves many factors: a different equilibrium volume fraction (Cu being the limiting solute, Al_2CuLi provides a higher volume fraction than Al_2Cu), a different strengthening mechanism, different habit planes ($\{100\}$ is intrinsically more effective as compared to $\{111\}$ [150]), different geometric characteristics. Actually it has been shown that to a certain extent a similar strength could be achieved by both types of particles [23]. In addition, when Mg-free alloys achieve highest hardness after 50 hours the differences to Mg containing alloys is still around 20 HV, the same as after natural aging. The S' phase and GPB zones still present at this stage must contribute to the strength, and thus it cannot be ruled out that the difference in peak strength between the two alloy families is mainly controlled by the presence of these phases. Therefore, the fact that we observe a higher peak strength when T_1 dominates the microstructure is consistent with the usually accepted fact that this phase is the most potent strengthener for AlCuLi alloys, but it is no easy task to demonstrate by what mechanism this effect can be rationalised.

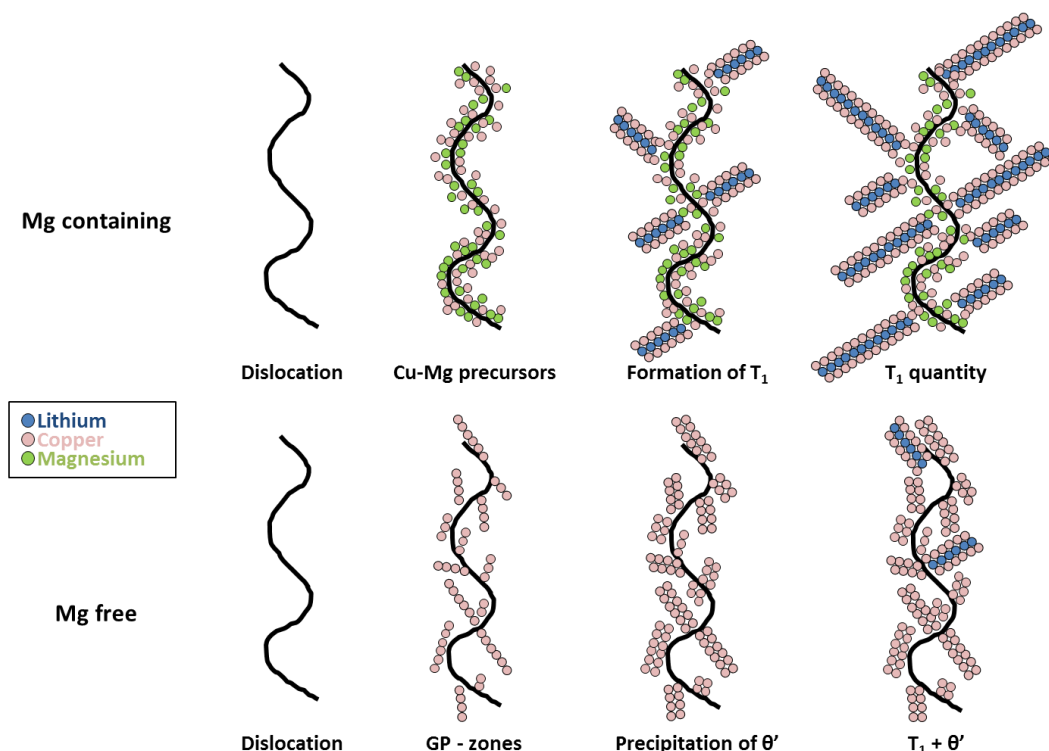


Figure 115: Simplified sketch to summarize the main differences in Mg containing and Mg-free alloys.

Figure 115 illustrates the main differences in precipitation for Mg containing and Mg-free alloys. In both families of alloys dislocations are present after pre-deformation. The microstructure in early aging stages differs quite a lot, exhibiting Cu-Mg containing precursors in Mg containing alloys and GP zones in Mg-free alloys. Subsequent artificial aging leads to the formation of mainly T_1 in Mg containing alloys and θ' phases in Mg-free alloys, respectively. The final microstructure is dominated by T_1 in high number density in Mg containing alloys and a mixture of θ' and T_1 in Mg-free alloys.

6.2. The effect of Ag and Zn on precipitation and strengthening

6.2.1. Influence of Ag addition in the Mg-free alloy

The addition of Ag to AlCuLi exhibits only a small effect in isothermal conditions at 155°C on hardness and precipitation kinetics obtained by SAXS measurements. However a much larger effect is observed by DSC curve in non-isothermal conditions: although AlCuLi and AlCuLi0.3Ag show a similar shape of the precipitation peak, which indicates the presence of similar phases, the addition of 0.3Ag shifts the peak to lower temperatures, which is associated to enhanced precipitation kinetics. This effect was not directly observed during isothermal heat treatment, although the microstructure observations show a higher amount of T_1 phase in the Ag containing alloy as compared to the Ag-free alloy. The difference between isothermal and non-isothermal experiments means that the effect of Ag is temperature dependent. Increased hardness values due to Ag addition to AlCuLi alloys were identified by Zheng et al. [98]. Huang et al. [99] showed that in the presence of Ag in AlCuLi, the GP zone formation was suppressed and consequently the θ' precipitate density was lower. However, this effect was cancelled when pre-deformation is introduced prior to artificial aging [98], which might explain similar hardness values for AlCuLi and AlCuLi0.3Ag in the present study.

TEM analysis of the microstructure of a fully precipitated condition reveals a higher surface fraction of T_1 in the presence of Ag compared to pure AlCuLi. The addition of Ag to aluminium alloys lowers the stacking fault energy [14] and its presence might facilitate the dissociation of dislocations and result in an increased number density of T_1 precipitates in the case where Mg containing precursors are not available to assist T_1 nucleation. This effect can be combined with an influence of Ag on limiting the precipitation of θ' , since it is known that Ag traps vacancies and thereby reduces the formation of GP zones in AlCuLi [51]. This would result in more controlled θ' precipitation, but could also stimulate the precipitation of Ω in addition to T_1 . Yet, this alloy was not investigated by atomic resolution microscopy. However, since no Ω phase was detected in the Mg & Ag containing alloy, it seems unlikely that it forms in the AlCuLi-Ag alloy.

In summary, the influence of Ag on precipitation in AlCuLi is to favour the T_1 phase in competition with the θ' phase. Although this does not result in measurable changes of precipitation and strengthening kinetics at 155°C, this effect is observed to be temperature dependent and more effective at the higher temperatures probed by DSC scanning. This effect may be related to the influence of Ag on the stacking fault energy of aluminium and its role on T_1 nucleation in Mg-free alloys, or to the effect of Ag on limiting the nucleation of θ' , or to a combination of both effects.

6.2.2. Influence of the addition of Zn and Ag in the presence of Mg

Effect on the microstructure

The addition of Zn and Ag to Mg containing alloys does not change qualitatively the microstructure or precipitation sequence. T_1 precipitates with constant thickness of one unit cell in average. T_1 remains the main precipitating phase for all alloys due to the presence of Mg. Precursors associated to dislocations are consistently observed. Heterogeneous nucleation of T_1 on dislocations is assumed to be the dominant nucleation mechanism. This mechanism is different to a continuous nucleation mechanism via GP zones as observed for Ω precipitation [52]. No GP zones on (111) planes were observed, and we did not observe either the presence of T_1 precursors such as claimed by Gao et al. [151]. Instead, we observed only fully precipitated T_1 precipitates even in the earliest stages, which exhibit a contrast of the overlapping aluminium matrix if the precipitate is small.

The segregation of Ag atoms to the T_1 /matrix interface is visible in HAADF images due to higher atomic number of Ag compared to other elements present in the matrix, such as Al, Cu, Li and Mg. A recent study [152] reveals the presence of Ag atoms randomly segregated to the interface layer between T_1 and the aluminium matrix. This study claims however, that Ag is only incorporated into T_1 after long aging times [152]. Our observations contradict this latter statement, since we observed Ag segregations to the T_1 interphase for all aging conditions, even the earliest ones. However, our observations and those in [152] are in good agreement with APT observations made by Araullo et al. [102]. They revealed that Ag segregates to the T_1 interface during all aging conditions. The Ag concentration of the matrix decreases with continuous aging time and reaches a constant level when reaching the fully precipitated condition [102]. APT experiments carried out at higher aging temperature by Gault et al [96] showed that the matrix concentration of Ag increases after having passed a minimum and concluded that Ag is rejected into the matrix during thickening. It is attributed to a catalytic effect for T_1 precipitation in the presence of Ag. Ag may play a role during nucleation, but might be less important during further growth [96]. Calculating an Ag concentration

on the precipitate/matrix interface is difficult because the thickness of the sample is missing. Therefore it cannot precisely be determined how many Ag-atoms per column are present.

In order to distinguish the position of Zn atoms, EDX measurement were conducted. For single layered T_1 precipitates it is difficult to clearly identify its position. It reveals for thicker precipitates that Zn substitute to the Cu-rich positions in the T_1 phase. Comparable observations were made in Cu containing Al-Zn-Mg alloys [85]. The main precipitating phase η' precipitates, which habit plane is $\{111\}$ like that of T_1 precipitates. Similarities between the T_1 and the η' interface layers with the matrix can be made in terms of atomic positions.

Effect on kinetics

The effect on precipitation kinetics for different additions of Ag, Zn or (Ag and Zn) is relatively small. An enhancement of precipitation kinetics is identified compared to pure AlCuLiMg, however much smaller than the modification brought by adding Mg to AlCuLi. Similarly to the effect of an addition of Ag to AlCuLi seen above, a stronger influence is observed in non-isothermal conditions by DSC as compared to isothermal ageing, indicating a temperature-dependent influence of the effect of Ag and Zn.

Ag segregations are observed in early aging conditions, namely in the 'EoR' and in 'nucleation' condition. No EDX measurements on T_1 precipitates in the Zn containing alloys could be performed for early aging times, but we assume that Zn segregations are probably also present, similar to Ag segregation. Both elements probably lower the nucleation energy. Consequently, the formation energy for T_1 is lowered and nucleation facilitated which supports nucleation and promotes faster kinetics. Ag being located specifically at the interface may have a larger effect on the interfacial energy, whereas Zn, which seems to substitute more generally to Cu, may influence more the volume free energy. In addition, by substituting to Cu in T_1 , a part of the effect of Zn may be simply related to increasing the alloy supersaturation (total amount of solute).

Effect on hardness

Ag and Zn additions result in slightly higher hardness values and enhanced hardening kinetics compared to AlCuLiMg. These effects are very subtle but however significant. After natural aging and ramp heating, no differences in hardness are observed and the effect of Zn and Ag on hardening kinetics is observed only during subsequent artificial aging.

The additional strengthening observed when Ag and Zn are added can be related to a higher volume fraction of induced precipitation, or to a higher strengthening efficiency of a same precipitate volume fraction. Both effects could of course also combine.

We determined the volume fraction of Mg containing alloys in the 'stabilised' condition by DSC measurements. We related the measured enthalpy to the volume fraction of T_1 precipitates using the assumption that in the presence of Mg, T_1 is the main precipitating phase, and using the relationship between normalised enthalpy and volume fraction established by Dorin et al. [116]. Differences in volume fractions between the present study and [116] are discussed in section 3.4.1. Once the volume fraction is calibrated in the 'stabilised' condition for each alloy, the volume fractions for other ageing times are available by the in-situ SAXS experiments. We can then relate the hardness of different aging times with the corresponding volume fraction. The results are presented in Figure 116 and Figure 117. The calibrated volume fraction is sketched versus hardness for a time period that includes the 'EoR' condition up to 50 hours artificial aging at 155 °C. In both figures a linear relationship between hardness and strengthening is observed, similarly to that observed by Dorin et al. [116] and expected by his strengthening model when the T_1 thickness remains that of one unit cell. Within experimental uncertainty, it is not possible to discriminate between the different slopes as function of addition of Ag, Zn or the combination of both. These results therefore rule out that the observed higher strength is not due to an increased strengthening efficiency of the T_1 precipitates in the presence of Ag and/or Zn. Instead, the higher hardness in these latter alloys is due to a higher overall precipitate volume fraction as confirmed by the DSC measurements.

As shown by Dorin [116] on a similar alloy, the volume fraction obtained in the 'stabilised' condition at 155°C is quite far from the equilibrium value, so that differences in volume fraction in such ageing conditions do not have to be related to changes of equilibrium volume fraction (which is probably only possible for Zn, see above), but can also be due to changes in the efficiency of accessing the solute during the precipitation process, particularly by promoting a more efficient nucleation.

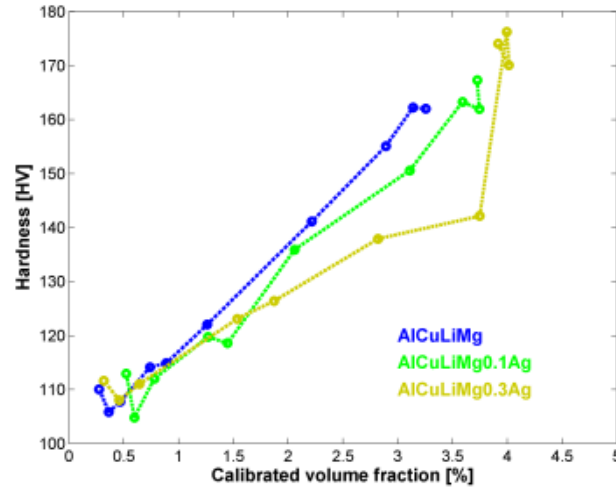


Figure 116: Relation between calibrated volume fraction and Hardness; Influence of Mg and Ag.

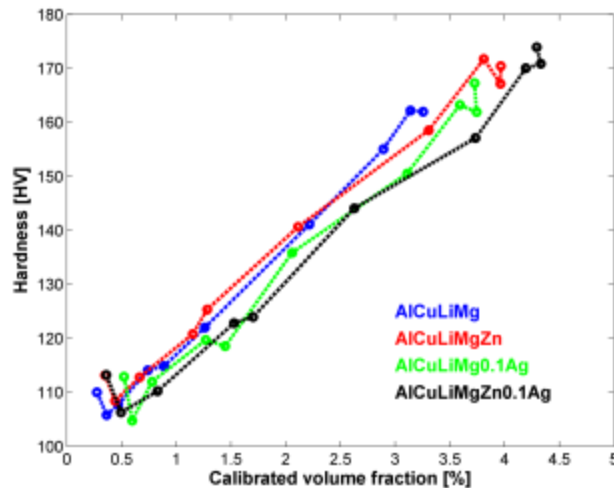


Figure 117: Relation between calibrated volume fraction and Hardness; Influence of Zn and Ag.

The precipitate volume fraction depends on the precipitate characteristics as follows:

$$f_V \propto \frac{N_V \pi t D^2}{4} \quad \text{Equation 11}$$

For the present heat treatment it is reasonable to assume constant thickness for the precipitates. An increased precipitate volume fraction is consequently influenced by two factors: an increase in number density of precipitates or an increase in the precipitate diameter. Increased number density is possible if the nucleation rate is enhanced, which could be related to the effect of Ag and Zn on the interface or volume free energy of the T_1 phase as discussed above, but could not be confirmed by

our TEM observations due to the uncertainties of sample thickness for the conventional dark field observations.

As seen in Equation 11, the influence of the diameter on the volume fraction is quite important. The measured diameters in the present study showed variations between 45 to 60 nm between alloys, but no clear trend could be observed with respect to minor alloying elements. Probably the variability of diameters in the microstructures is quite high and we could not determine their values with high enough precision. In conclusion, we claim that the volume fraction of T_1 precipitates increases with increasing concentration of minor alloying elements and highest hardness and volume fractions of T_1 were found in AlCuLiMg0.3Ag and AlCuLiMg0.1AgZn. It is likely that the minor solute elements provide a more efficient nucleation of the T_1 phase and thus helps reaching a higher volume fraction.

The measurement of a diffusion couple in which the Ag concentrations varied from 0 to 0.3 wt% reveal that the precipitation kinetics measured by SAXS were barely affected. Similar observations were made for initial hardening kinetics. However, a continuous increase in the end hardness is observed after 50 hours aging. The maximum hardness differences between the position without any Ag additions and maximum Ag concentration was 10 HV. This hardness difference is compatible with a change in maximum volume fraction.

In summary, the effect of Ag, Zn and combined (Ag and Zn) affects the volume fraction of T_1 precipitates, which is the main precipitating phase due to the presence of Mg. The increase of volume fraction can be directly related to an increase in hardness. Ag and Zn were found to segregate to the T_1 interphase and Zn was incorporated into the T_1 structure. We suggest that changes in 'nucleation' conditions due the presence of Ag and Zn cause the observed change in T_1 volume fraction.

Effect of Ag and Zn on thermal stability

The presence of Ag segregations at the interface of T_1 precipitates was observed over the whole aging range and is supposed to exist as well for precipitates in alloys with Zn addition, which were observed only in the 'stabilised' condition. The change of the local chemistry might influence the behaviour for longer aging times or aging at higher temperatures. Segregations could for example influence the thermal stability of T_1 precipitates with respect to precipitate thickening. To evaluate this possibility, we performed isothermal experiments at elevated temperature where precipitation thickening is expected. For the experimental setup we chose to start with a 'stabilised' condition which was obtained after 15 hours at 155 °C for all Mg containing alloys. The stabilised alloys were then subjected to an additional heat treatment at 190 °C for 70 hours. The measurement of the thickening kinetics was performed in-situ using SAXS measurements. The results are present in Figure

118. A logarithmic plot of the logarithmic thickness increase (with respect to initial thickness for each alloy) vs. ageing time reveals that the slopes and thereby the thickening exponents are very similar. This suggests that Ag and Zn segregations do not affect thickening kinetics and their contribution is mostly in increased strength and hardening response.

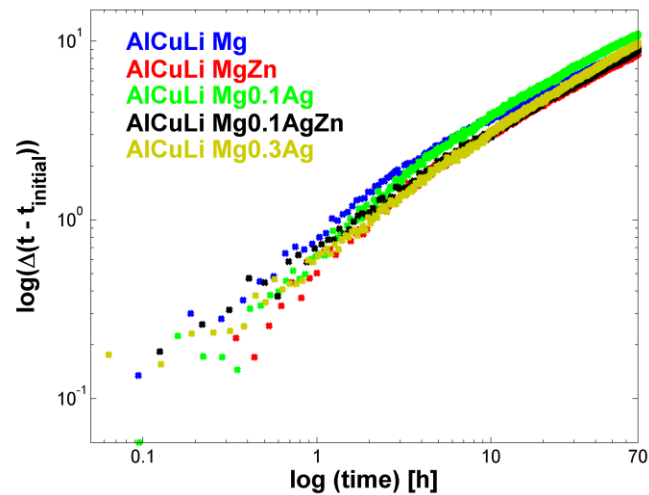


Figure 118: Thickness increase versus ageing time at 190 °C.

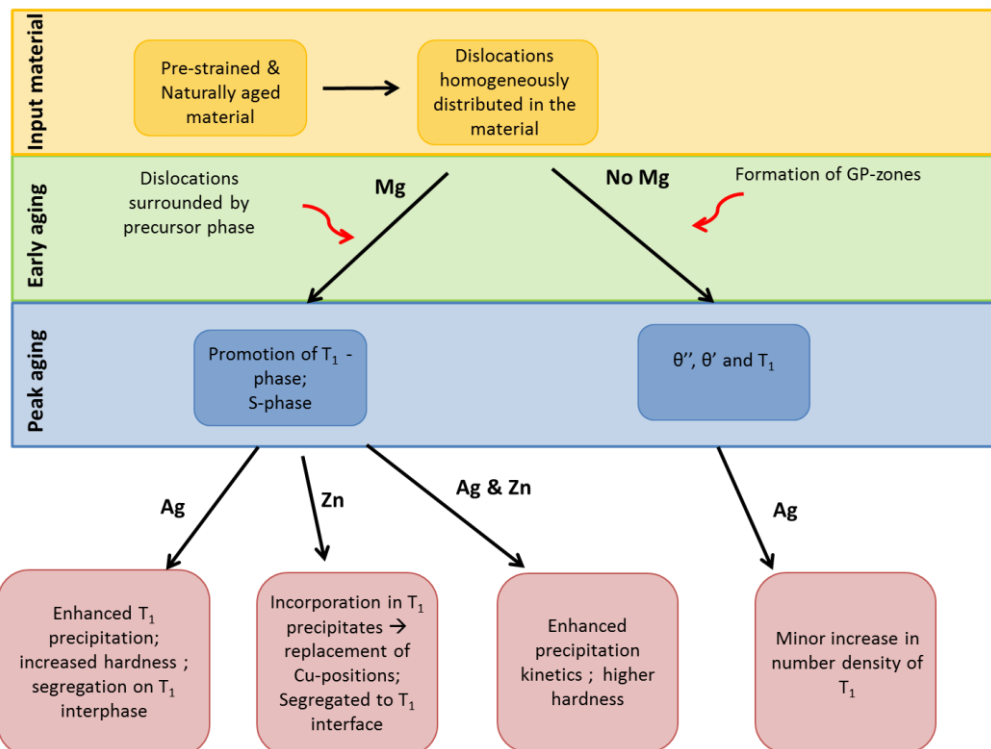


Figure 119: The effect of minor alloying elements during different aging stages.

Figure 119 summarizes the differences in precipitation sequence for different aging conditions. The effect of Mg is seen during early aging condition and separates the investigated alloys into two

different precipitation paths. Mg containing alloys reveal a high number density of T_1 precipitates, whereas Mg-free alloys are characterised by both θ' and T_1 precipitation in the peak-aged conditions. Furthermore, effects of additional minor alloying elements such as Zn and Ag are shortly summarized.

7. Conclusion

In this work, the effect of minor alloying elements on the precipitation path, on precipitation kinetics and on the related hardness in an Al-Cu-Li alloy was determined by different experimental methods. Conventional and atomic resolution TEM has been used to determine the structure and distribution of phases at the nanometre scale. The phase transformation kinetics was determined by hardness, DSC and SAXS measurements. The quantity of minor alloying elements that are necessary to affect precipitation was determined by diffusion couples analysed by hardness and in-situ SAXS measurements. We can now summarize the main findings that were obtained by combining our results.

The effect of Mg on precipitation and strengthening

- Cu-Mg containing precursors were observed on dislocations in Mg containing alloys in early ageing conditions. These precursors, which form very quickly and prior to T_1 precipitates, likely belong to the precipitation sequence leading to the S'/S phases. Very small concentrations of Mg should be sufficient to cover all dislocations by precursors with a composition similar to the S' phase (Al_2CuMg). In the same aging condition, the microstructure of Mg-free alloys was composed of GP zones, nucleated on dislocations. In both alloys sporadic T_1 precipitates are also present.
- During subsequent aging, Mg containing alloys reveal a higher number density of T_1 precipitates, nucleated on dislocations. The nucleation of these phases is likely to be facilitated by the presence of precursors, thereby limiting the precipitation of other phases in competition such as θ' and promoting a fast overall precipitation kinetics, attributed to a faster growth of T_1 phase compared to θ' phase.
- In Mg-free alloys, GP zones evolve to θ' precipitates. The presence of θ' on dislocations probably consumes most of the nucleation sites and consequently the fraction of T_1 is lower than in Mg containing alloys. Since T_1 and θ' compete for the same solute, namely Cu, the growth of T_1 in Mg-free alloys is subsequently impeded by the existing θ' .
- The effect of Mg on precipitation kinetics is observed to be effective when the concentration of Mg reaches 0.1 wt%, with a threshold effect. This abrupt change in precipitation kinetics as a function of alloy composition probably corresponds to the solubility of Mg in the alloy with respect to the formation of the precursors at the dislocations.
- The observed hardening kinetics was in good agreement with precipitation kinetics. Nearly constant hardness differences are found between Mg containing and Mg-free alloys from the

naturally aged up to the 'stabilised' condition. For early aging stages, the hardness difference is attributed to the presence of Cu-Mg precursors on dislocations. The ratio of T_1 and θ' phases, the presence of S phase on the dislocation and the different phase morphologies determine the final hardness. In Mg containing alloys, T_1 dominates the microstructure, which is the more potent strengthener. In Mg-free alloys, the higher proportion of θ' phase leads to a lower hardness.

The effect of Ag on precipitation and strengthening in the Al-Cu-Li alloy

- An addition of Ag, when no Mg is present in the alloy, leads to a higher proportion of T_1 precipitates, possibly due to an effect of Ag on the stacking fault energy of aluminium and to the trapping of vacancies by Ag, which reduces the GP zone formation and consequently θ' formation. The observed higher hardness in the presence of Ag can therefore be attributed to a higher proportion of T_1 .

The effect of Ag and Zn on precipitation and strengthening in an Al-Cu-Li-Mg alloy

- The microstructure and precipitation sequence are qualitatively not modified by the addition of Ag and Zn or a combination of these two elements.
- Ag segregations, identified as bright spots in HAADF-STEM images, were observed at the T_1 /matrix interface during all aging conditions. Similarly, Zn has been shown to incorporate the T_1 precipitates in substitution at the Cu-rich positions and possibly segregate at the precipitate interface. The addition of Ag and Zn slightly accelerates the precipitation kinetics.
- In the presence of Ag and Zn, the alloys show a higher hardness in the 'stabilised' condition, which is related to higher precipitate volume fractions. Enhanced hardening kinetics in the presence of Ag and Zn is associated to more efficient nucleation of the T_1 precipitates.

Perspectives

From these results, a number of perspectives can be drawn. A first set of perspectives arises from the scientific case of the thesis about the nucleation mechanisms in the complex alloys investigated. Although our study has unravelled some of the mechanisms that control the phase transformation path and kinetics and their dependence on alloy composition, a number of unanswered questions remain that deserve further investigation.

- The investigation of the microstructure reveals that there is a relation between precursors and subsequent T_1 precipitation. However, the precise nucleation mechanism of the T_1 phase could not be identified. It is still unclear if T_1 can nucleate on precursors themselves or if

precursors influence the chemical surrounding and thereby facilitate the precipitation of T_1 . Experimentally, this could be determined by in-situ atomic resolution TEM. A challenge of such TEM investigations would be that precursors and T_1 precipitates are not visible in the same zone axis. Another approach would be to perform atomistic simulations. This could provide more understanding on the interaction of precursors and T_1 precipitation. Realistic simulation configurations size might prove very challenging to ab initio methods, though.

- T_1 precipitates were observed sporadically in very early aging conditions. Their appearance was rather unexpected at this stage and it was assumed that they were related to minor nucleation sites like octahedral voids. To isolate the effect of such nucleation sites some work should be performed on undeformed material where dislocations are not dominating the nucleation process. In addition this could provide information on the influence of minor alloying elements on the number density of these heterogeneous nucleation sites.
- Minor alloying elements (Mg, Ag and Zn) are segregated to the T_1 /matrix interface. In addition Zn and Mg were incorporated into the T_1 phase. In order to reveal the precise position inside the T_1 structure, atomic resolution TEM in combination with atomic resolution EDS needs to be performed. For determining the effect of these minor alloying elements on the volume free energy, misfit strain and interfacial energy of the T_1 phase embedded in Al, ab initio modelling or molecular dynamics need to be performed. A challenge for the latter modelling is however to determine reasonable potentials in order to provide useful and exploitable results.

The microstructure in Al-Cu-Li alloys is quite complex and several precipitates are present simultaneously, which all contribute to the final strength, most importantly T_1 , θ' and S' . A quantitative evaluation of the relative quantities of each phase is rendered very complex by the different habit planes and morphologies of the precipitates. This could be at least partially resolved by the use of electron tomography analyses. The ratio of different phases determines the final strength properties of the material, but it remains unsolved to know how their contributions combine. In order to distinguish strengthening contributions of the different phases, simulations of the interaction of dislocations of individual precipitates and combinations of these precipitates would be valuable.

A second set of perspectives arises from the industrial viewpoint. Understanding the effect of minor alloying element on the microstructure may allow improving current alloy solutions and designing new Al-Cu-Li-based alloys.

- The addition of Ag is very costly, but essential to provide required mechanical properties. We have shown that as far as precipitation kinetics and hardness are concerned, it can, at least partly, be replaced by another element (Zn), leading to a significant cost reduction. However, product development demands a wider scope of characterisation to be performed. The influence of minor alloying elements on the mechanical properties such as fatigue, strength, toughness and corrosion resistance is unavoidable to analyse and evaluate, in order to approve the replacement of minor alloying elements or to validate complete new alloy compositions.
- The present study validates the methodology of using a material with a concentration gradient as a powerful tool for alloy design. To produce such gradients, linear friction welding has been shown to be a suitable method, providing high quality joints between dissimilar alloys. This methodology could be further extended to combine small angle X-ray scattering and wide angle X-ray scattering simultaneously for measuring compositionally graded material. This would allow identifying both the shape of precipitates and the crystal structure of the precipitating phase, so that it would be possible to clearly distinguish between the different types of precipitates. In case of the diffusion of Mg, this would add value to the measurements performed in this study, since the formation of T_1 and θ' could probably be distinguished and provide more precise information on their competition.
- Of course, this tool could be applied for other minor alloying elements, but also the main alloying elements such as Cu and Li could be varied. The amount of Li addition is a sensitive parameter since it controls the formation of the δ' phase, which has some contradictory effects on the mechanical properties. It could be also applied to other alloying systems (not only in aluminium), such as Al-Cu which for example would provide good contrast conditions for in-situ SAXS measurements. A possible application would be to measure the influence of Mg for different concentrations in this alloy.

References

- [1] I. J. Polmear, "Recent Developments in Light Alloys," *Materials Transactions, JIM*, vol. 37, no. 1, pp. 12–31, 1996.
- [2] R. J. Rioja and J. Liu, "The Evolution of Al-Li Base Products for Aerospace and Space Applications," *Metall and Mat Trans A*, vol. 43, no. 9, pp. 3325–3337, Sep. 2012.
- [3] J.-P. Immarigeon, R. T. Holt, A. K. Koul, L. Zhao, W. Wallace, and J. C. Beddoes, "Lightweight materials for aircraft applications," *Materials Characterization*, vol. 35, no. 1, pp. 41–67, Jul. 1995.
- [4] M. Lockheed, "Super Lightweight External Tank," NASA Facts.
- [5] J. Silcock, "The structural ageing characteristics of Al–Cu–Mg alloys with copper: magnesium weight ratios of 7: 1 and 2.2: 1," *J. Inst. Met*, vol. 89, pp. 203–210, 1960.
- [6] T. Warner, "Recently-Developed Aluminium Solutions for Aerospace Applications," *Materials Science Forum*, vol. 519–521, pp. 1271–1278, 2006.
- [7] I. Polmear, *Light Alloys: From Traditional Alloys to Nanocrystals*. Butterworth-Heinemann, 2005.
- [8] P. Paufler, "R. W. Cahn, P. Haasen (eds). Physical metallurgy 3rd revised and enlarged edition. North-Holland physics publishing, Amsterdam, Oxford, New York, Tokyo 1983, Part 1 and 2, 2050 pages. ISBN 0–444–86628–0," *Cryst. Res. Technol.*, vol. 20, no. 2, pp. 270–270, Feb. 1985.
- [9] E. Clouet, A. Barbu, L. Laé, and G. Martin, "Precipitation kinetics of Al₃Zr and Al₃Sc in aluminum alloys modeled with cluster dynamics," *Acta Materialia*, vol. 53, no. 8, pp. 2313–2325, May 2005.
- [10] M. Perez, M. Dumont, and D. Acevedo-Reyes, "Implementation of classical nucleation and growth theories for precipitation," *Acta Materialia*, vol. 56, no. 9, pp. 2119–2132, May 2008.
- [11] G. Gottstein, *Physikalische Grundlagen der Materialkunde*, 3rd ed. Springer Lehrbuch, 2007.
- [12] D. A. Porter, K. E. Easterling, and M. Y. Sherif, *Phase Transformations in Metals and Alloys, Third Edition (Revised Reprint) - CRC Press Book*. .
- [13] L. Bourgeois, C. Dwyer, M. Weyland, J.-F. Nie, and B. C. Muddle, "Structure and energetics of the coherent interface between the θ' precipitate phase and aluminium in Al–Cu," *Acta Materialia*, vol. 59, no. 18, pp. 7043–7050, Oct. 2011.
- [14] T. C. Schulthess, P. E. A. Turchi, A. Gonis, and T.-G. Nieh, "Systematic study of stacking fault energies of random Al-based alloys," *Acta Materialia*, vol. 46, no. 6, pp. 2215–2221, März 1998.
- [15] A. Guinier, "Le mécanisme de la précipitation dans un cristal de solution solide métallique.–Cas des systèmes aluminium-cuivre et aluminium-argent," *J. Phys. Radium*, vol. 3, no. 7, pp. 124–136, 1942.
- [16] "Structure of Age-Hardened Aluminium-Copper Alloys : Abstract : Nature." [Online]. Available: <http://www.nature.com/nature/journal/v142/n3595/abs/142569b0.html>.
- [17] V. Gervold, "The structure of Guinier–Preston zones in aluminum–copper alloys," *Acta Crystallographica*, vol. 11, no. 3, pp. 230–230, Mar. 1958.
- [18] S. P. Ringer and K. Hono, "Microstructural Evolution and Age Hardening in Aluminium Alloys: Atom Probe Field-Ion Microscopy and Transmission Electron Microscopy Studies," *Materials Characterization*, vol. 44, no. 1–2, pp. 101–131, Jan. 2000.
- [19] K. Hono and T. Satoh, "Evidence of multi-layered GP zones in al-1.7%Cu alloy," *Philosophical Magazine A*, no. 53, No.4, pp. 4958–504, 1986.
- [20] H. Fujita and C. Lu, "An Electron Microscope study of G. P. Zones and θ' -Phase in Al-1.6 at%Cu Crystals," *Materials Transactions, JIM*, vol. 33, no. 10, pp. 892–896, 1992.
- [21] B. Dubost and P. Sainford, "Durcissement par précipitation des alliages d'aluminium," in *Téchniques de l'ingénieur (M240)*, 1991.

- [22] J. M. Silcock, T. J. Heal, and H. K. Hardy, "Structural Ageing Characteristics of Binary Aluminium-Copper Alloys," *J. Inst. Metals*, vol. Vol: 82, Jan. 1954.
- [23] B. . Gable, A. . Zhu, A. . Csontos, and E. . Starke Jr., "The role of plastic deformation on the competitive microstructural evolution and mechanical properties of a novel Al–Li–Cu–X alloy," *Journal of Light Metals*, vol. 1, no. 1, pp. 1–14, Feb. 2001.
- [24] R. Yoshimura, T. J. Konno, E. Abe, and K. Hiraga, "Transmission electron microscopy study of the evolution of precipitates in aged Al–Li–Cu alloys: the θ' and T1 phases," *Acta Materialia*, vol. 51, no. 14, pp. 4251–4266, Aug. 2003.
- [25] B. Decreus, A. Deschamps, F. De Geuser, P. Donnadieu, C. Sigli, and M. Weyland, "The influence of Cu/Li ratio on precipitation in Al–Cu–Li–x alloys," *Acta Materialia*.
- [26] S. C. Wang and M. J. Starink, "Precipitates and intermetallic phases in precipitation hardening Al–Cu–Mg–(Li) based alloys," *International Materials Reviews, Volume 50, Number 4, August 2005*, pp. 193–215(23).
- [27] A. Deschamps, C. Sigli, T. Mourey, F. de Geuser, W. Lefebvre, and B. Davo, "Experimental and modelling assessment of precipitation kinetics in an Al–Li–Mg alloy," *Acta Materialia*, vol. 60, no. 5, pp. 1917–1928, Mar. 2012.
- [28] P. J. Gregson and H. M. Flower, " δ' precipitation in Al–Li–Mg–Cu–Zr alloys," *J Mater Sci Lett*, vol. 3, no. 9, pp. 829–834, Sep. 1984.
- [29] R. Yoshimura, T. J. Konno, E. Abe, and K. Hiraga, "Transmission electron microscopy study of the early stage of precipitates in aged Al–Li–Cu alloys," *Acta Materialia*, vol. 51, no. 10, pp. 2891–2903, Jun. 2003.
- [30] V. Radmilovic, G. Thomas, G. J. Shiflet, and E. A. Starke Jr., "On the nucleation and growth of Al₂CuMg (S') in Al–Li–Cu–Mg and Al–Cu–Mg alloys," *Scripta Metallurgica*, vol. 23, no. 7, pp. 1141–1146, Jul. 1989.
- [31] G. B. Winkelman, K. Raviprasad, and B. C. Muddle, "Orientation relationships and lattice matching for the S phase in Al–Cu–Mg alloys," *Acta Materialia*, vol. 55, no. 9, pp. 3213–3228, May 2007.
- [32] J. I. Pérez-Landazábal, M. L. Nó, G. Madariaga, and J. S. Juan, "Crystallographic structure of S' precipitates in Al–Li–Cu–Mg alloys," *Journal of Materials Research*, vol. 12, no. 03, pp. 577–580, 1997.
- [33] R. K. W. Marceau, G. Sha, R. Ferragut, A. Dupasquier, and S. P. Ringer, "Solute clustering in Al–Cu–Mg alloys during the early stages of elevated temperature ageing," *Acta Materialia*, vol. 58, no. 15, pp. 4923–4939, Sep. 2010.
- [34] R. K. W. Marceau, C. Qiu, S. P. Ringer, and C. R. Hutchinson, "A study of the composition dependence of the rapid hardening phenomenon in Al–Cu–Mg alloys using diffusion couples," *Materials Science and Engineering: A*, vol. 546, pp. 153–161, Jun. 2012.
- [35] L. Reich, S. P. Ringer, and K. Hono, "Origin of the initial rapid age hardening in an Al-1.7 at.% Mg-1.1 at.% Cu alloy," *Philosophical Magazine Letters*, vol. 79, no. 9, pp. 639–648, 1999.
- [36] S. P. Ringer, T. Sakurai, and I. J. Polmear, "Origins of hardening in aged Al–Cu–Mg–(Ag) alloys," *Acta Materialia*, vol. 45, no. 9, pp. 3731–3744, Sep. 1997.
- [37] Y. Bagaryatsky, "Mechanism of Artificial Aging of Al–Cu–Mg Alloy," *Doklady Akad Nauk SSSR*, pp. 397–400, 1952.
- [38] L. Kovarik, S. A. Court, H. L. Fraser, and M. J. Mills, "GPB zones and composite GPB/GPBII zones in Al–Cu–Mg alloys," *Acta Materialia*, vol. 56, no. 17, pp. 4804–4815, Oktober 2008.
- [39] S. C. Wang and M. J. Starink, "The assessment of GPB2/S" structures in Al–Cu–Mg alloys," *Materials Science and Engineering: A*, vol. 386, no. 1–2, pp. 156–163, Nov. 2004.
- [40] L. Kovarik and M. J. Mills, "Structural relationship between one-dimensional crystals of Guinier–Preston–Bagaryatsky zones in Al–Cu–Mg alloys," *Scripta Materialia*, vol. 64, no. 11, pp. 999–1002, Jun. 2011.
- [41] M. J. Styles, C. R. Hutchinson, Y. Chen, A. Deschamps, and T. J. Bastow, "The coexistence of two S (Al₂CuMg) phases in Al–Cu–Mg alloys," *Acta Materialia*, vol. 60, no. 20, pp. 6940–6951, Dezember 2012.

- [42] S. C. Wang and M. J. Starink, "Two types of S phase precipitates in Al–Cu–Mg alloys," *Acta Materialia*, vol. 55, no. 3, pp. 933–941, Feb. 2007.
- [43] C. B. Zhang, W. Sun, and H. Q. Ye, "Investigation of the crystallography and morphology of the S' precipitate in an Al(CuMg) alloy by HREM," *Philosophical Magazine Letters*, vol. 59, no. 6, pp. 265–271, Jun. 1989.
- [44] T. J. Bastow and A. J. Hill, "Early Stage Hardening in AlCuMg Alloy Studied by ⁶³Cu Nuclear Magnetic Resonance and Positron Annihilation," *Materials Science Forum*, vol. 519–521, pp. 1355–1360, 2006.
- [45] V. Radmilovic, R. Kilaas, U. Dahmen, and G. J. Shiflet, "Structure and morphology of S-phase precipitates in aluminum," *Acta Materialia*, vol. 47, no. 15–16, pp. 3987–3997, Nov. 1999.
- [46] T. S. Parel, S. C. Wang, and M. J. Starink, "Hardening of an Al–Cu–Mg alloy containing Types I and II S phase precipitates," *Materials & Design*, vol. 31, Supplement 1, pp. S2–S5, Jun. 2010.
- [47] J. D. Kim and J. K. Park, "Effect of stretching on the precipitation kinetics of an Al-2.0Li-2.8Cu-0.5Mg(-0.13Zr) alloy," *MTA*, vol. 24, no. 12, pp. 2613–2621, Dec. 1993.
- [48] Z. Feng, Y. Yang, B. Huang, M. Han, X. Luo, and J. Ru, "Precipitation process along dislocations in Al–Cu–Mg alloy during artificial aging," *Materials Science and Engineering: A*, vol. 528, no. 2, pp. 706–714, Dec. 2010.
- [49] K. M. Knowles and W. M. Stobbs, "The structure of {111} age-hardening precipitates in Al–Cu–Mg–Ag alloys," *Acta Crystallographica Section B Structural Science*, vol. 44, no. 3, pp. 207–227, Jun. 1988.
- [50] R. A. Herring, F. W. Gayle, and J. R. Pickens, "High-resolution electron microscopy study of a high-copper variant of weldalite 049 and a high-strength Al-Cu-Ag-Mg-Zr alloy," *Journal of Materials Science*, vol. 28, no. 1, pp. 69–73, 1993.
- [51] S. P. Ringer, B. C. Muddle, and I. J. Polmear, "Effects of cold work on precipitation in Al-Cu-Mg-(Ag) and Al-Cu-Li-(Mg-Ag) alloys," *MMTA*, vol. 26, no. 7, pp. 1659–1671, Jul. 1995.
- [52] K. Hono, M. Murayama, and L. Reich, "Clustering and Segregation of Mg and Ag Atoms during the Precipitation Processes in Al(-Li)-Cu-Mg-Ag Alloys."
- [53] C. R. Hutchinson, X. Fan, S. J. Pennycook, and G. J. Shiflet, "On the origin of the high coarsening resistance of Ω plates in Al–Cu–Mg–Ag Alloys," *Acta Materialia*, vol. 49, no. 14, pp. 2827–2841, Aug. 2001.
- [54] H. K. Hardy and J. M. Silcock, "The phase section at 500 °C and 350 °C of aluminium-rich Aluminium-Copper-Lithium alloys," *Journal of the Institute of Metals*, no. 84, pp. 423 – 428, 1956 1955.
- [55] B. Noble and G. E. Thompson, "T 1 (Al₂CuLi) Precipitation in Aluminium–Copper–Lithium Alloys," *Metal Science, Volume 6, Number 1, 1972*, pp. 167-174(8).
- [56] W. A. Cassada, G. J. Shiflet, and E. A. Starke, "Mechanism of Al₂CuLi (T 1) nucleation and growth," *Metallurgical Transactions A*, vol. 22, no. 2, pp. 287–297, Feb. 1991.
- [57] J. M. Howe, H. I. Aaronson, and R. Gronsky, "Atomic mechanisms of precipitate plate growth in the Al-Ag system—I. Conventional transmission electron microscopy," *Acta Metallurgica*, vol. 33, no. 4, pp. 639–648, Apr. 1985.
- [58] J. M. Howe, H. I. Aaronson, and R. Gronsky, "Atomic mechanisms of precipitate plate growth in the Al-Ag system—II. High-resolution transmission electron microscopy," *Acta Metallurgica*, vol. 33, no. 4, pp. 649–658, Apr. 1985.
- [59] J. C. Huang and A. J. Ardell, "Crystal structure and stability of T 1, precipitates in aged Al–Li–Cu alloys," *Materials Science and Technology*, vol. 3, no. 3, pp. 176–188, 1987.
- [60] W. A. Cassada, G. J. Shiflet, E. A. Starke, and Jr., "The effect of plastic deformation on T1 precipitation," *Le Journal de Physique Colloques*, vol. 48, no. C3, pp. C3–397–C3–406, Sep. 1987.
- [61] V. Radmilovic and G. Thomas, "ATOMIC RESOLUTION IMAGING IN Al-Li-Cu ALLOY," *Le Journal de Physique Colloques*, vol. 48, no. C3, pp. C3–385–C3–396, Sep. 1987.

- [62] J. M. Howe, J. Lee, and A. K. Vasudévan, "Structure and deformation behavior of T1 precipitate plates in an Al- 2Li- 1 Cu alloy," *Metallurgical Transactions A*, vol. 19, no. 12, pp. 2911–2920, Dec. 1988.
- [63] P. Donnadieu, Y. Shao, F. De Geuser, G. A. Botton, S. Lazar, M. Cheynet, M. de Boissieu, and A. Deschamps, "Atomic structure of T1 precipitates in Al–Li–Cu alloys revisited with HAADF-STEM imaging and small-angle X-ray scattering," *Acta Materialia*, vol. 59, no. 2, pp. 462–472, Jan. 2011.
- [64] S. Van Smaalen, A. Meetsma, J. L. De Boer, and P. M. Bronsveld, "Refinement of the crystal structure of hexagonal Al₂CuLi," *Journal of Solid State Chemistry*, vol. 85, no. 2, pp. 293–298, Apr. 1990.
- [65] C. Dwyer, M. Weyland, L. Y. Chang, and B. C. Muddle, "Combined electron beam imaging and ab initio modeling of T1 precipitates in Al–Li–Cu alloys," *Applied Physics Letters*, vol. 98, no. 20, pp. 201909–201909–3, May 2011.
- [66] S. P. Ringer, K. Hono, and T. Sakurai, "The effect of trace additions of Sn on precipitation in Al-Cu alloys: An atom probe field ion microscopy study," *MMTA*, vol. 26, no. 9, pp. 2207–2217, Sep. 1995.
- [67] R. Sankaran and C. Laird, "Effect of trace additions Cd, In and Sn on the interfacial structure and kinetics of growth of θ' plates in Al-Cu alloy," *Materials Science and Engineering*, vol. 14, no. 3, pp. 271–279, Jun. 1974.
- [68] J. M. Silcock and H. M. Flower, "Comments on a comparison of early and recent work on the effect of trace additions of Cd, In, or Sn on nucleation and growth of θ' in Al–Cu alloys," *Scripta Materialia*, vol. 46, no. 5, pp. 389–394, Mar. 2002.
- [69] J. B. M. Nuyten, "Quenched structures and precipitation in Al-Cu alloys with and without trace additions of Cd," *Acta Metallurgica*, vol. 15, no. 11, pp. 1765–1770, Nov. 1967.
- [70] B. Noble, "Theta-prime precipitation in aluminium-copper-cadmium alloys," *Acta Metallurgica*, vol. 16, no. 3, pp. 393–401, Mar. 1968.
- [71] A.-M. Zahra, C. Y. Zahra, K. Raviprasad, and I. J. Polmear, "Effects of minor additions of Mg and Ag on precipitation phenomena in Al–4 mass% Cu," *Philosophical Magazine*, vol. 84, no. 24, pp. 2521–2541, Aug. 2004.
- [72] B. M. Gable, G. J. Shiflet, and E. A. Starke Jr., "The effect of Si additions on Ω precipitation in Al–Cu–Mg–(Ag) alloys," *Scripta Materialia*, vol. 50, no. 1, pp. 149–153, Jan. 2004.
- [73] K. Raviprasad, C. R. Hutchinson, T. Sakurai, and S. P. Ringer, "Precipitation processes in an Al-2.5Cu-1.5Mg (wt. %) alloy microalloyed with Ag and Si," *Acta Materialia*, vol. 51, no. 17, pp. 5037–5050, Oct. 2003.
- [74] A.-M. Zahra, C. Y. Zahra, and M. Dumont, "Effects of Ag or Si on precipitation in the alloy Al-2.5 mass% Cu-1.5 mass% Mg," *Philosophical Magazine*, vol. 85, no. 31, pp. 3735–3754, Nov. 2005.
- [75] C. Macchi, A. Tolley, R. Giovachini, I. J. Polmear, and A. Somoza, "Influence of a microalloying addition of Ag on the precipitation kinetics of an Al–Cu–Mg alloy with high Mg:Cu ratio," *Acta Materialia*, vol. 98, pp. 275–287, Oct. 2015.
- [76] B. T. Sofyan, K. Raviprasad, and S. P. Ringer, "Effects of microalloying with Cd and Ag on the precipitation process of Al–4Cu–0.3Mg (wt%) alloy at 200°C," *Micron*, vol. 32, no. 8, pp. 851–856, 2001.
- [77] T. Saito, C. D. Marioara, S. J. Andersen, W. Lefebvre, and R. Holmestad, "Structural investigation of precipitates with Cu and Zn atomic columns in Al-Mg-Si alloys by aberration-corrected HAADF-STEM," *J. Phys.: Conf. Ser.*, vol. 522, no. 1, p. 012030, Jun. 2014.
- [78] T. Saito, S. Muraishi, C. D. Marioara, S. J. Andersen, J. Røyset, and R. Holmestad, "The Effects of Low Cu Additions and Predeformation on the Precipitation in a 6060 Al-Mg-Si Alloy," *Metall and Mat Trans A*, vol. 44, no. 9, pp. 4124–4135, Apr. 2013.
- [79] T. Saito, S. Wenner, E. Osmundsen, C. D. Marioara, S. J. Andersen, J. Røyset, W. Lefebvre, and R. Holmestad, "The effect of Zn on precipitation in Al–Mg–Si alloys," *Philosophical Magazine*, vol. 94, no. 21, pp. 2410–2425, Jul. 2014.

- [80] R. J. Livak, "The Effects of Copper and Chromium on the Aging Response of Dilute Al-Mg-Si Alloys," *MTA*, vol. 13, no. 7, pp. 1318–1321, Jul. 1982.
- [81] C. D. Marioara, S. J. Andersen, T. N. Stene, H. Hasting, J. Walmsley, A. T. J. V. Helvoort, and R. Holmestad, "The effect of Cu on precipitation in Al-Mg-Si alloys," *Philosophical Magazine*, vol. 87, no. 23, pp. 3385–3413, Aug. 2007.
- [82] K. Matsuda, S. Ikeno, Y. Uetani, and T. Sato, "Metastable phases in an Al-Mg-Si alloy containing copper," *Metall and Mat Trans A*, vol. 32, no. 6, pp. 1293–1299, Jun. 2001.
- [83] C. Cayron, L. Sagalowicz, O. Beffort, and P. A. Buffat, "Structural phase transition in Al-Cu-Mg-Si alloys by transmission electron microscopy study on an Al-4 wt% Cu-1 wt% Mg-Ag alloy reinforced by SiC particles," *Philosophical Magazine A*, vol. 79, no. 11, pp. 2833–2851, Nov. 1999.
- [84] T. Marlaud, A. Deschamps, F. Bley, W. Lefebvre, and B. Baroux, "Influence of alloy composition and heat treatment on precipitate composition in Al-Zn-Mg-Cu alloys," *Acta Materialia*, vol. 58, no. 1, pp. 248–260, Jan. 2010.
- [85] C. D. Marioara, W. Lefebvre, S. J. Andersen, and J. Friis, "Atomic structure of hardening precipitates in an Al-Mg-Zn-Cu alloy determined by HAADF-STEM and first-principles calculations: relation to η -MgZn₂," *J Mater Sci*, vol. 48, no. 10, pp. 3638–3651, May 2013.
- [86] J. Chen, Z. Chen, H. Yan, F. Zhang, and K. Liao, "Effects of Sn addition on microstructure and mechanical properties of Mg-Zn-Al alloys," *Journal of Alloys and Compounds*, vol. 461, no. 1–2, pp. 209–215, Aug. 2008.
- [87] P. Sainfort and B. Dubost, "Coprecipitation hardening in Al-Li-Cu-Mg alloys," *Le Journal de Physique Colloques*, vol. 48, no. C3, pp. C3-407–C3-413, Sep. 1987.
- [88] J. . Huang and A. . Ardell, "Addition rules and the contribution of δ' precipitates to strengthening of aged Al-Li-Cu alloys," *Acta Metallurgica*, vol. 36, no. 11, pp. 2995–3006, Nov. 1988.
- [89] W. A. Cassada, G. J. Shiflet, and E. A. Starke, "The effect of plastic deformation on Al₂CuLi (T 1) precipitation," *Metallurgical Transactions A*, vol. 22, no. 2, pp. 299–306, Feb. 1991.
- [90] B. Decreus, A. Deschamps, F. de Geuser, and C. Sigli, "Influence of Natural Ageing and Deformation on Precipitation in an Al-Cu-Li Alloy," *Adv. Eng. Mater.*, vol. 15, no. 11, pp. 1082–1085, Nov. 2013.
- [91] T. Dorin, A. Deschamps, F. D. Geuser, and C. Sigli, "Quantification and modelling of the microstructure/strength relationship by tailoring the morphological parameters of the T1 phase in an Al-Cu-Li alloy," *Acta Materialia*, vol. 75, pp. 134–146, Aug. 2014.
- [92] J. R. Pickens, F. H. Heubaum, T. J. Langan, and L. S. Kramer, "Al-(4· 5–6· 3) Cu–1· 3 Li–0· 4 Ag–0· 4 Mg–0· 14 Zr alloy weldalite 049.," *International Aluminum-Lithium Conference; 5th; Mar. 27-31, 1989; Williamsburg, VA; United States*, vol. 3, pp. 1397–1414, 1989.
- [93] G. Itoh, Q. Cui, and M. Kanno, "Effects of a small addition of magnesium and silver on the precipitation of T1 phase in an Al-4%Cu-1.1%Li-0.2%Zr alloy," *Materials Science and Engineering: A*, vol. 211, no. 1–2, pp. 128–137, Jun. 1996.
- [94] M. Murayama and K. Hono, "Role of Ag and Mg on precipitation of T1 phase in an Al-Cu-Li-Mg-Ag alloy," *Scripta Materialia*, vol. 44, no. 4, pp. 701–706, März 2001.
- [95] D. L. Gilmore and E. A. S. Jr, "Trace element effects on precipitation processes and mechanical properties in an Al-Cu-Li alloy," *Metall and Mat Trans A*, vol. 28, no. 7, pp. 1399–1415, Jul. 1997.
- [96] B. Gault, F. de Geuser, L. Bourgeois, B. M. Gable, S. P. Ringer, and B. C. Muddle, "Atom probe tomography and transmission electron microscopy characterisation of precipitation in an Al-Cu-Li-Mg-Ag alloy," *Ultramicroscopy*, vol. 111, no. 6, pp. 683–689, May 2011.
- [97] A. K. Khan and J. S. Robinson, "Effect of silver on precipitation response of Al-Li-Cu-Mg alloys," *Materials Science and Technology*, vol. 24, no. 11, pp. 1369–1377, 2008.
- [98] Z. Q. Zheng, S. Q. Liang, H. Xu, C. Y. Tan, and D. F. Yun, "Effect of 0.5% silver on the age hardening behaviour of an Al-Li-Cu-Mg-Zr alloy," *J Mater Sci Lett*, vol. 12, no. 14, pp. 1111–1113, Jan. 1993.

- [99] B.-P. Huang and Z.-Q. Zheng, "Independent and combined roles of trace Mg and Ag additions in properties precipitation process and precipitation kinetics of Al-Cu-Li-(Mg)-(Ag)-Zr-Ti alloys," *Acta Materialia*, vol. 46, no. 12, pp. 4381–4393, Jul. 1998.
- [100] S. Hirose, T. Sato, and A. Kamio, "Effects of Mg addition on the kinetics of low-temperature precipitation in Al-Li-Cu-Ag-Zr alloys," *Materials Science and Engineering: A*, vol. 242, no. 1–2, pp. 195–201, Feb. 1998.
- [101] B. Gault, X. Y. Cui, M. P. Moody, F. De Geuser, C. Sigli, S. P. Ringer, and A. Deschamps, "Atom probe microscopy investigation of Mg site occupancy within δ' precipitates in an Al-Mg-Li alloy," *Scripta Materialia*, vol. 66, no. 11, pp. 903–906, Jun. 2012.
- [102] V. Araullo-Peters, B. Gault, F. de Geuser, A. Deschamps, and J. M. Cairney, "Microstructural evolution during ageing of Al-Cu-Li-x alloys," *Acta Materialia*, vol. 66, pp. 199–208, März 2014.
- [103] T. Honma, S. Yanagita, K. Hono, Y. Nagai, and M. Hasegawa, "Coincidence Doppler broadening and 3DAP study of the pre-precipitation stage of an Al-Li-Cu-Mg-Ag alloy," *Acta Materialia*, vol. 52, no. 7, pp. 1997–2003, Apr. 2004.
- [104] B. Gault, M. P. Moody, J. M. Cairney, and S. P. Ringer, *Atom Probe Microscopy*. Springer Science & Business Media, 2012.
- [105] M. j.-F. Guinel, N. Brodusch, G. Sha, M. a. Shandiz, H. Demers, M. Trudeau, S. p. Ringer, and R. Gauvin, "Microscopy and microanalysis of complex nanosized strengthening precipitates in new generation commercial Al-Cu-Li alloys," *Journal of Microscopy*, vol. 255, no. 3, pp. 128–137, Sep. 2014.
- [106] R. J. Kilmer and G. E. Stoner, "Effect of Zn additions on precipitation during aging of alloy 8090," *Scripta Metallurgica et Materialia*, vol. 25, no. 1, pp. 243–248, Jan. 1991.
- [107] B. M. Gable, M. A. Pana, G. J. Shiflet, and E. A. J. Starke, "The Role of Trace Additions on the T_1 Coarsening Behavior in Al-Li-Cu-X Alloys," *Materials Science Forum*, vol. 396–402, pp. 699–704, 2002.
- [108] D. Tabor, *The hardness of metals*, vol. 10. ClarendonP., 1951.
- [109] W. D. Callister, *Materials science and engineering*, vol. Vol. 7. New York: Wiley., 2000.
- [110] D. B. Williams and C. B. Carter, "The Transmission Electron Microscope," in *Transmission Electron Microscopy*, Springer US, 1996, pp. 3–17.
- [111] "Transmission Electron Microscopy: Fundamentals of Methods and Instrumentation," in *Electron Microscopy of Polymers*, Springer Berlin Heidelberg, 2008, pp. 15–51.
- [112] S. J. Pennycook, "Z-contrast STEM for materials science," *Ultramicroscopy*, vol. 30, no. 1–2, pp. 58–69, Jun. 1989.
- [113] P. Sainfort, "Contribution à l'étude des relations microstructure-durcissement dans les alliages Al-Li et Al-Li-Cu = Contribution to the study microstructure-hardening relations in Al-Li and Al-Li-Cu alloys," Text, I.N.P. Grenoble, 1985.
- [114] O. Glatter and O. Kratky, *Small angle X-ray scattering*, vol. 102. Academic press London, 1982.
- [115] F. De Geuser and A. Deschamps, "Precipitate characterisation in metallic systems by small-angle X-ray or neutron scattering," *Comptes Rendus Physique*, vol. 13, no. 3, pp. 246–256, Apr. 2012.
- [116] T. Dorin, A. Deschamps, F. De Geuser, W. Lefebvre, and C. Sigli, "Quantitative description of the T_1 formation kinetics in an Al-Cu-Li alloy using differential scanning calorimetry, small-angle X-ray scattering and transmission electron microscopy," *Philosophical Magazine*, vol. 0, no. 0, pp. 1–19.
- [117] F. De Geuser, F. Bley, and A. Deschamps, "A new method for evaluating the size of plate-like precipitates by small-angle scattering," *Journal of Applied Crystallography*, vol. 45, no. 6, Nov. 2012.
- [118] F. De Geuser, B. Malard, and A. Deschamps, "Microstructure mapping of a friction stir welded AA2050 Al-Li-Cu in the T_8 state," *Philosophical Magazine*, vol. 94, no. 13, pp. 1451–1462, May 2014.

- [119] J. I. Goldstein, D. E. Newbury, P. Echlin, D. C. Joy, A. D. R. Jr, C. E. Lyman, C. Fiori, and E. Lifshin, "X-Ray Spectral Measurement: WDS and EDS," in *Scanning Electron Microscopy and X-Ray Microanalysis*, Springer US, 1992, pp. 273–339.
- [120] F. Brisset and G. national de M. E. à B. et de microanalyse, *Microscopie électronique à balayage et microanalyses*. EDP Sciences, 2012.
- [121] M. J. Starink, "Analysis of aluminium based alloys by calorimetry: quantitative analysis of reactions and reaction kinetics," *International Materials Reviews*, vol. 49, no. 3–4, pp. 191–226, Jun. 2004.
- [122] W. A. Cassada, G. J. Shiflet, and E. A. Starke Jr., "The effect of plastic deformation on T1 precipitation."
- [123] J. Weertman, "Helical Dislocations," *Phys. Rev.*, vol. 107, no. 5, pp. 1259–1261, Sep. 1957.
- [124] C. R. Hutchinson, A. Fuchsmann, H. S. Zurob, and Y. Brechet, "A novel experimental approach to identifying kinetic transitions in solid state phase transformations," *Scripta Materialia*, vol. 50, no. 2, pp. 285–290, Jan. 2004.
- [125] C. E. Campbell, J.-C. Zhao, and M. F. Henry, "Comparison of experimental and simulated multicomponent Ni-base superalloy diffusion couples," *J Phys Equil and Diff*, vol. 25, no. 1, pp. 6–15, Feb. 2004.
- [126] C. E. Campbell, J.-C. Zhao, and M. F. Henry, "Examination of Ni-base superalloy diffusion couples containing multiphase regions," *Materials Science and Engineering: A*, vol. 407, no. 1–2, pp. 135–146, Oct. 2005.
- [127] C. W. Sinclair, C. R. Hutchinson, and Y. Bréchet, "The Effect of Nb on the Recrystallization and Grain Growth of Ultra-High-Purity α -Fe: A Combinatorial Approach," *Metall and Mat Trans A*, vol. 38, no. 4, pp. 821–830, Apr. 2007.
- [128] E. Contreras-Piedras, H. J. Dorantes-Rosales, V. M. López-Hirata, F. Hernández Santiago, J. L. González-Velázquez, and F. I. López-Monrroy, "Analysis of precipitation in Fe-rich Fe–Ni–Al alloys by diffusion couples," *Materials Science and Engineering: A*, vol. 558, pp. 366–370, Dec. 2012.
- [129] R. S. Mishra and Z. Y. Ma, "Friction stir welding and processing," *Materials Science and Engineering: R: Reports*, vol. 50, no. 1–2, pp. 1–78, Aug. 2005.
- [130] A. Simar, Y. Bréchet, B. de Meester, A. Denquin, and T. Pardoën, "Microstructure, local and global mechanical properties of friction stir welds in aluminium alloy 6005A-T6," *Materials Science and Engineering: A*, vol. 486, no. 1–2, pp. 85–95, Jul. 2008.
- [131] A. A. M. da Silva, E. Arruti, G. Janeiro, E. Aldanondo, P. Alvarez, and A. Echeverria, "Material flow and mechanical behaviour of dissimilar AA2024-T3 and AA7075-T6 aluminium alloys friction stir welds," *Materials & Design*, vol. 32, no. 4, pp. 2021–2027, Apr. 2011.
- [132] A. Vairis and M. Frost, "High frequency linear friction welding of a titanium alloy," *Wear*, vol. 217, no. 1, pp. 117–131, Apr. 1998.
- [133] A. Vairis and M. Frost, "On the extrusion stage of linear friction welding of Ti 6Al 4V," *Materials Science and Engineering: A*, vol. 271, no. 1–2, pp. 477–484, Nov. 1999.
- [134] F. Rotundo, A. Marconi, A. Morri, and A. Ceschini, "Dissimilar linear friction welding between a SiC particle reinforced aluminum composite and a monolithic aluminum alloy: Microstructural, tensile and fatigue properties," *Materials Science and Engineering: A*, vol. 559, pp. 852–860, Jan. 2013.
- [135] J.-C. Zhao, "Combinatorial approaches as effective tools in the study of phase diagrams and composition–structure–property relationships," *Progress in Materials Science*, vol. 51, no. 5, pp. 557–631, Jul. 2006.
- [136] S. Vivès, P. Bellanger, S. Gorsse, C. Wei, Q. Zhang, and J.-C. Zhao, "Combinatorial Approach Based on Interdiffusion Experiments for the Design of Thermoelectrics: Application to the Mg₂(Si,Sn) Alloys," *Chem. Mater.*, vol. 26, no. 15, pp. 4334–4337, Aug. 2014.
- [137] A. Phillion, H. W. Zurob, C. R. Hutchinson, H. Guo, D. V. Malakhov, J. Nakano, and G. R. Purdy, "Studies of the influence of alloying elements on the growth of ferrite from austenite under

- decarburation conditions: Fe-C-Ni alloys," *Metall and Mat Trans A*, vol. 35, no. 4, pp. 1237–1242, Apr. 2004.
- [138] A. Borgenstam and M. Hillert, "Massive transformation in the Fe–Ni system," *Acta Materialia*, vol. 48, no. 11, pp. 2765–2775, Jun. 2000.
- [139] G. Purdy, J. Ågren, A. Borgenstam, Y. Bréchet, M. Enomoto, T. Furuhashi, E. Gamsjäger, M. Gouné, M. Hillert, C. Hutchinson, M. Militzer, and H. Zurob, "ALEMI: A Ten-Year History of Discussions of Alloying-Element Interactions with Migrating Interfaces," *Metall and Mat Trans A*, vol. 42, no. 12, pp. 3703–3718, Sep. 2011.
- [140] S. D. P. Vacher, "Bidimensional strain measurement using digital images. Proc Inst Mech Eng, C, J Mech Eng Sci," *Proceedings of The Institution of Mechanical Engineers Part C-Journal of Mechanical Engineering Science - PROC INST MECH ENG C-J MECH E*, vol. 213, no. 8, pp. 811–817, 1999.
- [141] D. Tsivoulas, "Heterogeneous Nucleation of the T1 Phase on Dispersoids in Al-Cu-Li Alloys," *Metall and Mat Trans A*, vol. 46, no. 6, pp. 2342–2346, Apr. 2015.
- [142] Shih, Jasmine C., Mathew Weyland, and B. C. Muddle., "Precipitation in a high-strength Al–Cu–Li alloy.," *Proc. 12th Int. Conf. on Aluminum Alloys*, Yokohama, pp. 2028–2033, 2010.
- [143] R. N. Wilson and P. G. Partridge, "The nucleation and growth of S' precipitates in an aluminium-2.5% copper-1.2% magnesium alloy," *Acta Metallurgica*, vol. 13, no. 12, pp. 1321–1327, Dec. 1965.
- [144] W. X. Feng, F. S. Lin, and E. A. Starke, "The effect of minor alloying elements on the mechanical properties of Al-Cu-Li alloys," *MTA*, vol. 15, no. 6, pp. 1209–1220, Jun. 1984.
- [145] Y. Nagai, M. Murayama, Z. Tang, T. Nonaka, K. Hono, and M. Hasegawa, "Role of vacancy–solute complex in the initial rapid age hardening in an Al–Cu–Mg alloy," *Acta Materialia*, vol. 49, no. 5, pp. 913–920, Mar. 2001.
- [146] Y. Du, Y. A. Chang, B. Huang, W. Gong, Z. Jin, H. Xu, Z. Yuan, Y. Liu, Y. He, and F.-Y. Xie, "Diffusion coefficients of some solutes in fcc and liquid Al: critical evaluation and correlation," *Materials Science and Engineering: A*, vol. 363, no. 1–2, pp. 140–151, Dezember 2003.
- [147] R. B. Nicholson and J. Nutting, "The metallography of precipitation in an Al-16% Ag alloy," *Acta Metallurgica*, vol. 9, no. 4, pp. 332–343, Apr. 1961.
- [148] I. S. Suh and J. K. Park, "Influence of the elastic strain energy on the nucleation of Ω phase in Al-Cu-Mg(-Ag) alloys," *Scripta Metallurgica et Materialia*, vol. 33, no. 2, pp. 205–211, Jul. 1995.
- [149] A. Deschamps, B. Decreus, F. De Geuser, T. Dorin, and M. Weyland, "The influence of precipitation on plastic deformation of Al–Cu–Li alloys," *Acta Materialia*, vol. 61, no. 11, pp. 4010–4021, Jun. 2013.
- [150] J. F. Nie and B. C. Muddle, "On the form of the age-hardening response in high strength aluminium alloys," *Materials Science and Engineering: A*, vol. 319–321, pp. 448–451, Dec. 2001.
- [151] Z. Gao, J. Z. Liu, J. H. Chen, S. Y. Duan, Z. R. Liu, W. Q. Ming, and C. L. Wu, "Formation mechanism of precipitate T1 in AlCuLi alloys," *Journal of Alloys and Compounds*, vol. 624, pp. 22–26, Mar. 2015.
- [152] S. J. Kang, T.-H. Kim, C.-W. Yang, J. I. Lee, E. S. Park, T. W. Noh, and M. Kim, "Atomic structure and growth mechanism of T1 precipitate in Al–Cu–Li–Mg–Ag alloy," *Scripta Materialia*.

Appendix I - Hardening kinetics at 140°C

The influence of temperature on the hardening kinetics was evaluated by performing heat treatments at a second temperature of 140°C. The artificial aging heat treatment was performed similarly to that at 155°C, including solution heat treatment at 505 °C for 30 minutes, followed by water quench and subsequent pre-deformation. A ramp heating of 20°C/h up to 140 °C was performed followed by artificial aging at 140 °C. The hardness graphs in Figure 120 and Figure 121 show the hardness measurements from the as-quenched condition up to 500 hours of artificial aging at 140 °C.

Figure 120 shows the influence of Mg and Ag. The as-quenched values are very similar for all alloys, and pre-deformation and subsequent natural aging shows the same differences in hardness between Mg containing and Mg-free alloys. This hardness difference stays nearly constant during all aging times. It seems that all alloys, i.e. both Mg containing and Mg-free alloys, reach the hardness plateau after same artificial aging of around 150 hours. For Mg-free alloys it clearly reveals that an Ag addition improves the hardening kinetics compared to AlCuLi. Significant higher end hardness is reached for AlCuLi0.3Ag (158 HV) compared to AlCuLi (145 HV). This shows that Ag affects the nucleation behaviour in AlCuLi alloys and probably favours the T_1 phase formation.

In Mg containing alloys, the addition of 0.1Ag seems to play a minor importance. Both hardening kinetics and end hardness are very similar for AlCuLiMg (170 HV) and AlCuLiMg0.1Ag (172 HV). The addition of 0.3 Ag increases the hardening kinetics, but only to a small extent. The end hardness reached for AlCuLiMg0.3Ag is increased (176 HV) compared to the two other alloys. This hardness value is 3 HV higher than the maximum hardness value for artificial aging at 155 °C.

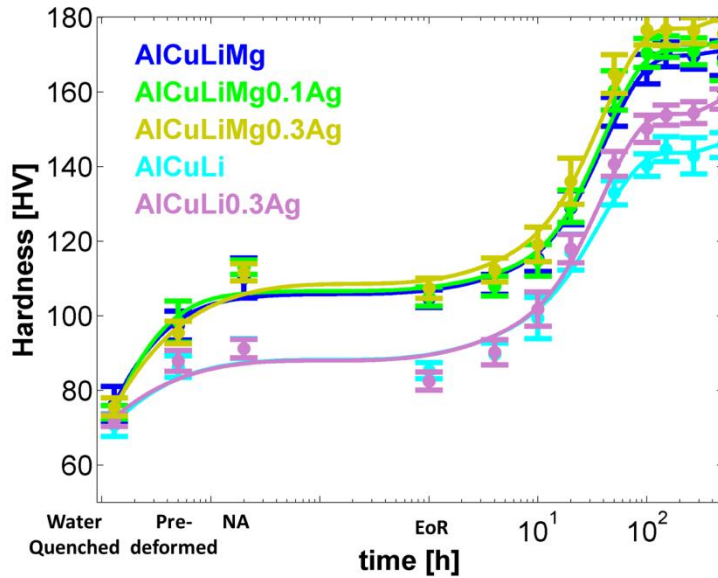


Figure 120: Influence of Mg and Ag on hardness for aging 140 °C.

Figure 121 shows the effect of Ag and Zn additions in the presence of Mg in AlCuLi Alloys. The differences are small. It reveals that the effect of Zn or (0.1Ag and Zn) enhances both hardening kinetics and the reached end hardness, whereas only the addition of 0.1Ag does not really affect the hardening behaviour. The obtained end hardness are 170HV for AlCuLiMg, 172 HV for AlCuLiMg0.1Ag, 175 HV for AlCuLiMgZn and AlCuLiMg0.1AgZn reaches 182 HV, respectively.

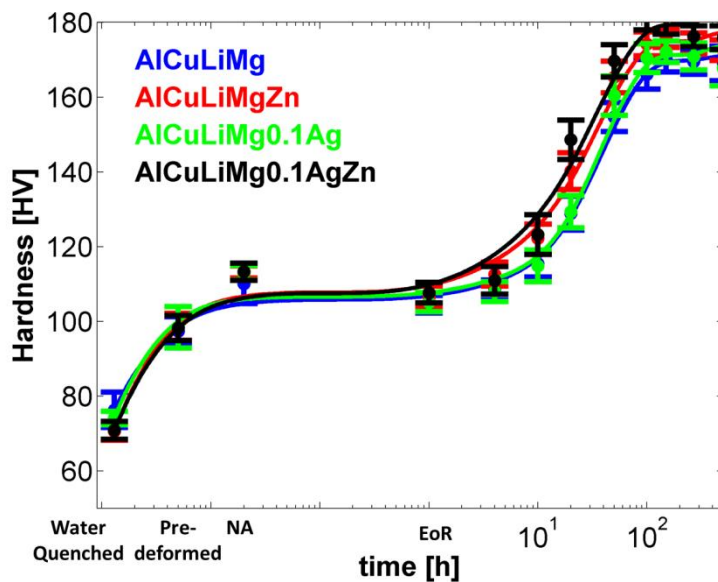


Figure 121: The effect of Ag and Zn on hardness for aging at 140 °C.

In general, the obtained end hardness values are slightly higher than for artificial aging at 155 °C, as summarized in Table 11. Largest differences are observed for AlCuLiMg and AlCuLiMg0.1AgZn for which the hardness value is 8 HV higher as the hardness value reached for artificial aging at 155 °C. The artificial aging time to reach this value is around 7 times longer than the aging time at 155 °C.

Table 11: Comparison of end hardness for two different artificial aging temperatures.

	155 °C	140 °C
AlCuLiMg	162 HV	170 HV
AlCuLiMg0.1Ag	170 HV	172 HV
AlCuLiMg0.3Ag	173 HV	176 HV
AlCuLiMgZn	170 HV	175 HV
AlCuLiMg0.1AgZn	174 HV	182 HV

As a summary, the effect of alloy composition on hardening kinetics is qualitatively similar at 140°C as compared to 155°C. All ageing times are of course much longer due to more sluggish diffusion. The slightly higher end hardness could be due to changes in nucleation, in precipitate morphology, or in end volume fraction. No detailed microstructural analysis was performed on these ageing conditions to discriminate between these effects.

Appendix II

The pre-print version of the paper which will be published in Scripta Materialia 2015 is attached.



Contents lists available at ScienceDirect

Scripta Materialia

journal homepage: www.elsevier.com/locate/scriptamat

A combinatorial approach for studying the effect of Mg concentration on precipitation in an Al–Cu–Li alloy

E. Gumbmann^{a,b,c}, F. De Geuser^{a,b}, A. Deschamps^{a,b,*}, W. Lefebvre^d, F. Robaut^e, C. Sigli^c

^a Université Grenoble Alpes, SIMAP, F-38000 Grenoble, France

^b CNRS, SIMAP, F-38000 Grenoble, France

^c Constellium Technology Center, CS 10027, 38341 Voreppe Cedex, France

^d Groupe de Physique des Matériaux, UMR CNRS 6634, Normandie University, University of Rouen and INSA Rouen, 76801 St. Etienne du Rouvray, France

^e Consortium des Moyens Technologiques Communs, Grenoble-INP, 38402 St. Martin d'Hères, France

ARTICLE INFO

Article history:

Received 27 May 2015

Revised 30 July 2015

Accepted 30 July 2015

Available online xxxxx

Keywords:

Precipitation

Aluminium alloy

Combinatorial metallurgy

Small-angle X-ray scattering

ABSTRACT

We apply a combinatorial approach to study the influence of Mg concentration on the precipitation kinetics in an Al–Cu–Li alloy using a diffusion couple made by linear friction welding. The precipitation kinetics is monitored in the composition gradient material using simultaneous space and time-resolved in-situ small-angle X-ray scattering measurements during ageing, and the strengthening of the precipitates is evaluated by micro-hardness profiles. This data provides an evaluation of the amount of Mg necessary to promote precipitation of the T_1 -Al₂CuLi phase.

© 2015 Acta Materialia Inc. Published by Elsevier Ltd. All rights reserved.

Al–Cu–Li alloys are currently experiencing a strong interest due to their combination of low weight, high strength and high toughness suitable for aerospace applications. In the latest generation of alloys (such as commercialized as AIRWARE[®]), the main strengthening phase sought is the T_1 phase of bulk composition Al₂CuLi. The bulk structure of this equilibrium phase was resolved by Van Smaalen et al. [1]. In aluminium, it appears as extremely thin platelets on $\{111\}_{Al}$ planes with aspect ratio up to 50–100. The structure of this phase embedded in the Al matrix has been resolved in detail by Donnadiu et al. [2] and Dwyer et al. [3]. Since earlier studies, it is known that obtaining an efficient precipitation strengthening in this system requires the addition of dislocations [4,5] and of minor solute elements, out of which the most prominent ones are Mg and Ag [5–7]. These elements have been shown to be included in the composition of the nanoscale T_1 phase [8,9]. Recently, atom probe tomography has demonstrated that they segregate to the T_1 /Al interface, and that the Mg atoms are involved in a co-clustering or co-precipitation with Cu, linked with dislocations, very early during the ageing process [10]. Now that the qualitative role of the minor solute elements on the precipitation of T_1 has been evidenced, there is a need to understand what solute content is necessary to obtain the desired effect. In particular, the

effect of minor solute element concentration on the precipitation of Cu and Li may be strongly non-linear, and even non monotonous as there may be a competition for solute (especially Cu) from the added Mg atoms that may hinder the formation of T_1 instead of promoting it. A traditional alloy series fabrication with a discrete distribution of minor solute concentrations would be extremely cumbersome and may not evidence some of these non-linear events. Instead, we propose to use a combinatorial approach using compositional gradient materials [11], where the main alloying content is kept constant and one minor solute content is varied. This approach has already been used to study composition effects on precipitation hardening in Al–Cu–Mg alloys [12]. However in this study the composition gradient was created simply by inter-diffusion between two alloys, which restricted the dimension of the concentration gradient zone to a few 100 μ m, and left at the interface a brittle oxide layer that prevented any mechanical loading of the gradient material. These characteristics are not suitable to the needs of our study for two reasons. First, because the study of T_1 precipitation requires the introduction of plastic deformation after the solution treatment, which would be impossible with the presence of an oxide layer within the inter-diffusion zone. Second, because we aim at characterizing the precipitation kinetics by small-angle X-ray scattering within the diffusion couple, using simultaneous time and space-resolved measurements, so that a full map of precipitation kinetics in the composition space is obtained in a single experiment. Such measurements require a

* Corresponding author at: Université Grenoble Alpes, SIMAP, F-38000 Grenoble, France.

E-mail address: alexis.deschamps@grenoble-inp.fr (A. Deschamps).

relatively large extension of the composition gradient compared to the spatial resolution of the experiment, which is limited by the beam size (1 mm) of the X-ray beam in SAXS measurements. Therefore, we have chosen to join the alloys of different composition by linear friction welding, which has been shown to be an efficient method for materials of dissimilar composition [13], ensuring a planar interface between the two welded materials, free of any oxide layer that is expelled by plastic flow during the welding process.

The two studied alloys have the same base composition of 3.5% Cu and 0.9% Li (in wt). One of the two alloys has in addition 0.35 wt% Mg. The two alloys were joined as plates of thickness 25 mm by linear friction welding performed by Thompson Friction Welding. Fig. 1 shows an optical micrograph of the interface between the two materials after welding and after the subsequent inter-diffusion treatment (see below). It is adequately planar and defect-free, so that the initial composition step between the two materials is well defined. Diffusion of Mg was activated by subjecting the joined couple to a homogenization heat treatment at 515 °C for 14 days. Slices of 6.5 mm in thickness parallel to the concentration gradient were cut. Subsequent hot rolling was then used to further enlarge the width of the diffusion gradient. The pre-heating temperature was 500 °C and the thickness reduction from 6.5 to 1.8 mm was performed by a single rolling step. The evolution of the composition gradient, measured by electron probe micro analysis (EPMA) (20 keV, 300 nA) during these different steps is shown in Fig. 2. The Mg gradient shows initially a sharp step and ends with a 10 mm length. The Cu concentration (no shown here) remains constant in all process steps. One can emphasize at this stage that such a large characteristic length of the diffusion process ensures that, at the scale of the precipitation process (100 nm at most) the local composition of the alloy can be considered as constant so that no coupling between the macroscopic solute diffusion and the microscopic precipitation mechanisms needs to be considered.

Following the hot rolling step, a solution treatment was performed at 505 °C for 30 min, using a slow heating ramp in order to avoid recrystallization. This step was used in order to obtain a controlled rolling texture, which, in certain conditions, can facilitate the SAXS pattern interpretation [14]. Optical microscopy observations confirmed that no recrystallization happened. Following a quench in cold water, a pre-deformation of 4% plastic strain (tensile) was introduced in order to introduce dislocations and facilitate the nucleation of the T₁-phase [4,5,15]. The tensile straining was performed normal to the original weld plane interface (materials loaded in series). It has been checked previously that the addition of 0.35% Mg to this alloy did not change significantly the flow stress of the Al–Cu–Li alloy in the as-quenched



Fig. 1. Optical micrographs of the linear friction weld (interface plane is vertical in the centre of the micrograph) in the as-welded state (top) and after the interdiffusion heat treatment (bottom).

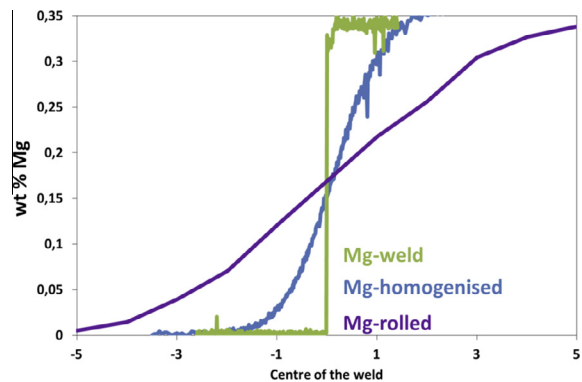


Fig. 2. Diffusion gradient measured by EPMA after linear friction welding (green), after 14 days homogenization treatment (blue) and after rolling (purple). (For interpretation of the references to colour in this figure legend, the reader is referred to the web version of this article.)

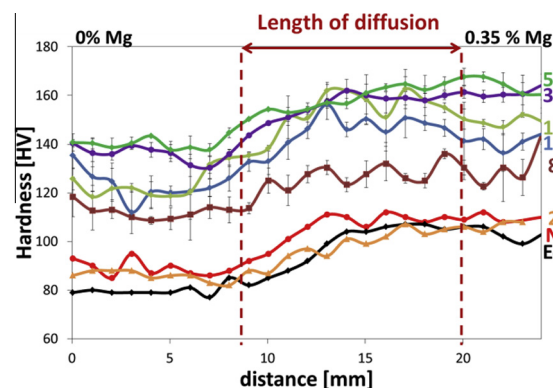


Fig. 3. Micro-hardness profiles across the diffusion gradient for different ageing times at 155 °C.

state so that the plastic strain (measured by an extensometer across the diffusion zone) was homogeneously distributed for all compositions. The material was kept for 3 days at room temperature before artificial ageing was performed. The precipitation ageing treatment included a ramp heating of 20 °C/h to 155 °C and further isothermal ageing at 155 °C for several days.

Precipitation kinetics was measured by small-angle X-ray scattering (SAXS). This method has been shown to be able to quantify in-situ the kinetics of T₁ phase precipitation in several recent studies [14,16,17]. It has also been shown to be capable of mapping heterogeneous microstructures in friction stir welds [18]. In the present case, we have combined spatial and time resolutions to perform a simultaneous evaluation of precipitation kinetics for the whole diffusion gradient. SAXS measurements were performed on a laboratory rotating anode at the Cu K α wavelength of 0.154 nm (8.048 keV), with a beam size diameter at the sample of 1 mm. The SAXS set-up allowed measurements in a range of scattering vectors of 0.06–0.4 Å⁻¹. The ageing treatment was conducted for more than 100 h of ageing in a specially designed furnace, which was placed inside the sample vacuum chamber. By displacing the sample in between each measuring point, the complete composition gradient was scanned. A 2D DECTRIS PILATUS[®] photon counter camera was used for data acquisition and the counting time was 100 s. 18 measurements points, separated by 1 mm steps, were acquired across the sample, allowing a time resolution for a given position in the couple (corresponding to a given Mg concentration) of 30 min. The acquired 2D scattering data was converted to intensity vs. scattering vector by radial averaging

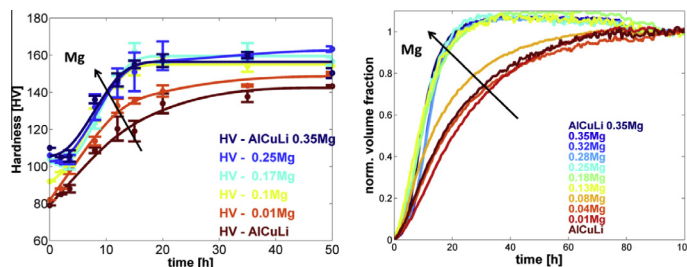


Fig. 4. (a) Evolution of micro-hardness with ageing time for a series of Mg concentrations characterized by their position within the diffusion gradient; (b) evolution of normalized precipitate volume fraction measured from the SAXS data as a function of ageing time at 155 °C for a series of Mg concentrations characterized by their position within the diffusion gradient.

[19]. In parallel, micro-hardness measurements were performed across a diffusion couple aged for different times in an oil bath. Measurements were made with a distance of 1 mm between each measurement with a Buehler Tukon™1102 automatic hardness machine using an applied load of 500 g with an indentation time of 10 s.

2. Hardness measurements

Fig. 3 shows the evolution of hardness across the diffusion gradient measured after different ageing times at 155 °C (EoR corresponds to the end of the heating ramp to 155 °C). There is a clear effect of Mg concentration on the hardness distribution in the composition gradient, at all stages of the ageing treatment. At the end of the ageing treatment (the maximum hardness stays constant for several hours of artificial ageing and resembles a plateau), a difference of 20 HV is observed between the Mg and non-Mg containing alloys. This difference is enhanced to almost 40 HV at intermediate times (12 h at 155 °C), showing that Mg promotes an acceleration of precipitation kinetics in the Al–Cu–Li alloy. The effect of Mg concentration is better evidenced by plotting the evolution of hardness vs. time for a series of Mg concentrations present in the diffusion couple (Fig. 4a). This figure shows that the hardening kinetics is indeed more sluggish in the Mg free Al–Cu–Li alloy as compared to the Mg-containing alloys. Looking at the alloys with highest and lowest Mg-content, namely AlCuLi0.35 Mg and AlCuLi, in Fig. 4a, it reveals that the initial hardening is faster for AlCuLiMg than for AlCuLi. Furthermore, maximum hardness for AlCuLiMg is reached after 15 h, whereas it takes up to 50 h at 155 °C for AlCuLi to reach maximum hardness. Moreover, the effect of Mg content on the precipitation kinetics is not linear. Above 0.1% Mg, the hardening kinetics is less dependent on Mg concentration therefore demonstrating saturation behaviour.

3. SAXS measurements

An evaluation of the volume fraction of precipitates was obtained from the SAXS data in the following way. First, it was assumed that no precipitates were present at the end of the heating ramp (which corresponds also to minimum hardness). Second, the volume fraction was assumed to be stabilized after 100 h of ageing based on earlier studies [16,17]. In between, the normalized volume fraction was calculated, proportional to the integrated intensity Q_0 [19]. One should remain careful about the interpretation of this normalized volume fraction, because changes of composition may promote changes of precipitate types in this complex system; in particular, the absence of Mg may promote formation of some θ' phase at the expense of the T_1 phase, with a resulting different X-ray contrast. With this in mind, Fig. 4b shows the evolution of normalized volume fraction with ageing time for different Mg concentrations in the diffusion gradient. Since the

diffusion gradient covers a length of 10 mm, but 18 mm were measured, several positions in the beginning and at the end of the gradient have the same composition. For the sake of clarity we show only one measurement for each composition. Similarly to the micro-hardness results, a strong effect of Mg concentration is evidenced, with faster precipitation kinetics in the Mg-rich regions. Around a Mg concentration of 0.1–0.2%, the transition between slow and fast precipitation kinetics is observed, which is also consistent with the change observed in the hardening kinetics. Both curves presented in Fig. 4a and b allow comparing hardening kinetics and the evolution of the precipitate volume fraction next to each other. The two results do correspond particularly well. In a recent study, Dorin et al. [17] have actually shown that the relationship between T_1 precipitate volume fraction and yield strength is almost linear when their thickness is kept constant, although the detail of the relationship is more complicated.

In conclusion, we have demonstrated a methodology for mapping the precipitation kinetics continuously in a material containing a composition gradient. This methodology involves the fabrication of a diffusion couple of sufficient dimensions using Linear Friction Welding followed by inter-diffusion heat treatment and hot rolling. This material is then subjected to an ageing treatment in a SAXS apparatus, where simultaneous space and time resolved measurements allow the precipitation kinetics characterization for a large number of compositions across the gradient. This methodology has been applied to evaluate the effect of Mg concentration on the precipitation kinetics and strengthening of an Al–Cu–Li alloy. We evidence that the addition of Mg accelerates the kinetics of precipitation and increases the strengthening capability. However the influence of Mg concentration on the precipitation kinetics is more pronounced for low additions. Our results help to determine the minimum amount of Mg necessary (around 0.1–0.2 wt%) to observe this effect. More detailed studies are under way to better understand the effect of Mg on the precipitation mechanisms and will be published elsewhere.

References

- [1] S. Van Smaalen, A. Meetsma, J.L.D. Boer, P.M. Bronsveld, J. Solid State Chem. 85 (2) (1990) 293–298.
- [2] P. Donnadieu, Y. Shao, F. De Geuser, G.A. Botton, S. Lazar, M. Cheynet, M. de Boissieu, A. Deschamps, Acta Mater. 59 (2) (2011) 462–472.
- [3] C. Dwyer, M. Weyland, L.Y. Chang, B.C. Muddle, Appl. Phys. Lett. 98 (20) (2011) 201909.
- [4] W.A. Cassada, G.J. Shiflet, E.A.J. Starke, Metall. Trans. A 22A (February) (1991) 287–297.
- [5] S.P. Ringer, B.C. Muddle, I.J. Polmear, Metall. Mater. Trans. A 26A (July) (1995) 1659–1671.
- [6] A.K. Khan, J.S. Robinson, Mater. Sci. Technol. 24 (11) (2008) 1369–1377.
- [7] B.P. Huang, Z.Q. Zheng, Acta Mater. 46 (12) (1998) 4381–4393.
- [8] M. Murayama, K. Hono, Scr. Mater. 44 (4) (2001) 701–706.
- [9] B. Gault, F. de Geuser, L. Bourgeois, B.M. Gable, S.P. Ringer, B.C. Muddle, Ultramicroscopy 111 (6) (2011) 683–689.
- [10] V. Araullo-Peters, B. Gault, F. de Geuser, A. Deschamps, J.M. Cairney, Acta Mater. 66 (2014) 199–208.

- [11] T. Miyazaki, *Prog. Mater. Sci.* 57 (6) (2012) 1010–1060.
- [12] R.K.W. Marceau, C. Qiu, S.P. Ringer, C.R. Hutchinson, *Mater. Sci. Eng. Struct. Mater. Prop. Microstruct. Process.* 546 (2012) 153–161.
- [13] F. Rotundo, A. Marconi, A. Morri, A. Ceschini, *Mater. Sci. Eng. -Struct. Mater. Prop. Microstruct. Process.* 559 (2013) 852–860.
- [14] F. De Geuser, F. Bley, A. Deschamps, *J. Appl. Crystallogr.* 45 (6) (2012).
- [15] B. Gable, A. Zhu, A. Csontos, E. Starke Jr., *J. Light Met.* 1 (1) (2001) 1–14.
- [16] B. Decreus, A. Deschamps, F. De Geuser, P. Donnadieu, C. Sigli, M. Weyland, *Acta Mater.* 61 (2013) 2207–2218.
- [17] T. Dorin, A. Deschamps, F. De Geuser, C. Sigli, *Acta Mater.* 75 (2014) 134–146.
- [18] F. De Geuser, B. Malard, A. Deschamps, *Philos. Mag.* 94 (13) (2014) 1451–1462.
- [19] F. De Geuser, A. Deschamps, *C. R. Phys.* 13 (3) (2012) 246–256.